THE UNIVERSITY OF ADELAIDE

DOCTORAL THESIS

Nuclear Structure Studies in the Quark-Meson Coupling Model

Author:
Kay Marie MARTINEZ

Supervisor:
Prof. Anthony THOMAS

A thesis submitted in fulfillment of the requirements
for the degree of Doctor of Philosophy
in the

Special Research Centre for the Subatomic Structure of Matter
School of Physical Sciences

September 15, 2020

Contents

List of Figures

List of Tables

THE UNIVERSITY OF ADELAIDE

Abstract

Faculty of Sciences
School of Physical Sciences

Doctor of Philosophy

Nuclear Structure Studies in the Quark-Meson Coupling Model

by Kay Marie MARTINEZ

The Quark-Meson Coupling (QMC) model provides a description for nuclear structure starting from the level of quarks within nucleons so that the nuclear interaction is described through the exchange of mesons. Apart from the central contribution derived from the model, spin-orbit and spin-tensor terms arise naturally within the QMC framework and are fully expressed in terms of existing QMC parameters, thus adding no new parameters in the model. The latest version, QMCπ-III, further derives the pairing interaction from the QMC model, so that the total number of parameters is significantly reduced to only five.

The focus of this research is on the parameter optimisation of the QMC model throughout the stages of its development and its implementation for the study of finite nuclei. The final sets of QMC parameters at each stage, consistent with nuclear matter properties, were determined using a robust optimisation procedure and then relevant statistics such as parameter errors and correlations were computed. The model was then used to investigate several nuclear properties for even-even nuclei across the present nuclear landscape.

The model showed a continuous improvement in comparison with experiment as the model developed, reproducing experimental data for various energy and radius observables even for nuclei which were not included in the fit. In QMCπ-III, binding energy and *rms* charge radius deviations from experiment were decreased to 0.3% and 0.5%, respectively, for all even-even nuclei with available data. Furthermore, calculations were extended for nuclear observables which had not been part of the fitting procedure. QMC results for separation energies and deformations up to the superheavy region, were shown to be compatible with data, as well as with results from other existing nuclear models.

Thesis Declaration

I certify that this work contains no material which has been accepted for the award of any other degree or diploma in my name, in any university or other tertiary institution and, to the best of my knowledge and belief, contains no material previously published or written by another person, except where due reference has been made in the text. In addition, I certify that no part of this work will, in the future, be used in a submission in my name, for any other degree or diploma in any university or other tertiary institution without the prior approval of the University of Adelaide and where applicable, any partner institution responsible for the joint-award of this degree.

I acknowledge that copyright of published works contained within this thesis resides with the copyright holder(s) of those works.

I also give permission for the digital version of my thesis to be made available on the web, via the University's digital research repository, the Library Search and also through web search engines, unless permission has been granted by the University to restrict access for a period of time.

Signed:

Date: September 15, 2020

Acknowledgements

My Ph.D. endeavour would have never been possible without the support and guidance of my principal supervisor, Prof. Anthony W. Thomas, who, from my application to the program up to completion, was always there to provide help and advice. His overall supervision through regular meetings and updates directed my research path until I am able to come to this point.

I would also like to thank two of our close research collaborators, Pierre A. M. Guichon and Jirina R. Stone, who have greatly contributed to my research. Our numerous discussions and their regular travels to Adelaide, encouraged and challenged me to further my research.

Life in Adelaide and being away from home would have been unbearable if not for my Filipino friends, from whom I continuously gathered support. To Rio, Mark, Jen, Jere, Ember, Glen, Mike, Elai, Edhen and Nory, maraming salamat!

Friends from our Physics office have also been helpful in several discussions, related or not to Physics, and in keeping my sanity. To Theo, Joe, Sofija and Skye, thank you for the interesting conversations over lunch, snacks and coffee.

Though I am geographically far, my closest friends in the Philippines never failed to keep in touch and check if I was doing fine. Thanks to Ate Ria, Diane, Marj, Ate Shiela for making me feel connected and updated with the happenings back home, and for constantly encouraging me to push through my studies. Thanks also to Mamoi and GP for constant communication despite already being in the UK.

My deepest gratitude to my parents, Ermar and Nenette, for their undying love and support. Since I was young, they have encouraged me to become successful in whatever I do and provided whatever I need so I can reach my dreams and goals. My siblings, Kim and Cute, have also been my source of motivation in every endeavour.

My dream to obtain a Ph.D. Physics degree was greatly inspired by the love of my life, my husband, Eliel, who actually loves physics more than I do. His enthusiam, passion and love for knowledge fuels me to become better until I am able to finish my studies. His unwavering love, care and support even when I was away, kept me intact despite all the challenges. All my hardwork are dedicated to our new little family.

Above all, I would like to thank my personal Lord and Saviour, Jesus Christ, from whom all blessings flow.

To my parents, Ermar and Nenette;
my siblings, Kim and Cute;
my husband, Eliel, and our baby . . .

Chapter 1

Introduction

1.1 Background

In the early nuclear theory, nucleons which compose the atomic nucleus were considered as structureless point particles and the nuclear forces between them were investigated on that basis. Several studies were made in this framework to understand nuclear structure which include effective field theory methods such as quantum hadrodynamics (QHD) [1, 2], and density dependent approaches like Gogny forces [3] and relativistic mean field (RMF) models [4, 5]. Numerous researchers have dealt in one of these frameworks in order to describe nucleon-nucleon (NN) interaction and to simulate nuclear properties consistent with experimental results.

A significant advance in understanding nuclear structure was made possible by working at the level of quarks and mesons within the nuclear environment. Ref. [6] reports this new outlook in describing nuclear structure and nuclear matter properties posing another perspective in the study of the strong nuclear force. The paper argued that the structure of a nucleon is altered when bound in the nuclear medium contrary to the conventional notion of being unaltered when it is deemed free.

The subnucleonic level prescription, referred to as the Quark-Meson Coupling (QMC) model, was first proposed by Guichon in 1988 [7] to explain the mechanism of nuclear matter saturation. The formalism is built on the quark composition of the nucleon such that NN interaction is characterized by their meson exchange and the strength of interaction is described by QMC parameters. In its original framework, QMC utilises the MIT bag model of a nucleon where the quark field equations are expressed as a function of spacetime coordinates of quarks within the bag, along with the bag radius and the coupling constants of quarks to the mean scalar and vector meson fields, $\bar{\sigma}$ and $\bar{\omega}$ respectively. Further,

the model assumes that nucleon bags do not overlap and that quarks, moving relativistically, will have enough time to adjust in the time-frame of nucleon motion. The advantage of the QMC model is that it takes into account the relativistic nature of quarks which results in a more rapid increase in ω-exchange repulsion than the σ-exchange attraction as the nucleon density increases thereby providing an explanation for nuclear matter saturation.

Another advantage of the QMC model is that it naturally incorporates all the contributions present in other established mean-field models, while the number of model parameters necessary to calculate various nuclear properties is significantly reduced. That is, while other models require ten or more parameters, the QMC model in its latest development, only needs five. In addition, the QMC parameters have direct physical significance as they describe the strength of NN interaction through the coupling of quarks to mesons, as opposed to the arbitrary parameters in other nuclear models [8, 9, 10]. More importantly, the QMC model can be subjected to fewer parameter variations, with only one final parameter set at every stage of model development, so that parametrisations are not as varied as in other existing models. Furthermore, application of the model promises a possible explanation for the nuclear EMC effect and poses a reconsideration of nuclear properties which can be subjected to future experimental verifications [6].

The study of nuclear structure and interactions at the subnucleonic level, gives new insights in understanding subatomic forces, most importantly the strong nuclear force which is not yet fully understood up to this day. Quantum chromodynamics (QCD), a local gauge field theory, is by far the leading theory to explain fundamental strong interactions, starting at the level of quarks and gluons. The QMC model, though employing mean-field approximations, is already built from the quark level so that it paves a way to a novel and arguably better picture of internucleon and even other hadron-hadron interactions.

1.2 Related literature

1.2.1 QMC model for infinite nuclear matter

Since the introduction of the simple QMC model, various studies have been devoted to its applications and development. Ref. [11] extended the model by adding some density dependence of the bag constant; one by coupling it directly to the scalar meson field and another by expressing it in terms of the effective nucleon mass. The latter resulted in a reduced bag constant as the nucleon density

increased, thereby substantiating the assertion that nucleon structure is affected in medium. This is also true when meson exchange effects and pionic contributions are incorporated to the simple QMC model where the readjustment of QMC constants is necessary to account for the corresponding responses of in-medium hadrons [12]. Furthermore, extending the model by adding Fock terms to better account for the exchange and pionic contributions, increased the single-nucleon scalar and vector potentials which is expected to play a role in the level splitting of finite nuclei. It also opened the question of how chiral symmetry affects in-medium nucleons and nuclear matter properties [13].

In another attempt to address chiral symmetry in the QMC model, gluonic exchange and pionic effects were included through a self-consistent approach by employing the cloudy bag model, instead of the MIT bag in the original QMC model, for symmetric nuclear matter having equal number of protons and neutrons [14]. This chiral QMC (CQMC) model investigated within the effective field theory adds an axial vector coupling constant which accounts for axial symmetry breaking. Results of CQMC show that the scalar polarisability, which characterises the quark response in the scalar meson field, decreases as the baryon density increases leading to nuclear matter saturation, and thus attaining an incompressibility value closer to experimental results compared to the traditional QHD calculations.

Nuclear matter can be studied within three broad categories: the symmetric nuclear matter (SNM) where there are equal number of protons and neutrons, pure neutron matter (PNM), and asymmetric nuclear matter (ANM) where there is neutron excess in the nuclei. In Ref. [15], the QMC model was studied for dense baryon matter applications. Nuclear properties like binding energy per particle and symmetry energy were calculated for pure neutron matter and symmetric nuclear matter and checked against the Skyrme counterpart. It was found that at higher densities, hyperons are present which contributes to the reduction of the maximum mass of neutron stars. The role of hyperons in neutron stars were further investigated in Ref. [16] where constraints due to its inclusion in the QMC equation of state were discussed.

Another development in QMC model was made in Ref. [17] where the simple QMC model was extended to include full Fock terms in addition to the Hartree mean-field approximation and applied to the case of infinite SNM, PNM, ANM, and even to accommodate a broader case of dense nuclear matter in β-equilibrium. Calculations for SNM and PNM in terms of the density-dependence of pressure falls within the upper limits of observational data even when they are constrained

due to charge symmetry and strangeness conservation. For the ANM case, computations are centered on the symmetry energy which is expressed in terms of an expansion containing its slope, curvature, and skewness. They found that the additional Fock terms result in a curvature for the symmetry energy as with its slope and although their values are larger, they still fall within the broader range of experimental and theoretical results. Furthermore, calculated values around nuclear matter densities agree with the chiral effective theory for PNM densities, though they give a stiffer equation of state compared to other models above saturation density values.

In Ref. [18], a modified QMC (MQMC) approach is presented wherein relativistic independent quarks in an equally mixed scalar-vector harmonic potential is considered instead of the MIT bag model for the nucleon in the original QMC configuration. Further in this new set-up, they have taken into account the spurious center of mass corrections, one-gluonic exchange and pionic effects due to chiral symmetry restoration. Nuclear matter saturation properties are then computed for SNM for chosen quark masses and compared to the results from simple QMC and other point-like nucleon models. Ref. [19] further enhanced the MQMC model by adding the previously neglected isovector ρ meson contribution and is then utilised to study symmetry energy of ANM. The symmetry energy equation used is the same as that in Ref. [17] where it is taken as the difference between the binding energy per nucleon in PNM and in SNM. It must be reiterated that this approximation is only valid under the earlier stated assumptions in Ref. [17].

1.2.2 QMC model: Towards finite nuclei

All of the mentioned modifications to the original QMC model aimed to exploit the present knowledge of nucleon structure for nuclear matter but it is also sought to extend these developments to physical finite nuclei which is the main focus in nuclear physics. The first development of the original QMC model from the nuclear matter set-up to the case of finite nuclei, is reported in Ref. [20]. By imposing the Born-Oppenheimer approximation to determine the equation of motion of the nucleon through an effective field theory, the meson mean fields were obtained through a self-consistent approach and the model was also extended to the relativistic case. This general formalism was shown to be applicable in the study of both nuclear matter and finite nuclei. For the latter case, initial results from the model are comparable with the earlier results from QHD [1] and experimental data for ^{16}O and ^{40}Ca nuclei.

Another extension towards finite nuclei was made in Ref. [21] by dealing with the spatial nonuniformity of the equations of meson fields within the nucleon bag and throughout the nucleus. Spherical finite nuclei were considered with this treament and found to be consistent with results of other earlier methods. The study opened new pathways in the treatment of finite nuclei and their properties across the nuclear chart but it must be noted that in their treatment, problems of spurious center of mass and pionic contributions are not yet addressed.

A comprehensive review of the QMC model and its developments for the non-relativistic and relativistic cases and for both nuclear matter and finite nuclei is presented in Ref. [22]. A number of specific closed shell finite nuclei were taken and the treatment was even extended to strange and exotic hypernuclei. Results for the nuclear properties show significant improvement over the conventional QHD and RMF models, which is attributed to the fact that the QMC framework naturally includes spin-orbit splitting inherent to finite nuclei. The QMC configuration utilised in their study addressed the center of mass correction and takes into account pionic effects under two QMC model variations: QMC-I where mesons are considered structureless, and QMC-II where the quark-nature of mesons are taken into account. Despite the success of the results, it is noted that further examination must be performed for scalar polarizability which affects the QMC computations. Additionally, the set-up can be used to study other finite nuclei and compute their nuclear properties.

A significant development in the study of finite nuclei within the QMC model was reported in Ref. [8], where the QMC energy density functional (EDF) was employed to investigate nuclear properties of even-even finite nuclei across the nuclear chart. This version of the QMC EDF only contains four model parameters, namely, the coupling strengths of the σ, ω, and ρ mesons, and the σ meson mass. Further, the EDF can be divided into its various contributions: the density-dependent terms, effective nucleon mass term, finite size effects and spin-orbit coupling terms. The last two components are for finite nuclei and are equal to zero for infinite nuclear matter. QMC results were shown to be generally consistent with experiment as well as with results from the finite-range droplet model (FRDM) [23] and Skyrme force SV-min [24]. Notably, QMC gives smaller root-mean-square deviation for superheavy nuclei and predictions for the deformation parameter are also comparable to those of FRDM and SV-min, even with significantly fewer parameters in the QMC model. It is found, however, that the value of the incompressibility obtained from QMC has a higher value compared

to those of Skyrme models. It was noted in the paper that inclusion of the single-pion exchange, which will be reported in the future, is expected to lower the value of incompressibility closer to the acceptable range.

In a recent progress report in Ref. [25], a comprehensive survey of the QMC model and its developments were presented, alongwith its applications in the study of finite nuclei and hadronic matter in neutron stars. The underlying physical theory of the model was reviewed and necessary equations were rederived. Results from the latest developments of the model showed significant improvements in its predictions for several observables in both nuclear matter and finite nuclear systems. More importantly, since QMC is built on the idea that hadron structure changes when it is bound in-medium, signatures of these changes in view of the EMC effect and Coulomb sum rule, were discussed. These results are much anticipated in future experiments.

In this research, it is proposed to extend the applicability of the QMC model towards a broader study of nuclear structure for finite nuclear systems across the nuclear chart. This is done by implementing a robust optimisation procedure to determine the sets of QMC parameters at each stage of model development, such that available experimental data for several nuclear observables of even-even finite nuclei, are reproduced. Theoretical predictions for regions where data is unavailable, are also sought for. These results will be useful in the near future as experiments work closely with theory to gain deeper understanding on the physics behind the structure of an atomic nucleus.

This thesis is arranged as follows. In Chapter 2, the mean-field contributions to the QMC model energy density functional are derived along with discussions on other contributions coming from Coulomb terms, pairing interaction and center-of-mass correction. Various nuclear observables are then reviewed and discussed in Chapter 3 which are used in the description of nuclear properties in the succeeding chapters. Chapter 4 presents the QMC model developments as well as the modern optimisation procedure done in the latest versions of the model. In Chapter 5, QMC results for nuclear properties along magic chains of nuclei are presented and discussed. In Chapter 6, calculations for energy observables and deformation properties using the QMC model are extended to the superheavy region. In Chapter 7, QMC model predictions are then extended for all even-even nuclei in the nuclear chart with discussions on energies, nuclear sizes and shapes. Finally, Chapter 8 presents the summary and conclusion as well as some outlook for future work.

Chapter 2

The QMC model energy density functional

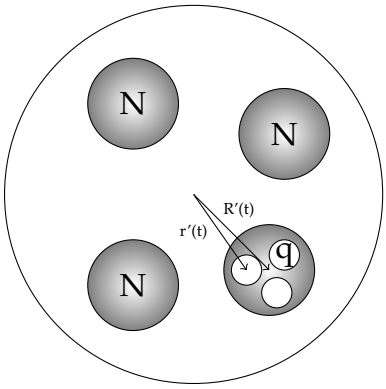

FIGURE 2.1: The atomic nucleus in the QMC model.

In this chapter, the physical theory behind the QMC model is discussed. From the model, an energy density functional (EDF) is derived in a low density and non-relativistic regime, which gives the mean-field contributions to the total energy of an atomic nucleus. Other contributions to the total energy which are coming from Coulomb effects, pairing interaction and center-of-mass correction, are also presented in this chapter.

In the framework of the QMC model, the atomic nucleus is pictured as composed of non-overlapping nucleon bags, Figure 2.1. Using the MIT bag model, three quarks are confined in each bag. Since quark motion is relativistic, they are assumed to have enough time to adjust to the local applied fields in the instantaneous rest frame, $R'(t)$, of the nucleon. As quarks couple to mesons in the nuclear medium, interactions are described through the scalar σ meson which corresponds to the intermediate range attraction and the vector meson ω which corresponds to the short range repulsion. The vector-isovector ρ meson accounts

for isospin dependence [20]. Contributions coming from very short distance interactions, which are the δ piece and tensor effects, are removed since the model assumes that the bags do not overlap. The derivation for the QMC model can be found in Ref. [25]. Here, the necessary derivations are reiterated along with discussions of the latest developments in the model.

The total energy in the QMC model is the sum of energies of the quarks and the mesons [25],

$$E_{QMC} = \sum_{i=1,\ldots} \sqrt{P_i^2 + M_i^{\star 2}(\sigma(\vec{R}_i))} + g_\omega^i \omega(\vec{R}_i) + g_\rho \vec{I}_i \cdot \vec{B}(\vec{R}_i) + E_\sigma + E_{\omega,\rho}\,, \quad (2.1)$$

where $M_i^\star(\sigma), \vec{R}_i, \vec{P}_i$ are the effective mass, position and momentum of baryon i, respectively, and $\sigma(\vec{R}_i)$, $\omega(\vec{R}_i)$ and $\vec{B}(\vec{R}_i)$ are the meson fields. Note that $\vec{B}$ is used for the ρ meson field so as not to confuse with the nucleon density ρ . Further in the ρ contribution, $\vec{I}_i$ is the isospin of the baryon.

The nucleon moves in the external σ field, thereby effecting a change in the nucleon mass. The effective nucleon mass, $M^\star(\sigma)$, determined by solving the bag equations, is defined as

$$M^\star(\sigma) \;=\; M - g_\sigma \sigma + \frac{d}{2}(g_\sigma \sigma)^2\,, \quad (2.2)$$

where M is the nucleon mass, g_σ is the coupling to the σ meson in free space, and d, a unique quantity of the QMC model, is referred to as the *scalar polarisability*. The value of d is dependent on the chosen bag radius. For finite nuclei, it is taken as $d \approx 0.18$ fm, corresponding to a bag radius of 1 fm.

Apart from the energy of quarks, the mesons also contribute to the total energy of the nuclear system. The static energy of the meson fields are expressed as

$$\begin{aligned} E_\sigma &= \int d\vec{r} \left[\frac{1}{2}\left(\vec{\nabla}\sigma\right)^2 + V(\sigma)\right], \\ E_{\omega,\rho} &= -\frac{1}{2}\int d\vec{r} \left[\left(\vec{\nabla}\omega\right)^2 + m_\omega^2\omega^2 + \left(\vec{\nabla}B_\alpha \cdot \vec{\nabla}B_\alpha\right) + m_\rho^2 B_\alpha B_\alpha\right], \end{aligned}$$

where $V(\sigma)$ is the potential energy which will be defined in the following section. m_ω and m_ρ are the masses of the vector mesons and the subscript α of the ρ meson field $\vec{B}$, represents the isospin component where only $\alpha = 3$ contributes in the mean-field approximation.

The meson contribution to the total energy are then eliminated by solving the equations of motion:

$$\frac{\delta E_{QMC}}{\delta\sigma(\vec{r})} = \frac{\delta E_{QMC}}{\delta\omega(\vec{r})} = \frac{\delta E_{QMC}}{\delta B_\alpha(\vec{r})} = 0\,.$$

Each of these contributions to the total QMC Hamiltonian are discussed in the following sections.

2.1 The σ meson Hamiltonian

Upon solving for the equation of motion of the σ meson contribution, the field equation for σ can be expressed as

$$-\nabla^2\sigma(\vec{r}) + \frac{dV}{d\sigma(\vec{r})} = -\sum_i \delta(\vec{r}-\vec{r}_i)\frac{\partial}{\partial\sigma}\sqrt{P_i^2 + M_i^{\star 2}(\sigma)}\,. \tag{2.3}$$

The potential $V(\sigma)$ is chosen as

$$V(\sigma) = \frac{1}{2}(m_\sigma\sigma)^2 + \frac{\lambda_3}{3!}(g_\sigma\sigma)^3 + \frac{\lambda_4}{4!}(g_\sigma\sigma)^4 \tag{2.4}$$

accounting for σ mass and its cubic self-coupling. The quartic term ensures the existence of solution in high densities. For finite nuclei, where saturation density is only $\rho \approx 0.16$ fm^{-3}, the parameter λ_4 can simply be set to zero.

2.1.1 Expansion about the mean σ field

To solve for the σ Hamiltonian, it is assumed that the σ field can be written into its mean and fluctuation parts, $\sigma = \bar{\sigma} + \delta\sigma$. Then, an operator K is defined such that

$$K = \sum_i \delta(\vec{r}-\vec{r}_i)\sqrt{P_i^2 + M^{\star 2}(\sigma)} \tag{2.5}$$

The σ field equation in Eq. (2.3) can then be expressed as

$$-\nabla^2(\bar{\sigma}+\delta\sigma) + \frac{dV}{d\sigma}(\bar{\sigma}+\delta\sigma) = -\frac{\partial K}{\partial\sigma}(\bar{\sigma}+\delta\sigma)\,. \tag{2.6}$$

For brevity, $\vec{r}$ dependence is dropped for the moment. To separate the mean and fluctuation parts further, the derivatives of K are expanded about their expectation values such that

$$\begin{aligned} -\nabla^2(\bar{\sigma}+\delta\sigma)+\frac{dV}{d\sigma}(\bar{\sigma}+\delta\sigma) &= -\frac{\partial K}{\partial\sigma}(\bar{\sigma})-\delta\sigma\frac{\partial^2 K}{\partial^2\sigma}(\bar{\sigma})-\ldots \\ &= -\left[\langle\frac{\partial K}{\partial\sigma}(\bar{\sigma})\rangle+\delta\left(\frac{\partial K}{\partial\sigma}(\bar{\sigma})\right)\right] \\ &\quad -\delta\sigma\left[\langle\frac{\partial^2 K}{\partial^2\sigma}(\bar{\sigma})\rangle+\delta\left(\frac{\partial^2 K}{\partial^2\sigma}(\bar{\sigma})\right)\right]. \end{aligned}$$

The fluctuations $\delta\sigma$, $\delta\left(\frac{\partial K}{\partial\sigma}(\bar{\sigma})\right)$ and $\delta\left(\frac{\partial^2 K}{\partial^2\sigma}(\bar{\sigma})\right)$ are then considered as small quantities.

Solving the σ meson field equation order by order gives, for the mean part,

$$-\nabla^2\bar{\sigma}+\frac{dV}{d\sigma}(\bar{\sigma}) = -\langle\frac{\partial K}{\partial\sigma}(\bar{\sigma})\rangle, \tag{2.7}$$

and for the fluctuation part,

$$-\nabla^2\delta\sigma+\frac{dV}{d\sigma}(\delta\sigma) = -\delta\left(\frac{\partial K}{\partial\sigma}(\bar{\sigma})\right)-\delta\sigma\left[\langle\frac{\partial^2 K}{\partial^2\sigma}(\bar{\sigma})\rangle\right]. \tag{2.8}$$

The fluctuation part is simplified further by multiplying both sides of the equation by $\delta\sigma$ and then integrating by parts so that the first term of the left-hand side of the equation becomes $\int d\vec{r}\left(-\delta\sigma\nabla^2\delta\sigma\right)=\int d\vec{r}\left(\vec{\nabla}\delta\sigma\right)^2$, where total derivatives vanish. On the right-hand side, the identity

$$\frac{\partial K}{\partial\sigma}(\bar{\sigma})=\langle\frac{\partial K}{\partial\sigma}(\bar{\sigma})\rangle+\delta\left(\frac{\partial K}{\partial\sigma}(\bar{\sigma})\right) \tag{2.9}$$

is again used to rewrite the first term. Now, Eq. (2.8) becomes

$$(\vec{\nabla}\delta\sigma)^2 = \delta\sigma\left[-\frac{\partial K}{\partial\sigma}(\bar{\sigma})+\langle\frac{\partial K}{\partial\sigma}(\bar{\sigma})\rangle-\delta\sigma\langle\frac{\partial^2 K}{\partial^2\sigma}(\bar{\sigma})\rangle-\frac{dV}{d\sigma}(\delta\sigma)\right] \tag{2.10}$$

Note that the term $\delta\sigma\frac{dV}{d\sigma}(\delta\sigma)=m_\sigma^2(\delta\sigma)^2+\ldots$ contains higher orders of fluctuation. Keeping only terms up to the first order in fluctuation, this contribution from the potential, as well as the contribution from the second derivative of K in Eq. (2.10) will be neglected.

Thus, the σ part of the QMC Hamiltonian, including the mean and fluctuation parts of the σ meson field, can be written as

$$H_\sigma = \int d\vec{r} \left[K(\bar{\sigma}) + V(\bar{\sigma}) + \frac{1}{2}(\vec{\nabla}\bar{\sigma})^2 + \frac{1}{2}\delta\sigma \left(\frac{\partial K}{\partial \sigma}(\bar{\sigma}) - \langle \frac{\partial K}{\partial \sigma}(\bar{\sigma}) \rangle \right) \right] \tag{2.11}$$

Taking the expectation value of H_σ in Eq. (2.11) and splitting the expression into its mean, $\langle H_\sigma^m \rangle$, and fluctuation, $\langle H_\sigma^f \rangle$, parts, yields

$$\langle H_\sigma^m \rangle = \int d\vec{r} \left[\langle K(\bar{\sigma}) + V(\bar{\sigma}) \rangle + \frac{1}{2} \langle (\vec{\nabla}\bar{\sigma})^2 \rangle \right] , \tag{2.12}$$

and

$$\langle H_\sigma^f \rangle = \int d\vec{r} \left[\frac{1}{2} \langle \delta\sigma \frac{\partial K}{\partial \sigma}(\bar{\sigma}) \rangle \right] , \tag{2.13}$$

where $\langle \delta\sigma \rangle = 0$ was set in $\langle H_\sigma^f \rangle$.

Now, in the fluctuation part, an expression for $\delta\sigma$ is needed. Going back to the field equation in Eq. (2.8), with $\frac{dV}{d\sigma} \approx m_\sigma^2 \delta\sigma$ and using the identity in Eq. (2.9), gives

$$-\nabla^2\delta\sigma + m_\sigma^2\delta\sigma = -\frac{\partial K}{\partial \sigma}(\bar{\sigma}) + \langle \frac{\partial K}{\partial \sigma}(\bar{\sigma}) \rangle - \delta\sigma \left[\langle \frac{\partial^2 K}{\partial^2 \sigma}(\bar{\sigma}) \rangle \right] .$$

Solving this equation iteratively yields

$$\delta\sigma = \frac{1}{m_\sigma^2} \left[-\frac{\partial K}{\partial \sigma}(\bar{\sigma}) + \langle \frac{\partial K}{\partial \sigma}(\bar{\sigma}) \rangle - \delta\sigma \langle \frac{\partial^2 K}{\partial^2 \sigma}(\bar{\sigma}) \rangle + \frac{1}{m_\sigma^2} \nabla^2 \left(-\frac{\partial K}{\partial \sigma}(\bar{\sigma}) + \langle \frac{\partial K}{\partial \sigma}(\bar{\sigma}) \rangle \right) \right] . \tag{2.14}$$

Finally, the fluctuation part of the σ Hamiltonian can be expressed as

$$\begin{aligned} \langle H_\sigma^f \rangle \;=\; & \frac{1}{2m_\sigma^2} \int d\vec{r} \left[-\langle \left(\frac{\partial K}{\partial \sigma}(\bar{\sigma}) \right)^2 \rangle + \langle \frac{\partial K}{\partial \sigma}(\bar{\sigma}) \rangle^2 \right] \\ & + \frac{1}{2m_\sigma^4} \int d\vec{r} \langle \frac{\partial K}{\partial \sigma}(\bar{\sigma}) \nabla^2 \left(-\frac{\partial K}{\partial \sigma}(\bar{\sigma}) + \langle \frac{\partial K}{\partial \sigma}(\bar{\sigma}) \rangle \right) \rangle , \end{aligned} \tag{2.15}$$

where again $\langle \delta\sigma \rangle$ was set to zero.

In the expressions for the mean and fluctuation parts of $\langle H_\sigma \rangle$ in Eqs.(2.12) and (2.15), what is now left to be solved are the expressions for K and its derivative. A quantum form of K is taken as

$$K(\bar{\sigma}) = \sum_{\alpha\beta} K_{\alpha\beta}(\bar{\sigma}) a_\alpha^\dagger a_\beta ,$$

where $a^\dagger_\alpha, a_\alpha$ are the creation and annihilation operators for the complete 1-body basis $|\alpha\rangle$. In the momentum-space representation, K is expressed as

$$K(\bar{\sigma}) = \frac{1}{2V}\sum_{\vec{k},\vec{k}'} e^{i(\vec{k}-\vec{k}')\cdot\vec{r}}\left(\sqrt{k^2+M^{\star 2}(\bar{\sigma})}+\sqrt{k'^2+M^{\star 2}(\bar{\sigma})}\right)a^\dagger_{\vec{k}}a_{\vec{k}'}\,, \tag{2.16}$$

where V is the normalisation volume.

2.1.2 Expansion for finite nuclei

In a non-relativistic expansion, the number density $D(\vec{r})$ and the kinetic density $\xi(\vec{r})$ can be defined as

$$\begin{aligned} D(\vec{r}) &= \frac{1}{V}\sum_{\vec{k},\vec{k}'} e^{i(\vec{k}-\vec{k}')\cdot\vec{r}}a^\dagger_{\vec{k}}a_{\vec{k}'}\,, \\ \xi(\vec{r}) &= \frac{1}{V}\sum_{\vec{k},\vec{k}'} e^{i(\vec{k}-\vec{k}')\cdot\vec{r}}\frac{k^2+k'^2}{2}a^\dagger_{\vec{k}}a_{\vec{k}'}\,. \end{aligned}$$

Using these expressions, the operator K in Eq. (2.16) and its derivative become

$$K(\bar{\sigma}) = D(\vec{r})M^\star(\bar{\sigma}) + \frac{\xi(\vec{r})}{2M^\star(\bar{\sigma})}\,, \tag{2.17}$$

and

$$\frac{\partial K}{\partial\sigma}(\bar{\sigma}) = \left[D(\vec{r})-\frac{\xi(\vec{r})}{2M^{\star 2}(\bar{\sigma})}\right]\frac{\partial M^\star(\bar{\sigma})}{\partial\sigma} = \left[D(\vec{r})-\frac{\xi(\vec{r})}{2M^{\star 2}(\bar{\sigma})}\right](-g_\sigma + dg_\sigma\bar{\sigma})\,, \tag{2.18}$$

where the derivative of $M^\star(\bar{\sigma})$ in Eq. (2.2) is used in the last equation. Applying these expressions to the σ meson field equation in Eq. (2.7) and upon using the expression for potential in Eq. (2.4), gives

$$-\nabla^2\bar{\sigma} + m_\sigma^2\bar{\sigma} + \frac{\lambda_3}{2}g_\sigma^3\bar{\sigma}^2 = \langle D(\vec{r}) - \frac{\xi(\vec{r})}{2M^{\star 2}(\bar{\sigma})}\rangle g_\sigma\,(1-dg_\sigma\bar{\sigma})\,. \tag{2.19}$$

The expectation value on the right-hand side of the equation is solved using the Fermi traces in Appendix B.1, so that it can be rewritten as

$$\langle D(\vec{r}) - \frac{\xi(\vec{r})}{2M^{\star 2}(\bar{\sigma})}\rangle = \left[\rho - \frac{1}{2M^{\star 2}(\bar{\sigma})}\left(\tau - \frac{1}{2}\nabla^2\rho\right)\right]\,, \tag{2.20}$$

where ρ and τ are the particle and kinetic densities, respectively.

To simplify the σ field equation, both sides of Eq. (2.19) are multiplied with the factor $\frac{g_\sigma}{m_\sigma^2}$ and then we let $g_\sigma\bar{\sigma} = v(\rho, \tau, \nabla^2\rho, (\vec{\nabla}\rho)^2)$ and $\rho_s = \left[\rho - \frac{1}{2M^{\star 2}}\left(\tau - \frac{1}{2}\nabla^2\rho\right)\right]$, to get

$$-\frac{1}{m_\sigma^2}\nabla^2 v + v + \frac{\lambda_3}{2}\frac{g_\sigma^2}{m_\sigma^2}v^2 = \rho_s\frac{g_\sigma^2}{m_\sigma^2}(1 - dv)\,.$$

Then, defining the parameter $G_\sigma = \frac{g_\sigma^2}{m_\sigma^2}$ and rewriting in powers of v, the σ field equation is now expressed as

$$\frac{\lambda_3}{2}G_\sigma v^2 + (1 + dG_\sigma\rho_s)\,v - G_\sigma\rho_s = \frac{1}{m_\sigma^2}\nabla^2 v\,. \tag{2.21}$$

Now let v_0 be the solution of the homogeneous equation

$$\frac{\lambda_3}{2}G_\sigma v_0^2 + (1 + dG_\sigma\rho_s)\,v_0 - G_\sigma\rho_s = 0\,.$$

Then,

$$v_0(\rho_s) = \frac{-(1 + dG_\sigma\rho_s) \pm \sqrt{(1 + dG_\sigma\rho_s)^2 + 2\lambda_3 G_\sigma^2\rho_s}}{\lambda_3 G_\sigma}\,. \tag{2.22}$$

Going back to the field equation in Eq. (2.21), one can write the complete solution as $v = v_0(\rho_s) + \delta v$. Taking $(\delta v)^2 = 0$ and $\nabla^2\delta v = 0$, δv can be expressed as

$$\delta v = \frac{1}{\lambda_3 G_\sigma v_0 + (1 + dG_\sigma\rho_s)}\left(\frac{\nabla^2 v_0}{m_\sigma^2}\right) \equiv \Lambda\left(\frac{\nabla^2 v_0}{m_\sigma^2}\right)\,. \tag{2.23}$$

At the leading order, $v_0 \to v_0(\rho)$ and $\rho_s \to \rho$ for δv. Then, the complete solution $v = v_0(\rho_s) + \delta v$ has the explicit expression,

$$v = v_0(\rho) - \frac{v_0'(\rho)}{2M^{\star 2}(\bar{\sigma})}\left(\tau - \frac{1}{2}\nabla^2\rho\right) + \frac{\Lambda}{m_\sigma^2}\left[v_0'(\rho)\nabla^2\rho + v_0''(\rho)\left(\vec{\nabla}\rho\right)^2\right]\,.$$

The σ mean field solution can then be written as

$$g_\sigma\bar{\sigma} = v_0(\rho) - \frac{1}{2M^{\star 2}(\bar{\sigma})}v_0'(\rho)\tau + \left(\frac{1}{4M^{\star 2}(\bar{\sigma})} + \frac{\Lambda}{m_\sigma^2}\right)v_0'(\rho)\nabla^2\rho + \frac{\Lambda}{m_\sigma^2}v_0''(\rho)(\vec{\nabla}\rho)^2\,.$$

Finally, applying this solution to the σ field Hamiltonian in Eqs. (2.12) and (2.15) and keeping only terms linear in τ and ∇^2, yields, for the mean-field part,

$$\langle H_\sigma^m \rangle = \rho M^\star(\bar{\sigma}) + \frac{1}{2M^\star(\bar{\sigma})}\left(\tau - \frac{1}{2}\nabla^2\rho\right) + \frac{v_0^2(\rho)}{2G_\sigma} + \frac{\lambda_3 v_0^3(\rho)}{3!} + \frac{1}{g_\sigma^2}\left(\vec{\nabla} v_0(\rho)\right)^2 , \tag{2.24}$$

and for the fluctuation part,

$$\begin{aligned}\langle H_\sigma^f \rangle &= \left[\frac{m_\sigma^2}{4}p^2 - \frac{p'^2}{4}(\vec{\nabla}\rho)^2\right]\sum_m \rho_m^2 + \frac{q}{4}\sum_m\left(\rho_m\nabla^2\rho_m - 2\rho_m\tau_m\right) \\ &\quad + \frac{p^2}{8}\sum_m\left[\left(\vec{\nabla}\rho_m\right)^2 + 2J_m^2\right] ,\end{aligned} \tag{2.25}$$

where m is the isospin projection with values $m = 1/2$ for protons and $m = -1/2$ for neutrons, and

$$p = \frac{1}{m_\sigma^2}\frac{\partial M^\star(\bar{\sigma})}{\partial\bar{\sigma}} = -\frac{\sqrt{G_\sigma}}{m_\sigma}\left[1 - dv_0(\rho)\right] , \qquad p' = \frac{\sqrt{G_\sigma}}{m_\sigma}dv_0'(\rho) ,$$

$$q = \left(\frac{m_\sigma^2}{2M^{\star 2}} + 1\right)p^2 .$$

The simplification employed for the fluctuation part is detailed in Appendix B.2.

2.2 The ω meson Hamiltonian

The field equation for the ω meson is

$$-\nabla^2\omega(\vec{r}) + m_\omega^2\omega(\vec{r}) = g_\omega\sum_i \delta\left(\vec{r} - \vec{R}_i\right) = g_\omega D(\vec{r}) ,$$

where $D(\vec{r})$ is the normal density operator from the source of the ω meson field. Solving iteratively, yields an expression for the ω field solution:

$$\omega(\vec{r}) = \frac{g_\omega}{m_\omega^2}\left[D(\vec{r}) + \frac{1}{m_\omega^2}\nabla^2 D(\vec{r}) + \ldots\right] .$$

Thus, the ω contribution to the total QMC Hamiltonian is then

$$\begin{aligned}H_\omega &= \frac{1}{2}g_\omega\int d\vec{r}\,\omega(\vec{r})D(\vec{r}) \\ &= \frac{g_\omega^2}{2m_\omega^2}\int d\vec{r}\left[D(\vec{r}) + \frac{1}{m_\omega^2}\nabla^2 D(\vec{r}) + \ldots\right]D(\vec{r}) .\end{aligned}$$

Taking the expectation value and defining the parameter $G_\omega = \frac{g_\omega^2}{m_\omega^2}$, gives

$$\langle H_\omega \rangle = \frac{G_\omega}{2}\left[\langle D^2 \rangle + \frac{1}{m_\omega^2}\langle D\nabla^2 D\rangle\right].$$

Using the Fermi traces in Appendix B.1 for the expectation values, the final expression for the ω contribution will be

$$\langle H_\omega \rangle = \frac{G_\omega}{2}\left[\rho^2 - \frac{1}{2}\sum_m \rho_m^2 + \frac{1}{m_\omega^2}\left(\rho\nabla^2\rho - \sum_m\left[\frac{1}{4}\rho_m\nabla^2\rho_m - \rho_m\tau_m + \frac{1}{2}J_m^2\right]\right)\right].$$

2.3 ρ Meson Hamiltonian

For the ρ meson, the field equation is

$$-\nabla^2 B_\alpha(\vec{r}) + m_\rho^2 B_\alpha(\vec{r}) = g_\rho \sum_i \delta\left(\vec{r} - \vec{R}_i\right) I_i^\alpha = g_\rho D^\alpha(\vec{r}),$$

where I is the isospin operator and, in the last equation, D^α is the density operator for the source of the ρ meson field with isospin index α. Again, solving the differential equation iteratively, the field solution can be expressed as

$$B_\alpha(\vec{r}) = \frac{g_\rho}{m_\rho^2}\left[D^\alpha(\vec{r}) + \frac{1}{m_\rho^2}\nabla^2 D^\alpha(\vec{r}) + \ldots\right].$$

The ρ meson contribution to the total QMC Hamiltonian is then

$$\begin{aligned} H_\rho &= \frac{1}{2}g_\rho \int d\vec{r} B_\alpha(\vec{r}) D^\alpha(\vec{r}) \\ &= \frac{g_\rho^2}{2m_\rho^2}\int d\vec{r}\left[D^\alpha(\vec{r}) + \frac{1}{m_\rho^2}\nabla^2 D^\alpha(\vec{r}) + \ldots\right] D^\alpha. \end{aligned}$$

Solving for the expectation value and defining the parameter $G_\rho = \frac{g_\rho^2}{m_\rho^2}$ yields

$$\langle H_\rho \rangle = \frac{1}{2}G_\rho\left[\langle D^\alpha D^\alpha\rangle + \frac{1}{m_\rho^2}\langle D^\alpha \nabla^2 D^\alpha\rangle\right].$$

With the expectation values given in Appendix B.1, the ρ meson Hamiltonian can be written as

$$\begin{aligned}\langle H_\rho \rangle &= \frac{G_\rho}{2}\sum_{mm'}\left(mm' - \frac{1}{2}\vec{I}_{mm'}\cdot\vec{I}_{m'm}\right)\rho_m\rho_{m'} + \frac{G_\rho}{2m_\rho^2}\sum_{mm'}mm'\rho_m\nabla^2\rho_{m'} \\ &\quad -\frac{G_\rho}{2m_\rho^2}\sum_{mm'}\left[\vec{I}_{mm'}\cdot\vec{I}_{m'm}\left(\frac{1}{4}\rho_m\nabla^2\rho_{m'} - \rho_m\tau_{m'} + \frac{1}{2}\vec{J}_m\cdot\vec{J}_{m'}\right)\right],\end{aligned}$$

where $\vec{I}_{mm'}\cdot\vec{I}_{m'm} = \delta_{mm'}m^2 + (\delta_{m,m'+1} + \delta_{m',m+1})/2$.

2.4 Spin-dependent interaction

The contribution of spin-orbit force in the QMC Hamiltonian was first derived by effecting a slowly-varying field in the nuclear volume. Taking the nucleon motion to be non-relativistic, it can then be assumed that quarks, which are moving relativistically, will have enough time to adjust to the local fields. The interaction Lagrangian is obtained through the self-consistent interaction of the quarks to the scalar and vector mesons. This allows one to rewrite the total Hamiltonian into the central and the spin-orbit part, with the latter taken as a perturbation [20].

The spin-orbit interation can be written as a sum of the magnetic and precession components. The magnetic part accounts for the magnetic interaction between quarks and the mean fields, while Thomas precession accounts for the rotation of baryon spin. These terms are expressed as [25]:

$$\begin{aligned}V^b_{magn} &= \frac{1}{MM^\star(\sigma)}\left(\frac{\mu_{IS}(\sigma)}{\mu_N}\vec{S}\cdot\vec{\nabla}(g^b_\omega\omega) + \frac{\mu_{IV}(\sigma)}{\mu_N}\vec{S}\cdot\vec{\nabla}(g_\rho\vec{B}\cdot\vec{I})\right)\times\vec{P}, \\ V^b_{prec} &= = -\frac{1}{2M^{\star 2}(\sigma)}\vec{S}\cdot\vec{\nabla}\left(M_b(\sigma) + g^b_\omega\omega + g_\rho\vec{B}\cdot\vec{I}\right)\times\vec{P},\end{aligned} \tag{2.26}$$

where M is the free nucleon mass, $M^\star(\sigma)$ is the effective nucleon mass, $\vec{S}$ and $\vec{P}$ are the spin and momentum of the baryon, $\vec{I}$ is its isospin, $\vec{B}$ is the isovector field and $\mu_{IS,IV}(\sigma)$ are the isoscalar and isovector magnetic moments taken in the local scalar field.

The expressions for the spin-orbit contribution in Eq. (2.26), arise solely from the time component of the vector meson fields. To account for the space components of the vector mesons, one can start from the One Boson Exchange potential where both time and space components can be derived. The complete derivation is presented in Appendix B.3.

Dropping some terms which are time-reversal odd and not needed in the present work, the full spin dependence of the EDF derived from the QMC model with both time and space parts, has the form,

$$\begin{aligned}\langle H_{SO}\rangle &= -\left(C_{IS}+\frac{G_\rho \mu_{IV}}{8M^2}\right)\rho\vec{\nabla}\cdot\vec{J} \\ &\quad -\left(\frac{1}{2}C_{IS}+\frac{3}{8}C_{IV}+\frac{G_\omega\mu_{IS}}{4M^2}-\frac{G_\rho\mu_{IV}}{16M^2}\right)\sum_m \rho_m\vec{\nabla}\cdot\vec{J}_m \\ &\quad +\frac{G_\rho}{32M^2}J^2-\frac{1}{16M^2}\left[(G_\sigma-G_\omega)+\frac{1}{4}G_\rho\right]\sum_m J_m^2\,,\end{aligned}$$

where the coefficients $C_{IS,IV}$ are defined as

$$\begin{aligned}C_{IS} &= \frac{1}{4M^2}\left[G_\sigma+(2\mu_{IS}-1)\,G_\omega\right]\,, \\ C_{IV} &= \frac{1}{4M^2}\left(2\mu_{IV}-1\right)G_\rho\,.\end{aligned}$$

2.5 The single pion exchange contribution

Due to the long range nature of pion exchange, its contribution cannot be taken as in the heavy mesons but is, instead, solved using low density approximation. Starting from the interaction of a nucleon in a nuclear pion field ϕ^α, one can write an expression for the energy in terms of the source $\vec{j}^\alpha_\pi(\vec{r})$ and then construct the Hamiltonian, H_π. Solving for the expectation value of H_π leads to computing at local density utilising Fermi gas approximation. The pionic contribution can then be written as:

$$\begin{aligned}\langle\mathcal{H}_\pi\rangle_{mn} &= -\frac{9m_\pi^2 g_A^2}{32f_\pi^2}\int d\vec{R}\frac{\rho_m(\vec{R})\rho_n(\vec{R})}{k_{Fm}^3(\vec{R})k_{Fn}^3(\vec{R})} \\ &\quad \int_0^{k_{Fm}(\vec{R})}dk\int_0^{k_{Fn}(\vec{R})}dk'\int_{-1}^{1}du\frac{k^2k'^2}{k^2+k'^2-2kk'u+m_\pi^2}\,.\end{aligned}$$

where $g_A = 1.26$, $f_\pi = 0.93$ MeV, the pion mass is taken to be $m_\pi = 140$ MeV and k_F is the Fermi momentum. The derivation for this expression can be found in Appendix B.4.

2.6 Other contributions to the total EDF

Just as in the traditional liquid-drop model, the binding energy of the atomic nucleus has other contributing factors aside from the volume and surface terms. These two terms together with the asymmetry affects are already contained in the QMC Hamiltonian using mean-field theory. The other contributions coming from Coulomb and pairing interactions, as well as the center-of-mass corrections, are discussed in this section.

2.6.1 Coulomb terms

In a nuclear system, an additional interaction exists between protons as they are charged. The standard prescription for Coulombic interaction is taken on top of the QMC model as in the Skyrme forces in Refs. [24, 26], for instance.

The direct term for Coulomb can be calculated exactly for point-like protons with density ρ_p using

$$\mathcal{E}^{\mathrm{C}}_{\mathrm{direct}} = \frac{e^2}{2}\int d^3r d^3r' \frac{\rho_p(\vec{r})\rho_p(\vec{r}')}{|\vec{r}-\vec{r}'|}\,, \tag{2.27}$$

where e is the electric charge. The exchange term, on the other hand, is computed in the Slater approximation [27] using the expression

$$\mathcal{E}^{\mathrm{C}}_{\mathrm{exchange}} = -\frac{3e^2}{4}\left(\frac{3}{\pi}\right)^{1/3}\rho_p^{4/3}. \tag{2.28}$$

2.6.2 Pairing functionals

Pairing is an essential component to the overall energy of a nuclear system as it accounts for the occupation of nucleon states in the single-particle spectra. There are a number of available energy functionals that can be employed to describe the pairing interaction. For modeling of the finite nucleus, the QMC EDF is augmented by a pairing functional using BCS occupation amplitudes given by the expression,

$$\mathcal{E}_{pair,q} = \frac{1}{4}G_q(\vec{r})\breve{\rho}_q^2\,,$$

where $q \in (p, n)$ for pairing between protons and between neutrons. The pairing strength, $G_q(\vec{r})$, is generally expressed as

$$G_q(\vec{r}) = V_q \left[1 - \left(\frac{\rho(\vec{r})}{\rho_c}\right)^{\alpha}\right], \tag{2.29}$$

where V_q is the pairing strength parameter, ρ_c is the critical density which is usually approximated to be equal to the saturation density, $\rho_0 = 0.16$ fm^{-3}, and α is an additional parameter to further simulate a density-dependent pairing interaction throughout the nuclear volume. The pairing density, $\check{\rho}_q$, is defined as

$$\check{\rho}_q^2 = \int \chi_q \chi_q^{\dagger}, \quad \text{with} \quad \chi_q(\vec{r}) = \sum_{a \in q} u_a v_a |\phi_a(\vec{r})|^2, \tag{2.30}$$

where v_a and $u_a = \sqrt{1 - v_a^2}$ are the BCS occupation amplitudes and a stands for quantum numbers of a single-particle state.

From the expression for $G_q(\vec{r})$, one can choose to employ a volume/delta force (DF) pairing, a surface/density-dependent delta interaction (DDDI) pairing, or a mixed pairing by setting the following values:

$$\rho_c = \infty \qquad \text{volume or DF pairing} \tag{2.31}$$

$$\rho_c \sim 0.16 \text{ fm}^{-3}; \quad \alpha = 1.0 \qquad \text{surface or DDDI pairing} \tag{2.32}$$

$$\rho_c \text{ and } \alpha \text{ are variables} \qquad \text{mixed pairing} \tag{2.33}$$

The pairing strengths V_p and V_n for proton and neutron, are two additional parameters which need to be fitted to experimental pairing gap data.

Within the QMC framework, the pairing force can be seen as the interaction between nucleons modified by medium effects. In the same way as the HF potential is treated in the Bogoliubov theory, the pairing potential can be computed with the QMC Hamiltonian as

$$V_{pair} = -\left(\frac{G_\sigma}{1 + d' G_\sigma \rho(\vec{r})} - G_\omega - \frac{G_\rho}{4}\right) \delta(\vec{r} - \vec{r}'), \tag{2.34}$$

where scalar polarisability is modified to $d' = d + \frac{1}{3} G_\sigma \lambda_3$ due to the cubic self-interaction of the σ meson. Up to the first order in density, Eq. (2.34) can be written as

$$V_{pair} = -\left(G_\sigma - G_\omega - G_\rho/4\right)\left(1 - \frac{d G_\sigma^2}{G_\sigma - G_\omega - G_\rho/4} \rho(\vec{r})\right) \delta(\vec{r} - \vec{r}'). \tag{2.35}$$

Upon comparison with Eq. (2.29), this allows one to identify

$$V_q = G_\sigma - G_\omega - G_\rho/4\,, \qquad \rho_c = \frac{G_\sigma - G_\omega - G_\rho/4}{dG_\sigma^2}\,, \qquad \text{and} \qquad \alpha = 1\,. \quad (2.36)$$

2.6.3 Center-of-mass correction

Apart from Coulomb and pairing contributions in the total QMC EDF, the center-of-mass correction, $\mathcal{E}_{\text{c.o.m.}}$, is also taken outside of the mean-fields. As in the Skyrme forces SV in Ref. [24], its functional is taken as

$$\mathcal{E}_{\text{c.o.m.}} = -\frac{\langle \hat{P}_{cm}^2 \rangle}{2mA}\,,$$

where $\hat{P}_{cm} = \sum_i \hat{p}_i$ is the total momentum, m is the nucleon mass and A is the atomic number.

Chapter 3

Nuclear Observables

The ultimate goal of an energy density functional (EDF) is to be able to simulate real-life, measureable quantities as well as to provide predictions for those which are not yet known experimentally. There are two areas in nuclear structure which an EDF should be able to describe: 1) a system of infinite nuclear matter, and 2) a system of finite composition as in the case of the atomic nucleus. In this chapter, various nuclear observables are discussed which are used to characterize the two areas of study.

3.1 Infinite nuclear matter

In the domain of infinite nuclear matter, nucleons are taken to interact with each other with uniform density ρ over an infinite volume such that surface effects are neglected. The EDF then greatly simplifies since all gradient terms which account for finite-size will vanish. Here, $\langle H \rangle$ is reduced to $\langle H \rangle_{NM}$ for the nuclear matter energy density which is fully expressed in terms of the total density $\rho = \rho_p + \rho_n$ where $\rho_{p,n}$ are proton and neutron number densities.

It is helpful to consider three different categories of nuclear matter. The most common is symmetric nuclear matter (SNM) which is an idealized infinite system containing equal numbers of protons and neutrons. In this case, the nucleon densities can be written as

$$\rho_p = \rho_n = \frac{\rho}{2}\,, \tag{3.1}$$

so that the EDF is only a function of the total density.

The difference in proton and neutron numbers can be accounted by defining the asymmetry parameter $\beta = \frac{\rho_n - \rho_p}{\rho}$ and expressing the nucleon densities as

$$\rho_{p,n} = \frac{\rho}{2}\left[1 \mp \beta\right]\,. \tag{3.2}$$

The special case $\beta = 0$ then corresponds to SNM. When $\beta = 1$ the proton density becomes zero and the total density is just that of the neutrons; such is the case for pure neutron matter (PNM).

Where β lies between 0 and 1 gives a combination of unequal numbers of protons and neutrons and their ratio can be expressed as

$$\frac{\rho_n}{\rho_p} = \frac{1-\beta}{1+\beta}. \tag{3.3}$$

This case is referred to as the asymmetric nuclear matter (ANM).

To summarize, the energy density for the three types of nuclear matter in terms of ρ and β can be written as

$$\langle H \rangle_{NM}(\rho, \beta) = \begin{cases} \langle H \rangle_{SNM} & \text{if } \beta = 0, \\ \langle H \rangle_{ANM} & \text{if } 0 < \beta < 1, \\ \langle H \rangle_{PNM} & \text{if } \beta = 1. \end{cases} \tag{3.4}$$

In the following subsections, the properties related to the three cases of nuclear matter are discussed.

3.1.1 Energy and pressure

One significant description for the structure of nuclear matter is how much energy each bound nucleon has, as it interacts with all the other particles in the system. The binding energy per particle E of cold matter containing protons and neutrons is expressed as a function of density, ρ, and the asymmetry parameter, β:

$$E(\rho, \beta) = \frac{\langle H \rangle_{NM}(\rho, \beta)}{\rho}\,. \tag{3.5}$$

Nuclear matter reaches saturation when the binding energy per nucleon is a minimum; that is, when the nucleonic pressure, P, goes to zero. The density where this occurs is known as the saturation point, ρ_0, and energy at this point is often called the saturation energy, $E_0 = E(\rho_0)$.

$$P = \rho^2 \frac{\partial E}{\partial \rho} \to 0, \quad \rho = \rho_0\,. \tag{3.6}$$

SNM is known to be bound at $\rho_0 \sim 0.16$ fm^{-3} with energy $E_0 \sim$ –16 MeV. It is customary to use properties of the SNM at saturation to constrain parameters of

nuclear structure models.

Figures 3.1 (a) to (c) show the binding energy per nucleon as a function of the density for the three different cases of nuclear matter. For (a) SNM and (b) PNM, the plots show curves predicted by several density functionals, while in (c) ANM curves from one of the Skyrme forces, UNEDF1 [28], are shown for different values of β. The saturation point for SNM is well reproduced by the functionals in the plot. For PNM, energy density curves somewhat vary with crossing density around the vicinity of the saturation point. In Figure 3.1 (c), the evolution of energy curves can be seen as β goes from 0 to 1, which corresponds to curves from SNM and PNM, respectively.

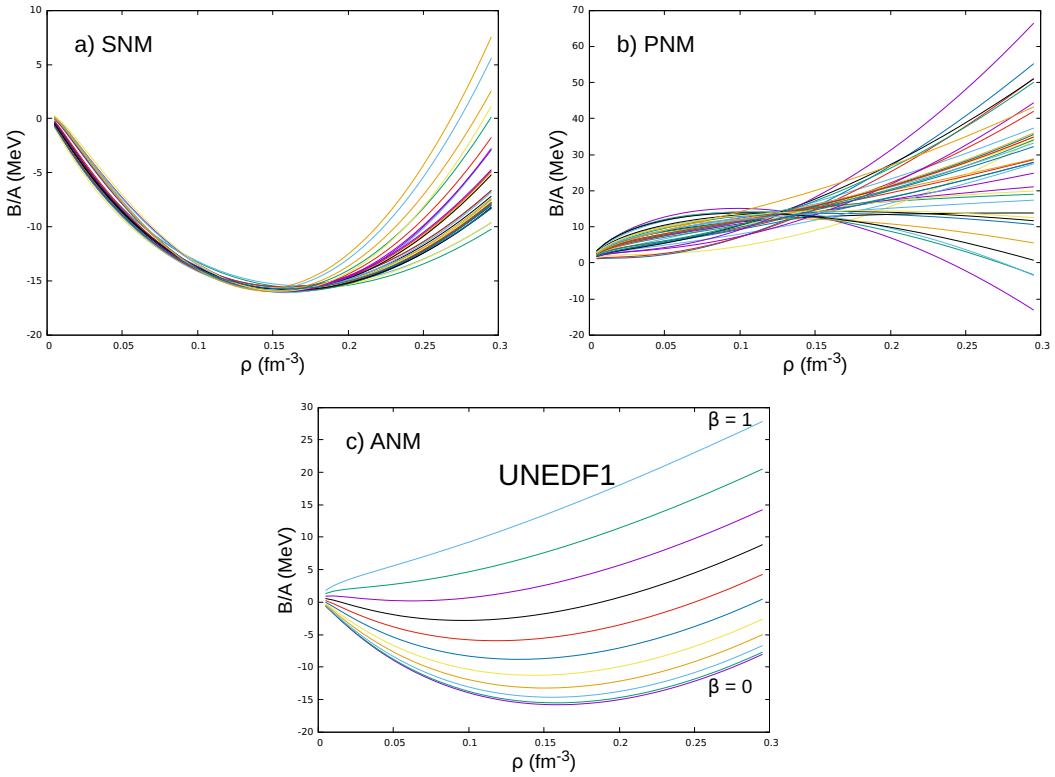

FIGURE 3.1: Binding energy per nucleon, B/A, as a function of nucleonic density, ρ, for the three cases of nuclear matter. Plots (a) and (b) show the SNM and PNM cases, respectively, from several density functionals while plot (c) shows B/A curves for ANM using the Skyrme force, UNEDF1 [28].

3.1.2 Other saturation properties of nuclear matter

Apart from energy and pressure, other bulk properties of nuclear matter at saturation can be derived from the expression of binding energy per nucleon $E(\rho, \beta)$ in Eq. (3.5). Again, in particular, SNM is used to calculate saturation properties so that the energy per nucleon is simply $E(\rho)$. If $E(\rho)$ is expanded about ρ, the first-order term corresponds to pressure, Eq. (3.6), which was discussed in the previous subsection. The second- and third- order terms of the expansion, $K(\rho)$ and $Q(\rho)$, correspond to the nuclear incompressibility K_0 and skewness coefficient Q_0, respectively, when evaluated at the saturation point ρ_0.

$$K_0 = 9\rho_0^2 \frac{\partial^2 E}{\partial \rho^2}|_{\rho=\rho_0} = 9\frac{\partial P}{\partial \rho}|_{\rho=\rho_0}\,, \tag{3.7}$$

$$Q_0 = 27\rho_0^3 \frac{\partial^3 E}{\partial \rho^3}|_{\rho=\rho_0}\,. \tag{3.8}$$

Figure 3.2 presents K as a function of ρ from several density functionals. A re-analysis of data from giant monopole resonances provided a range for K_0 from 250 to 315 MeV [29], while other recommended values are in the range 200 to 260 MeV [30]. As seen in Figure 3.2, at the saturation point, some models are within the range expected from experiment while the others are above the upper bound. For Q_0, the range of accepted values taken from empirical and experimental data is within -1200 to -200 MeV [30].

Another important property of nuclear matter is the symmetry energy $S(\rho)$, as it relates to the isospin symmetry effects of the system. The same quantity is referred to as the *asymmetry coefficient* in the semi-empirical mass formula. $S(\rho)$ is defined as the difference between binding energies per nucleon of SNM and that of PNM [31]

$$S(\rho) = E_{SNM} - E_{PNM}\,. \tag{3.9}$$

This is equivalent to taking the second-derivative of $E(\rho, \beta)$ with respect to the asymmetry parameter β then evaluating at $\beta = 0$ [31],

$$S(\rho) = \frac{1}{2}\frac{\partial^2 E}{\partial \beta^2}|_{\beta=0}\,. \tag{3.10}$$

The value of the symmetry energy at saturation, $S_0 = S(\rho_0)$, is commonly used as another constraint for nuclear structure. Ref. [32] summarises 28 available

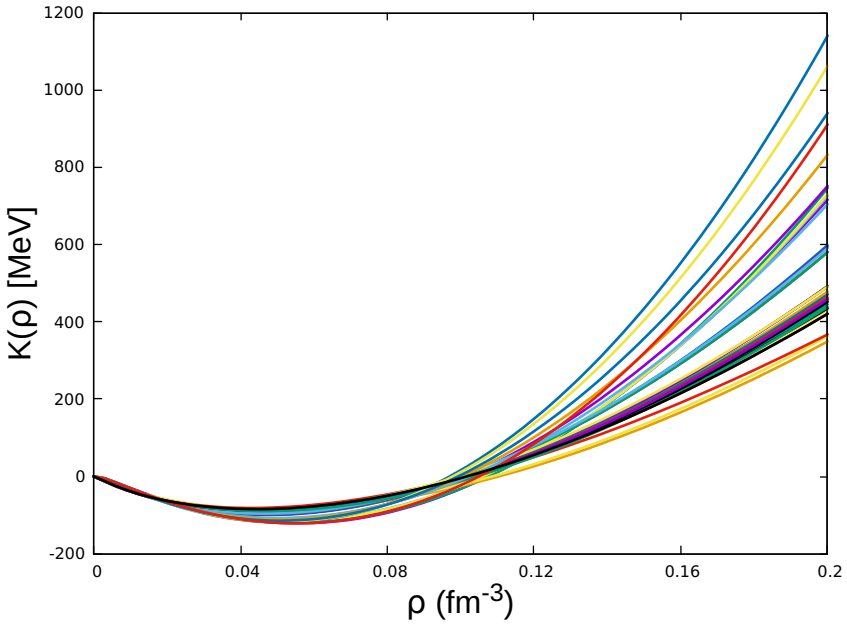

FIGURE 3.2: K, as a function of density, ρ, for SNM from several density functionals.

results from various terrestrial measurements and astrophysical observations for S_0 which varies from around 29 MeV to 33 MeV.

A related quantity to the symmetry energy is its slope at saturation L_0 defined by the equation

$$L_0 = 3\rho_0 \left(\frac{\partial S}{\partial \rho}\right)|_{\rho=\rho_0}, \tag{3.11}$$

Recently, by studying the radioactivity of 19 proton emitters having large isospin asymmetry, L_0 was constrained to have a value of 51.8 ± 7.2 MeV [33]. From the terrestrial and astrophysical measurements in Ref. [32], the average value of L_0 is 58.9 MeV.

The second and third derivative of the symmetry energy relates to its curvature and skewness, respectively, defined as

$$K_{sym} = 9\rho^2 \frac{\partial^2 S}{\partial \rho^2}\bigg|_{\rho=\rho_0}, \tag{3.12}$$

$$Q_{sym} = 27\rho^3 \frac{\partial^3 S}{\partial \rho^3}\bigg|_{\rho=\rho_0}. \tag{3.13}$$

These are similar to the expressions for K_0 and Q_0 in Eqs. (3.7) and (3.8) but with derivatives of $S(\rho)$ instead of $E(\rho)$. K_{sym} is usually referred to as the symmetry incompressibility. In addition, the isospin incompressibility, K_τ, can be

computed as

$$K_\tau = K_{sym} - L_0 \left[6 + \left(\frac{Q_0}{K_0} \right) \right] . \tag{3.14}$$

Finally, the isoscalar and isovector effective masses are computed by expressing the energy in terms of the kinetic density $\tau = \frac{3}{5}(3\pi^2/2)^{2/3}\rho^{5/3}$. The two quantities are defined as

$$M_s^* = M \left(1 + \frac{2M}{\hbar^2} \frac{\partial E}{\partial \tau} \right)^{-1} |_{\rho=\rho_0} \tag{3.15}$$

$$M_v^* = M \left[1 + \frac{2M}{\hbar^2} \frac{\partial}{\partial(\tau_n - \tau_p)} \frac{\partial E}{\partial(\rho_n - \rho_p)} \right]^{-1} |_{\rho=\rho_0} \tag{3.16}$$

where M is the nucleon mass.

3.2 Finite nuclei

The structure of an atomic nucleus can be described through several properties relating to energies, density distributions, and deformations. Ground-state observables are discussed in this section which will be of significance in investigating various results from QMC and in comparing them with results from other nuclear models.

3.2.1 Energy observables

The most common and widely used quantity in the study of finite nuclei is the ground state binding energy, BE, which is directly available from the solution of mean field equations and can be readily extracted from highly precise measurements of atomic masses. Mean-field theories incorporate the volume, surface and symmetry effects to the binding energy while Coulomb and pairing energies are conventionally added as separate functionals.

Figure 3.3 shows the binding energy contributions as predicted by the semi-empirical mass formula [34]. The BE per nucleon is expected to be around 8 MeV for most nuclei while light nuclei tend to be less bound.

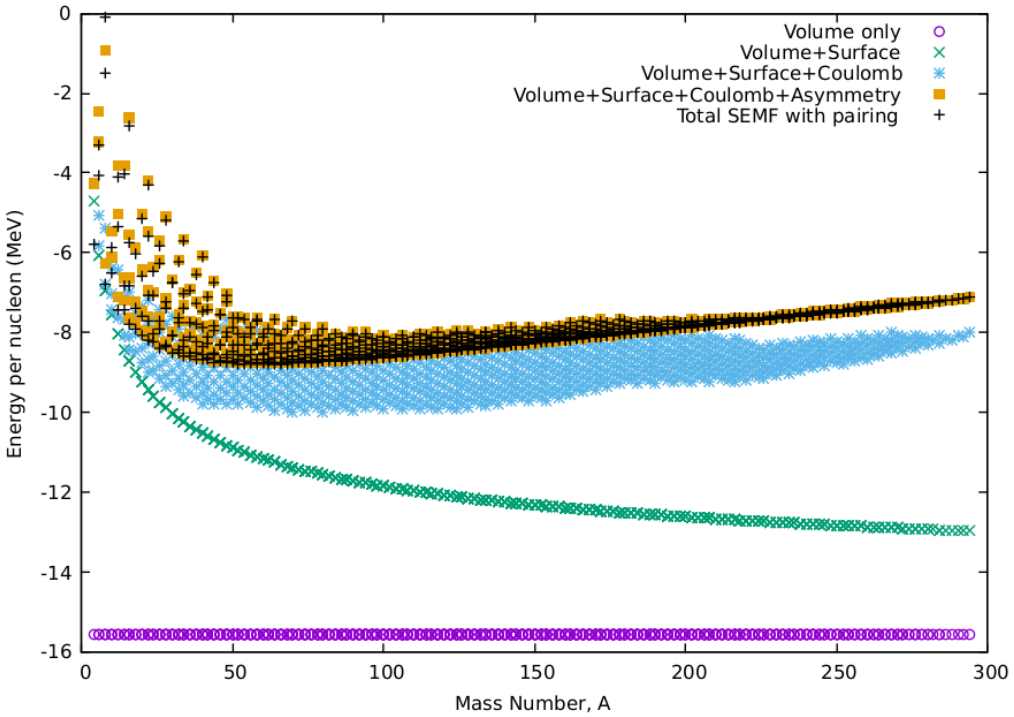

FIGURE 3.3: Binding energy contributions as predicted by the semi-empirical mass formula [35].

Single-particle energies

In nuclear models, the total binding energy of the nucleon is obtained by solving the Hartree-Fock equations. This is done by filling up the single-particle states up to the Fermi energy level of a particular nucleus given its proton number, Z, and neutron number, N. These states, shown in Figure 3.4, are labeled in the form of nlj, where n is the principal quantum number, l is the orbital angular momentum quantum number and j is the total angular momentum, which arises from the splitting of states due to the spin-orbit force. Note that nlj are good quantum numbers if spherical symmetry of the mean-field is enforced.

As observed from experiment, gaps in the nuclear shells form at particular levels after filling up certain shells. These are referred to as the 'magic numbers' which are currently known for protons at 8, 20, 28, 50, 82 while for neutrons magicity occurs at 8, 20, 28, 50, 82 and 126. When a nucleus has both Z and N at magic numbers, it is called 'doubly-magic'. If either of them is a magic number and the other is not, the nucleus is referred to as 'semi-magic' or at times simply 'magic'.

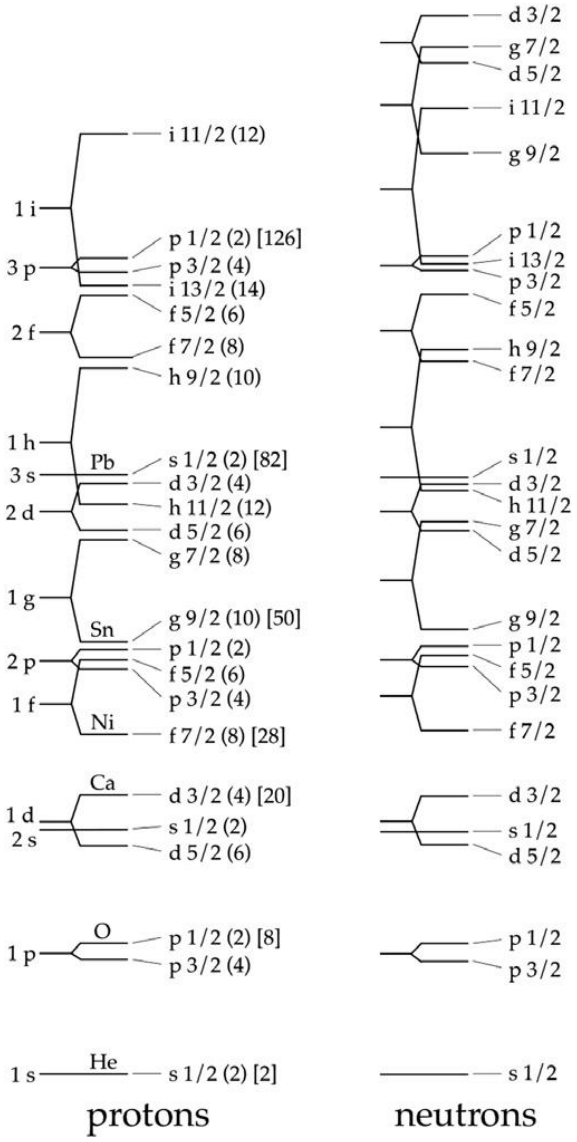

FIGURE 3.4: Single-particle occupation in the standard shell-model configuration. The levels are labelled in the form of nlj, where n is the principal quantum number, l is the orbital angular momentum quantum number and j is the total angular momentum. Figure is taken from Ref. [36].

Figure 3.5 shows the single-particle states of doubly-magic nuclei obtained from experiment [37], showing the particle and hole occupations above and below the Fermi-level. The Fermi energies λ_F corresponding to proton (π) and neutron (ν) as well as the Coulomb effects, ΔE_C, are subtracted from the single-particle energies, E_{sp}, to normalize the values. The actual E_{sp} values from experiment are written above or below the lines corresponding for each state. For symmetric nuclei ($Z = N$) in Figure 3.5 (a), the proton and neutron states are

expected to be more on less on the same level after the Fermi and Coulomb energies are subtracted. For neutron-rich nuclei in Figure 3.5 (b), neutron states are expected to be pushed down compared to the equivalent proton levels due to asymmetry effects.

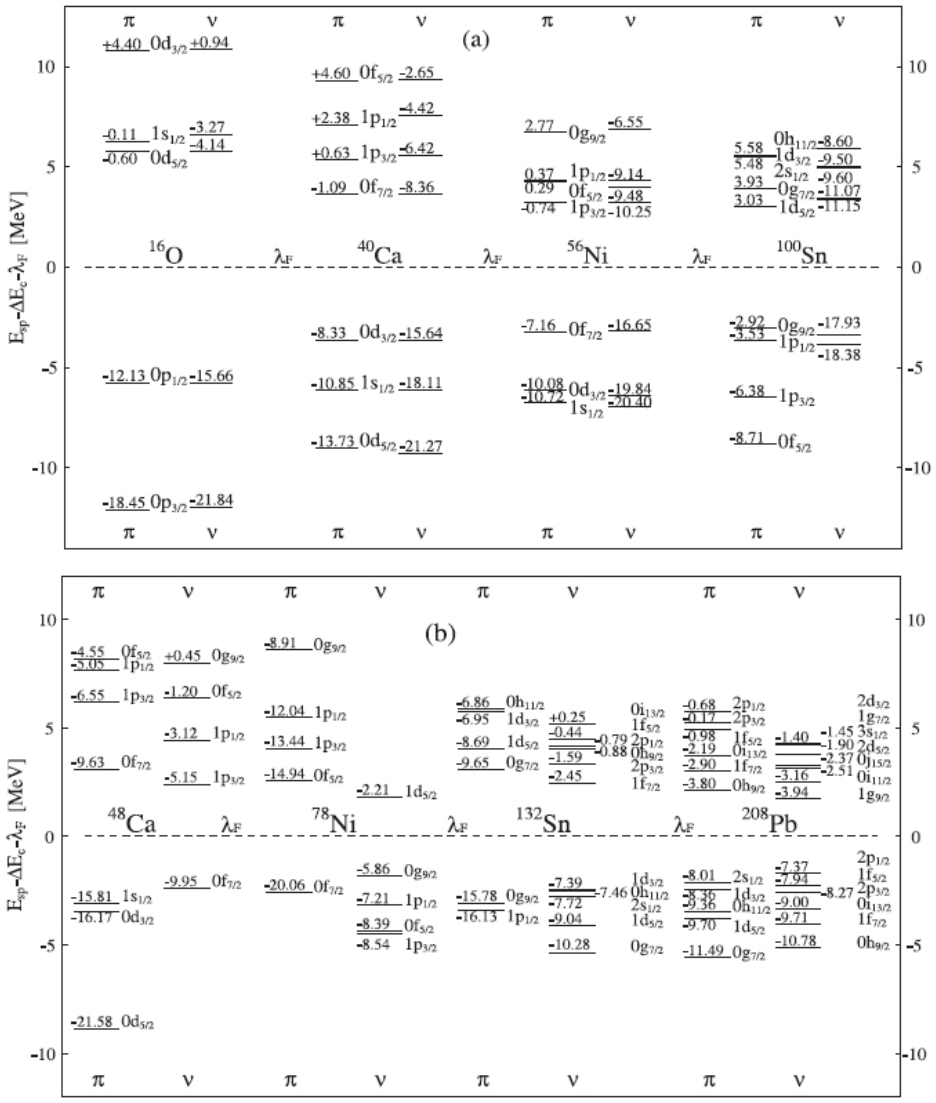

FIGURE 3.5: Proton π and neutron ν states of doubly-magic nuclei obtained from experiment. The single-particle energies, E_{sp}, are normalised by subtracting the Coulomb and Fermi energies. Actual E_{sp} values are written above or below the lines corresponding to each state. Figure is taken from Ref. [37].

Separation energies

From the total binding energy of the atomic nucleus, several other nuclear observables can be obtained. One is the separation energy, which as the name implies,

is the energy required to remove nucleons from a given atomic nucleus. This is further divided into two: 1) the one-nucleon separation energy $S_{1q=p,n}$ where either a proton or a neutron is removed; and, 2) the two-nucleon separation energy $S_{2q=p,n}$ where either two protons or two neutrons are removed from the nucleus. These quantities can be calculated using

$$S_{1p}(Z,N) = BE(Z,N) - BE(Z-1,N)\,, \tag{3.17}$$
$$S_{2p}(Z,N) = BE(Z,N) - BE(Z-2,N)\,, \tag{3.18}$$

and similar expressions for neutron separation energies.

Another separation energy observable is the Q_α, which is the energy required to remove an α particle from the nucleus. This is calculated through the expression

$$Q_\alpha(Z,N) = BE(Z,N) - BE(Z-2,N-2) - BE(2,2)\,, \tag{3.19}$$

where $BE(2,2) = -28.296$ MeV is the energy of an α particle (^{4}He).

Figures 3.6 (a)-(c) show the S_{2p}, S_{2n} and Q_α values, respectively, calculated from experimental masses in Ref. [38]. From the separation energy plots, one can notice the existence of lines where there are abrupt changes in the values of energies. These lines occuring at particular proton and neutron numbers suggest the existence of shell closures or subshell closures as the energy requirement is relatively smaller right after the nucleons reach certain numbers. In the plots, these shell closures appear at the locations of the magic numbers since magic nuclei are more bound compared to its neighboring nuclei.

From the Q_α energies, one can compute the half-life against α decay, $T_{1/2}$ in seconds, using the Viola-Seaborg relationship [39]

$$log_{10}(T_{1/2}) = \frac{aZ+b}{\sqrt{Q_\alpha}} + cZ + d\,, \tag{3.20}$$

where $a = 1.66175, b = -8.5166, c = -0.20228, d = -33.9069$.

Moving further away from the stability line in the current nuclear landscape, a limit exists as to the number of nucleons that can be added in an atomic nucleus. When this limit is reached, the nucleons would spontaneously drip from the nucleus as it can no longer physically take in more nucleons. This then gives bounds on both sides of the nuclear chart; to the left, when plotted with Z against N, this limit is known as the proton dripline while to the right, is the neutron

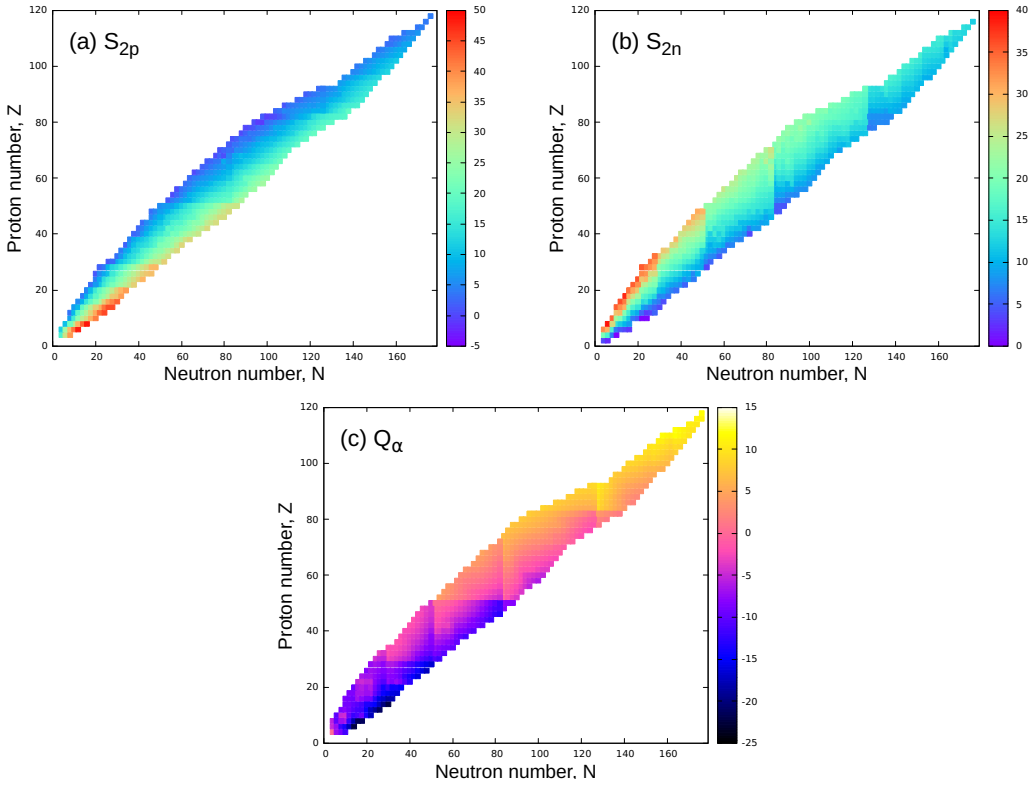

FIGURE 3.6: Separation energies, (a) S_{2p}, (b) S_{2n}, and (c) Q_α calculated from experimental masses in Ref. [38]. Note the existence of lines occuring at the locations of magic numbers signifying the shell closures.

dripline. Dripline calculations are essential as they give predictions up to which isotope or isotone can be physically observed. The locations of driplines can be determined using the separation energies, when the value becomes negative as protons(neutrons) are added along isotopic(isotonic) chains.

Shell gaps

The difference in separation energies is another finite nucleus observable known as the shell gaps. This observable is usually calculated to get a clear picture of the shell and subshell closures in chains of nuclei. The two-proton shell gap is defined as

$$\delta_{2p}(Z,N) = S_{2p}(Z-2,N) - S_{2p}(Z,N)\,, \tag{3.21}$$

and a similar expression for two-neutron shell gap, δ_{2n}. Figure 3.7 shows the experimental two-proton and two-neutron shell gaps, respectively, for all known even-even nuclei. Notice that the shell closures are visible and are signified by the peaks in shell gap values.

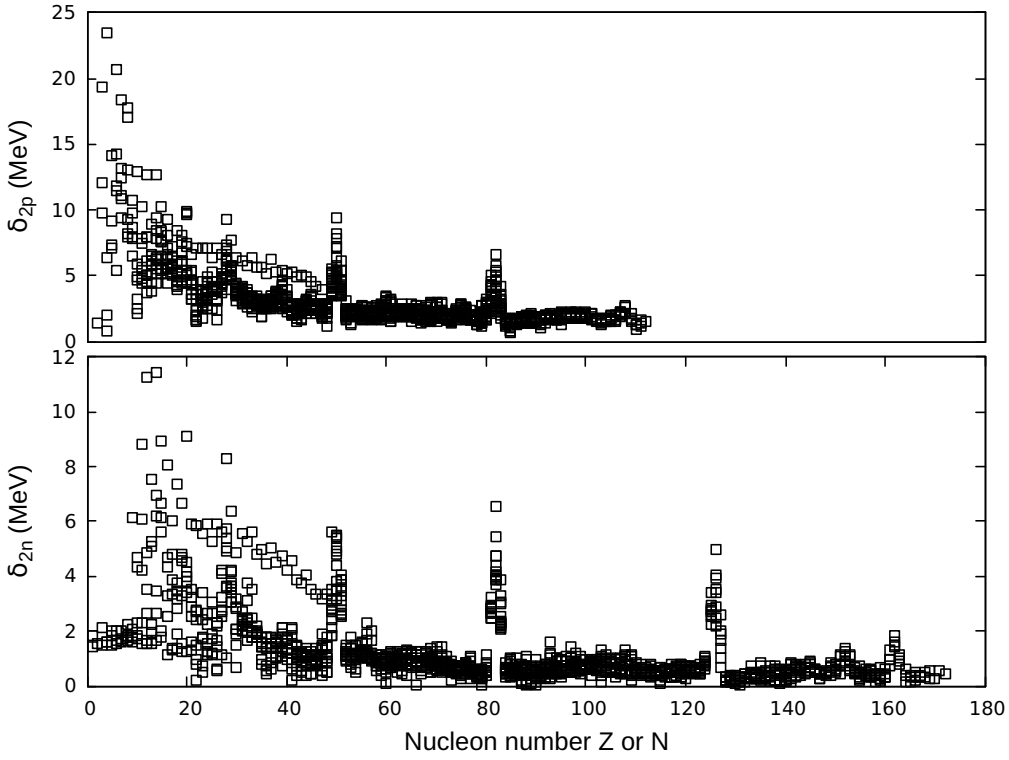

FIGURE 3.7: Proton and neutron shell gaps, δ_{2p} and δ_{2n}, respectively, computed from experimental masses in Ref. [38]. The shell closures are signified by the peaks in shell gaps where the difference in separation energies are greatest along isotopic and isotonic chains.

Pairing gaps and odd-even staggering

A measure of nuclear pairing correlations known as the pairing gap is a quantity that can be extracted from experimental odd-even staggering (OES) in binding energies. Two available definitions can be used to calculate OES known as the three-point [40] and five-point [24] formula given by the following equations

$$\Delta_n^{(3)}(Z,N) = \frac{(-1)^N}{2}\left[BE(Z,N-1) - 2BE(Z,N) + BE(Z,N+1)\right], \quad (3.22)$$

$$\begin{aligned}\Delta_n^{(5)}(Z,N) &= \frac{1}{2}\left[BE(Z,N-1) + BE(Z,N+1)\right] \\ &\quad -\frac{1}{8}\left[BE(Z,N-2) + BE(Z,N+2)\right] - \frac{3}{4}BE(Z,N)\,,\end{aligned} \quad (3.23)$$

and equivalent expressions for the proton pairing gap. However, it is complicated to calculate the OES in mean field models [41, 24], as it involves solving odd-A neighbors of even-even nuclei. Another measure of pairing correlations is instead

commonly used known as the average spectral gap defined as

$$\langle uv\Delta \rangle_q = \frac{\Sigma_{\alpha \in q} u_\alpha v_\alpha \Delta_\alpha}{\Sigma_{\alpha \in q} u_\alpha v_\alpha}, \tag{3.24}$$

where v_α, $u_\alpha = \sqrt{1 - v_\alpha^2}$ are the BCS occupation amplitudes and Δ_α is the state-dependent single-particle pairing gap [42].

As noted in [24], $\langle uv\Delta \rangle_q$ and $\Delta^{(5)}_{n,p}$ are reasonably well related in mid-shell regions but exhibit different behaviour in the vicinity of (semi)magic nuclei, which may introduce a larger difference between experiment and model predictions. Figure 3.8 shows a comparison of the different pairing gap calculations using DF and DDDI pairing functionals, as discussed in Section 2.6.2, along Sn and $N = 82$ chains.

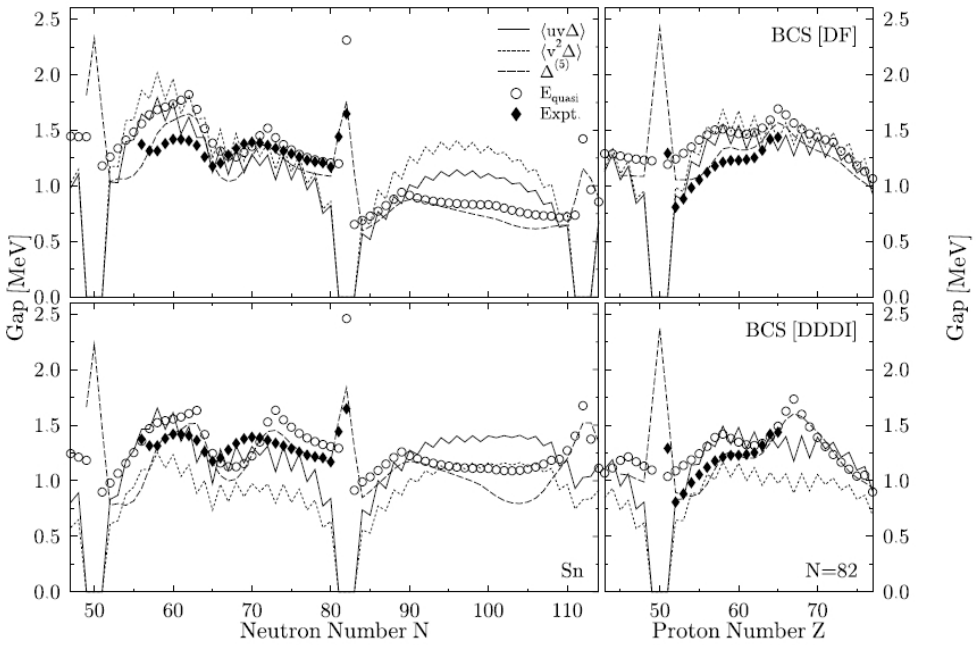

FIGURE 3.8: Comparison of different pairing gap calculations for Sn and $N = 82$ chains using DF and DDDI pairing interaction. $\langle uv\Delta \rangle_q$ and $\langle v^2\Delta \rangle_q$ are the spectral gaps while $\Delta^{(5)}$ is the five-point gap. Also shown are E_{quasi}, which is another approximation for odd-even staggering, and pairing gaps from experiment. Figure is taken from Ref. [41].

3.2.2 Nuclear sizes and shapes

Another important nuclear parameter relates to the density distribution of nucleons in the atomic nucleus. From its calculation, one can compute several observables like sizes and shapes of a nucleus. Elastic electron scattering experiments and optical methods provide information on charge density distribution in a nucleus and its mean-square charge radius, $\langle r^2 \rangle$. This finite nucleus observable, like BE, is widely used to compare results from theoretical nuclear models. In this subsection, ground-state observables relating to the density distribution will be discussed.

Charge density distributions

There are several definitions for charge distribution in a nuclear volume which are fitted from results of electron and muon scattering experiments. The common definitions are the following [43]:

i) Fermi distribution

$$\rho(r) = \frac{\rho_0}{1 + e^{(r-c)/a}}, \tag{3.25}$$

ii) parabolic Fermi

$$\rho(r) = \frac{\rho_0(1 + wr^2/c^2)}{1 + e^{(r-c)/a}}, \tag{3.26}$$

iii) modified Gaussian

$$\rho(r) = \frac{\rho_0(1 + wr^2/c^2)}{1 + e^{(r^2-c^2)/a^2}}, \tag{3.27}$$

where ρ_0 is the normalization constant, c is defined as the halfway radius so that $\rho(c) = 0.5\rho_0$, a is the diffuseness parameter and w is a free parameter to model the bump just before the charge density rapidly decreases near the nuclear surface.

Another form for charge density in Ref. [44] is taken as

$$\rho(r) = \frac{\rho_0 \left[1 + w(r/c)^\alpha\right]}{1 + e^{(r^2-c^2)/a^2}}. \tag{3.28}$$

Note that this is the same expression as in Eq. (3.27) with $\alpha = 2$. Yet another definition for the charge distribution is through Fourier-Bessel coefficients expressed as

$$\rho(r) = \sum_1^\nu a_\nu J_0\left(\frac{\nu\pi r}{R}\right), \tag{3.29}$$

where J_0 is the zeroth Bessel function also known as the Hankel function, and a_ν and R are free parameters which are fitted for each nucleus from electron scattering experiments.

Figure 3.9 shows a comparison of the definitions of charge density, available for the doubly-magic ^{208}Pb.

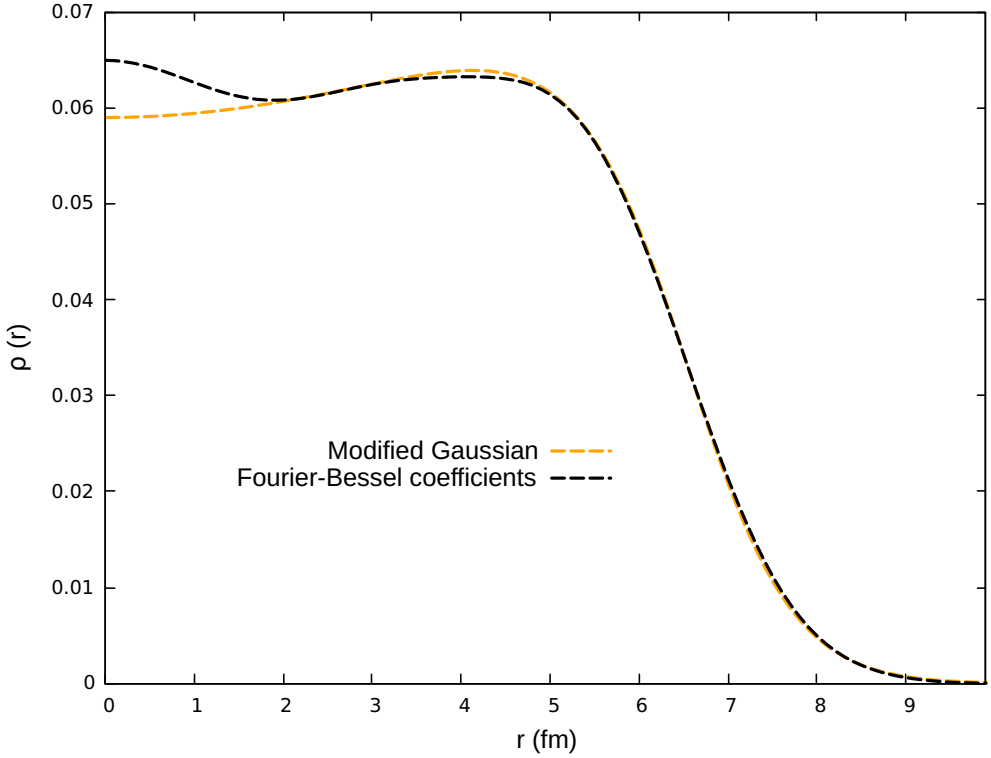

FIGURE 3.9: Comparison of charge density distributions for ^{208}Pb from various definitions fitted to electron scattering data.

Radius parameters

The nuclear form factor, $F(\vec{q})$, as a function of momentum $\vec{q}$ is defined as the Fourier transform of the charge density,

$$F(\vec{q}) = \int e^{i\vec{q}\cdot\vec{r}}\rho(\vec{r})d^3\vec{r}\,. \tag{3.30}$$

For a spherical density distribution, the form factor can be expressed in terms of the spherical Bessel function j_0 such that

$$F(q) = 4\pi \int j_0(qr)\rho(r)r^2 dr\,. \tag{3.31}$$

From the charge form factor, three ground state radius parameters can be deduced. The most common is the root-mean-square charge radius, R_{ch}, which can be expressed as

$$R_{ch} = \sqrt{\langle r_{ch}^2 \rangle} = \frac{-3}{F(0)} \lim_{q \to 0} \frac{d^2 F(q)}{dq^2} \,. \tag{3.32}$$

Another way to calculate the charge radius is directly from the mean-square radius of the proton distribution, assuming the protons are point-like particles without internal structure. The geometrical radius of the proton is taken directly from the proton density distribution through the equation

$$R_p = \frac{\int r^2 \rho(\vec{r}) d^3\vec{r}}{\int \rho(\vec{r}) d^3\vec{r}} \,. \tag{3.33}$$

The two quantities, R_{ch} and R_p, are reasonably well related [26] as

$$R_{ch}^2 = R_p^2 + \langle r_p^2 \rangle + \frac{N}{Z} \langle r_n^2 \rangle \,, \tag{3.34}$$

with the free proton and neutron charge radii taken as $\langle r_p^2 \rangle = 0.7071$ fm^2 and $\langle r_n^2 \rangle = -0.1161$ fm^2 [45]. Note that the standard relation in Eq. (3.34) is valid for spherical nuclei. In Ref. [46], an additional term appears in Eq. (3.34) for the charge radii of deformed nuclei. The other two radius parameters are defined using the Helm model which is discussed in the following subsection.

The Helm model

In the traditional Helm model, the charge density distribution has the form of a Gaussian convoluted to a Heaviside step function [47]

$$\rho_H(\vec{r}) = \frac{\rho_0}{(2\pi)^{3/2}} \int e^{-(\vec{r}-\vec{r}')^2/2\sigma^2} \Theta(R_0 - |\vec{r}'|) d^3\vec{r}' \,, \tag{3.35}$$

where $\rho_0 = (3Z)/(4\pi R_0^3)$, with Z as the proton number. The Helm model charge form factor can be explicitly written as

$$F_H(q) = \frac{3Z}{qR_0} j_1(qR_0) e^{-\sigma^2 q^2/2} \,, \tag{3.36}$$

where $j_1(x)$ is the Hankel function of the first kind.

Aside from R_{ch} , another radius parameter is the diffraction radius R_0 which relates to the first zero of the Helm form factor. Setting Eq. (3.36) to zero means

that $j_1(qR_0) = 0$ and thus R_0 can be expressed as

$$R_0 = \frac{4.49431}{q_0^{(1)}}\,, \tag{3.37}$$

where $q_0^{(1)}$ is the location of the first zero.

The third radius parameter is the surface thickness, σ_s , which is calculated using the first maximum of the form factor, q_m in fm^{-1}. The square of σ_s is defined as

$$\sigma_s^2 = \frac{2}{q_m^2} \ln\left[\frac{3Zj_1(q_mR_0)}{q_mR_0F(q_m)}\right]\,. \tag{3.38}$$

To obtain q_m, the equation $F'(q) = 0$ must first be solved,

$$\begin{aligned} F'(q) &= \frac{\left(3Ze^{-\sigma^2q^2/2}\right)\left[\sin(qR_0) - \left(q^2\sigma^2+3\right)j_1(qR_0)\right]}{q^2R_0} \\ 0 &= \sin(qR_0) - \left(q^2\sigma^2+3\right)j_1(qR_0) \end{aligned} \tag{3.39}$$

Figure 3.10 shows the charge form factor for ^{208}Pb as a function of momentum q using the Helm model. The inset plot zooms in to the location of the first three zeros and extrema of the form factor.

Figure 3.11 shows the zeros of $F'(q)$ plotted against the product qR_0 using the experimental values of R_0 and σ_s for some chosen nuclei. Zooming in, the locations of the first two zeros of $F'(q)$, which correspond to the first two maxima of the charge form factor, can be determined. These are shown in Figure 3.12.

It can be seen that the location of the maxima changes with proton number, having slightly lower(higher) values for light(heavy) nuclei. The first maximum can be averaged at around $q_mR_0 \approx 5.56$, which is widely used to compute the surface thickness [24].

In the Helm model, the three radius parameters are related through the equation

$$R_{ch}^2 = \frac{3}{5}R_0^2 + 3\sigma_s^2\,. \tag{3.40}$$

The uncertainties coming from the Helm model are acknowledged, however, it produces a reasonable density distribution which leads to an explicit expression for the form factor and thus, is widely used to compare predictions from nuclear models. In Ref. [47], a nuclear halo parameter is introduced to account for the difference between the geometric and Helm radius for neutron-rich nuclei. A more

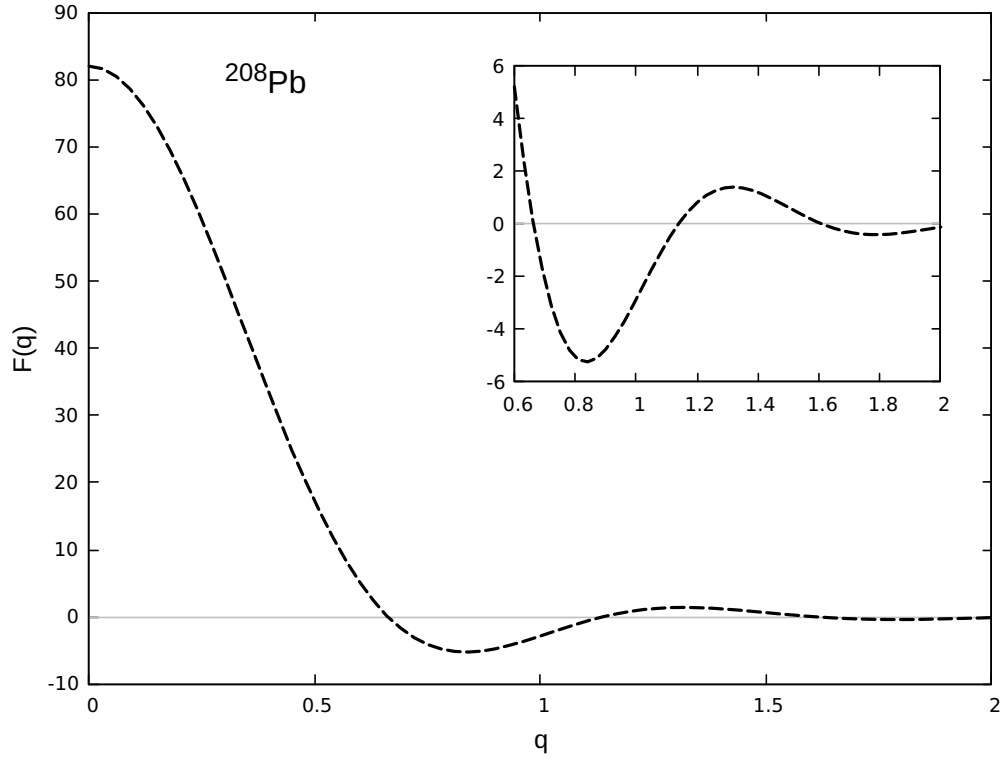

FIGURE 3.10: Charge form factor for ^{208}Pb as a function of q using the Helm model. Inset plot zooms in to the location of the first maximum and the first three zeros of the form factor.

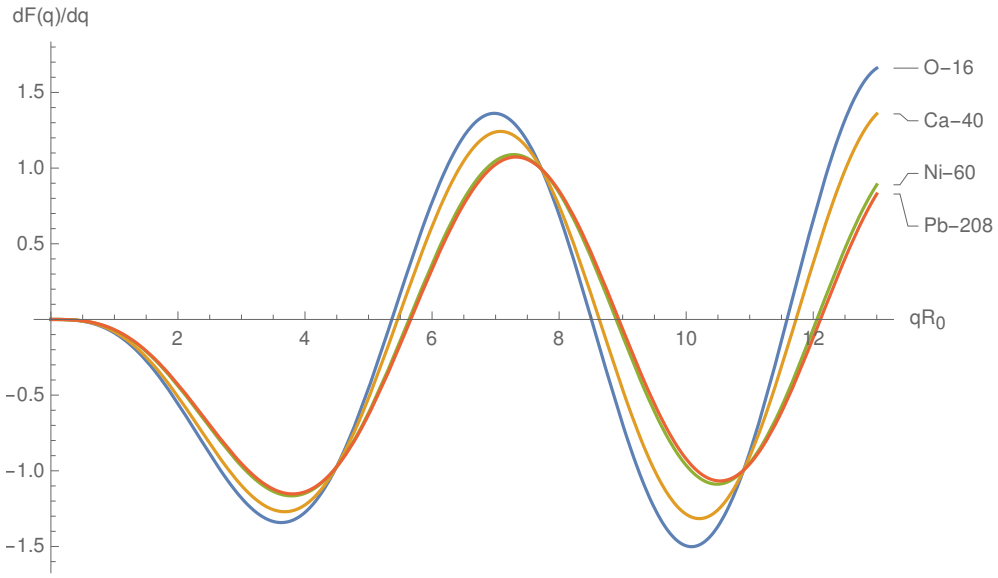

FIGURE 3.11: $F'(q)$ as a function of the product (qR_0) for some chosen nuclei. Note that experimental R_0 and σ_s corresponding to each nucleus are used to produce the Helm model form factors.

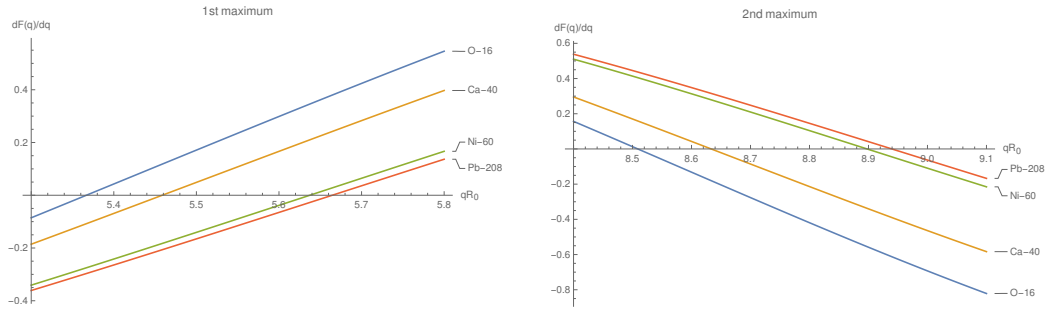

FIGURE 3.12: First two zeros of $F'(q)$, which correspond to the first two maxima of the charge form factor, for some chosen nuclei.

recent paper [48] uses a symmetrized Fermi function with a closed analytic expression for the form factor, which maybe used in future developments of radius and surface structure calculations.

Another related observable to σ_s is the difference in radius when density falls from $0.90\rho_0$ to $0.10\rho_0$. This is referred to as the skin thickness, t, and should not be confused with σ_s . The two observables are related by the equation

$$t = 2.54\sigma_s \,. \tag{3.41}$$

Surface thickness is also related to the diffuseness parameter, a, in Eq. (3.28) by the equation [49]

$$a = 0.58\sigma_s \,. \tag{3.42}$$

Thus, for Fermi density, one can get the relation

$$R_{ch} = \frac{3}{5}c^2 + \frac{7}{5}\pi^2 a^2 \,. \tag{3.43}$$

Optical shifts

To measure the size of an atomic nucleus, the quantity that is actually accessible from experiment is the optical shift, $\delta\langle r^2\rangle$. This observable is defined as

$$\delta\langle r^2\rangle^{A',A} = \langle r^2\rangle^{A'} - \langle r^2\rangle^{A} \tag{3.44}$$

where $\langle r^2\rangle$ is the mean-square charge radius, A is the reference isotope along the chain, and A' is the isotope for which the charge radius is to be measured.

Figure 3.13 shows the experimental optical shifts for isotopic chains of Ca, Ni, Sn and Pb from the doubly-magic reference isotopes ^{40}Ca , ^{56}Ni , ^{100}Sn and ^{208}Pb , respectively. One interesting behaviour is that $\delta\langle r^2\rangle$ tends to have a different

slope at $A' - A = 0$, which is the shift from the closed shell reference isotope. The same behaviour can be seen at $A' - A = 8$ for Ca which corresponds to the second doubly-magic isotope, ^{48}Ca , along the Ca chain. The optical shift for the Ca chain has been studied in various nuclear models as it shows a 'bump' between ^{40}Ca and ^{48}Ca . For the Ni chain, $\delta\langle r^2\rangle$ is somewhat linear from $A' - A = 0$ but slightly changes in slope starting at $A' - A = 6$, which corresponds to ^{62}Ni. For both Sn and Pb chains, the $\delta\langle r^2\rangle$ trends are linear but again with different slopes before and after the shell closures.

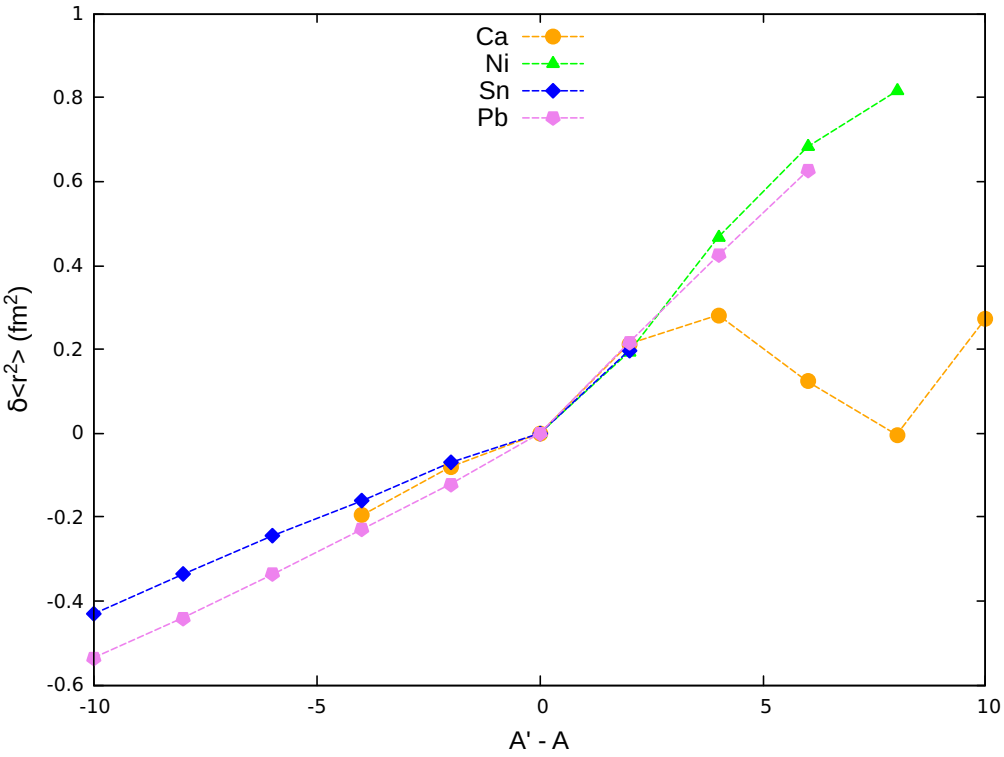

FIGURE 3.13: Experimental optical shifts, $\delta\langle r^2\rangle$, plotted against the mass difference $A - A'$, for isotopic chains of Ca, Ni, Sn and Pb from the reference isotopes ^{40}Ca , ^{56}Ni , ^{100}Sn and ^{208}Pb , respectively. Experimental data are taken from Ref. [50] and errors are smaller than the symbols used in the plot.

Skin thickness

One property of finite nucleus which directly correlates with the slope of symmetry energy, L_0, in nuclear matter is the skin thickness, Δr_{np}. This observable is defined as the difference between the neutron and proton geometrical radii,

$$\Delta r_{np} = R_n - R_p \,. \tag{3.45}$$

Figure 3.14 shows Δr_{np} plotted against L_0 for ^{208}Pb, as predicted by several nuclear models [51]. It can be seen that the two observables are linearly related as suggested by the models.

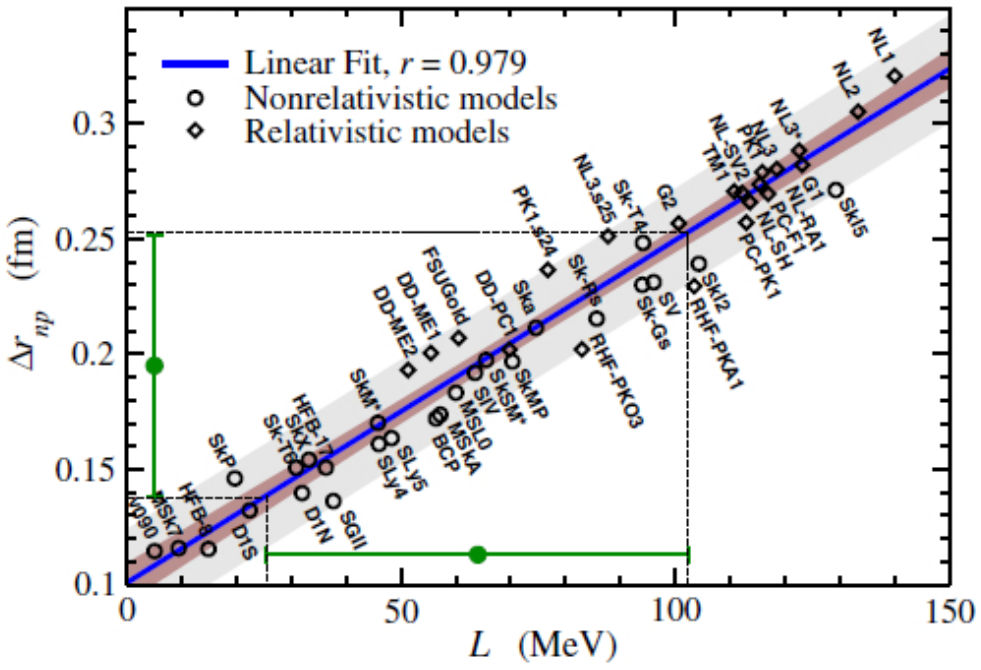

FIGURE 3.14: Δr_{np} for ^{208}Pb plotted against L_0 from several nonrelativistic and relativistic nuclear models. Plot shows a linear relation between the two observables, thus suggesting a link between nuclear matter and finite nuclei. Figure is taken from Ref. [51].

Nuclear deformations

Across the nuclear chart, most nuclei are actually deformed in their ground-states. The deformation properties are usually expressed in terms of parameters β which describe the nucleus spatially. The most common is the quadrupole deformation parameter, β_2, which directly gives a description of whether the nucleus is oblate ($\beta_2 < 0$) or prolate-shaped ($\beta_2 > 0$). Figure 3.15 shows a total of 328 available $|\beta_2|$ values across the chart taken from Ref. [52].

The β_2 values are deduced from experiment where the transition probabilities are actually measured. The transition amplitude from the ground state to the first 2^+ excited state, $B(E2)\uparrow$, is related to β_2 by the equation [52],

$$\beta_2 = \frac{4\pi}{3ZR_0^2}\left[B(E2)\uparrow/e^2\right]^{1/2}, \tag{3.46}$$

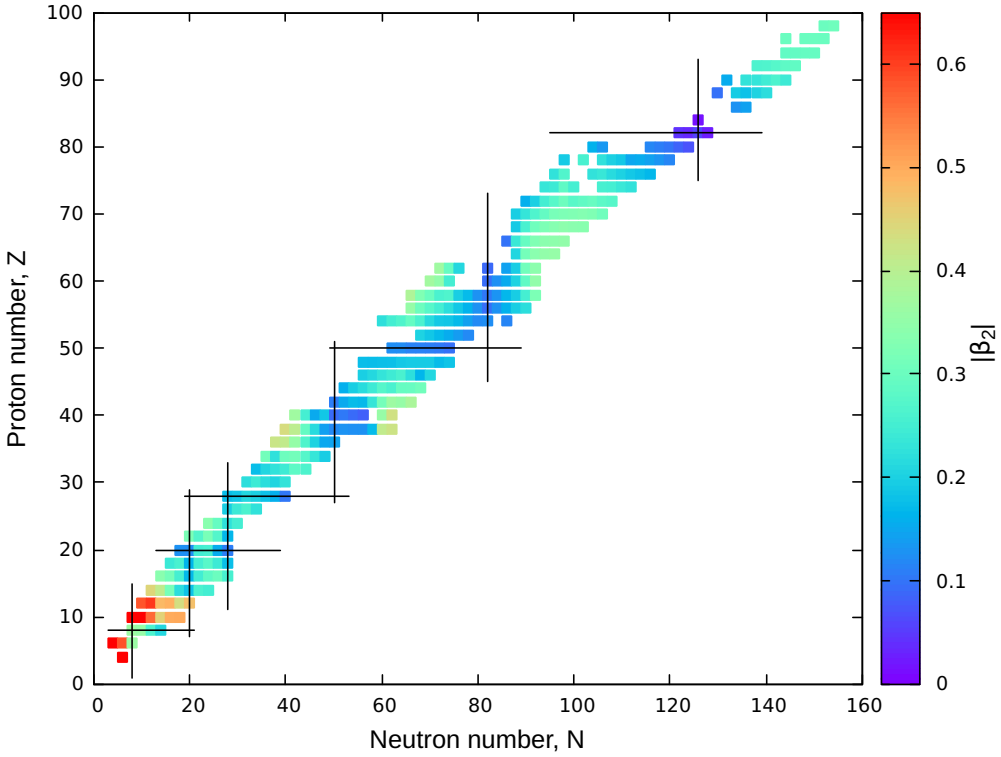

FIGURE 3.15: Absolute values of experimental quadrupole deformation parameter, $|\beta_2|$, across the nuclear chart. Data are taken from Ref. [52].

where $R_0 = 1.2A^{1/3}$ fm and e is the electron charge. $B(E2)\uparrow$ is usually expressed in $e^2\text{b}^2$ where one barn [b] is equal to 100 fm^2. Another related quantity to deformation is the intrinsic quadrupole moment, Q_0, which is computed as

$$Q_0 = \left[\frac{16\pi}{5} B(E2)\uparrow / e^2\right]^{1/2} . \tag{3.47}$$

Chapter 4

QMC model developments and optimisation

As the QMC model continues to develop, more physics is being incorporated in the model and the parametrisation procedure necessary to reproduce experimental data is also improved. In this chapter, the developments done in each QMC version along with the optimization and fitting protocols employed at each stage of the model, are discussed.

4.1 Improvements in the QMC EDF

Table 4.1 presents the developments of QMC giving an overview of how the versions differ from each other.

TABLE 4.1: QMC EDF versions and the developments in the physics of the model.

version	pion	$\tilde{m}_\sigma$	σ self-coupling	spin-orbit	spin-tensor
QMC-I [8]		✓(2-body)		time only	
QMCπ-I [53]	✓	✓(2-body)		time only	
QMCπ-II [54]	✓	m_σ	✓	time+space	
QMCπ-III [55]	✓	m_σ	✓	time+space	✓

The first version of the QMC model, which is referred to in here as QMC-I, has the simple version of the EDF presented in Chapter 2. The σ meson mass is taken to be density-dependent although its expression only includes up to two-body interactions. Some results of this version for even-even finite nuclei across the nuclear chart can be found in Ref. [8]. Already in this first version, QMC was found to be at par with other existing nuclear models and performs even better in the superheavy region despite having significantly fewer number of parameters in the model.

In the following version, QMCπ-I [53], the pion exchange Fock term was added to the QMC-I functional. This development was expected to improve the value of incompressibility of nuclear matter, K_0, which was relatively high in QMC-I. K_0 decreased by around 20 MeV in QMCπ-I, however, the value is still slightly above the upper bound of the range from experimental data. Nevertheless, results from QMCπ-I are again exemplary especially in superheavies, even with a total of only four model parameters as in QMC-I.

The third version of QMC for finite nuclei, QMCπ-II, contains the σ-self interaction which appears in the potential as discussed in Chapter 2, as well as the full spin-orbit contribution containing both space and time components [54]. Furthermore, the σ meson mass is deemed density-independent in this version as opposed to the previous versions. This is consistent with the other meson masses, which are also density-independent, although m_σ is still fitted as a parameter in the optimization procedure. It was seen that taking m_σ to be dependent on density resulted in higher- order fluctuations in the σ field which contributed to the high nuclear incompressibility values in the earlier versions. The final QMCπ-II parameter set along with the necessary statistics and some significant results for several ground state observables are presented in Ref. [54]. A copy of the QMCπ-II published paper is included in Appendix A.

Apart from the developments done in QMCπ-II, the latest QMC model, referred to as QMCπ-III, is improved to include the spin-tensor component of the EDF which comes in quadratic terms of $\vec{J}$. Derivations in Chapter 2 include these J^2 terms but were set to zero in all previous versions of QMC. This latest version have the following additional terms in the QMC Hamiltonian:

$$H^J_{\sigma,\omega,\rho} = \left[\frac{G_\sigma(1-dv_0)^2}{4m_\sigma^2} - \frac{G_\omega}{4m_\omega^2}\right]\sum_m \vec{J}_m^2 - \frac{G_\rho}{4m_\rho^2}\sum_{m,m'} S_{m,m'}\vec{J}_m\cdot\vec{J}_{m'} \quad \text{central part}$$

$$H^J_{SO} = -\frac{G_\sigma - G_\omega}{16M^2}\sum_m \vec{J}_m^2 + \frac{G_\rho}{16M^2}\sum_{mm'} S_{m,m'}\vec{J}_m\cdot\vec{J}_{m'} \quad \text{spin-dependent part}$$

where $S_{m,m'} = \delta_{m,m'}m^2 + \frac{1}{2}(\delta_{m,m'+1} + \delta_{m',m+1})$.

Another significant development in QMCπ-III is that the pairing functional, traditionally taken as detailed in Section 2.6.2 for mean-field models, is now derived within the QMC framework [55]. The pairing EDF is taken to be density-dependent, as opposed to the previous QMC versions where pairing was taken

to have constant strength thoughout the nuclear volume. Furthermore, the QMC pairing functional is fully expressed in terms of the existing QMC parameters so that the number of parameters is reduced to only five, compared to QMCπ-II where there were a total of seven. This QMC pairing is taken in the form of Eq. (2.34) as discussed in the last part of Section 2.6.2.

4.2 Nuclear matter properties

As discussed in Chapter 3, the saturation values of the quantities ρ_0, E_0 and S_0 are commonly used to constrain nuclear observables. In the optimization of the QMC model, it is required that the combination of QMC parameters satisfy the nuclear matter properties at saturation. The widely accepted values for these NMPs are adopted

$$\rho_0 \approx 0.16 \quad (\text{fm}^{-3}),$$
$$E_0 \approx -16 \quad (\text{MeV}),$$

and are allowed to be within 10% uncertainty. The symmetry energy S_0 is allowed to be in the range 29 – 33 MeV. In addition, the σ meson mass is also allowed to vary from 450 to 750 MeV. In QMCπ-II and QMCπ-III, the additional λ_3 parameter needs to be fitted. As in Ref. [54], this parameter is constrained in the range 0.0 to 0.05 so as not to destroy the saturation effects in the QMC model.

All possible combinations of the QMC parameters are identified within the nuclear matter constraints which resulted in distributions defining the parameter spaces of each QMC version. Figures 4.1 (a) to (c) show these distributions which then set the bounds for each of the parameters.

The addition of single-pion exchange in QMCπ-I resulted in a shift of the G_σ and G_ρ parameters to the left while the G_ω distribution remained almost the same compared to the version without pion contribution, QMC-I. Furthermore, the inclusion of higher-order density-dependence starting from QMCπ-II shifted the distributions of the three QMC couplings to the left. Meanwhile, the full σ Hamiltonian expansion used in QMCπ-III only resulted to a slight shift of parameters to the left, compared to the distributions of QMCπ-II parameters where the σ Hamiltonian was approximated.

Figure 4.2 shows the corresponding distributions for (a) the slope of symmetry energy, L_0, and (b) incompressiblity, K_0, of nuclear matter obtained from the combinations of parameters presented in Figure 4.1.

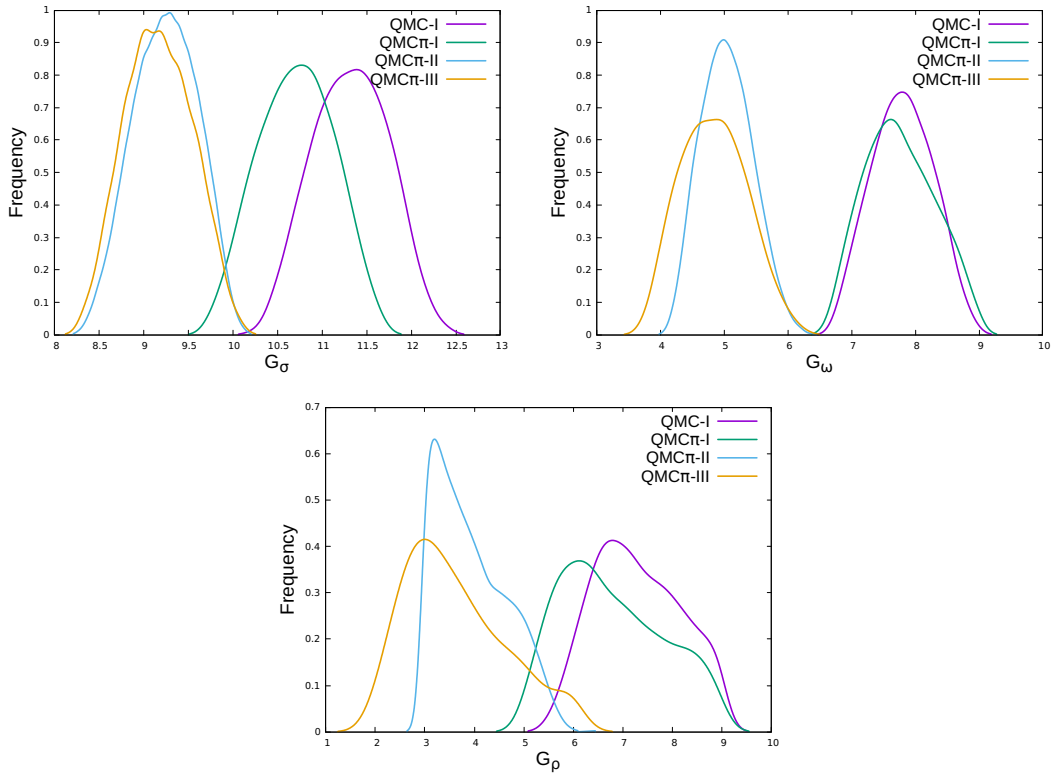

FIGURE 4.1: Distributions of QMC parameters from different versions, constrained by properties of nuclear matter.

In Figure 4.2 (a), single-pion exchange did not change the L_0 distribution significantly when comparing results from QMC-I and QMCπ-I. However, the addition of the higher density-dependence in the kinetic and gradient terms starting in QMCπ-II, shifted the distribution for L_0 to the right, thereby increasing the values. It is emphasised that the low value for L_0 had been a drawback in the earlier versions of the QMC model, which was basically the reason why it was developed to include more density dependence.

For K_0 in Figure 4.2 (b), the range is effectively constrained by the values of the λ_3 parameter. For both QMC-I and QMCπ-I, where λ_3 is effectively zero, the incompressibility values are relatively high. The effect of adding the single-pion exchange in QMCπ-I resulted in a slight shift of K_0 distribution to the left but the values are still above the upper limit of the range set by experimental data. K_0 values are significantly decreased starting from QMCπ-II due to a couple of improvements in the EDF. One is the addition of the σ-self coupling contribution which included higher-order density dependence in the functional. Another enhancement is that the σ mass, m_σ, is taken to be density-independent. In the

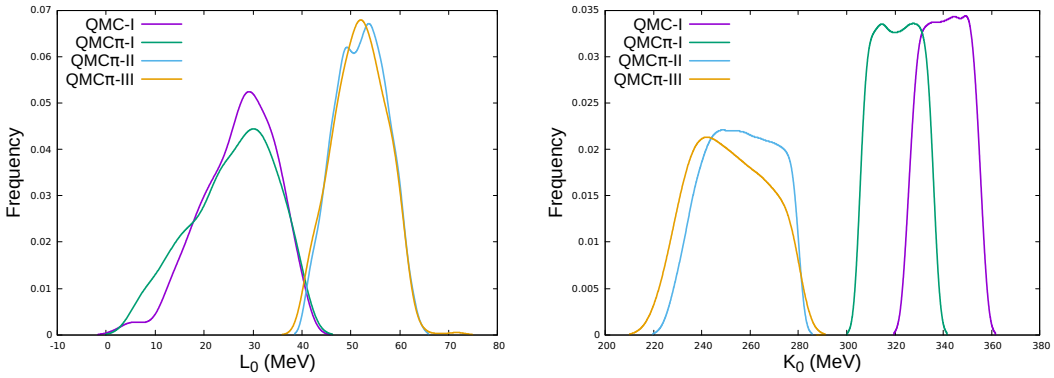

FIGURE 4.2: Distributions of QMC parameters constrained by properties of nuclear matter.

earlier versions, the density-dependence of the effective $\tilde{m}_\sigma$ appears in the fluctuation part of the σ Hamiltonian as

$$\tilde{m}_\sigma = m_\sigma(1 + dG_\sigma\rho)\,.$$

Since the factor goes in the denominator as in Eq. (2.14), its overall effect is a decrease in the contribution from the σ fluctuation part. This then resulted in high values of K_0 in QMC-I and QMCπ-I where m_σ was taken to be dependent on the density.

4.3 Fit to finite nuclei

Once the parameter space and thus, the bounds for the QMC parameters are set by the nuclear matter constraints, the next step is to search for the best parameter set which minimizes the least squares of deviations of finite nuclei observables from those of available experimental data. The algorithm used in the fitting procedure was already laid out in Ref. [54]. Here the procedure is summarised and the important quantities and measures are reviewed which will also be used in the succeeding chapters.

4.3.1 Fit observables

Binding energies, BE, root-mean-square rms charge radii, R_{ch} , and proton and neutron pairing gaps, $\Delta_{p,n}$, for seventy magic and doubly-magic nuclei with $Z, N = 8, 20, 28, 50, 82$ and $N = 126$ were included in the fit. This same set of even-even nuclei was used in Ref. [24] to fit parameters for the Skyrme SV EDF. For the

QMC parameter fit, some values were updated for binding energies taken from Ref. [38] and for *rms* charge radius from Ref. [50]. Figure 4.3 shows the data points included in the fit. Some nuclei only have BE data available and some have known R_{ch} , while some have pairing gaps. These available data points for each nuclei which enter the fitting procedure, are indicated with different colors in the figure.

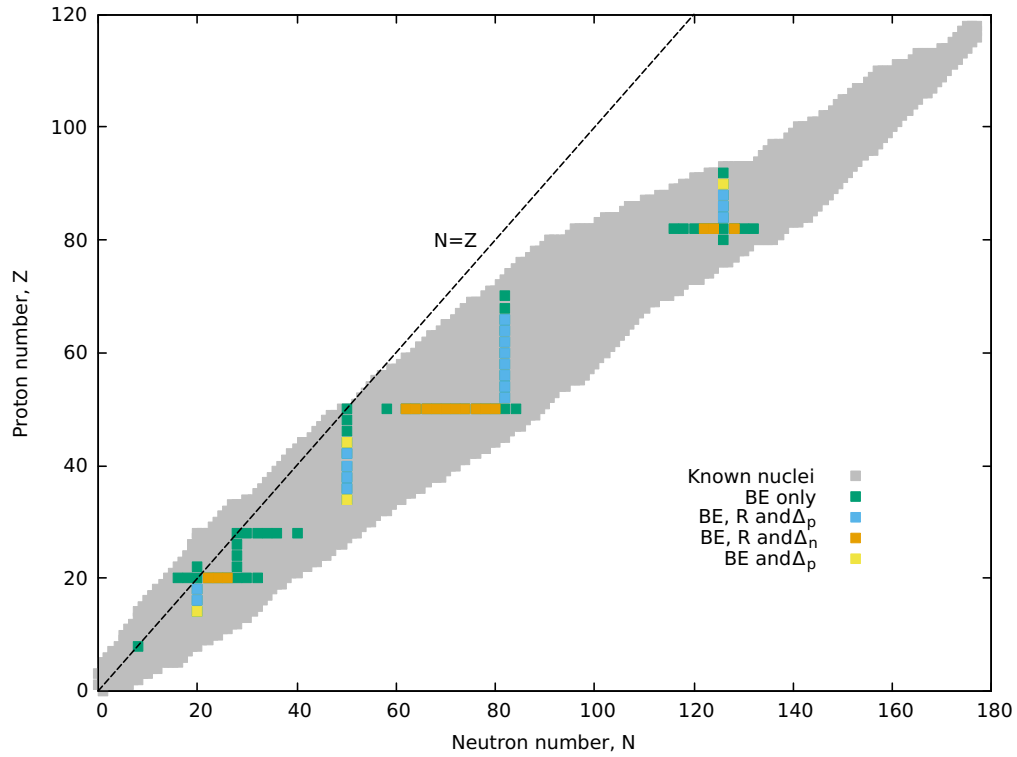

FIGURE 4.3: Doubly magic and semi-magic nuclei included in the fit. The nuclear observables and the number of data points per nucleus entering the fitting procedure are indicated. See text for more explanation.

Table 4.2 presents the fitting procedures implemented in each of the QMC versions.

Apart from the improved physics included in the QMCπ-II model, the approach to optimisation is also developed. The first two versions included data for diffraction radius R_0 and surface thickness σ_s as in [24] but after preliminary tests in the QMCπ-II, the two observables did not contribute much to the fit and results are almost the same, even without their data included. Thus to save computation time, both R_0 and σ_s data points are excluded starting from QMCπ-II.

TABLE 4.2: QMC EDF fitting protocols

version	Fit observables
QMC-I (PRL)	$BE, R_{ch}, \sigma_s, R_0, \Delta_{p,n}$
QMCπ-I	$BE, R_{ch}, \sigma_s, R_0, \Delta_{p,n}$
QMCπ-II	$BE, R_{ch}, \Delta_{p,n}$
QMCπ-III	BE, R_{ch}

Further in QMCπ-III, since pairing strengths are no longer fitted as separate parameters, the pairing gap data are also removed from the fit.

4.3.2 POUNDerS algorithm

To find the best fit parameters, the algorithm called **P**arameter **O**ptimization **U**sing **N**o **Der**ivatives for **S**um of Squares (POUNDerS) is employed which is made available by Portable, Extensible Toolkit for Scientific Computation PETSc [56, 57, 58]. The objective function $F(\hat{\mathbf{x}})$ for minimization was expressed in the form

$$F(\hat{\mathbf{x}}) = \sum_{i}^{n} \sum_{j}^{o} \left(\frac{\bar{s}_{ij} - s_{ij}}{w_j} \right)^2 , \tag{4.1}$$

where n is the total number of nuclei, o is the total number of observables and s_{ij} and $\bar{s}_{ij}$ are the experimental and fitted values, respectively. To make the objective function dimensionless, the difference $\bar{s}_{ij} - s_{ij}$ is divided by a chosen *effective* error, w_j, for each observable. In the QMC fit, these errors are set to $w_{BE} = 1$ MeV, $w_{R_{ch}} = 0.02$ fm and $w_{\Delta_{p,n}} = 0.12$ MeV for all nuclei.

To find the correlation between the QMC best fit parameters, the covariance matrix is first solved using the expression from Ref. [26],

$$\mathrm{Cov}(\hat{\mathbf{x}}) \approx \frac{\chi^2}{d-p} \left(\mathbf{J}^{\mathbf{T}} \mathbf{J} \right)^{-1} , \tag{4.2}$$

where J is the Jacobian matrix with derivatives computed using finite differences, d is the total number of data points and p is the number of parameters. The objective function is evaluated at $\{\hat{\mathbf{x}} \pm \eta e_j\}$, with η set to 10^{-3} and e_j being the scale used for each parameter during the search.

The square root of the diagonal terms of the covariance matrix gives the *standard deviation* σ for each parameter and the off-diagonal terms give the correlation

coefficient between any two parameters x_k and x_l through the expression,

$$\mathrm{Cor}(x_k, x_l) = \frac{\mathrm{Cov}(x_k, x_l)}{\sqrt{\sigma^2_{x_k}\sigma^2_{x_l}}}. \tag{4.3}$$

Throughout the discussions in the succeeding chapters, some other measures are used. One is the *residual*, defined as the difference between the theoretical and experimental results, $\bar{s}_{ij} - s_{ij}$. Another measure is the *root-mean-square deviation* for each observable, j, defined as

$$\mathrm{RMSD}(j) = \sqrt{\frac{1}{n}\sum_i^n (\bar{s}_{ij} - s_{ij})^2}. \tag{4.4}$$

Finally, the *percentage deviation* from experiment of each data point, is calculated using $(\mathrm{dev})_{ij} = 100 * \left(\frac{\bar{s}_{ij} - s_{ij}}{s_{ij}}\right)$ so that the *root-mean-square percent deviation* for each observable is expressed as

$$rms\ \%\ \mathrm{deviation}(j) = \sqrt{\frac{1}{n}\sum_i^n (\mathrm{dev})^2_{ij}}. \tag{4.5}$$

Chapter 5

QMC results along magic chains of nuclei

In this chapter, results from the different versions of the QMC model are presented. The final parameter sets and corresponding nuclear properties are compared for each version and correlation matrices for the QMC parameters computed. Several nuclear observables defined in Chapter 3 are calculated to compare the effect of the developments incorporated in each version of the QMC model.

5.1 QMC parameters, NMPs and fit results

Table 5.1 presents the final parameters for each of the QMC versions. It can be seen that upon the inclusion of higher-order density dependence in the central σ part of the Hamiltonian for QMCπ-II and QMCπ-III, the parameters correspondingly decreased in value. Recall that in Section 4.2, it was already seen that the parameter space for QMCπ-II is shifted to the left as a result of including higher densities. There is a very slight change in the final set of QMCπ-III parameters

TABLE 5.1: QMC and pairing parameters of various QMC versions.

Parameters	QMCπ-III [55]	QMCπ-II [54]	QMCπ-I [53]	QMC-I [8]
G_σ [fm^2]	9.62	9.66	11.16	11.85
G_ω [fm^2]	5.21	5.23	8.00	8.27
G_ρ [fm^2]	4.71	4.75	6.38	7.68
M_σ [MeV]	503	493	712	722
λ_3 [fm^{-1}]	0.05	0.05	-	-
V_p [MeV]	-	258	302	284
V_n [MeV]	-	237	291	326

compared to that of QMCπ-II even with the inclusion of the spin-tensor terms

in the latest version. The addition of single-pion exchange slightly decreased the values of QMC parameters as seen in QMCπ-I and QMC-I. Note that since there is no σ self-coupling in the first two versions, the λ_3 parameter is not included there.

As discussed in Section 4.1, the latest QMCπ-III functional employs a QMC-derived pairing functional such that the two pairing strength parameters are now expressed in terms of the QMC parameters. Hence, in Table 5.1, there are only five parameters for QMCπ-III. Recall also that in QMCπ-III, a density-dependent pairing is implemented while the previous versions employed constant pairing throughout the nuclear volume where pairing strengths were fitted to pairing gap data.

Figure 5.1 shows the correlation matrices for both QMCπ-II and QMCπ-III. The correlation coefficient between any two parameters were calculated using Eq. (4.3) as discussed in Section 4.3.2. It can be seen from QMCπ-II that the QMC parameters have very small correlation to the pairing strengths. For both QMCπ-II and QMCπ-III, G_σ and G_ω have relatively high correlation as well as G_ρ with both m_σ and λ_3 . The σ mass is also highly correlated to λ_3 for both versions.

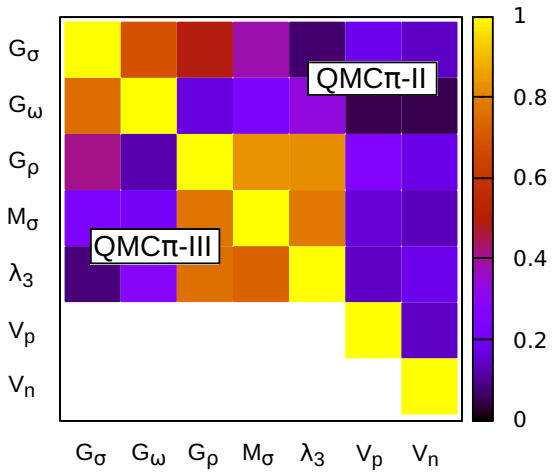

FIGURE 5.1: Correlation matrices for QMCπ-II and QMCπ-III parameters.

Table 5.2 shows the corresponding NMPs for the QMC parameters presented in Table 5.1. The saturation density, ρ_0, binding energy per nucleon, E_0, and symmetry energy, S_0, are almost the same from all versions of the model while significant improvements for L_0 and K_0 are seen in the last two versions. The previous versions, QMC-I and QMCπ-I, give very high K_0 and very low slope L_0 where expected values as discussed in Section 3.1.2, lie in the range 200 to 315 MeV for K_0 while average value for L_0 is 58.9 MeV. This is improved starting from QMCπ-II where we get better values for both NMPs. In Ref. [54] it has been shown that to be consistent with experimental data on giant monopole resonances, K_0 should be in the lower bound of the accepted range.

TABLE 5.2: Nuclear matter properties from different QMC models.

NMP	QMCπ-III [55]	QMCπ-II [54]	QMCπ-I [53]	QMC-I [8]
ρ_0 (fm^{-3})	0.15	0.15	0.15	0.16
E_0 (MeV)	-15.7	-15.7	-15.8	-15.9
S_0(MeV)	29	29	30	30
L_0 (MeV)	43	40	17	23
K_0 (MeV)	233	230	319	340

Table 5.3 shows the *rms* percent deviations of finite nuclei observables for the 70 semi-magic nuclei in the fit. There are significant improvements in QMCπ-III predictions for binding energies of nuclei included in the fit, compared to the other versions, and even with the Skyrme-type force SV-min [24]. For radii, marginally better predictions are seen in the earlier versions QMC-I and QMCπ-I.

TABLE 5.3: Comparison of percent deviations for BE and R_{ch} of 70 magic nuclei included in the fit of QMC models and SVmin.

Data	QMCπ-III [55]	QMCπ-II [54]	QMCπ-I [53]	QMC-I [8]	SV-min
BE	0.20	0.48	0.44	0.42	0.24
R_{ch}	0.58	0.59	0.43	0.50	0.52

Figure 5.2 shows the deviations for energies and charge radii of the 70 semi-magic isotopes and isotones comparing results from the fit of the various QMC versions. In general, energy predictions are improved for both QMCπ-II and QMCπ-III compared to the previous versions, most especially for nuclei with $Z, N < 28$. For radii, however, QMC-I and QMCπ-I give better predictions for most nuclei especially in the Pb chain except for light Sn isotopes, where the last two versions are slightly better.

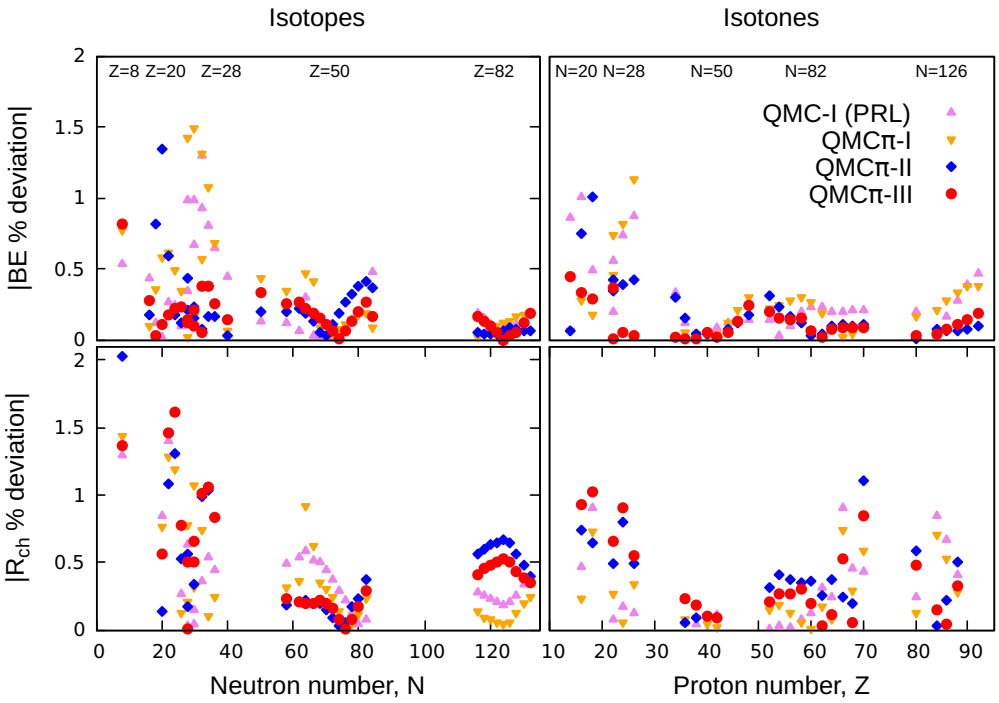

FIGURE 5.2: Percent deviations for BE and R_{ch} of the 70 magic isotopes and isotones from different QMC model versions.

5.2 Binding energy curves

As seen in Figure 3.3, the value for BE per nucleon of an atomic nucleus is expected to be at around 8 MeV. The exact values however, depend on the number of protons and neutrons in a particular nucleus such that it forms a curve between the proton-rich and the neutron-rich sides along isotopic or isotonic chains. In this section, energy curves for magic isotopes and isotones which were included in the fit are presented.

Figures 5.3 and 5.4 show comparisons of (a) the binding energy per nucleon and (b) the BE residuals along Ca and Ni, and along Sn and Pb isotopic chains, respectively, from the different QMC versions and from experimental data.

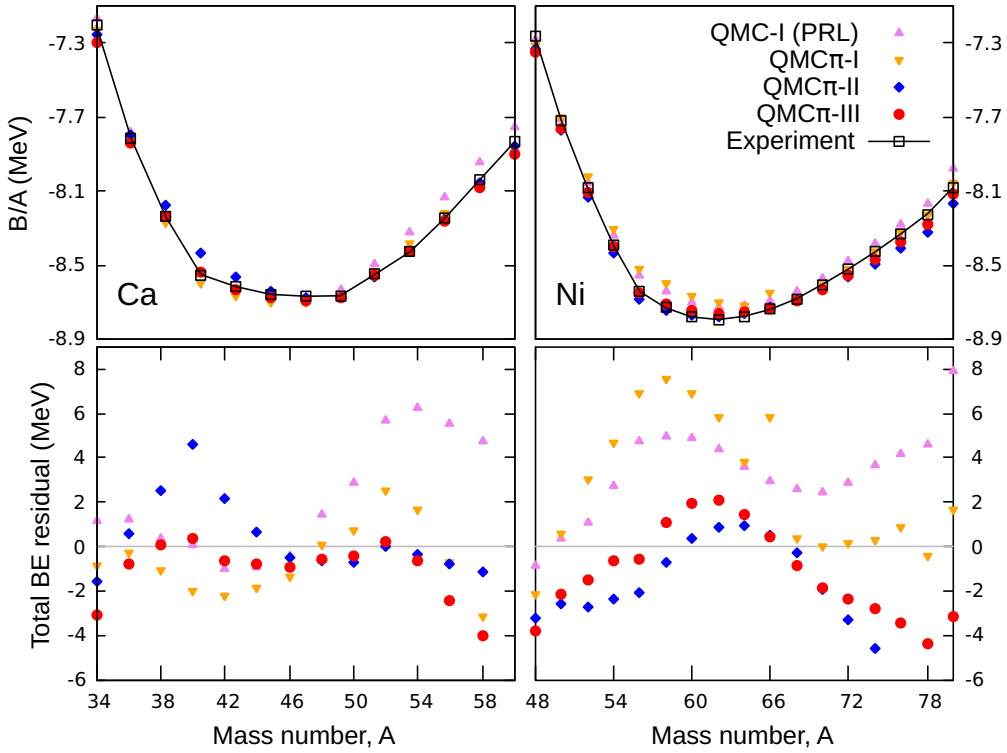

FIGURE 5.3: Comparison of BE per nucleon (top plots) and total BE residual (bottom plots) from various QMC versions for the Ca and Ni isotopic chains. Also added are values from experiment taken from Ref. [38] and errors are smaller than the symbols used in the plot.

For the Ca isotopes in Figure 5.3, more binding is expected between the doubly-magic ^{40}Ca and ^{48}Ca isotopes which is replicated well by QMCπ-III. Results from QMCπ-II show underbinding for isotopes with masses $A < 46$ with residual of up to 5 MeV while QMC-I predicts underbinding for isotopes with $A > 48$ with residual of up to around 7 MeV. These are corrected in the QMCπ-III version where residuals only vary from around 0 to -2 MeV except for the proton-rich ^{34}Ca and neutron-rich ^{58}Ca where residuals are relatively higher.

For the Ni chain in Figure 5.3, there is expected more binding between the doubly-magic ^{56}Ni and ^{78}Ni isotopes compared to other isotopes in the chain. Both QMC-I and QMCπ-I predict underbinding along the chain compared to that of experiment while QMCπ-II and QMCπ-III predict overbinding in most isotopes except for the region around ^{62}Ni where there is slight underbinding.

The overall better agreement between theory and experiment for QMCπ-III is very noticeable.

In the Sn and Pb chains in Figure 5.4, there appears a linear trend in B/A right after the doubly-magic ^{132}Sn and ^{208}Pb isotopes. For the Sn chain, the expected minimum in the energy curve is around the mid-shell $^{114-116}$Sn isotopes, while for Pb it is around the ^{202}Pb isotope. BE residuals for Sn tend to be larger around the mid-shell and around the closed shell ^{132}Sn for QMC versions with the pion while QMC-I version had smaller residuals at mid-shell Sn but starts to increase up to 8 MeV towards neutron-rich Sn isotopes.

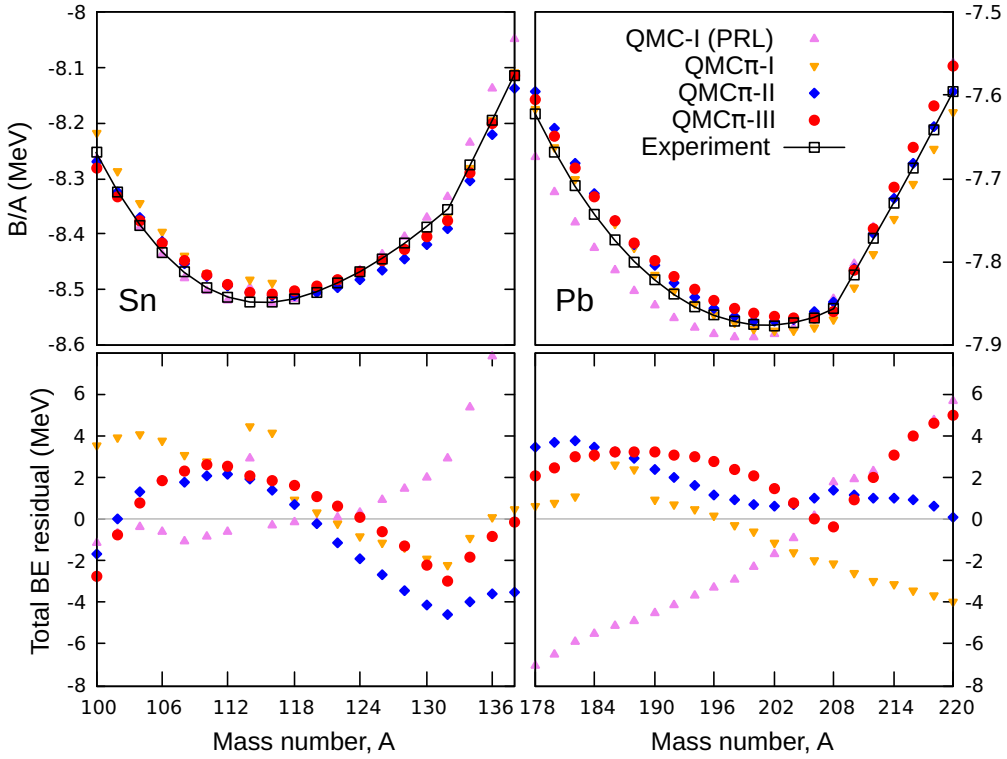

FIGURE 5.4: Same as in Figure 5.3 but for the Sn and Pb isotopic chains.

For the Pb chain, QMCπ-II predicts best, having residuals of only up to 4 MeV compared to the other versions. BE residuals from QMCπ-III slightly increase up to ^{190}Pb and start to decrease towards ^{208}Pb but then again increase up to 5 MeV as mass A further increases. QMCπ-I has relatively good predictions for light Pb isotopes while residuals start to increase towards the neutron-rich side with residuals up to -4 MeV. QMC-I, on the other hand, had huge range of residuals predicting overbinding to the left of ^{208}Pb up to -7 MeV and underbinding to the right of ^{208}Pb up to 6 MeV.

Along magic isotonic chains, Figures 5.5 to 5.7 show (a) the binding energy per nucleon and (b) the BE residuals along $N = 20$ and $N = 28$, and along $N = 50$ and $N = 82$ isotopic chains, respectively, from the different QMC versions and from experimental data.

For both $N = 20$ and $N = 28$ isotonic chains in Figure 5.5, the binding energy curves are well-reproduced in the QMCπ-III version when compared to that of experiment. For the previous versions, QMCπ-II predicted underbinding in $N = 20$ where QMCπ-I predicted mostly overbinding, while for $N = 28$ isotones, QMCπ-II predicted overbinding where QMCπ-I again predicted otherwise. The developments done in QMCπ-III improved the energies for these isotones so that the residuals are now smaller.

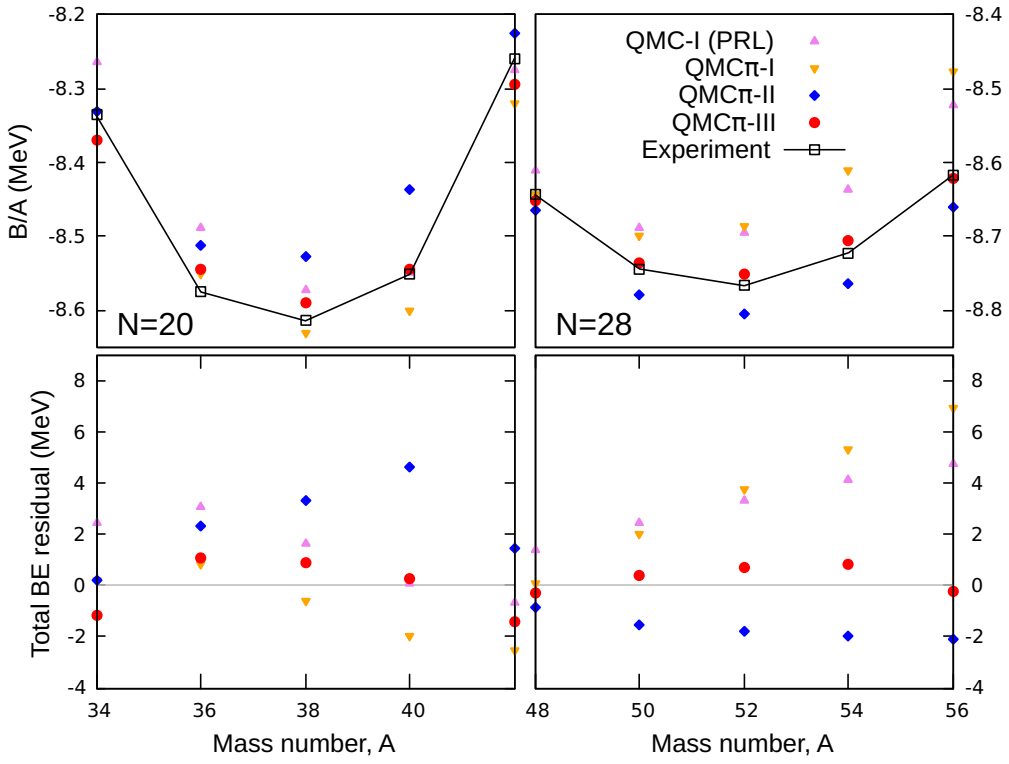

FIGURE 5.5: Same as in Figure 5.3 but for the $N = 20$ and $N = 28$ isotonic chains.

For $N = 50$ isotonic chain in Figure 5.6, the minimum of the curve is at around mass $A = 88$ which corresponds to ^{88}Sr nuclei. QMC predictions are quite good around this minimum but residuals increase as A increases so that at $A = 100$, which corresponds to the doubly-magic ^{100}Sn isotope, residuals reach up to 4 MeV for QMCπ-I and up to 3 MeV for QMCπ-III. For $N = 82$ isotones still in Figure 5.6, the minimum of the curve is at around $A = 136$, which is the ^{136}Xe nucleus. BE residuals are smaller for QMCπ-III around this minimum and the residuals continue to decrease up to $A = 144$ and then slowly increase up to around 1.5 MeV as A further increases. QMCπ-II and QMCπ-III have almost the same behaviour for residuals except for the proton-deficient side where QMCπ-II has relatively higher values. The earlier versions also have higher BE residuals with values up to 3 MeV for QMC-I and around -4 MeV for QMCπ-I.

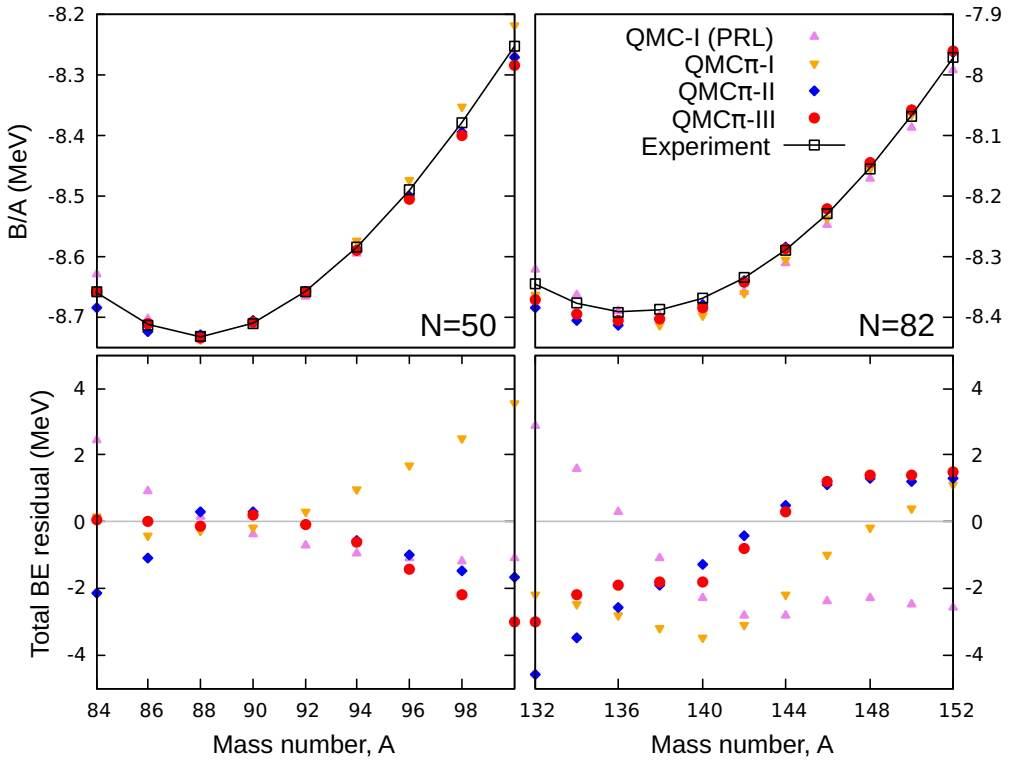

FIGURE 5.6: Same as in Figure 5.3 but for the $N = 50$ and $N = 82$ isotonic chains.

Lastly for binding energy curves, Figure 5.7 shows the magic $N = 126$ isotonic chain. Note that there is a steady increase in B/A starting from the doubly-magic ^{208}Pb nuclei which is well-reproduced by QMCπ-II. Compared to QMCπ-I and QMCπ-III which predict overbinding in most nuclei, QMCπ-II predicts slight underbinding. The higher density dependence in both QMCπ-II and QMCπ-III significantly improves the energies along this chain, where the early versions had high residuals reaching up to around -6 MeV and -8 MeV for QMCπ-I and QMC-I, respectively, in the proton-rich side of the $N = 126$ isotonic chain.

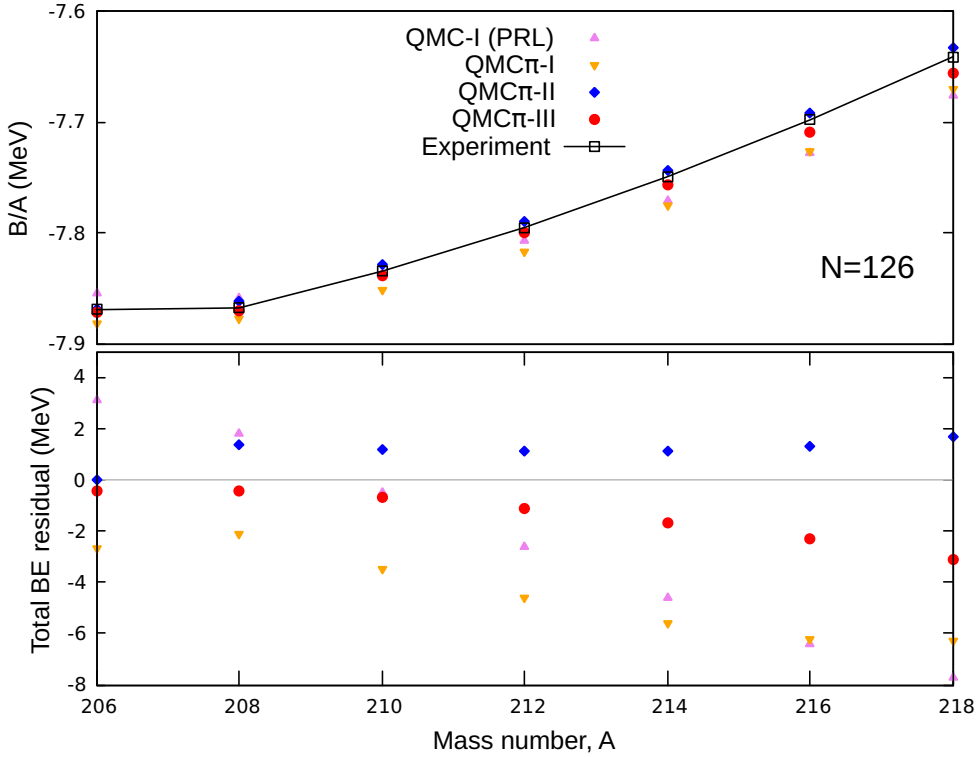

FIGURE 5.7: Same as in Figure 5.3 but for the $N = 126$ isotonic chain.

5.3 *rms* charge radius

Aside from binding energies, all of the QMC versions were also fitted to the *rms* charge radii, R_{ch} , of magic nuclei. In this section, predictions for R_{ch} from the various versions are presented for nuclei along magic isotopic and isotonic chains.

Figures 5.8 and 5.9 show the (a) R_{ch} and (b) R_{ch} residuals along magic isotopic chains. For the Ca chain in Figure 5.8, a well-known 'bump' from experimental data appears between the two doubly-magic isotopes ^{40}Ca and ^{48}Ca. Most mean-field models are not able to get this behaviour and instead predict a continued increase in Ca radii along the chain. This is also true for QMC for all versions. It is interesting to note, however, that predictions get better for QMCπ-II where both ^{40}Ca and ^{48}Ca radii are closer to that of experiment compared to the other versions which underestimated radii values of Ca with $A < 48$. QMCπ-III is able to predict the ^{48}Ca radius really well but R_{ch} residuals are slightly higher than those of QMCπ-II for the other isotopes. More discussion on the Ca radii trend will be tackled in the discussion of optical shifts in Section 5.6.

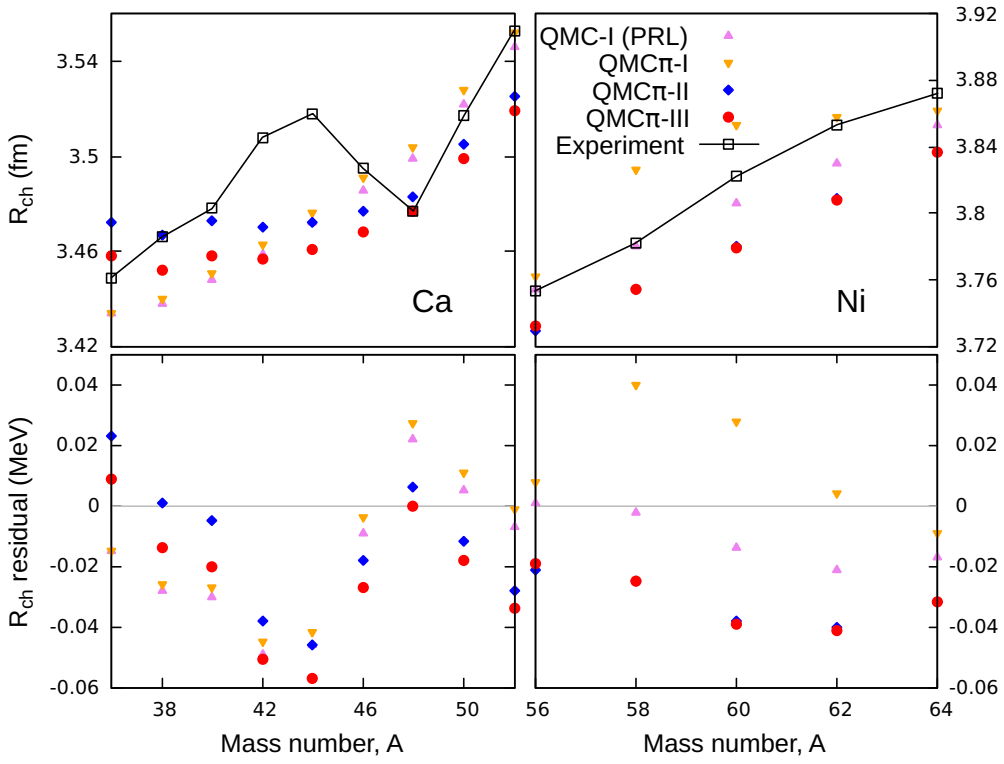

FIGURE 5.8: Comparison of R_{ch} (top plots) and R_{ch} residuals (bottom plots) from various QMC versions for the Ca and Ni isotopic chains. Also added are values from experiment taken from Ref. [50] and errors are smaller than the symbols used in the plot.

For the Ni chain in Figure 5.8, charge radius predictions from the first two versions are slightly better compared to those of QMCπ-II and QMCπ-III. Nevertheless, the residuals are within the same range of values.

Along the Sn chain in Figure 5.9, QMCπ-III yields good results for charge radii with residuals well within the preferred error of $\pm$0.02 fm. QMCπ-II has slightly higher residuals than that of the latest version but still has residuals within the same range. QMC-I and QMCπ-I give good predictions around the doubly-magic ^{132}Sn but residuals are higher at lower masses of Sn isotopes compared to the last two QMC versions. An interesting feature of the experimental data for Sn is the slight curve in R_{ch} starting from the proton-rich side up to ^{132}Sn and a different slope towards ^{134}Sn. This behaviour also appears in Ca in Figure 5.8 where there tends to be a steeper slope after the closure at ^{48}Ca. Predictions from QMC, however, fail to replicate this behaviour at ^{132}Sn, where it has relatively higher residual compared to other isotopes in its neighborhood.

For the Pb chain shown in Figure 5.9, the same trend appears as in Ca and Sn where there is a steeper slope after the closure at the doubly-magic ^{208}Pb. Again, results from QMC do not reproduce this trend. The residuals also went higher with QMCπ-II and QMCπ-III compared to the earlier versions.

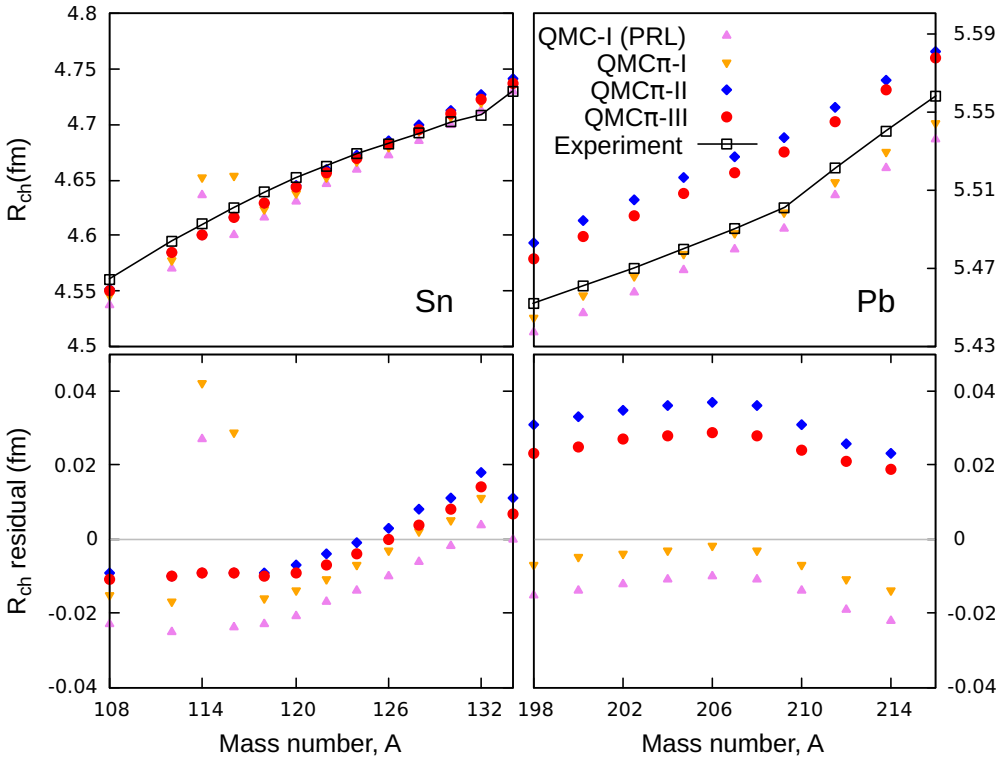

FIGURE 5.9: Same as in Figure 5.8 but for the Sn and Pb isotopic chains.

Figures 5.10 to 5.12 show the (a) R_{ch} and (b) R_{ch} residuals along magic isotonic chains. There are only three isotones with available data in the $N = 20$ chain which includes ^{36}S and ^{38}Ar and the doubly-magic ^{40}Ca as shown in Figure 5.10. The residuals are comparable along the chain with the QMCπ-III version having slightly higher values compared to the other versions.

For the $N = 28$ chain, residuals are again, in general, relatively smaller for QMC-I and QMCπ-I. Most R_{ch} values along this chain are slightly underestimated by the last two QMC versions especially as A increases. Both QMCπ-II and QMCπ-III, however, are able to get good values for the doubly-magic ^{48}Ca nucleus. Furthermore, the residuals for all QMC versions are still within the satisfactory range of $\pm$ 0.03 fm, which corresponds to less than 1% deviation from experimental data.

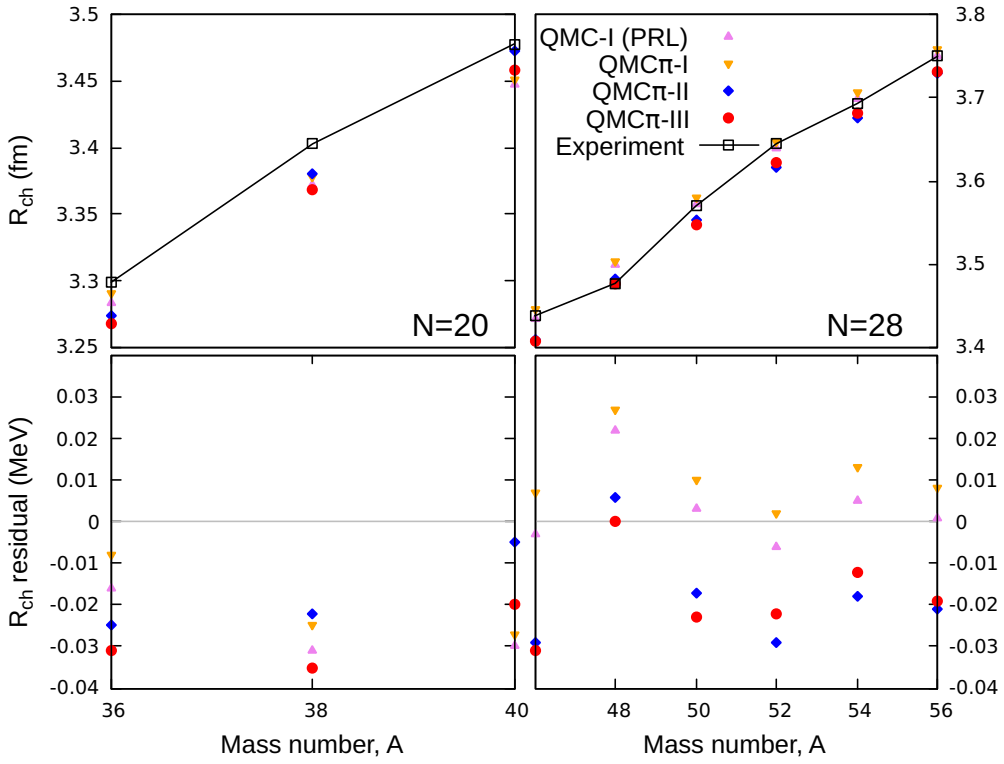

FIGURE 5.10: Same as in Figure 5.8 but for the $N = 20$ and $N = 28$ isotonic chains.

Along the $N = 50$ isotonic chain shown in Figure 5.11, QMC results are quite impressive with residuals within the range $\pm$ 0.01 fm, although again, the earlier versions perform slightly better. Also in the same figure is the $N = 82$ chain. It is interesting to note that a curve appears starting from $A = 146$ to $A = 152$ from experiment, however, this is not reproduced by QMC. This curve may suggest a deformed structure for these isotopes, but which is not accounted for in the QMC fits since spherical shapes were strictly imposed along magic chains. More discussion on deformation will be covered in Section 7.4. Nevertheless, the residuals are still satisfactory ranging from $\pm$ 0.06 fm corresponding to around 1% deviation from experiment.

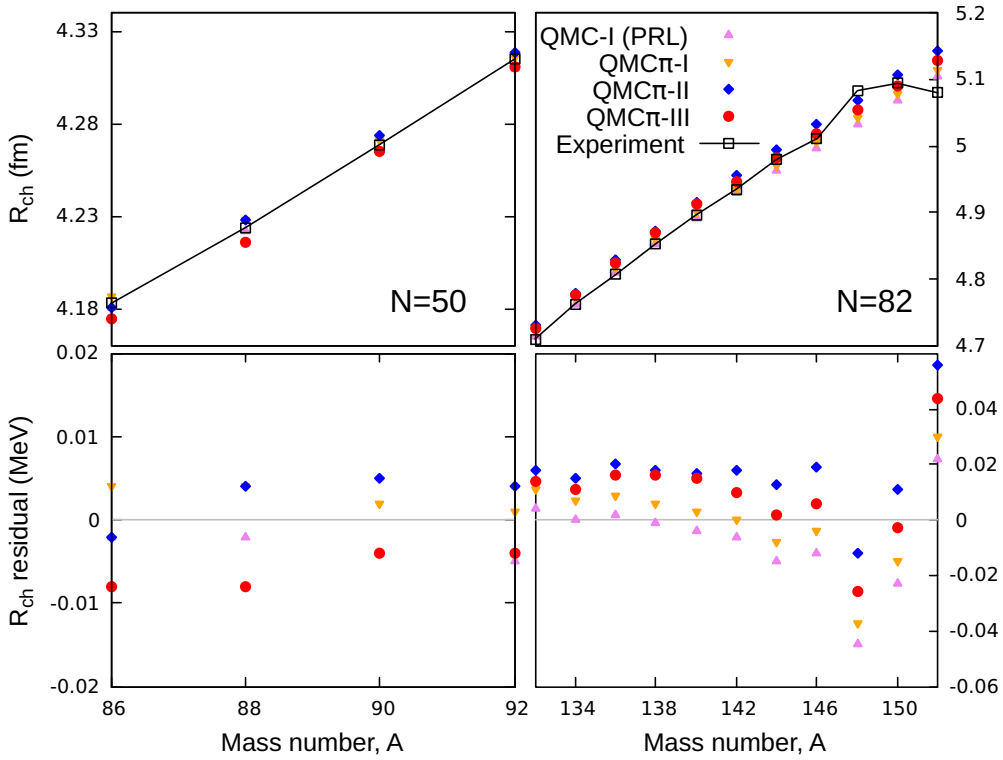

FIGURE 5.11: Same as in Figure 5.8 but for the $N = 50$ and $N = 82$ isotonic chains.

Lastly for R_{ch} is the $N = 126$ chain shown in Figure 5.12. As before, note that there appears a different slope after the doubly-magic ^{208}Pb nuclei from experimental data. The different versions of QMC do not quite reproduce this trend but instead predict a constant increase in R_{ch} . QMCπ-II and QMCπ-III predictions have slightly higher residuals for lower A isotones but values get better as A increases compared to the earlier versions.

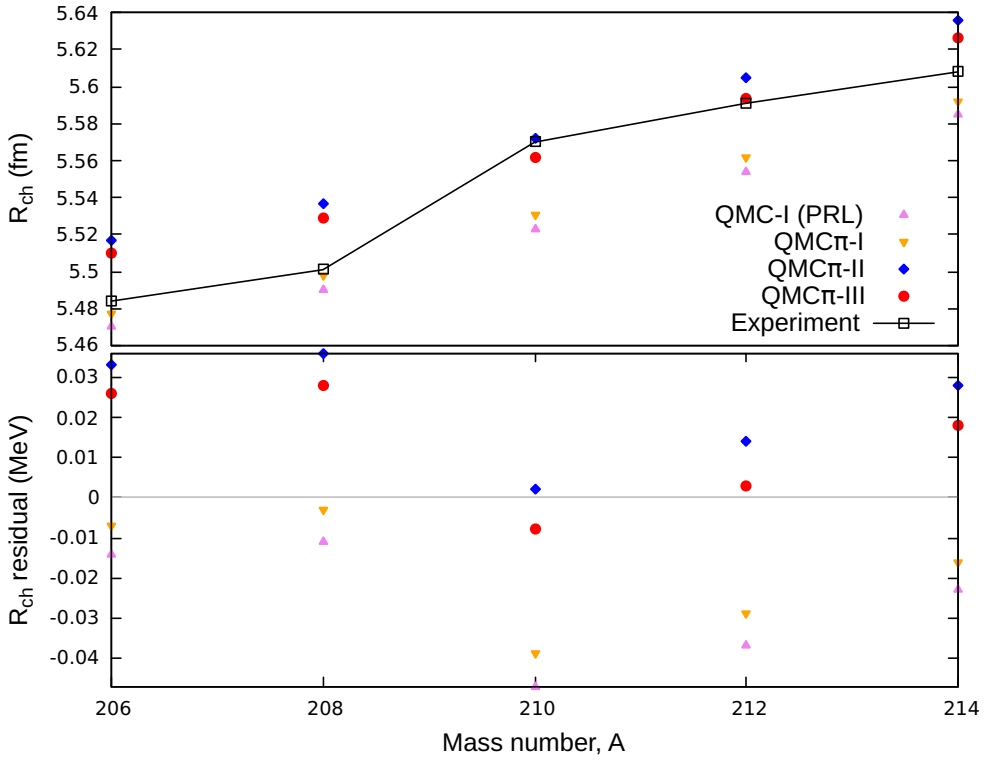

FIGURE 5.12: Same as in Figure 5.8 but for the $N = 126$ isotonic chain.

Overall, for the fit observable R_{ch} , results from QMC-I and QMCπ-I are slightly better compared to the last two versions. This is seen in the summary of deviations in Table 5.3 and from the figures shown in this section. As discussed for the Pb chain, the small increase in residuals for QMCπ-II and QMCπ-III are attributed to two factors: 1) the effect of including the space part of the spin-orbit term and 2) not including R_0 and σ_s in the fitting procedure. It should be emphasized, however, that both contributions significantly improve the values for binding energies which are more preferred. Moreover, the deviations so far for R_{ch} in the QMC fits are still satisfactory with values only reaching up to 1.6% error from experimental data.

5.4 Charge density distributions

Electron scattering experiments provide data for the charge density distribution of several nuclei through a model-independent analysis using Fourier-Bessel coefficients (FBC). In this section, charge densities for some nuclei included in the fit will be discussed.

Figure 5.13 shows the charge density distributions of doubly-magic nuclei ^{16}O , ^{40}Ca , ^{48}Ca and ^{90}Zr from QMC and results taken from elastic electron scattering data. For ^{16}O , QMCπ-I compares well with experiment starting from the nuclear core by replicating the bump, although the model falls off slightly later near the surface. Both QMCπ-II and QMCπ-III, however, overestimate the bump and also thereby falling off later near the surface compared to that of experiment. The same is true for the rest of the nuclei included in the plot, where the QMC model tends to push nucleons more towards the surface where the charge density starts to fall off. For ^{40}Ca , the three versions of QMC behave in almost the same way having slightly higher density at the core compared to that of experiment and also overestimating the location of the bump along the radius by around 1 fm. For ^{48}Ca , predictions from QMCπ-II and QMCπ-III somewhat create a slightly

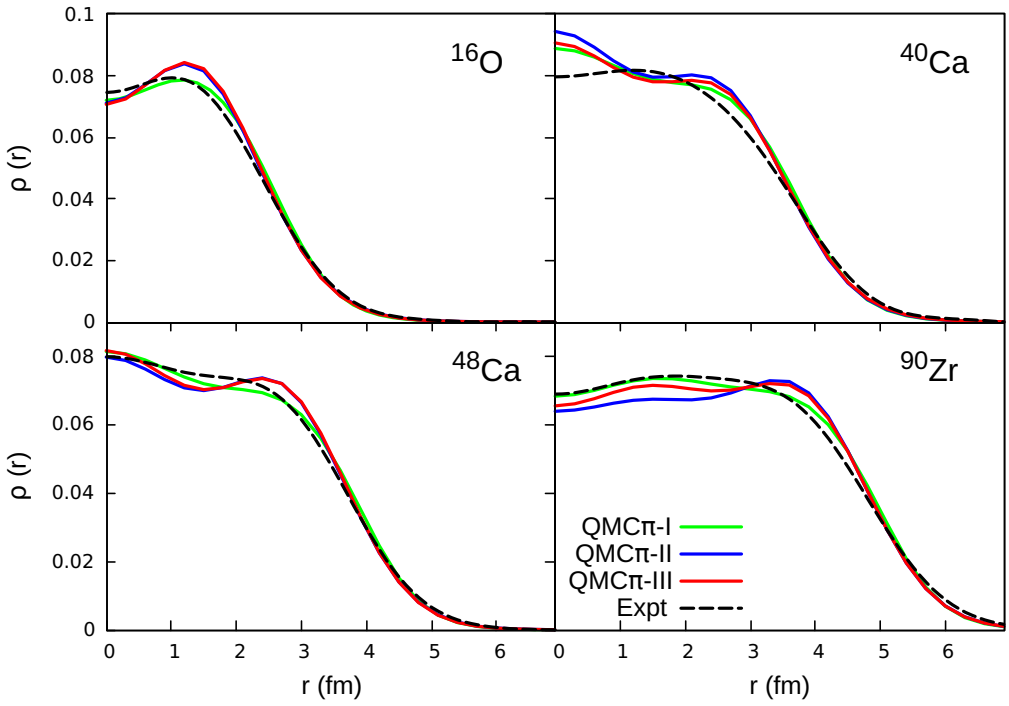

FIGURE 5.13: Charge density distributions of doubly-magic nuclei ^{16}O, ^{40}Ca , ^{48}Ca and ^{90}Zr from QMC and data from electron scattering experiments.

deeper minimum compared to data near the core, just before the appearance of the bump. QMCπ-I has shallower minimum compared to the other two versions but slightly underestimates the densities towards the location of the bump. For ^{90}Zr , QMCπ-I is again able to reproduce the densities fairly well across the nuclear volume, but just as for ^{16}O , the model tends to fall off a little bit later than that of experiment. The last two QMC versions, on the other hand, both underestimate the densities at lower r, though there seems to be a small improvement for QMCπ-III compared to that of QMCπ-II. Near the surface, the bump is defined for both QMCπ-II and QMCπ-III which then results to a slightly later fall of densities compared to data.

Figure 5.14 shows a comparison of proton and neutron density distributions of the doubly-magic ^{208}Pb isotope from QMC and experimental data. Experimental values for R_0 and σ_s were used for Helm model while parameters for modified Gaussian and FBC are taken from fits to electron and muonic scattering in Refs. [43] and [59], respectively.

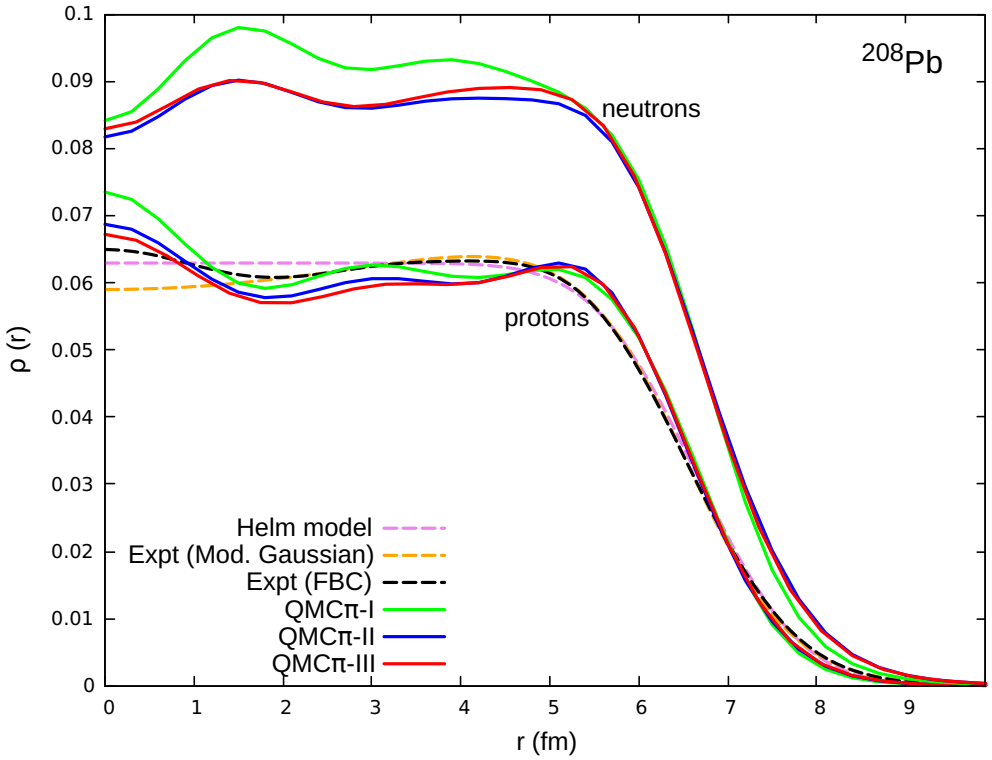

FIGURE 5.14: Proton and neutron density distributions of doubly-magic ^{208}Pb nuclei from QMC, Helm model, modified Gaussian and FBC parameters from electron and muonic scattering experiments.

For the proton, equivalently the charge distribution, Helm model shows flat

distribution from the nuclear core then starts to fall off at around $r = 5$ fm together with data from the scattering experiments. The modified Gausssian, however, starts with a slightly lower density at the core and models a bump near the surface. Data using FBC shows a shallow minimum at around $r = 1.8$ fm, then the density slightly increases creating a bump just before the density falls off. Predictions from QMC have slightly higher density at the nuclear core compared to data, then, develop two minima at around $r = 1.8$ fm and $r = 4$ fm before having a defined bump near the surface. The protons are also slightly pushed towards the surface compared to those of experimental data so that densities fall off a little bit later. Also shown in Figure 5.14 are neutron density distributions predicted from QMC. Both QMCπ-II and QMCπ-III have almost the same behaviour for neutron densities throughout the nuclear volume. In contrast, QMCπ-I predicts a slightly different curve from the core towards $r = 5$ fm, where the density starts to fall off. This earlier version shows relatively more defined bumps around $r = 1.5$ fm and $r = 4$ fm and are at higher densities compared to those of QMCπ-II and QMCπ-III. Lastly, it should be noted that in Figure 5.9 of the previous section, QMCπ-I is able to replicate the charge radius really well for ^{208}Pb compared to the other QMC versions. As discussed in Sec. 3.2.2, R_{ch} is calculated from both proton and neutron geometric radii which are taken from the density distributions.

5.5 Radius parameters

In this section, QMC predictions for the other radius parameters, namely diffraction radii, R_0 , and surface thickness, σ_s , defined in Sec. 3.2.2, are presented. Note that as mentioned in Section 4.3, these two observables for finite nuclei were included in the QMC-I and QMCπ-I fits but were left out for QMCπ-II and QMCπ-III fits. Figure 5.15 shows the R_0 and σ_s percent deviations of QMC results from experimental data. To check the effect of including both observables in the fitting procedure, a refit is done for the QMCπ-III version which is shown in the plot labelled 'QMCπ-III-Rσ '.

For R_0 , deviations are smaller from QMCπ-II and QMCπ-III for nuclei around $A \sim 50$ even though this observable was not included in their corresponding fits. Around $A \sim 90$, QMCπ-II suffers slightly higher deviations compared to the other QMC versions while at around $A \sim 210$, QMC-I and QMCπ-I perform better than the last two versions. As seen in the plot, the inclusion of R_0

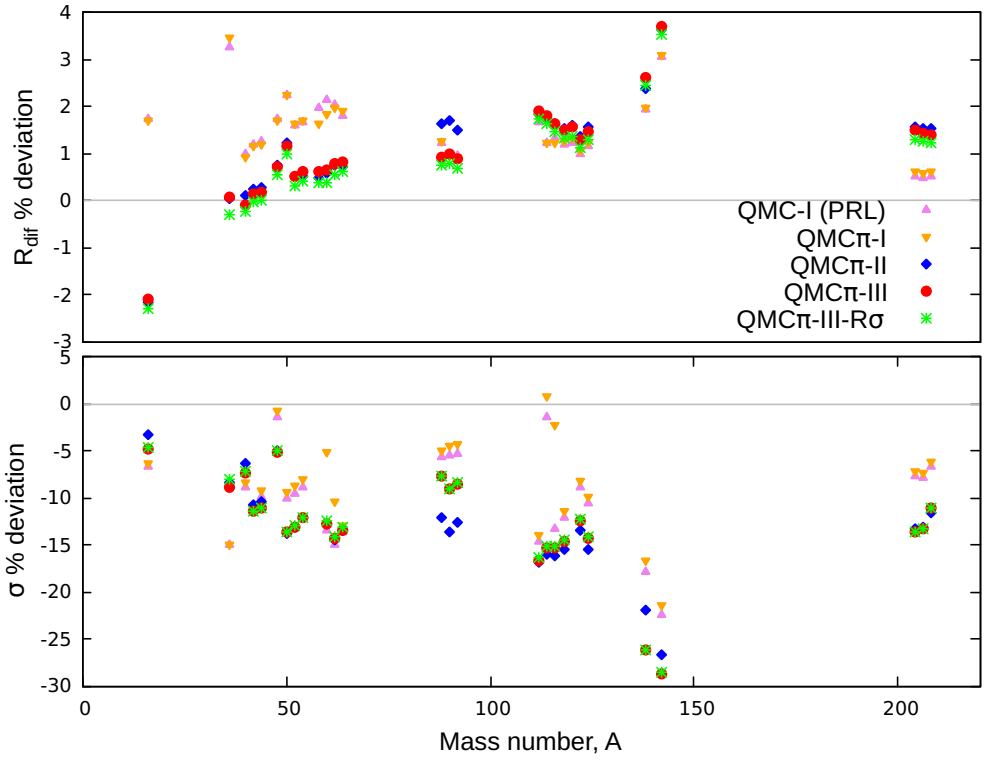

FIGURE 5.15: R_0 and σ_s percent deviations of QMC results. Experimental data are taken from Ref. [24]. The plot legend is located on the top panel.

in the QMCπ-III-Rσ fit does not change the results that much compared to that of QMCπ-III. Thus, it can be said that the discrepancy in the results of QMC is not majorly due to this difference in the fitting protocol but in the difference of the contibutions included in the QMC functionals. In general, QMC predictions overestimate R_0 with deviations up to around 4%.

For σ_s shown in the bottom plot of Figure 5.15, QMC predictions mostly underestimate the experimental values with deviations reaching up to 30%. Both QMC-I and QMCπ-I perform better compared to the last two versions, however, again it is stressed that this is not due to the inclusion of σ_s in their fits. As can be seen in QMCπ-III and QMCπ-III-Rσ , the results do not change upon the inclusion of σ_s in the fitting procedure just as in the case of R_0 . In Figures 5.13 and 5.14, it was seen that for charge densities, QMC tends to push protons near the nuclear surface compared to that of experiment. As a result, the difference between the locations of $0.9\rho_0$ and $0.1\rho_0$ decreases which also decreases the σ_s values.

5.6 Optical shifts

As discussed in Sec. 3.2.2, charge radii are obtained from experiment by actually measuring the optical shift from a reference isotope. In Figure 5.16, isotopic shifts predicted by QMC for Ca chain with stable reference isotope ^{40}Ca are plotted against mass number A. As noted in the discussion of R_{ch} in Section 5.3, the experimental data shows a bump between the doubly-magic ^{40}Ca and ^{48}Ca isotopes which, of course, also appears for $\delta\langle r^2\rangle$ as shown in the plot. Compared to the later QMC functionals, QMC-I and QMCπ-I predict a steeper increase in $\delta\langle r^2\rangle$ which trend cuts through the bump. Both versions underestimate the values for ^{42,44}Ca and overestimate those for the neutron-rich Ca isotopes especially for ^{48}Ca reaching a residual of around 0.4 fm^2. For the proton-rich Ca isotopes ^{36,38}Ca, QMC overestimate the experimental $\delta\langle r^2\rangle$ with both QMCπ-II and QMCπ-III predicting almost the same sizes for ^{36}Ca and ^{40}Ca isotopes. Although the last two versions predict lower values for ^{42,44}Ca and with trends that increase slower from the reference isotope, their $\delta\langle r^2\rangle$ predictions for ^{48}Ca are closer to that of experiment.

Further investigation of the behaviour of charge radius and optical shift for Ca chain is done by looking at the possible deformed structures of some isotopes along the chain. Figure 5.17 shows the experimental data as well as QMC values for the deformation parameter β_2 along Ca chain. It can be seen that from experiment some of the isotopes have ground-state deformations which are not reproduced by the model. For the QMC fits, it was imposed in the first place, that all magic nuclei included in the fit are spherical. If, on the other hand, the known deformations are imposed through a constrained HF calculation, labelled QMCπ-III-def in the plot, the bump in Ca radii trend is manifested as can be seen in the inset plot.

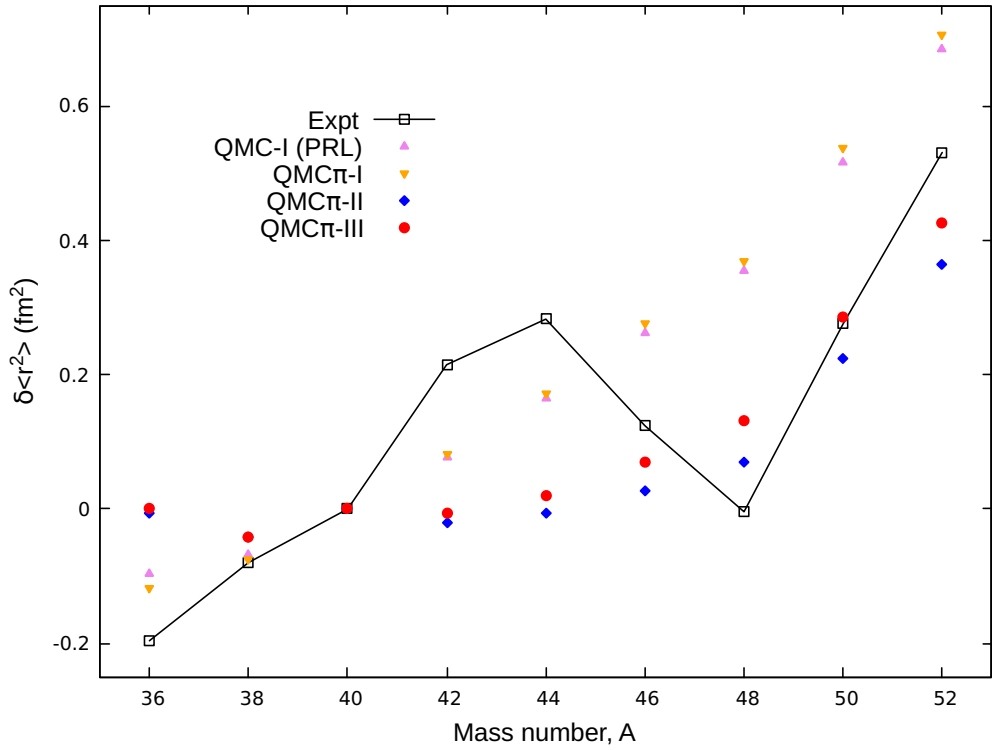

FIGURE 5.16: Isotopic shifts for Ca chain with stable reference isotopes ^{40}Ca plotted against mass number A. Experimental data are taken from Ref. [50] and errors are smaller than the symbols used in the plot.

For the Pb chain, optical shifts are shown in Figure 5.18 from the reference isotope ^{208}Pb and plotted against mass number. It was seen in Figure 5.9 that QMCπ-II and QMCπ-III both overestimate the charge radii and that the earlier versions predict better values. For $\delta\langle r^2\rangle$, however, the values are almost the same for all QMC versions. A slight 'bump' forms in the proton-rich side of Pb which is not replicated by the model. This may again suggest deformed structures in this region similar to the behaviour seen in Ca. This will be further investigated in Section 7.6.

5.7 Skin thickness

Another finite nucleus observable that is related to the geometric radius of nucleons is the neutron skin thickness, or simply skin thickness, Δr_{np} . As defined in Section 3.2.2, Δr_{np} is the difference between the neutron and the proton geometric radii.

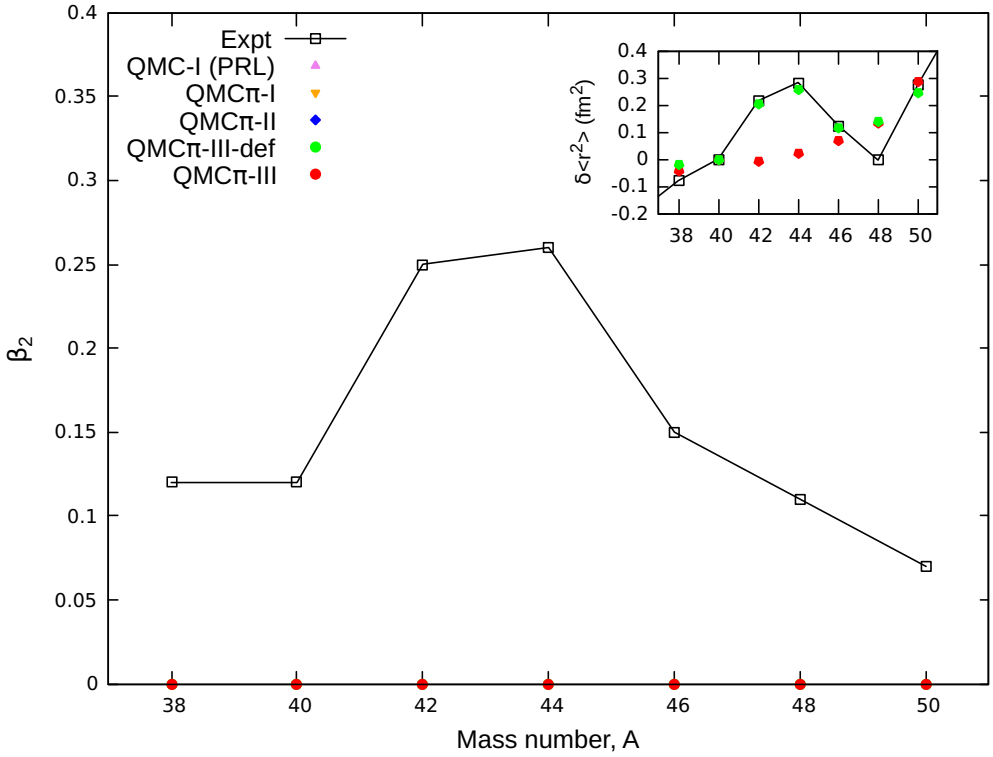

FIGURE 5.17: Deformation parameter, β_2, for the Ca chain plotted against mass number A. Inset: Isotopic shifts for Ca chain with stable reference isotopes ^{40}Ca plotted against mass number A. QMCπ-III-def are results from imposing the experimentally known deformations in QMCπ-III through a constrained HF calculation. Experimental data are taken from Ref. [52] and errors are smaller than the symbols used in the plot.

Figure 5.19 shows Δr_{np} for nuclei included in the QMC fit as a function of the neutron excess $I = (N - Z)/A$ along with data from antiprotonic x-ray and hadron scattering experiments. It can be seen that results from the different versions of QMC do not change a lot and are all within the band of Δr_{np} fit to experimental data. Hadron scattering provides data for ^{208}Pb which is slightly different from that of x-ray results but whose error bars overlap. The QMC predictions for ^{208}Pb are within the errors of both experiments. Both ^{40}Ca and ^{58}Ni isotopes have very large errors whose lower bound are trimmed in the plot for visual purposes. There are currently no data for ^{36,38}Ca nuclei but QMC predictions are added for future reference. As these Ca isotopes are proton-rich with negative values for I, Δr_{np} are also expected to be negative and much smaller than that of ^{40}Ca .

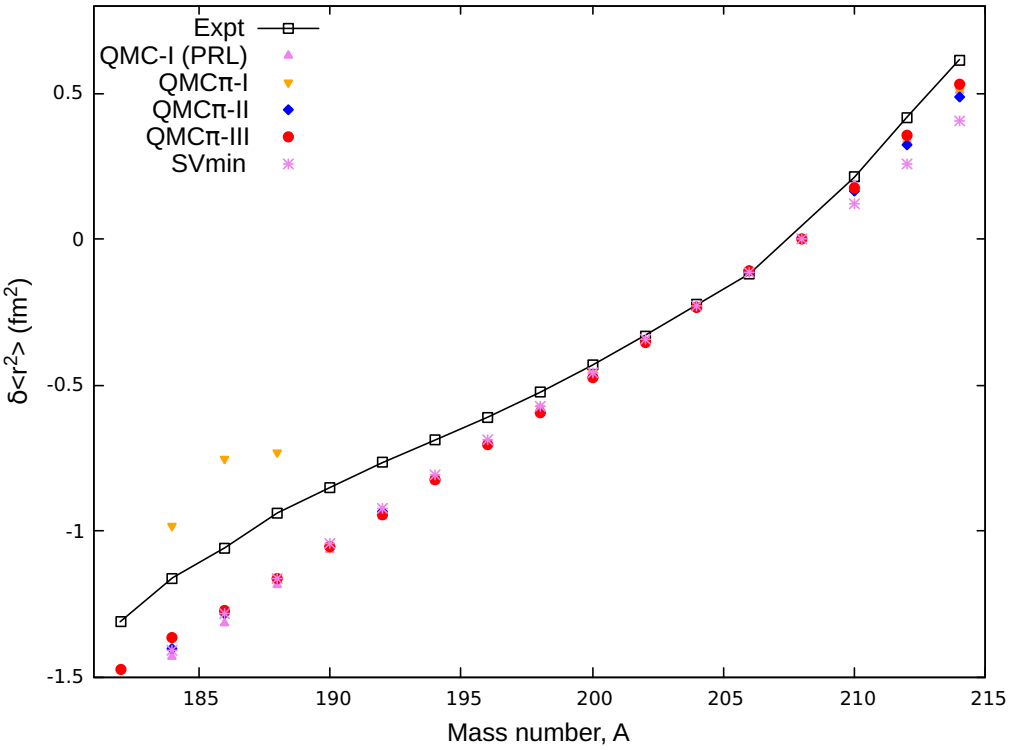

FIGURE 5.18: Isotopic shifts for Pb chain with stable reference isotopes ^{208}Pb plotted against mass number A. Experimental data are taken from Ref. [50] and errors are smaller than the symbols used in the plot.

As shown in Figure 3.14, Δr_{np} is seen to be directly correlated to the slope of symmetry energy L_0 in nuclear matter. For QMC and some mean-field models, Δr_{np} values for ^{48}Ca and ^{208}Pb are plotted against L_0 shown in Figure 5.20. These two nuclei are of particular interest as experiments have currently been done and new data are anticipated in the near future. Since the earlier QMC versions yielded very low values for L_0, their results lie a little bit outside the linear fit to values from other models. In contrast, both QMCπ-II and QMCπ-III have improved in the value for L_0 and as shown in the plot, their values lie within the linear fit.

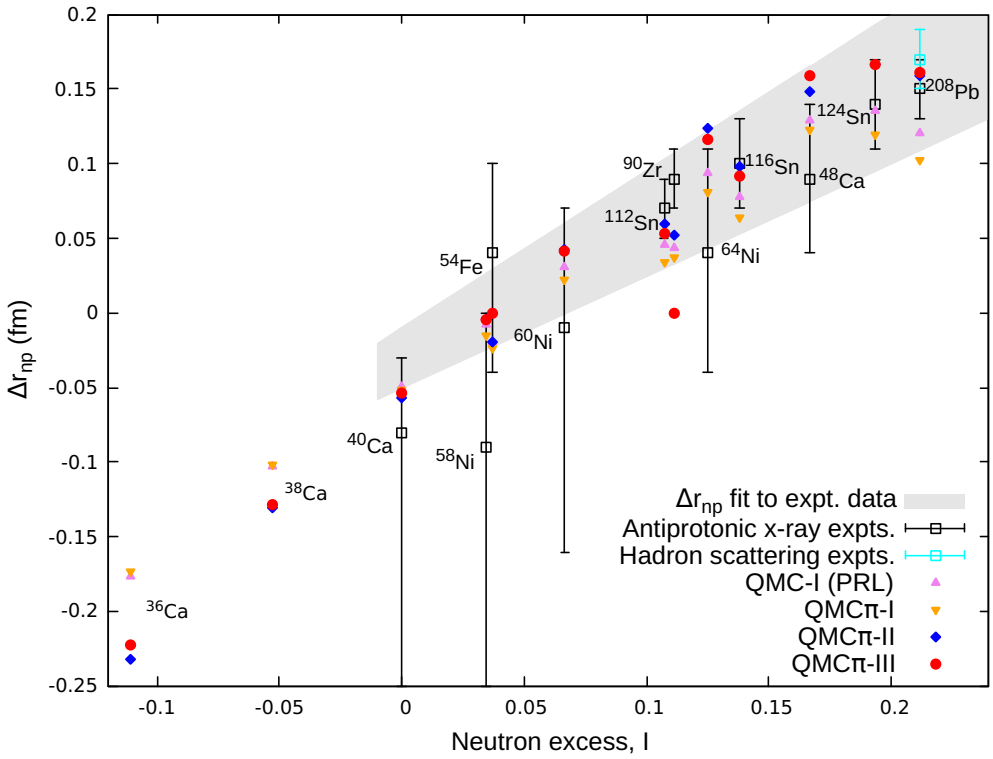

FIGURE 5.19: Skin thickness for nuclei included in the QMC fit as a function of the neutron excess. Experimental data are taken from Ref. [60].

5.8 Two-neutron separation energies

Nuclear structure in terms of shell closures can be investigated by looking at the separation energies. Signatures of these closures are in the sudden drop of separation energies as nucleon number increases. Figures 5.21 and 5.22 show the two-neutron separation energies, S_{2n}, for Ca, Ni, Sn, and Pb isotopic chains as a function of the neutron number N.

For the Ca chain in Figure 5.21, the shell closures at $N = 20$ and $N = 28$ are seen from experiment and from QMC results. QMCπ-II predicts a relatively low shell gap around the $N = 20$ shell which is improved in the QMCπ-III version. However, for neutron-rich Ca isotopes, QMCπ-I and QMCπ-III slightly overestimate the S_{2n} values. Also note that there appears a slight drop at $N = 32$ which is an expected shell closure for some nuclei around Ca. This will be further discussed in the following section where signatures of shell closures are more appreciable.

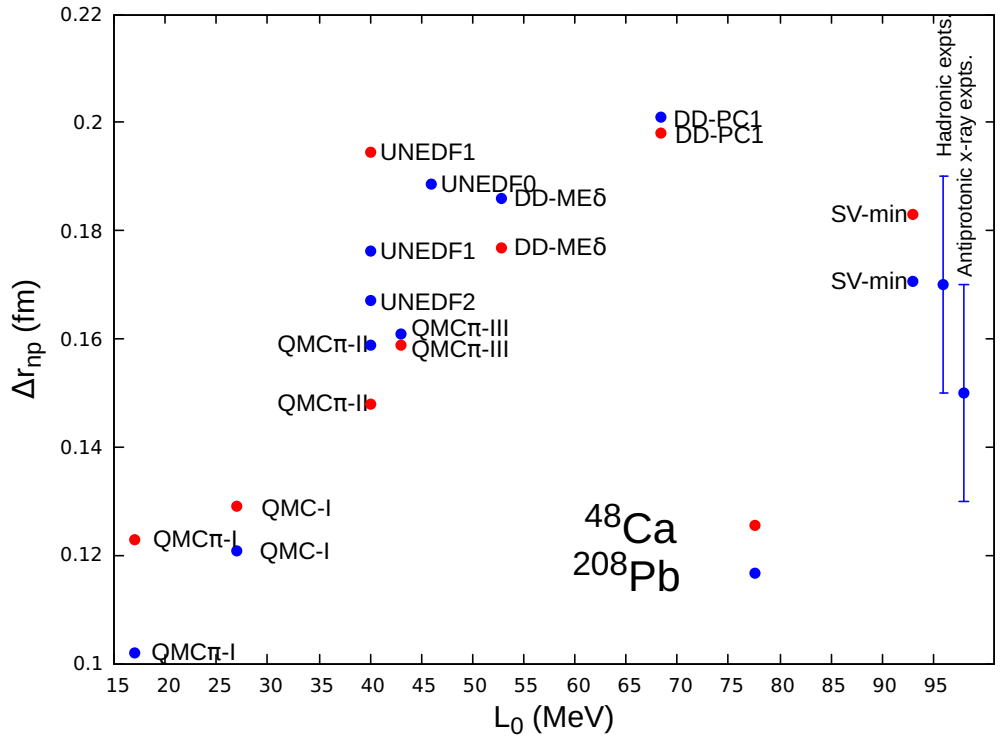

FIGURE 5.20: Neutron skin thickness plotted against L_0 for isotopes ^{48}Ca (red) and ^{208}Pb (blue) from various nuclear models. Also shown as blue symbols with vertical errorbars are experimental data for ^{208}Pb from hadron scattering and anti-protonic x-rays. For comparison, refer to Figure 3.14 where a linear correlation is shown between Δr_{np} and L_0 for ^{208}Pb.

For the Ni chain, shell closures can be seen at $N = 28$ and $N = 50$. This time for both QMCπ-II and QMCπ-III, shell gaps are overestimated a little bit while in QMCπ-I, the gap at $N = 28$ is slightly underestimated. There are also relatively higher residuals from QMCπ-II for isotopes toward the $N = 50$ closure. Another subshell closure appears at $N = 40$ with a much smaller dip in S_{2n} compared to the major shells. This will also be discussed further in the next section.

For the Sn chain in Figure 5.22, shell closure is at $N = 82$. Both QMCπ-II and QMCπ-III underestimate S_{2n} values for neutron-deficient Sn isotopes up to $N = 60$ as well as on the neutron-rich side after the shell closure. Starting from $N = 64$ and towards $N = 82$, QMC predictions mostly overestimate S_{2n}. QMCπ-I, nevertheless, has almost the same slope as that of experiment for Sn isotopes before the shell closure.

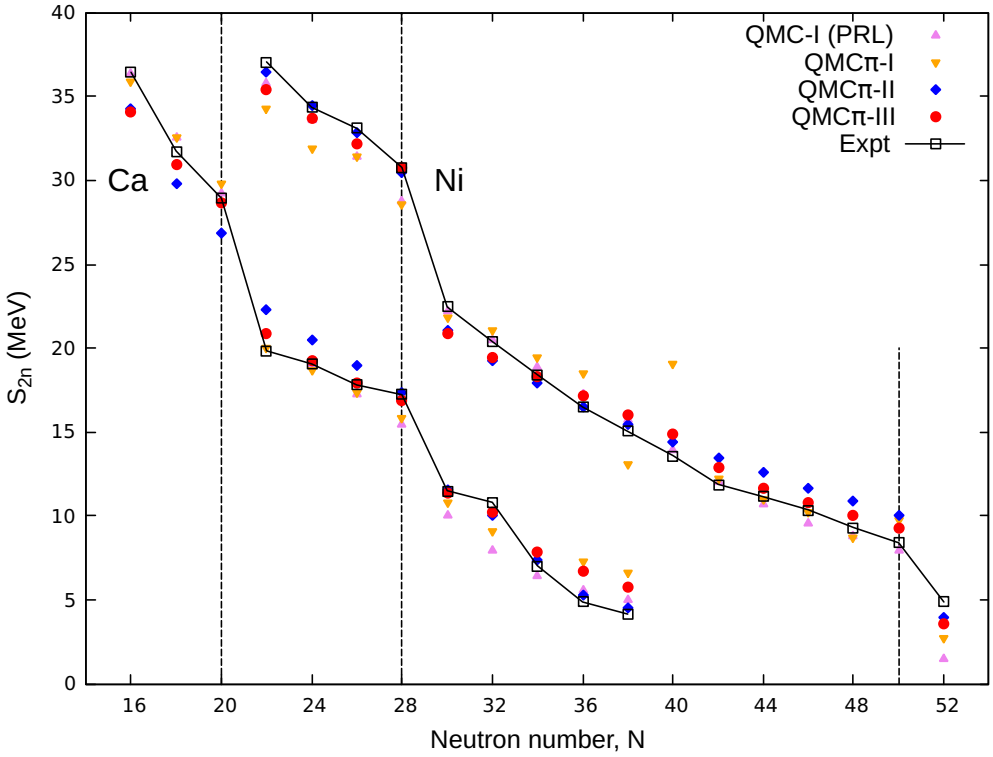

FIGURE 5.21: Two-neutron separation energies for Ca and Ni isotopes as a function of the neutron number. Experimental data are taken from Ref. [38] and errors are smaller than the symbols used in the plot.

For the Pb chain, both QMCπ-I and QMCπ-II give really good predictions for S_{2n} while the QMCπ-III version has higher residuals around the the shell closure at $N = 126$. Just as in the Sn chain, results from QMCπ-III slightly overestimate S_{2n} for some nuclei before the closure, while values are underestimated after the closure thereby having larger shell gap at $N = 126$ compared to that of experiment.

5.9 Two-neutron shell gaps

Shell closures can be further investigated by looking at the difference between separation energy values of two consecutive nuclei along isotopic or isotonic chains. This observable is known as the two-nucleon shell gap, $\delta_{2q=p,n}$, as discussed in Section 3.2.1. Peaks in shell gaps signify the closures as these are the locations where the separation energies are greatest.

Figure 5.23 shows the δ_{2n} values along Ca, Ni, Sn, and Pb chains from QMC and from experiment, plotted against neutron number.

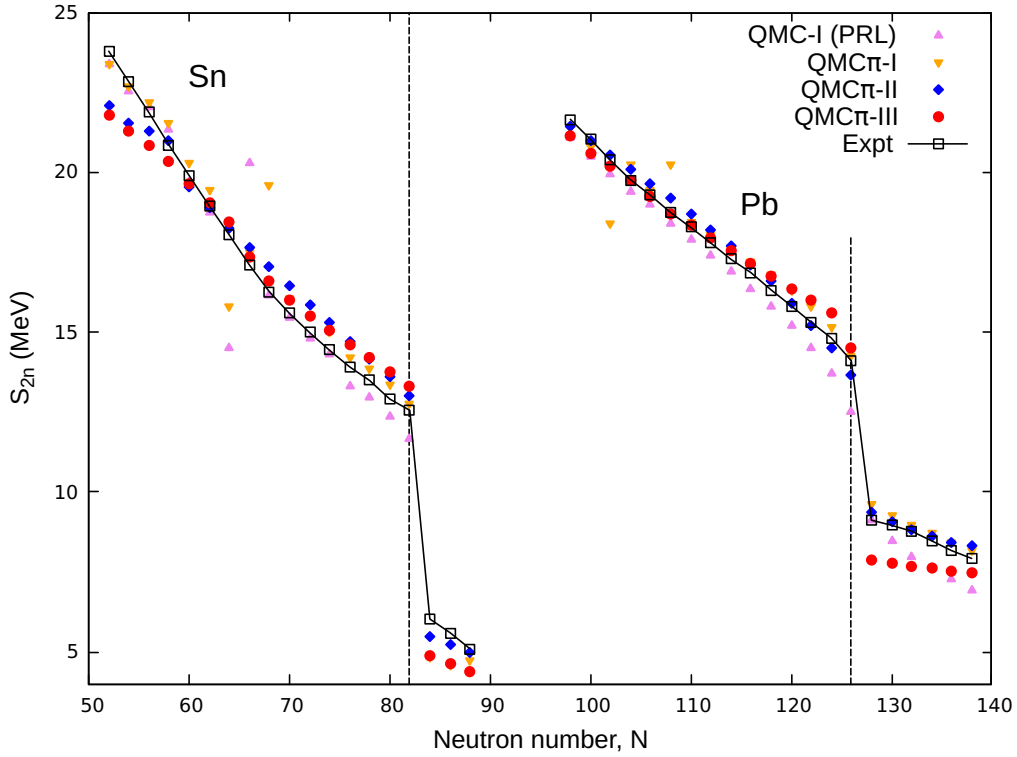

FIGURE 5.22: Same as in Fig. 5.21 but for Sn and Pb isotopes.

For Ca isotopes, as discussed in the previous section, major shell closures are at $N = 20$ and $N = 28$. However, subshell closures also appear at $N = 32$ and $N = 34$ for the Ca chain where δ_{2n} have relatively higher values compared to those of the neighboring isotopes. These subshell closures are also predicted from Skyrme model [61]. From experiments, it was observed that ^{54}Ca is doubly-magic [62]. $N = 32$ subshell also appears for other nuclei around Ca like Ti and Cr [63, 64] but starts to disappear as Z further increases. Results from QMC predict the major shells, although QMCπ-II yields a low shell gap at $N = 20$, which we have already seen in Figure 5.21. For the $N = 32$ and $N = 34$ subshells, QMC-I and QMCπ-I fail to predict the closures which are both present in QMCπ-II. The QMCπ-III version is able to predict closure at $N = 32$ but underestimates that at $N = 34$. These closures are further investigated in Section 7.5.4.

For the Ni chain, the major shells are at $N = 28$ and $N = 50$, which are somewhat overestimated in QMCπ-II and QMCπ-III by up to around 2 MeV. The expected closure at $N = 40$ shows a small peak along the Ni chain which is only captured by the QMCπ-III version, but not in QMCπ-II. Meanwhile, QMCπ-I highly overestimates the δ_{2n} value at $N = 36$ and $N = 40$.

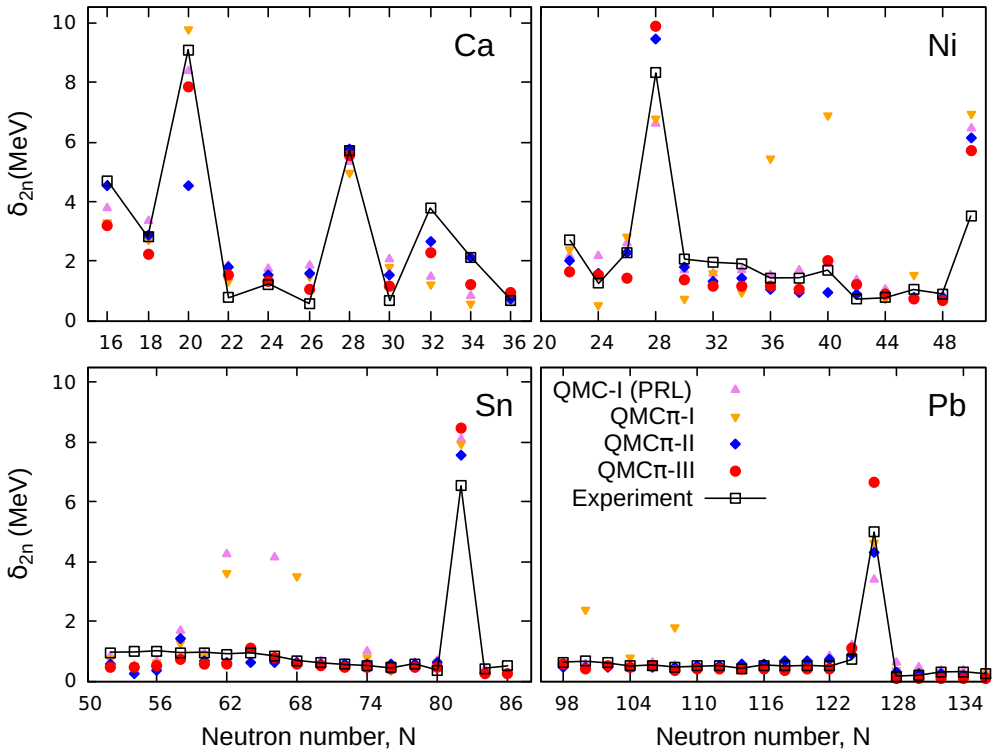

FIGURE 5.23: Two-neutron shell gaps plotted against neutron number from various QMC versions. Experimental data are taken from the differences of S_{2n} in Ref. [38] and errors are smaller than the symbols used in the plot. Plot legend is located at the bottom right panel.

For Sn and Pb, closures are at $N = 82$ and $N = 126$, respectively, which are again somewhat overestimated in QMCπ-III. However, it is significant to note that from QMC results, the closures are properly located at the major shells and that in general QMCπ-III is relatively more sensitive to minor shell closures compared to the other versions.

5.10 Dripline calculations

To determine the limits of adding more nucleons along magic chains, two-nucleon separation energies are calculated for magic nuclei which are not yet physically observed. Recall that when the value of the separation energies become negative, nucleons will spontaneously drip out of the nucleus which then corresponds to the dripline. Figures 5.24 and 5.25 show the driplines along magic isotopic and isotonic chains, respectively, predicted from QMC. The predicted heaviest isotopes and isotones along the chains are labelled in the plot.

For the magic isotopic chains in Figure 5.24, predictions from QMCπ-III for the neutron driplines are shown. Presently, the heaviest known Ca isotope is ^{60}Ca from Ref. [65] but from Ref. [38], ^{58}Ca is the heaviest Ca with available mass.

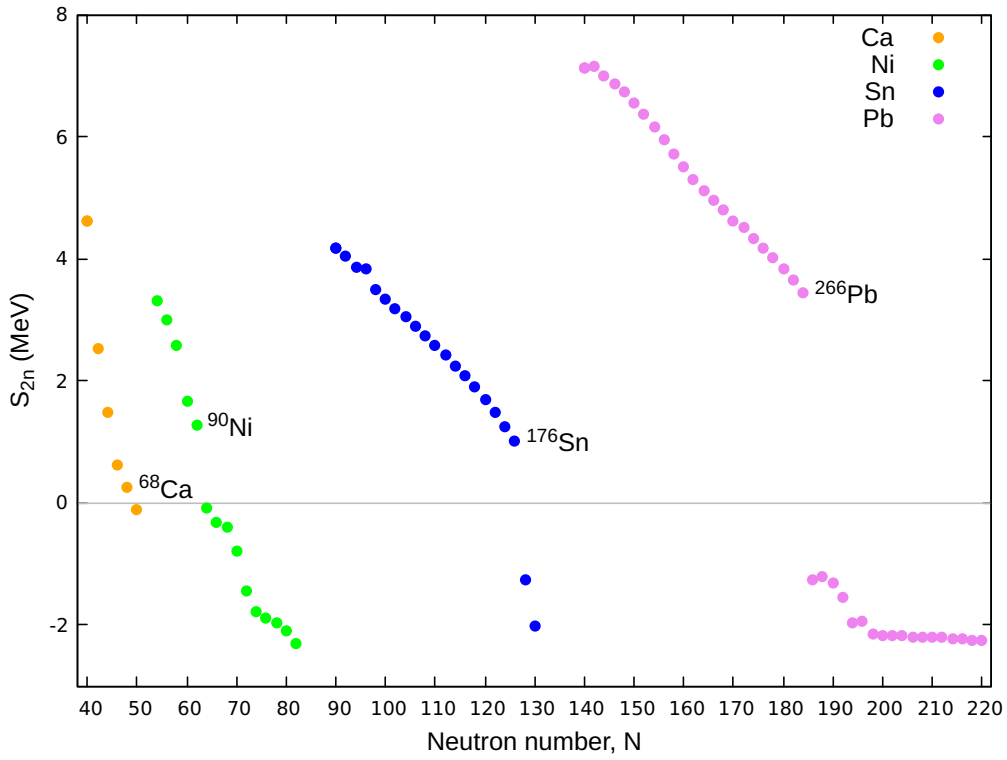

FIGURE 5.24: Two-neutron separation energies for Ca, Ni , Sn and Pb isotopic chains as a function of the neutron number. The neutron dripline is determined by the last isotope in the chain with a positive value for S_{2n}.

QMCπ-III predicts that the Ca dripline is after ^{68}Ca, although ^{70}Ca may still be observed as it has a very small negative S_{2n} value. The same is true in the Ni chain where the predicted dripline is at ^{90}Ni but the next three even-even isotopes has S_{2n} values very close to zero. For Sn and Pb chains, the dripline from QMCπ-III are well-defined and the predicted heaviest isotopes are ^{176}Sn and ^{266}Pb, respectively. The heaviest known isotopes for Ni, Sn and Pb from Ref. [38] are ^{80}Ni, ^{139}Sn and ^{220}Pb, respectively. One possible limitation in these calculations is that the BCS pairing used may have resulted to spurious effects for weakly bound neutron rich nuclei. In this case, full HFB should be implemented.

For magic isotones shown in Figure 5.25, S_{2p} values are plotted against Z to determine the proton dripline. The heaviest known isotones in the $N = 20$ and $N = 28$ chains are ^{48}Ni and ^{61}As, respectively. QMCπ-III predicts that the driplines in these isotonic chains are after ^{46}Fe and ^{60}Ge, respectively, which slightly underestimates the location of the dripline. For the $N = 50$ chain, the heaviest known isotone is ^{100}Sn which is also the predicted heaviest isotone that can be observed from QMCπ-III.

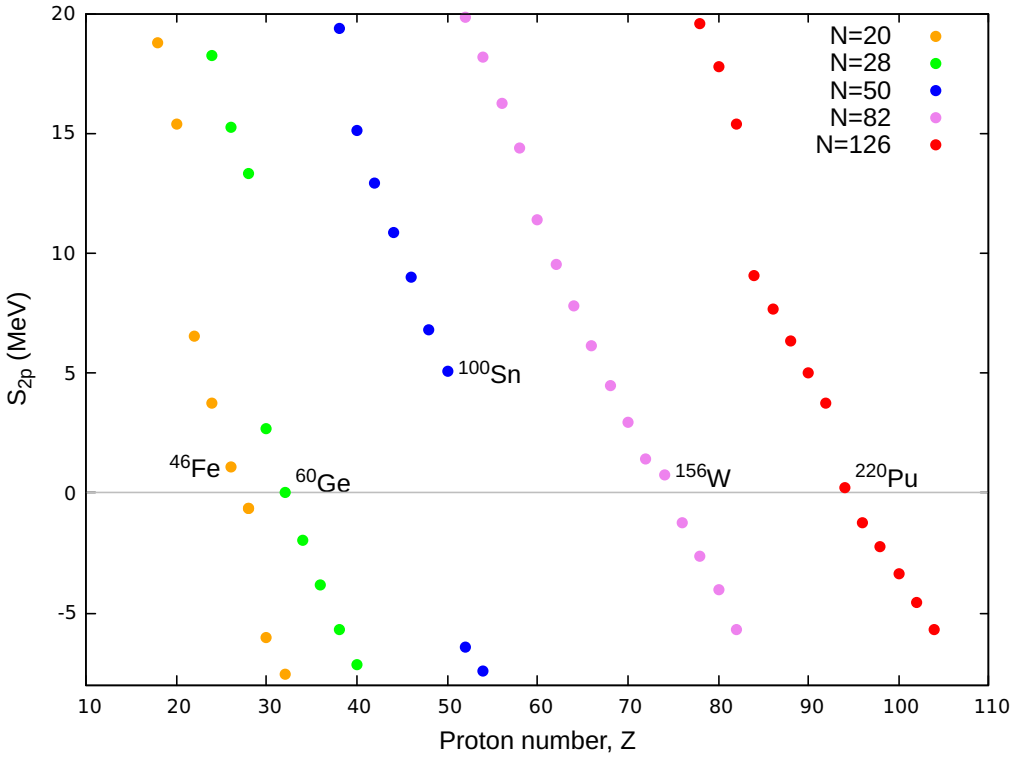

FIGURE 5.25: Two-proton separation energies for $N = 20$, 28, 50, 82 and 126 isotonic chains as a function of the proton number. The proton dripline is determined by the last isotone in the chain with a positive value for S_{2p}.

For $N = 82$ chain, the heaviest known isotone is ^{155}Ta and QMCπ-III predicts that the next isotone ^{156}W, will be the last isotone before its predicted dripline. Finally, for $N = 126$ chain, ^{218}U is the heaviest known isotone and the next even-even isotone ^{220}Pu is predicted by QMCπ-III to be the last isotone before the proton dripline.

5.11 Single-particle energies

For doubly-magic nuclei, data is available for the single-particle (sp) energies which can be used to check the predictions from QMC in the filling of sp states [37]. Predictions for proton and neutron sp energies at sphericity for ^{100}Sn and ^{132}Sn, computed from various versions of QMC model, alongwith data from experiment, are shown in Figures 5.26 to 5.27, respectively.

For ^{100}Sn in Figure 5.26, proton states are predicted in correct order from QMC, however, states in QMCπ-II and QMCπ-III appear to be squeezed compared to those of the earlier versions and from experiment. Nevertheless, the sp gap at $N = 50$ is predicted fairly well in all QMC versions. For the neutron states, QMCπ-II and QMCπ-III predict the correct order while in QMC-I and QMCπ-I, states $2d_{3/2}$ and $3s_{1/2}$ are inverted. Further in the first two versions, the states appear to be more spread out compared to those of the later versions and from experiment. Neutron states from QMCπ-II are slightly squeezed and a gap opens between the $1g_{7/2}$ and $2d_{5/2}$ states where there should be none as shown from data. These are improved in QMCπ-III in comparison with experiment although the $1g_{9/2}$ state is slightly pushed up, thereby decreasing the sp gap at $N = 50$.

For ^{132}Sn in Figure 5.27, proton states are in the correct order compared to that of experiment, except for QMCπ-II where $1h_{11/2}$ and $2d_{3/2}$ states are inverted. Both QMC-I and QMCπ-I have spread out proton states compared to data which are improved in the later versions. The sp gaps at $N = 50$ are slightly smaller from QMC compared to experiment as the $1g_{9/2}$ state is pushed up closer the the Fermi level. Further, a relatively larger gap appears between $1g_{7/2}$ and $2d_{5/2}$ states from QMC in comparison to data. For the neutron states, some inversions occur again from QMC results owing to the very close sp energy values. Both QMC-I and QMCπ-I predict more spread out neutron states while in QMCπ-II, the states appear to be more squeezed compared to experiment. This is improved in QMCπ-III where the states are mostly in the correct order. The sp gap at $N =$

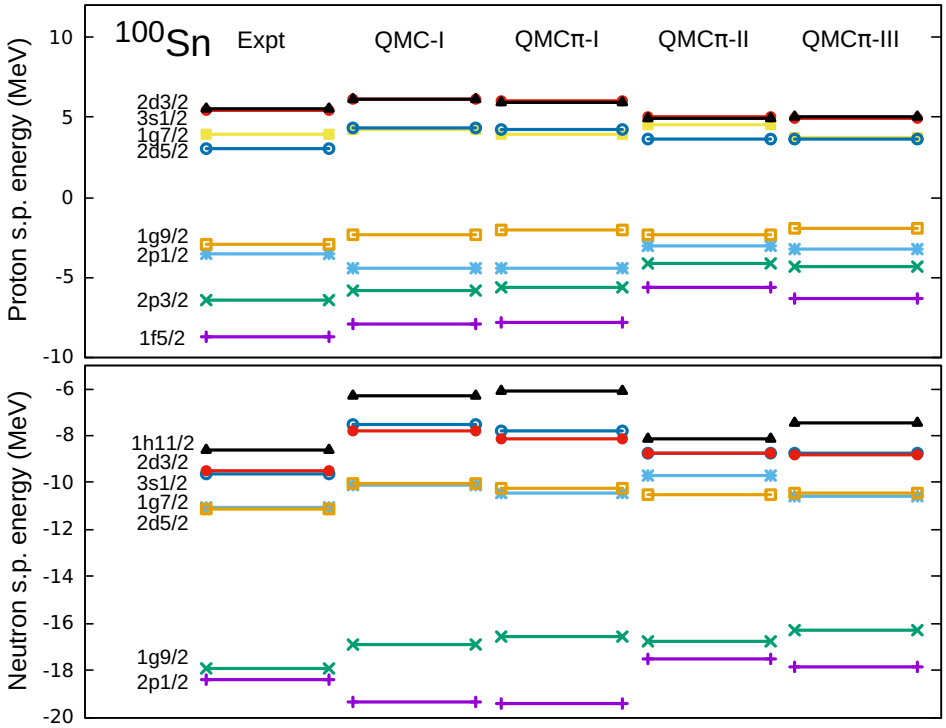

FIGURE 5.26: Proton and neutron single-particle energies for ^{100}Sn obtained from different QMC versions. Experimental data is taken from [37]. Single-particle levels are shown in different colors and labels are placed before the experimental data for each level.

82 are overestimated in the early QMC versions and is somehow improved in QMCπ-II and QMCπ-III.

In summary, the QMC model proved to be successful its predictions for several observables for even-even nuclei along magic chains. An overall improvement is seen as the model developed, both for nuclear matter properties and for observables of finite nuclei. Apart from binding energies and charge radii which were included in the fitting procedure, other nuclear observables which had not been part of the fit, were also fairly well reproduced. Charge density distributions for chosen nuclei agree well with data from scattering experiments, as well as QMC results for optical shifts and skin thickness. Shell closures were located from looking at separation energies and shell gaps, and predictions for proton and neutron driplines along the magic chains were also computed. Shell structure was also further investigated by computing the single-particle energies. Results for both doubly-magic isotopes, ^{100}Sn and ^{132}Sn, were comparable to data, showing some improvements as the QMC model developed.

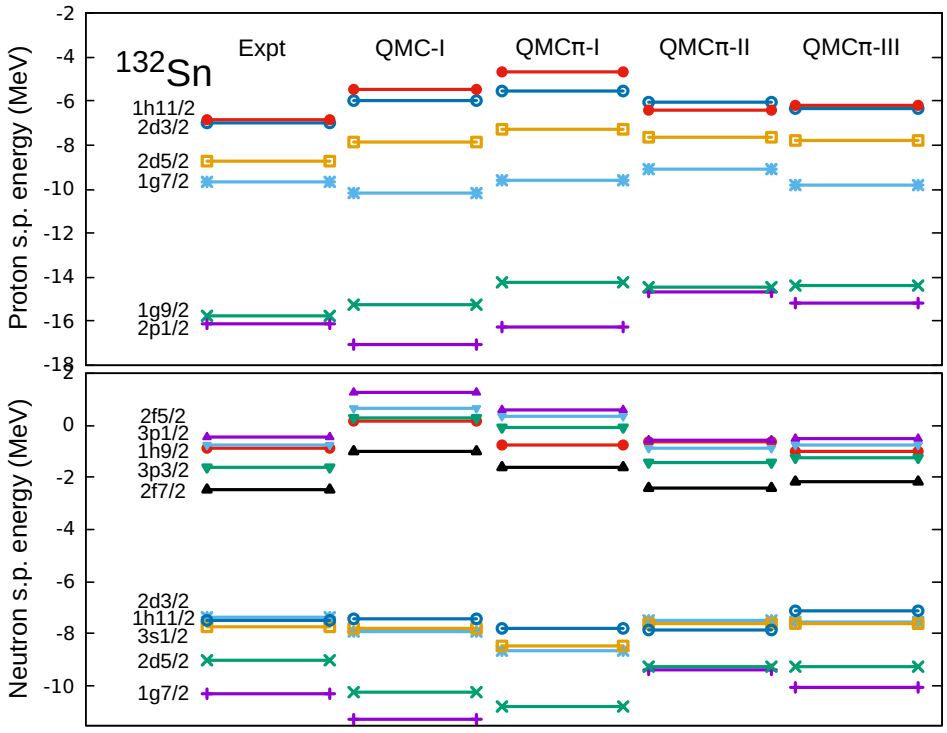

FIGURE 5.27: Same in Figure 5.26 but for ^{132}Sn .

Chapter 6

Predictions in the superheavy region

The QMC model has shown outstanding predictions for superheavy elements (SHE) even in its early stages of development for finite nuclei. Ref. [8] reported that the QMC-I version had an absolute *rms* residual of 1.97 MeV for SHE even in its simple form with only four model parameters. In comparison, SV-min [24] yielding an *rms* residual of 6.17 MeV had thirteen parameters. Calculations were extended for elements up to predicted proton and neutron driplines for energies and deformation in QMCπ-I where the results were found to agree well with available data and were comparable to results of other nuclear models where data is not yet known [53]. Moreover, predictions for binding energies of SHE were improved in QMCπ-II, yielding an *rms* residual of 2.0 MeV compared to those of SV-min [24] and DD-MEδ [66] yielding 6.8 and 2.5 MeV, respectively, for the same set of nuclei [54].

In this chapter, more calculations are reported for various ground-state observables in the SHE region. Results are then compared for the different versions of QMC in comparison to the results from other nuclear models. It is emphasised that QMC parameter optimisation does not include SHE data in the fit and that the final QMC parameters were only adjusted to the data presented in Section 4.3.1. Even so, it is seen that the QMC model is able to give excellent predictions in the SHE region.

6.1 Binding energies in the SHE region

Atomic mass is one of the most readily accessible ground-state observable. In the superheavy region, data are available for known elements from ^{248}Fm ($Z = 100$) to ^{294}Og ($Z = 118$). To get an overview of how QMC performs in the superheavy region, Table 6.1 presents the *rms* percent deviations and *rms* residuals from QMC, as well as results from other nuclear models.

TABLE 6.1: Comparison of *rms* percent deviations and *rms* residuals from QMC and from other nuclear models for SHE with available data.

	rms % deviation	*rms* residual (MeV)
QMCπ-III	0.03	0.52
QMCπ-II [54]	0.11	2.04
QMCπ-I [53]	0.12	2.42
QMC-I [8]	0.08	1.50
FRDM [23]	0.11	2.25
SV-min [24]	0.36	6.99
UNEDF1 [28]	0.07	1.31
DD-MEδ [66]	0.12	2.28

A significant improvement in BE is seen in the latest version, QMCπ-III, where the *rms* % deviation and *rms* residual are only 0.03% and 0.52 MeV, respectively, compared to the older QMC versions which have values up to four times larger. Furthermore, QMCπ-III performs even better compared to FRDM, which was seen to have outstanding energy predictions in the light to heavy mass regions. SV-min is seen to underestimate BE, as also reported in Ref. [8], while predictions are improved in another Skyrme-type force UNEDF1 [28]. Meanwhile, the covariant EDF, DD-MEδ [66], performs at a level comparable to QMCπ-I.

Figure 6.1 shows the BE residuals from QMCπ-II and QMCπ-III along with results from the other nuclear models, plotted against mass number A. Predictions from QMCπ-III are significantly improved for all SHE included in the plot compared to QMCπ-II, and are even better compared to the results from other models. The residuals from QMCπ-III vary only between ± 1 MeV where for SV-min varied up to around 8 MeV. FRDM appears to have increasing residuals for SHE as A increases. Meanwhile, QMCπ-II yields comparable results to DD-MEδ, with residuals varying from 0 to 4 MeV, while residuals from UNEDF1 vary up to 2 MeV.

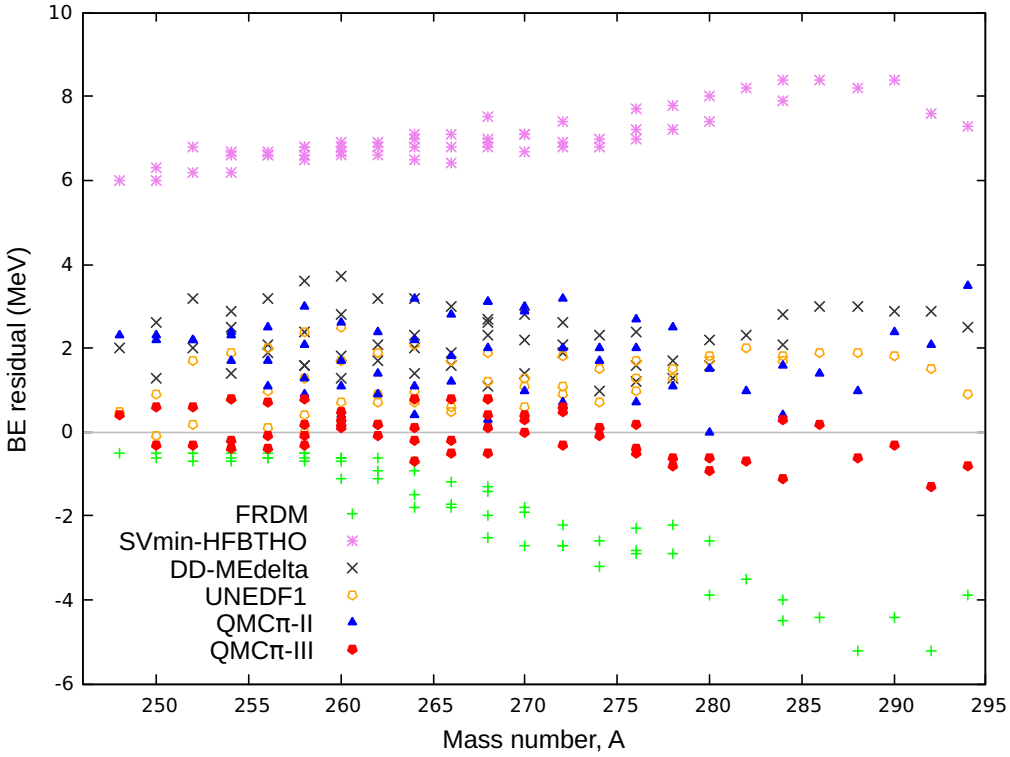

FIGURE 6.1: SHE binding energy residuals for nuclei with $Z \geq 100$ plotted against mass number A.

Energies are further investigated within the QMC model by looking at the binding energy curves and total BE residuals along isotopic chains for each SHE. These are shown in Figures 6.2 to 6.4 for nuclei with $100 \leq Z \leq 110$. For elements with $Z > 110$, the results are summarised in Table 6.2.

For both the Fm and No chains in Figure 6.2, QMCπ-III is able to replicate the experimental values really well compared to the previous QMC versions. QMCπ-II predicts underbinding, while energies from QMCπ-I are overbound, with total BE residuals reaching 4.5 MeV for the heaviest Fm and No nuclei. QMC-I, on the other hand, predicts overbinding for the lighter isotopes and underbinding for the heavier nuclei with total residuals ranging between ± 3 MeV. For the Fm chain, light isotopes with $142 \leq N \leq 150$ are more bound and binding decreases towards the heavier isotopes. For the No chain, a flat trend appears for $146 \leq N \leq 152$, then there is a steady increase in B/A as N further increases.

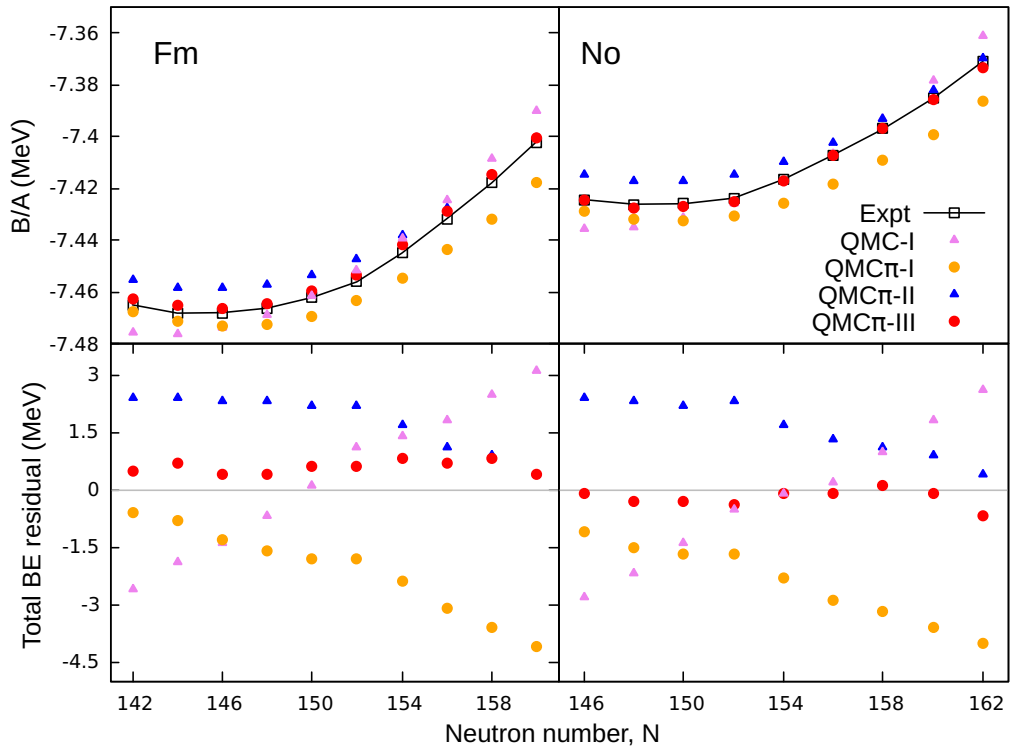

FIGURE 6.2: BE per nucleon and total BE residuals along Fm and No chains. Experimental data are taken from Ref. [38] and errors are smaller than the symbols used in the plot. Plot legend is located in the top right panel.

Just as in the Fm and No chains, predictions for Rf and Sg, shown in Figure 6.3, behave in the same way for the different QMC versions. QMC-I predicts overbinding for the lighter isotopes and underbinding on the heavier side while again, QMCπ-I predicts overbinding for both Rf and Sg chains with increasing residuals as N increases. QMCπ-II also predicts underbinding as before, with decreasing residuals towards the heavier isotopes. QMCπ-III is able to reproduce the experimental values very well for both chains. Isotopes on the lighter side of the chain and around $N = 152$, appear to be more bound compared to the heavier nuclei in both chains of Rf and Sg.

For the Hs and Ds chains in Figure 6.4, an almost flat trend appears from the lighter isotopes in the chain up to $N = 162$, then, a steady increase in B/A is seen as N further increases. Just as for Fm to Sg, QMCπ-I predicts overbinding for both the Hs and Ds chains, while QMCπ-II predicts underbinding. QMCπ-III predicts slight underbinding on the lighter isotopes in both chains but still yields results that agree really well with experiment compared to the other versions, with total BE residuals of only less than 1 MeV.

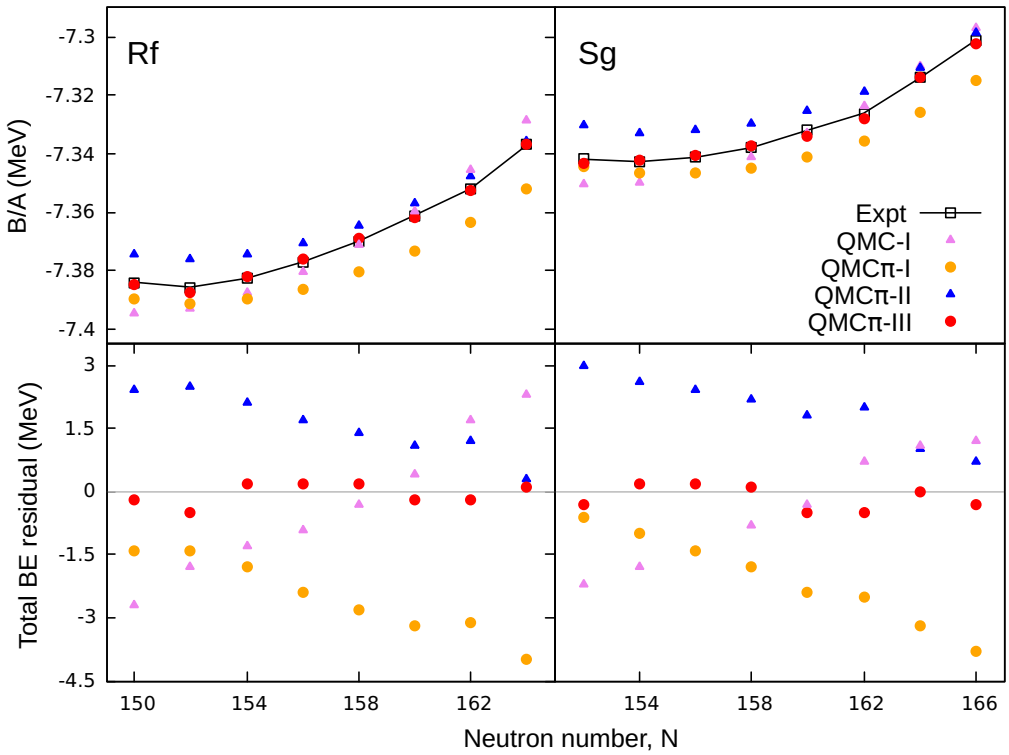

FIGURE 6.3: *BE* per nucleon and total *BE* residuals along Rf and Sg chains. Experimental data are taken from Ref. [38] and errors are smaller than the symbols used in the plot. Plot legend is located in the top right panel.

For $Z \geq 112$, since there are few isotopes known in this region, the total *BE* residuals are instead listed in Table 6.2. Both QMC-I and QMCπ-I predict overbinding for most of the nuclei with $Z \geq 112$, with residuals reaching up to 1.8 MeV and 3.4 MeV, respectively. QMCπ-II again predicts underbinding with residuals up to 3.5 MeV for ^{294}Og which is the heaviest known SHE. QMCπ-III improves the predictions compared to the previous versions with highest residual of only 1.3 MeV for ^{292}Lv.

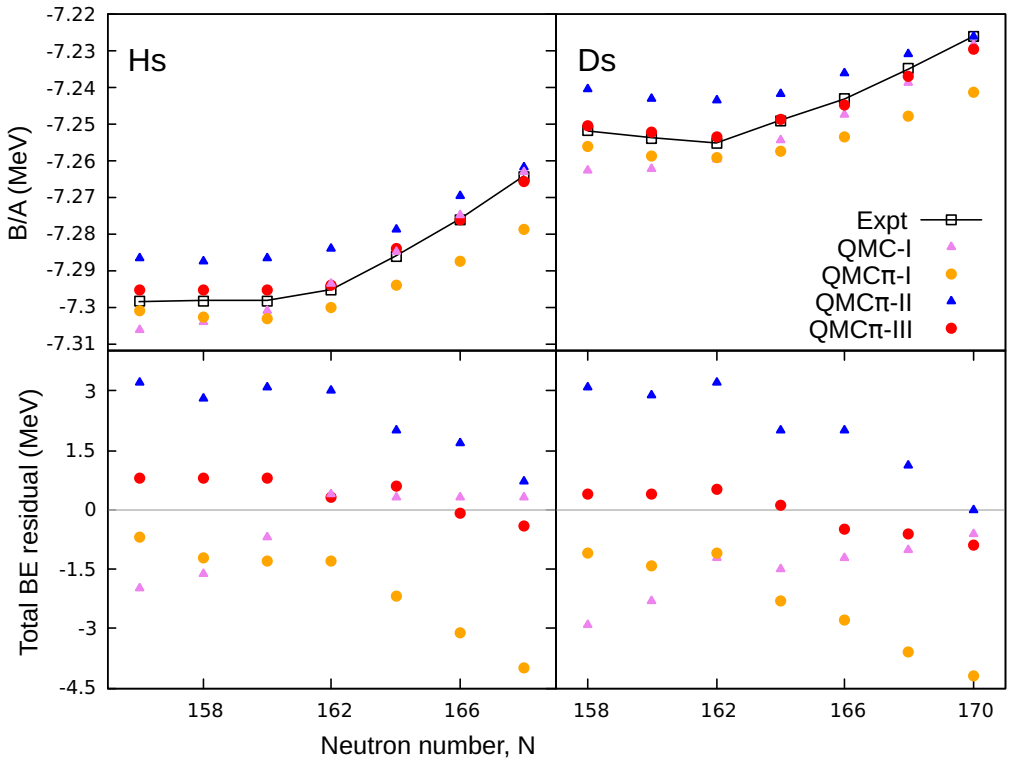

FIGURE 6.4: BE per nucleon and total BE residuals along the Hs and Ds chains. Experimental data are taken from Ref. [38] and errors are smaller than the symbols used in the plot. Plot legend is located in the top right panel.

TABLE 6.2: Comparison of total BE residuals for $Z \geq 112$ from different QMC versions.

Element	Z	N	QMC-I	QMCπ-I	QMCπ-II	QMCπ-III
Cn	112	164	-1.8	-1.2	2.7	0.2
	112	166	-1.7	-1.9	2.5	-0.8
	112	168	-1.4	-2.5	1.5	-0.6
	112	170	-0.8	-2.8	1.0	-0.6
	112	172	-0.4	-3.4	0.4	-1.1
Fl	114	170	-1.2	-1.7	1.6	0.3
	114	172	-0.5	-2.0	1.4	0.2
	114	174	0.1	-2.4	1.0	-0.6
Lv	116	174	-0.4	-1.2	2.4	-0.3
	116	176	0.3	-1.6	2.1	-1.3
Og	118	176	-0.7	-0.8	3.5	-0.8

6.2 Subshell closures

In the previous section, it was seen that SHE isotopes tend to be more bound in the region around $N = 152$ and $N = 162$. These neutron numbers are in fact seen

to display a subshell closure behaviour from experimental data. This behaviour can be checked in QMCπ-III by calculating separation energies and shell gaps as what was done in Sections 5.8 and 5.9 to identify the shell closures along isotopic chains.

Figure 6.5 shows the two-neutron shell gaps plotted against N, from experimental masses and from various QMC versions. It can be seen that, indeed, data suggests subshell closures at $N = 152$ and $N = 162$. These are not very well reproduced in both QMCπ-I and QMCπ-II. A small peak at $N = 162$ is seen from QMCπ-I with around half the δ_{2n} value from experiment, while for QMCπ-II, the peak is displaced at $N = 164$. Results from QMCπ-III predict the presence of subshell closures although the peaks appear to be somewhat overestimated. The latest version tends to be very sensitive around the $N = 162$ closure such that the δ_{2n} values appear to fluctuate in that region.

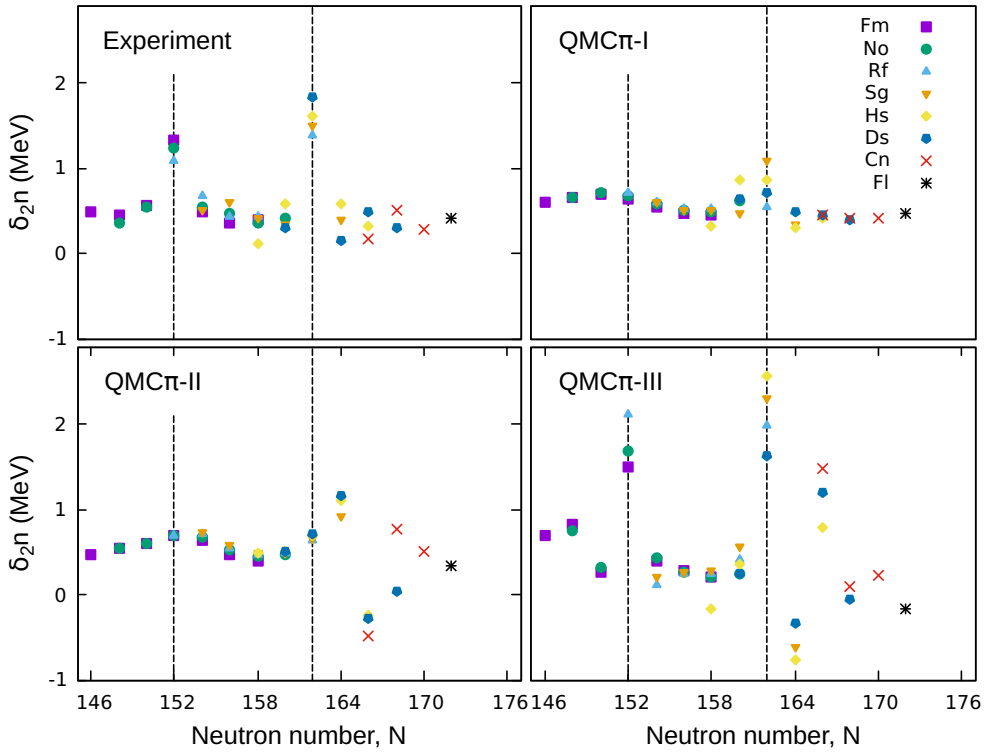

FIGURE 6.5: Two-neutron shell gaps plotted against neutron number from various QMC versions. Experimental data are taken from the differences of S_{2n} in Ref. [38]. Subshell closures at $N = 152$ and $N = 162$ are indicated with dashed lines. Plot legend is located in the top right panel.

Figure 6.6 shows the two-neutron separation energy, S_{2n}, plotted against N, from QMCπ-III and from experiment. Predictions from QMCπ-III, shown as filled symbols, mostly lie within the errors of experimental data which are shown as empty symbols with vertical errorbars. As discussed in the previous section, QMCπ-III is able to reproduce the subshell closures at $N = 152$ and $N = 162$. This can be seen in the sudden drop in S_{2n} values at these closures which are indicated with dashed lines in the figure. The inset figure shows S_{2n} values plotted against N for SHE with $Z \geq 112$. QMCπ-III predictions are again within the errors of available data and there are no expected closures for N from experiment for the region $Z \geq 112$.

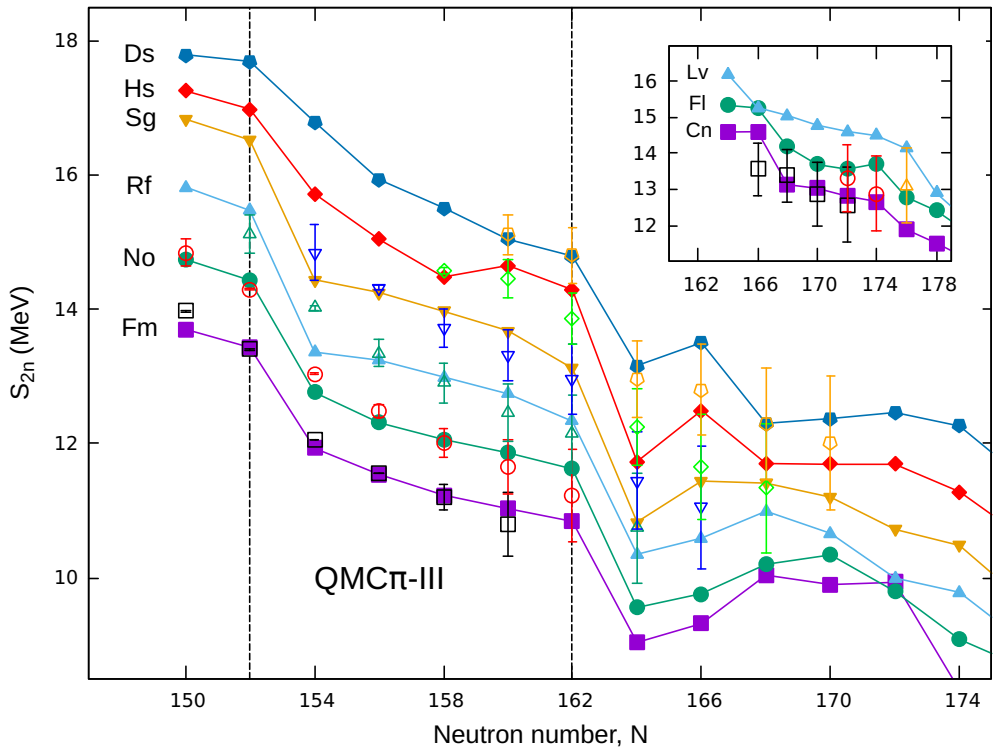

FIGURE 6.6: Two-neutron separation energies plotted against neutron number. Results from QMCπ-III are shown as filled symbols and connected by lines while experimental data and errors, taken from Ref. [38], are shown as empty symbols with vertical errorbars. Subshell closures at $N = 152$ and $N = 162$ are indicated with dashed lines. Inset shows the S_{2n} values plotted against N for SHE with $Z \geq 112$.

Table 6.3 compares the S_{2n} and δ_{2n} *rms* residuals from QMC and from other nuclear models for SHE with available data. For S_{2n} and within the QMC model, the *rms* residual is decreased as the model is improved so that in the latest version, the value is only around 0.39 MeV. SV-min which had higher residuals for total BE, predicts very well for S_{2n} , even better than the other models listed in the table. For δ_{2n} , residuals from QMCπ-III slightly increased compared to the other versions of the model but still at a small value of half an MeV. The other nuclear models performed slightly better but with very close values to that of QMC. It should be noted that while the *rms* residuals give an overall check for the predictions of the various models, it is more important to look at the nuclear structure revealed in the values from S_{2n} and δ_{2n} . It was seen that among the QMC models, only QMCπ-III is able to reproduce the subshell closures well, even though it showed slightly higher δ_{2n} residuals than the previous versions.

TABLE 6.3: Comparison of S_{2n} and δ_{2n} *rms* residuals from QMC and from other nuclear models for SHE with available data.

	S_{2n} *rms* residual (MeV)	δ_{2n} *rms* residual (MeV)
QMCπ-III [55]	0.39	0.51
QMCπ-II [54]	0.46	0.44
QMCπ-I [53]	0.51	0.34
QMC-I [8]	0.62	0.37
FRDM [23]	0.44	0.36
SV-min [24]	0.24	0.29
UNEDF1 [28]	0.31	0.26

6.3 Two-particle driplines

To determine the two-particle driplines, the calculations for separation energies are extended on both sides of the nuclear chart. Recall that on the proton side, the dripline can be determined by adding more protons in a given isotone then calculating S_{2p} until the value becomes negative. The last isotone with positive S_{2p} determines the two-proton dripline. The same is done at the neutron-rich side by adding more neutrons to a given isotope until S_{2n} becomes negative. The last isotope with positive value for S_{2n} will then determine the two-neutron dripline.

Figure 6.7 shows the two-proton separation energy for nuclei with $Z \geq 100$ calculated from QMCπ-III. Shown in boxes are the currently known SHE while the rest of the nuclei shown have unknown experimental masses. The proton

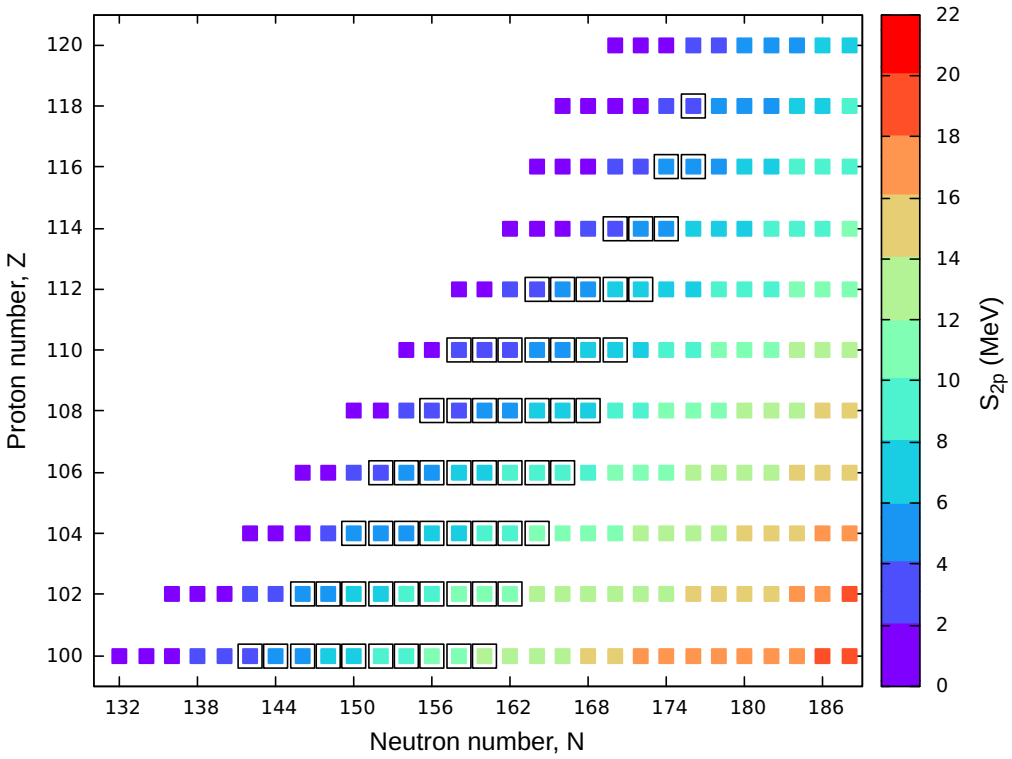

FIGURE 6.7: Two-proton separation energy for nuclei with $Z \geq 100$. Calculations are extended up to the proton dripline which is determined by nuclei with $S_{2p} \geq 0$. Nuclei with currently known masses are specified in black boxes.

dripline is not very far from the last known nucleus on the proton-rich side of each isotope. For instance, for the heaviest known element ^{294}Og, the predicted dripline is at ^{284}Og which is only ten neutrons to the left of ^{294}Og. To the right of the chart, the proton separation energies increase since it will require more energy to pluck out protons from a given element with more neutrons.

Figure 6.8 shows the two-neutron separation energy for nuclei with $Z \geq 100$ from QMCπ-III. Again, known nuclei are specified in black boxes while the rest of the nuclei shown have unknown masses. The neutron dripline is located much farther at the right side of the chart with neutron number extending up to around $N \approx 280$ for the heaviest known element Og. This is due to the fact that more neutrons can be contained in superheavies owing to their large number of protons.

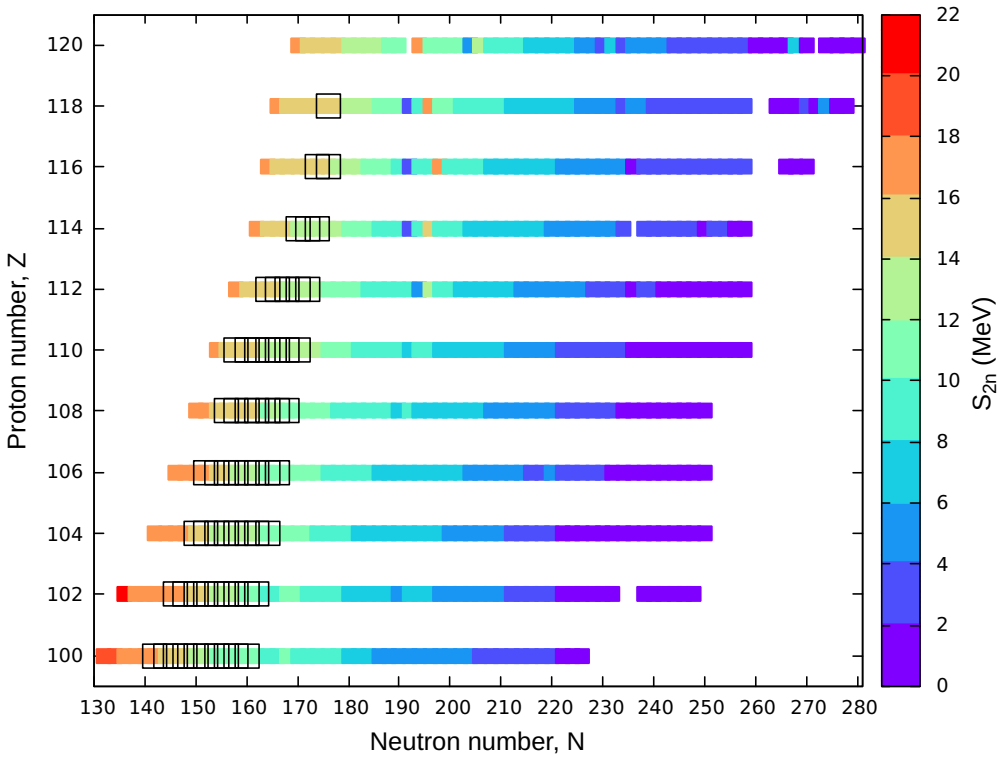

FIGURE 6.8: Two-neutron separation energies for nuclei with $Z \geq 100$. Calculations are extended up to the neutron dripline which is determined by nuclei with $S_{2n} \geq 0$. Nuclei with currently known masses are specified in black boxes.

6.4 Q_α energies and half-life

Apart from two-particle separation energies, the Q_α energies discussed in Section 3.2.1 can also reveal shell structures in an atomic nuclei. At a shell closure, Q_α is expected to have a smaller value compared to that of the next isotope as it requires more energy to remove an α particle from a nucleus right after a closed shell.

Figure 6.9 shows the Q_α energy for known nuclei with $Z \geq 100$ plotted against neutron number N. Results from QMCπ-II in the top panel and QMCπ-III in the bottom panel, are shown as filled symbols and connected by lines, while experimental data are shown as empty symbols with vertical errorbars. QMCπ-II predicts a somewhat smooth decrease in Q_α as N increases along the isotopic chains, thereby missing the dips at the shell closures $N = 152$ and $N = 162$ which are seen from experimental data. For nuclei outside shell closures, QMCπ-II predictions are slightly better compared to QMCπ-III. It is important to note, however, that the latest version is able to replicate the dips in Q_α energies that are expected

at the shell closures.

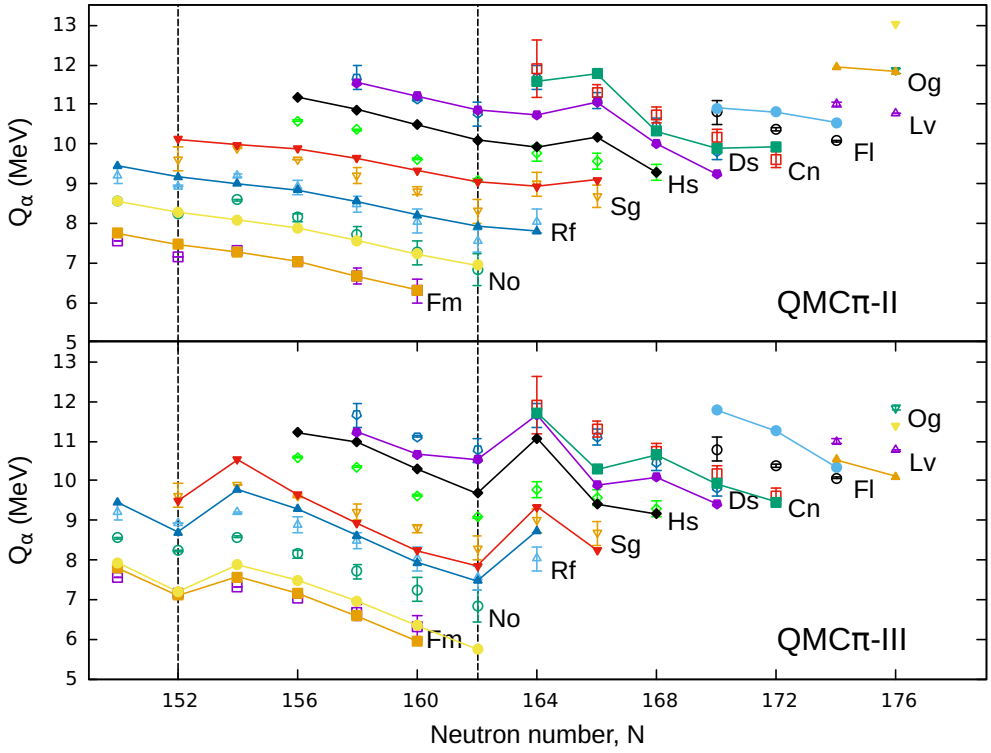

FIGURE 6.9: Q_α energy for nuclei with $Z \geq 100$ plotted against neutron number N. Results from the QMC model are shown as filled symbols and connected by lines, while experimental data and errors, taken from Ref. [38], are shown as empty symbols with vertical errorbars. Subshell closures at $N = 152$ and $N = 162$ are indicated with dashed lines.

Using the Q_α values, half-lives can be calculated using the Viola-Seaborg relationship as discussed in Section 3.2.1. The $\log_{10}(T_{1/2})$ values are very sensitive to Q_α , such that a change of 1 MeV, results in a change of around three orders of magnitude for $\log_{10}(T_{1/2})$. Figure 6.10 shows a comparison of $\log_{10}(T_{1/2})$ predictions from FRDM, SV-min and QMCπ-III along with values obtained from available data. Boxes shown in violet have half-lives less than 10^{-4} s while those in red have $T_{1/2} > 10^{10}$ s. Closer to the proton dripline, the nuclei are seen to have shorter half-lives while towards the neutron dripline, half-lives against α decay are longer. QMCπ-III predictions are almost comparable to those of FRDM and SV-min where neutron-rich SHE with $Z \leq 110$ appear to have $T_{1/2} > 10^{10}$ s.

Table 6.4 shows a comparison of Q_α and $\log_{10}(T_{1/2})$ *rms* residuals from QMC and from other nuclear models for SHE with available data. As seen in Figure 6.9, Q_α values from QMCπ-III are slightly off for some isotopic chains, resulting

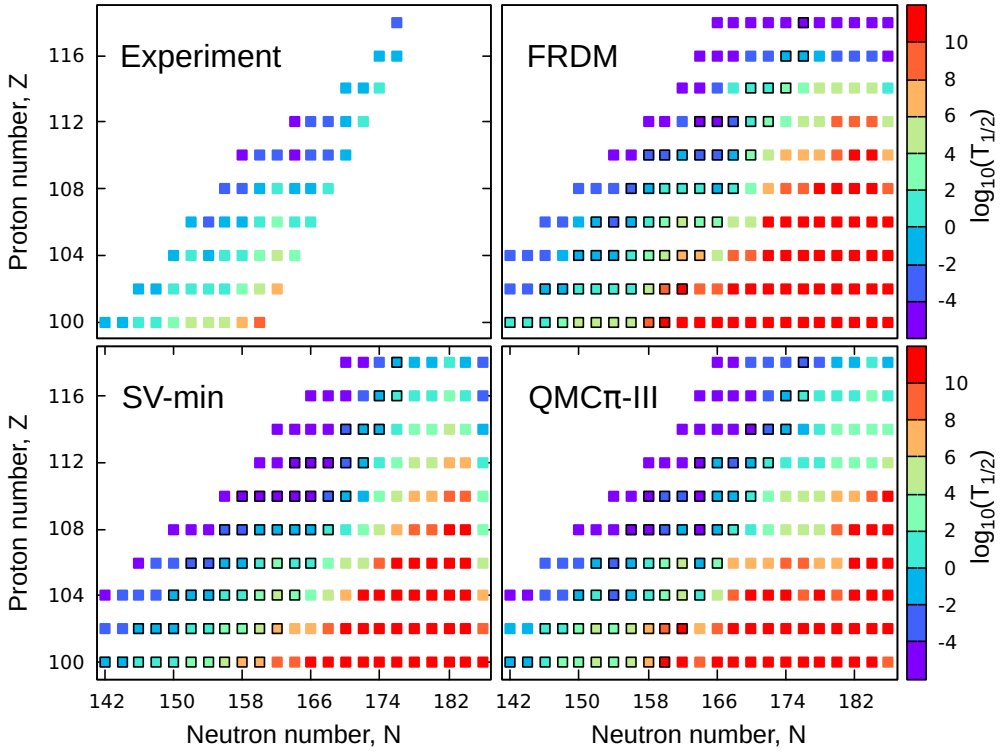

FIGURE 6.10: Comparison of $\log_{10}(T_{1/2})$ predictions from FRDM, SV-min and QMCπ-III along with values obtained from available data.

in higher residuals compared to QMCπ-I and QMCπ-II. Nevertheless, the *rms* residual for Q_α is still well below 1 MeV, which is quite reasonable knowing that energy differences were not included in the QMC fitting procedure. In the table, QMCπ-III has an *rms* residual of around $10^{1.8} \approx 63$ s for the half-life against α decay. This is quite comparable to FRDM results but SV-min and UNEDF1 perfom better for Q_α , and thus for $\log_{10}(T_{1/2})$.

TABLE 6.4: Comparison of Q_α and $\log_{10}(T_{1/2})$ *rms* residuals from QMC and from other nuclear models for SHE with available data.

	Q_α *rms* residual (MeV)	$\log_{10}(T_{1/2})$ *rms* residual (s)
QMCπ-III	0.56	1.80
QMCπ-II [54]	0.43	1.16
QMCπ-I [53]	0.43	1.18
QMC-I [8]	0.67	2.28
FRDM [23]	0.52	1.67
SV-min [24]	0.36	0.98
UNEDF1 [28]	0.28	0.92

6.5 Deformation properties

In this section, the deformation properties of SHE are investigated in detail. Figures 6.11 and 6.12 show the deformation energy, E_{def} , plotted against the quadrupole deformation parameter, β_2 , obtained from QMCπ-III. E_{def} is defined as the energy difference between the total BE of deformed states from the total BE at a spherical shape. The minimum of deformation curves correspond to the equilibrium shape of the nucleus.

Figures 6.11 (a) to (f) show the deformation plots for SHE with $100 \leq Z \leq 110$ and with N from the proton dripline up to $N \leq 186$. Note that the calculations include isotopes which are not yet observed experimentally but lie within the proton and neutron driplines predicted by QMCπ-III. From the plots, the following trends are observed:

- For $148 \leq N \leq 164$, the isotopes have prolate minima around $\beta_2 \approx 0.3$ which becomes shallow as N increases.
- At $N = 166$ and $N = 168$ and starting from the Fm chain, a shape coexistence develops with prolate and oblate minima at $\beta_2 \approx 0.2$ and $\beta_2 \approx -0.2$, respectively. The prolate minimum moves closer to the spherical shape ($\beta_2 = 0$) as N increases in each of the isotopic chain. Further, the oblate minimum slowly vanishes as Z increases towards the Ds chain so that the isotopes become primarily prolate.
- From $N = 170$ and $N = 178$, the shape coexistence behaviour persists but starting from the Rf chain, an additional third minimum starts to develop at $\beta_2 \approx 0.4$. This prolate shape becomes more apparent towards the Ds chain and as N increases, so that the $N = 178$ isotones appear to have three coexisting shapes: oblate, spherical, and prolate.
- For $N = 180$ and $N = 186$ and starting from the Fm chain, isotopes appear to be mostly spherical, though a small oblate minimum also starts to develop as Z increases. Further, a third prolate minimum at $\beta_2 \approx 0.5$ also develops so that starting from the Sg chain, the isotopes appear again to have tri-shapes. The highly prolate shape overcomes the other shapes as both Z and N increase further.

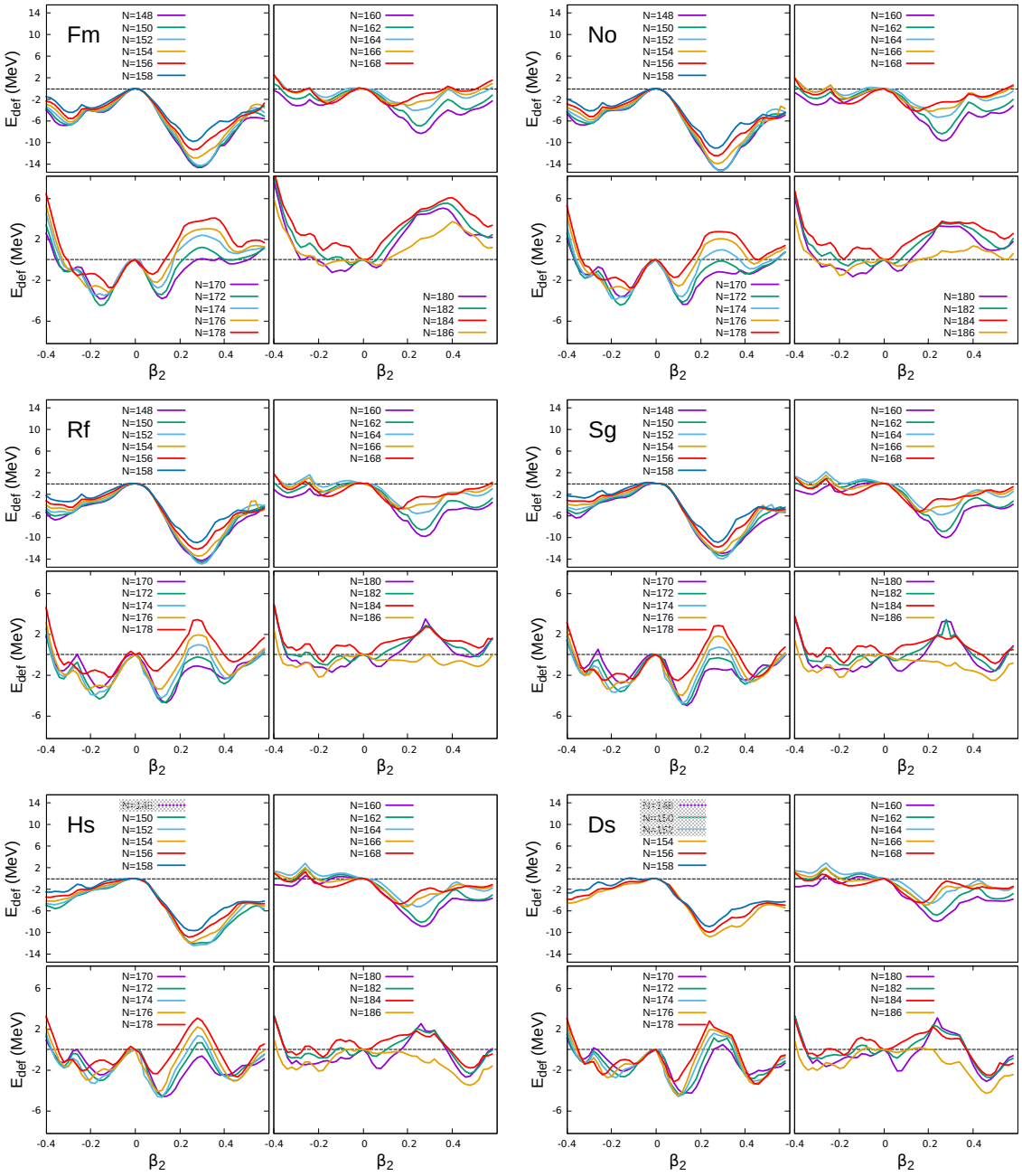

FIGURE 6.11: Deformation plots for even-even SHE with $100 \leq Z \leq 110$ and with N from the proton dripline up to $N \leq 186$ obtained from QMCπ-III. Plot legends are placed at each panel for all isotopic chains.

Figures 6.12 (a) to (d) show the deformation plots for SHE with $112 \leq Z \leq 118$ and with N from the proton dripline up to $N = 186$.

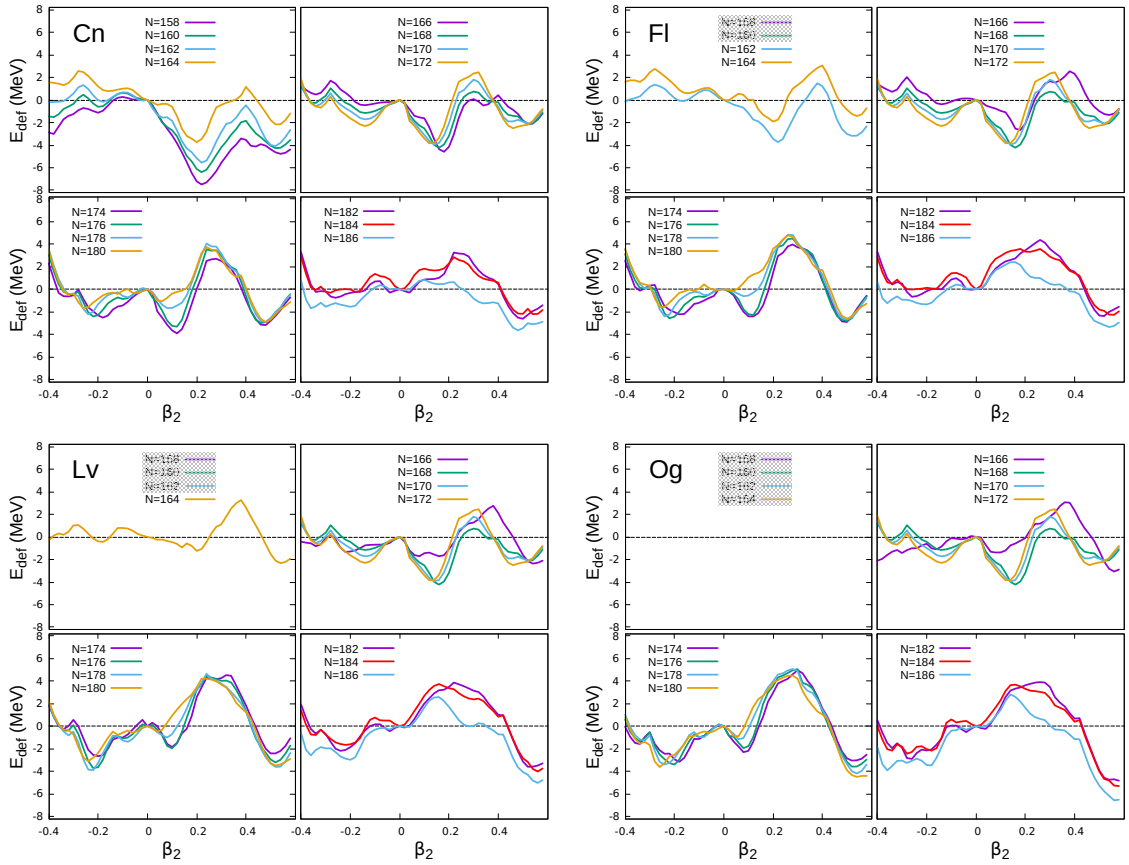

FIGURE 6.12: Same in Figure 6.11 but for $112 \leq Z \leq 118$.

For SHE with $112 \leq Z \leq 118$, the following trends are observed:

- From $158 \leq N \leq 172$, the isotopic chains have primarily prolate shapes at $\beta_2 \sim 0.2$. This minimum moves toward the spherical shape as both Z and N increase. Further, an oblate minimum at $\beta_2 \sim$ -0.2 and another prolate minimum at $\beta_2 \sim 0.5$ start to develop which balances out with the first minimum as mass increases so that tri-shapes tend to appear for heavier isotopes.

- The tri-shape coexistence persists for isotopes with $174 \leq N \leq 180$, although the first minimum, now at $\beta_2 \sim 0.1$, slowly disappears as N increases in each isotopic chain. This then leaves the other oblate and highly prolate minima for the heavier isotopes.

- For $182 \leq N \leq 186$, the isotopes appear to have highly prolate shapes.

Since there are no available data for the deformation of SHE, QMC predictions are instead compared with results from other nuclear models. Figures 6.13 to 6.15 present a comparison of quadrupole deformations along SHE isotopic chains from several models. Recall that from QMCπ-III deformation plots, shape coexistence can appear in some isotopes. Thus for QMCπ-III, the plots show the first minima as filled red symbols while the other minima, which are very close to the first one, are shown as empty red symbols and labelled 'QMCπ-III*'.

For the Fm, No and Rf chains in Figure 6.13, QMCπ-III predict prolate shapes from the proton dripline up to around $N = 170$ and then changes shape to being oblate from $N = 172$ to $N = 180$ as with other models.

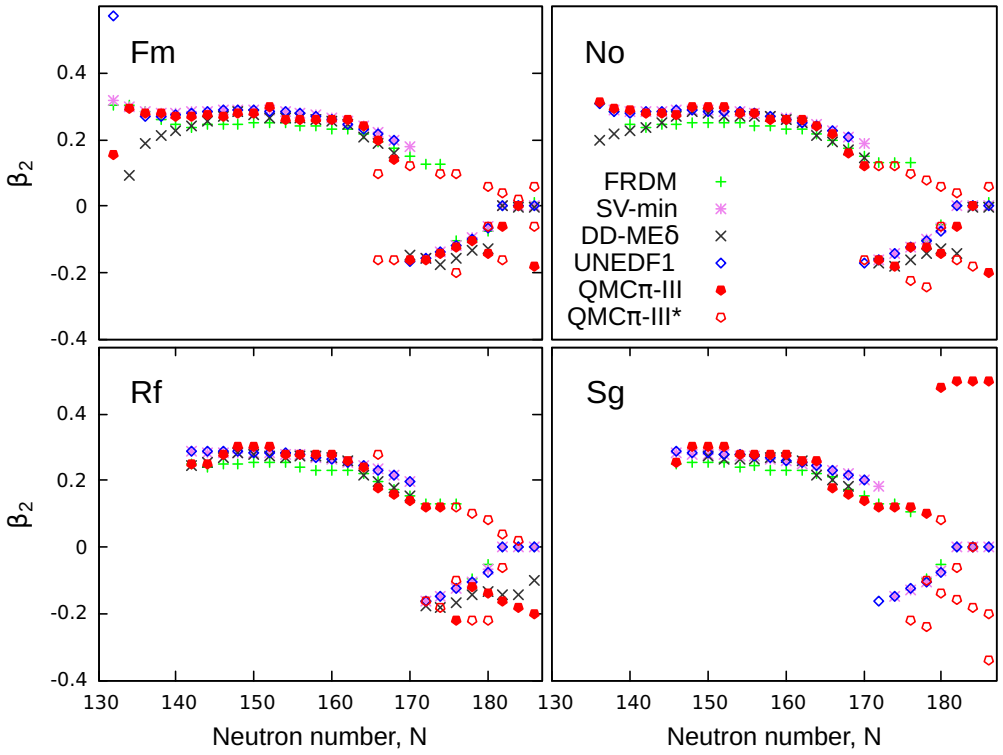

FIGURE 6.13: Comparison of deformation parameter, β_2 , values along the Fm, No, Rf, and Sg isotopic chains from several nuclear models. For QMCπ-III, the first minima are shown as filled red symbols, while the other minima, which are very close to the first, are shown as empty red symbols and labelled 'QMCπ-III*'. Plot legend is located in the top right panel.

Further for QMCπ-III, a second prolate minimum appears for the isotopes with $172 \leq N \leq 180$. Around the predicted shell closure at $N = 184$, QMC predicts shape coexistence of spherical and oblate shapes for Fm, Rf and No isotopic chains, where most of the other models predict spherical shapes only. For

the Sg chain, however, QMCπ-III yields prolate shapes up to $N = 180$ with the deformation increasing further around $N = 184$. Other minima predicted from QMCπ-III give spherical and oblate shapes for Sg around $N = 184$ where, again, the other models predict spherical shapes only.

For the Hs, Ds, Cn and Fl isotopic chains in Figure 6.14, QMC predicts primarily prolate shapes up to $N = 178$. Some isotopes with $170 \leq N \leq 178$ develop shape coexistence as Z increases. Starting from $N = 180$, deformation further increases from $\beta_2 \sim 0.5$ to 0.6 in QMCπ-III. The other models predict prolate shapes as well up to around $N = 174$ but give oblate to spherical shapes as N increases. Around the supposed $N = 184$ closure, QMCπ-III yields highly prolate shapes while the other models still predict the isotones to be spherical.

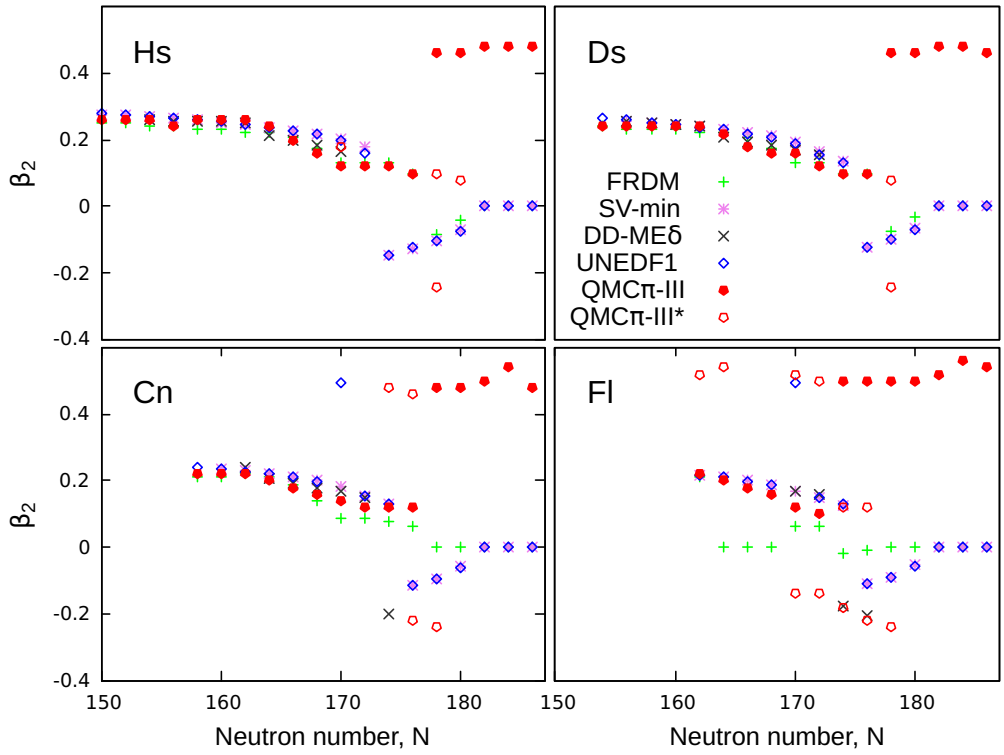

FIGURE 6.14: Same as in Figure 6.13 but for Hs, Ds, Cn and Fl isotopic chains.

For the Lv and Og isotopic chains in Figure 6.15, shape coexistence occurs in most of the isotopes as predicted by QMCπ-III. Meanwhile, the other models give prolate to oblate shapes as N increases then spherical shapes around $N = 184$.

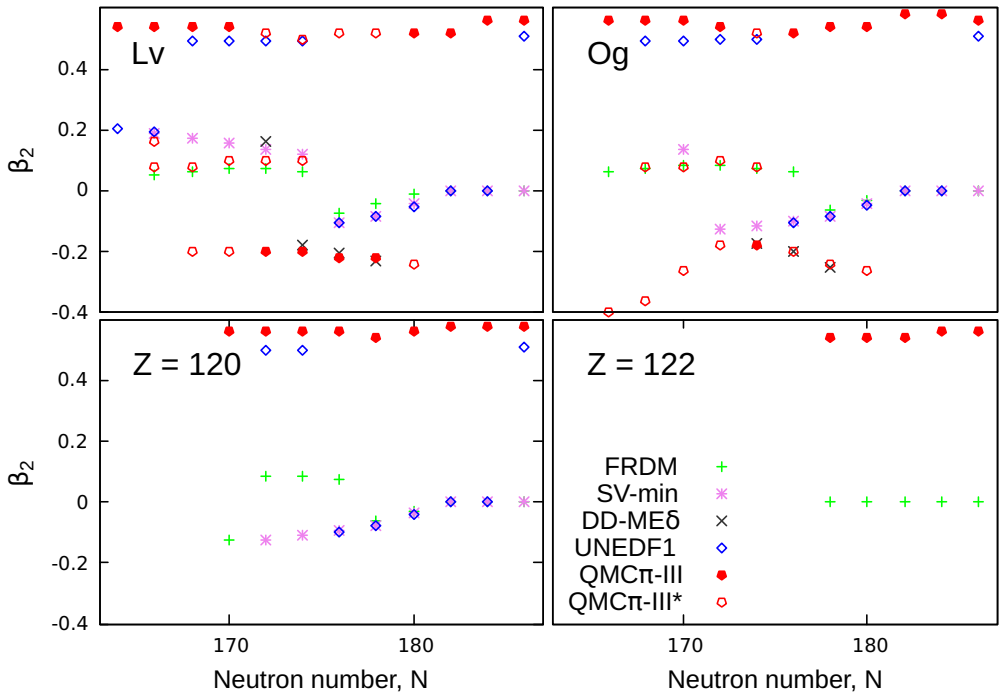

FIGURE 6.15: Same as in Figure 6.13 but for Lv, Og, $Z = 120$ and $Z = 122$ isotopic chains. Plot legend is located at the bottom right panel.

Calculations are extended to the chains of $Z = 120$ and $Z = 122$, which are yet unknown SHE. In the bottom plots of Figure 6.15, FRDM and SV-min give spherical shapes for both chains, while UNEDF1 predicts prolate to spherical behaviour as N increases for $Z = 120$ chain. On the other hand, QMCπ-III gives highly prolate shapes along both chains.

Overall, the latest version of the QMC model is able to perform very well in the superheavy region, yielding excellent results for binding energies and energy differences compared to available data. The improvement in predictions were seen as the QMC model developed. Furthermore, in regions where data for ground-state observables are not yet available, QMCπ-III showed comparable results to other nuclear models eventhough there are significantly fewer number of parameters in the QMC model. In the succeeding chapter, QMC predictions are further investigated throughout the present nuclear landscape.

Chapter 7

The QMC model across the nuclear landscape

In Chapter 5, the success of the QMC model was demonstrated along magic chains of nuclei. The model developments and significant improvements in predictions for nuclear observables in that region naturally suggest that calculations should be extended to other regions in the nuclear chart. In this chapter, the latest version, QMCπ-III, is used to explore several properties and observables for all even-even nuclei within the current nuclear landscape.

7.1 Binding energies

At the valley of stability, atomic nuclei are more bound compared to nuclei closer to the driplines. Figure 7.1 shows the binding energy per nucleon, B/A, for even-even nuclei with $Z, N \geq 8$ across the nuclear chart obtained from QMCπ-III. Closer to black are nuclei which are more stable and those closer to yellow have less binding. It can be seen that B/A changes relatively quicker at magic numbers as can be seen by the sudden change in shade at those regions. This behaviour is more visible in the differences of energies which will be taken up in Section 7.3. In light nuclei, the decrease in binding is easily seen as isotopic chains reach the driplines. Further, B/A decreases as atomic number increases up in the chart towards the superheavy region.

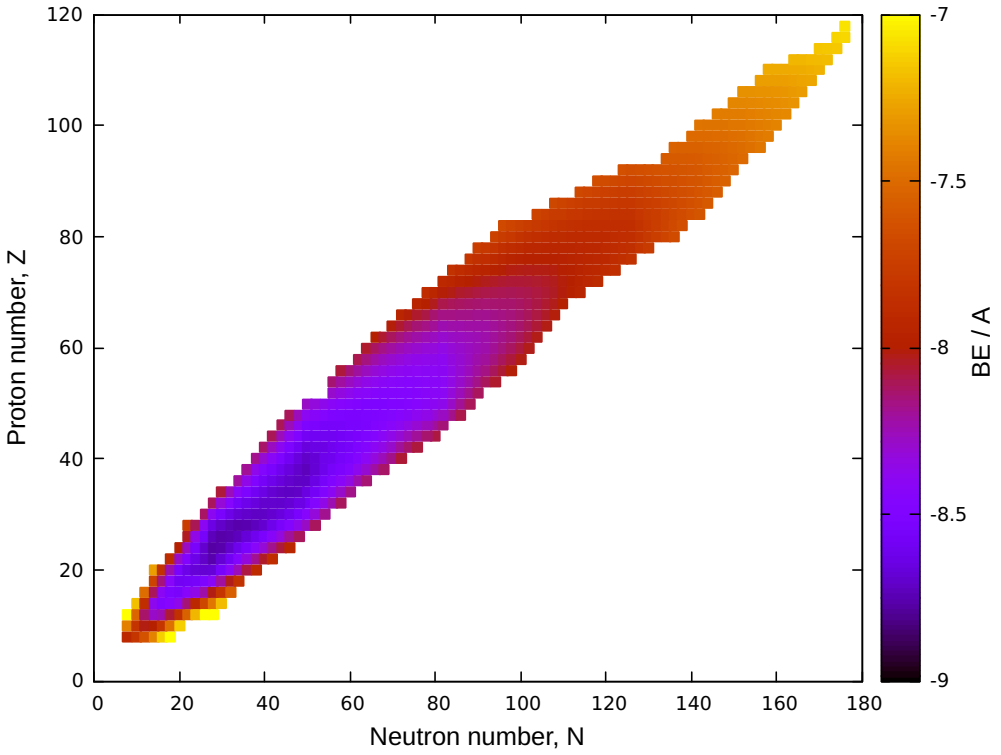

FIGURE 7.1: Binding energy per nucleon for even-even nuclei with $Z, N \geq 8$ across the nuclear chart predicted by QMCπ-III. Closer to black are nuclei with more binding while closer to yellow are those with less binding.

The performance of the latest QMC version for even-even nuclei can be evaluated by looking at the deviation of QMCπ-III results from experimental data. Figures 7.2 (a) and (b) show the BE residuals and the percent deviations, respectively, as defined in Section 4.3.2. For QMCπ-III, residuals for total BE vary from around $\pm$ 5 MeV and deviations are up to around 1%. Residuals are seen to be relatively higher for symmetric nuclei with $Z = N$. Such discrepancy may be attributed to Wigner energy [67, 68, 69] due to proton-neutron pairing, which is conventionally neglected in mean-field theories. Symmetric nuclei will be discussed in detail in Section 7.5.1. Further, residuals are also relatively higher with predicted overbinding, for heavy isotopes of Ca and Ni as well as for heavy $N = 126$ isotones. There is also predicted underbinding for Pb isotopes closer to the driplines. Looking at the percent deviations, values are relatively higher for light nuclei closer to the driplines and again, for $Z = N$. Note that one cannot expect perfect agreement with data for very light nuclei as well as for soft nuclei since they can exhibit other correlations beyond mean-fields. It is emphasized, however, that these BE results are already outstanding as can be seen in

comparison with other model predictions.

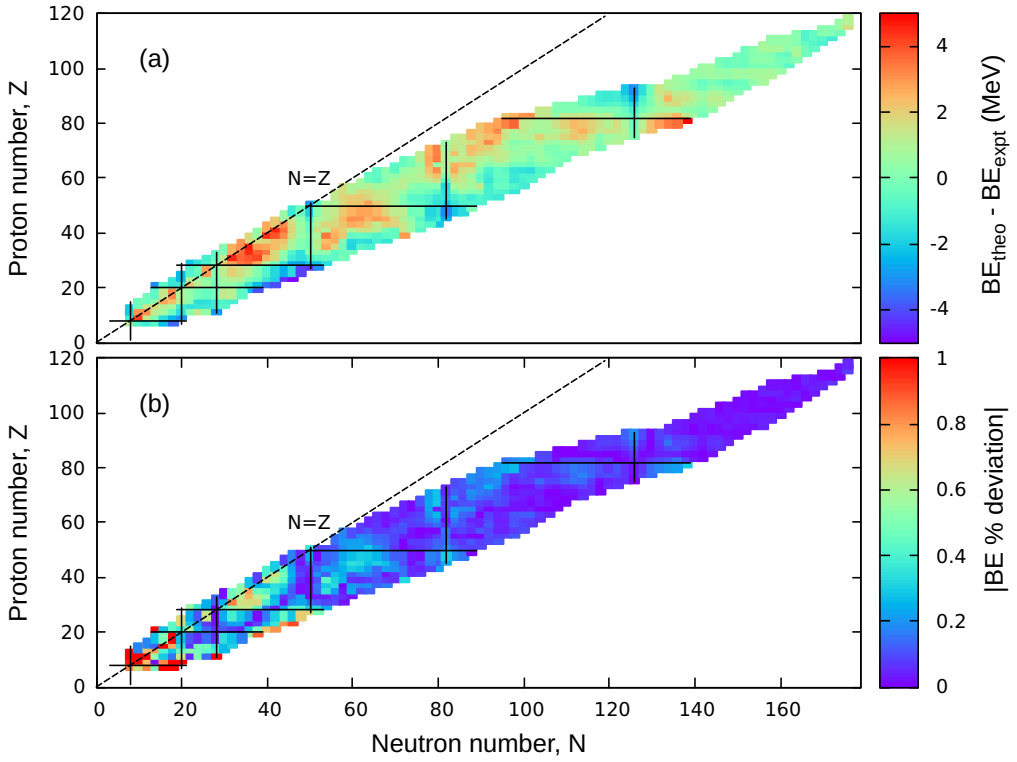

FIGURE 7.2: QMCπ-III predictions for (a) BE residuals and (b) absolute BE % deviation for even-even nuclei with known masses. Magic numbers are specified with solid lines while symmetric nuclei, $Z = N$, are shown with dashed lines.

To compare the results from QMCπ-III to the predictions of the previous QMC versions as well as with other existing models, Table 7.1 lists both the *rms* residual and *rms* % deviation for total BE. The improvement in BE predictions through-

TABLE 7.1: Comparison of BE *rms* residual and *rms* % deviation from QMC and other nuclear models. There are a total of 820 even-even nuclei with available masses included in the calculation and shown in Figure 7.2.

Model	*rms* residual (MeV)	*rms* % deviation
QMCπ-III	1.59	0.29
QMCπ-II	2.34	0.39
QMCπ-I	2.78	0.50
QMC-I	3.84	0.69
SV-min	3.64	0.38
UNEDF1	2.06	0.55
DD-MEδ	2.41	0.42
FRDM	0.89	0.18

out the chart can be seen as the QMC model develops, giving an *rms* residual of only 1.59 MeV and an *rms* % deviation of 0.29 in the latest version. These values are even smaller compared to the predictions from the Skyrme forces, SV-min [24] and UNEDF1 [26], and with the covariant EDF, DD-MEδ [66]. FRDM [23] still gives the best predictions for masses but QMCπ-III results are already fairly comparable.

7.2 RMS charge radius

Apart from binding energy, charge radius is also investigated across the chart. Figure 7.3 shows the QMCπ-III predictions for (a) R_{ch} residuals and (b) R_{ch} % deviation for even-even nuclei with known radii. Note that there are fewer available data for radii than there are for energies. Residuals for R_{ch} vary from around $\pm$ 0.05 fm while the deviations are up to around 1%. Deviations from experiment are relatively higher for light nuclei particularly in the regions of ^{16}O and ^{40}Ca. Further, residuals are also relatively higher just below the Pb chain as well as in the uranium ($Z = 92$) region. Not included in the plot, for visual purposes, is the curium ($Z = 96$) chain where residuals are up to 0.1 fm and deviations are as much as 2%.

Table 7.2 shows the performance of QMCπ-III for R_{ch} in comparison with previous QMC versions and other nuclear models. Just as in BE, improvements are

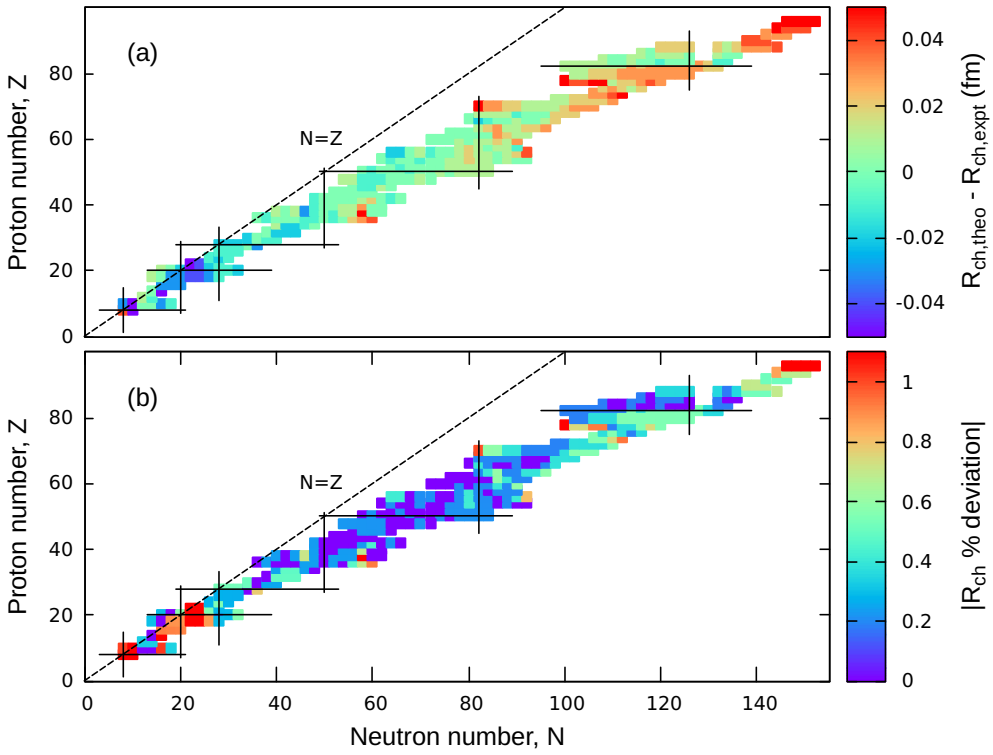

FIGURE 7.3: QMCπ-III predictions for (a) R_{ch} residuals and (b) R_{ch} % deviation for even-even nuclei with known radii. Magic numbers are specified with solid lines while symmetric nuclei, $Z = N$, are shown with dashed lines.

seen in the latest QMC version where *rms* residual decreased to 0.024 fm and deviation to only 0.5% compared to the slightly higher values in the earlier versions. Looking at the percent deviations, QMCπ-III results are slightly better compared to the values from SV-min and UNEDF1 as well as from DD-MEδ. Note that FRDM does not provide data for R_{ch} .

TABLE 7.2: Comparison of R_{ch} *rms* residual and *rms* % deviation from QMC and other nuclear models. There are a total of 350 even-even nuclei with available radii and with $Z \leq 96$ included in the calculation.

Model	*rms* residual (fm)	*rms* % deviation
QMCπ-III	0.024	0.50
QMCπ-II	0.029	0.66
QMCπ-I	0.028	0.65
QMC-I	0.030	0.66
SV-min	0.024	0.61
UNEDF1	0.029	0.65
DD-MEδ	0.035	0.78

7.3 Shell closures

As mentioned in Section 7.1, the locations of magic numbers can be rendered more visible by looking at energy differences. Figure 7.4 shows the two-particle separation energies and two-particle shell gaps computed from atomic masses in QMCπ-III. For S_{2n} and S_{2p} , sudden drops in separation energy values signify the locations of shell closures. These are seen at the magic numbers $Z, N = 20, 28, 50, 82$ and at $N = 126$ by the lines forming at these particle numbers. The values for S_{2n} decrease as N increases along isotopic chains. In the same way, S_{2p} values also decrease as Z increase along isotonic chains. Recall that extending the calculations for separation energies will eventually reach a limit for each chain which determines the dripline.

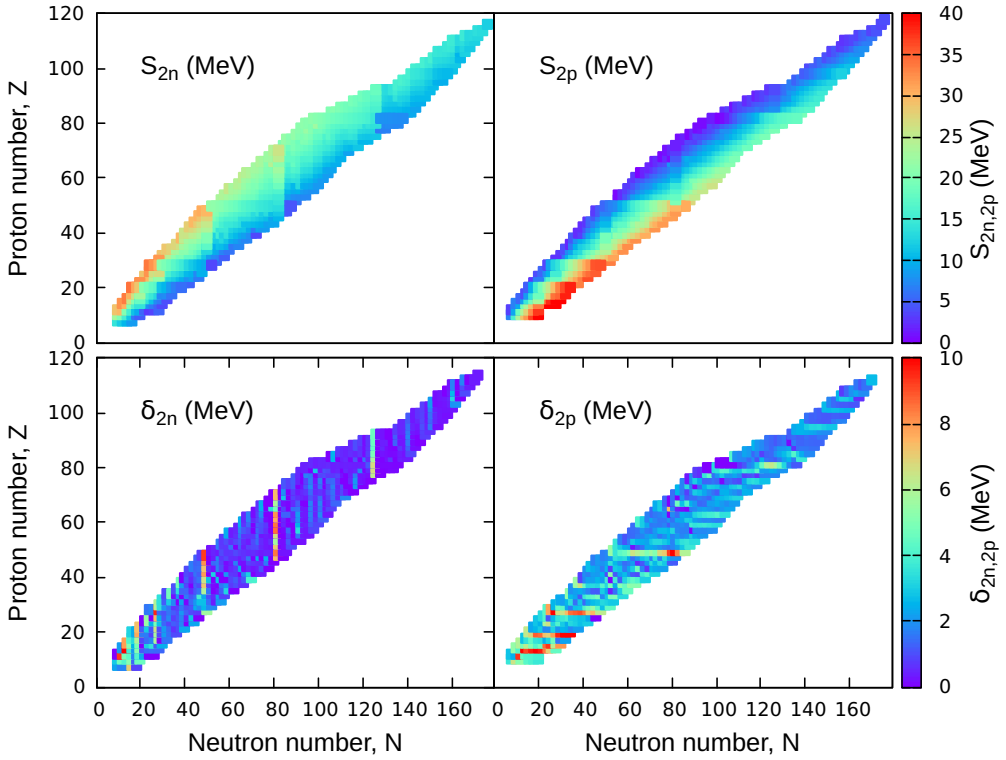

FIGURE 7.4: Two-particle separation energies and shell gaps for known even-even nuclei predicted by QMCπ-III. Note the existence of shell closures seen from the lines forming at the locations of magic numbers.

For the two-particle shell gaps, defined in Eq. (3.21), predictions from QMCπ-III fluctuate along the chains of nuclei. Nevertheless, the locations of the shell closures are visible. Note that since separation energies are larger at magic numbers, the corresponding shell gap will also be relatively higher compared to those of other nuclei along isotopic and isotonic chains. Shell closures are identified by the peaks in shell gaps which are again seen by the lines forming at the locations of magic numbers for δ_{2p} and δ_{2n} in Figure 7.4.

From Q_α energies, shell closures can also be identified where the values along isotopic chains create a minimum. Figure 7.5 shows the Q_α predictions from QMCπ-III across the chart as well as the corresponding half-lives for α decay. Half-lives are calculated using the Viola-Seaborg relation given in Eq. (3.20). Nuclei with $Q_\alpha < 0$ are stable against α decay while those with $Q_\alpha > 0$ are unstable. The plot for half-lives only shows values for nuclei that are predicted to be unstable against α decay.

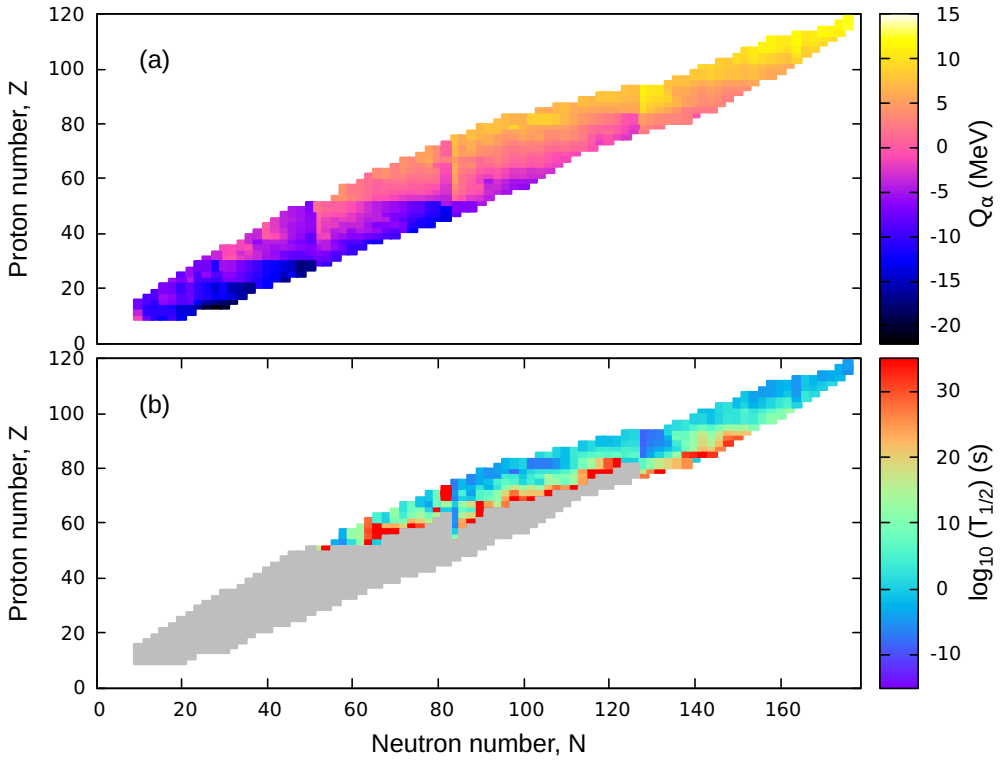

FIGURE 7.5: (a) Q_α predictions from QMCπ-III across the chart and (b) the corresponding half-lives for α decay. Note that only nuclei which are unstable against α decay ($Q_\alpha > 0$) are shown in (b).

In Figure 7.5 (a), the shell closures are once again seen from Q_α values by the lines forming at the magic numbers. Along isotopic chains, Q_α decreases as N increases but suffers an abrupt increase in Q_α right after a closure, thereby

creating a minimum at the location of the closure. This behaviour was also seen, for example, along SHE chains in Figure 6.9 of the previous chapter.

Corresponding half-lives for α decay in Figure 7.5 (b), show that heavy nuclei closer to the proton dripline have shorter predicted lifetimes compared to lighter nuclei along isotonic chains. It can also be seen that the isotonic chains $N = 82, 126, 162$ have somewhat visible lines showing shorter lifetimes right after these closures compared to the $T_{1/2}$ values along their isotopic chains. This corresponds to the minima in Q_α energies at the locations of the shell closures.

Table 7.3 shows a comparison of *rms* residuals for separation energies from QMC and from other nuclear models. QMCπ-II and QMCπ-III have comparable results for separation energies with the latest version only improving marginally for S_{2n} , S_{2p} and Q_α . Both SV-min and UNEDF1 are good in predicting energy differences despite having higher residuals for absolute BE values. Meanwhile, DD-MEδ have comparable values to those of QMC while FRDM gives the best predictions for separation energies.

TABLE 7.3: Comparison of *rms* residuals for separation energies (in MeV) from QMC and from other nuclear models.

Model	S_{2n}	S_{2p}	δ_{2n}	δ_{2p}	Q_α
QMCπ-III	0.97	0.95	1.24	1.28	1.07
QMCπ-II	1.03	1.08	1.20	1.25	1.19
SV-min	0.77	0.82	0.87	1.00	0.79
UNEDF1	0.74	0.82	0.85	0.90	0.80
DD-MEδ	1.01	1.05	1.12	1.11	1.30
FRDM	0.50	0.55	0.61	0.75	0.61

7.4 Nuclear deformation

Across the nuclear chart, shapes of even-even nuclei are investigated by computing their ground-state quadrupole deformation. Figure 7.6 shows (a) the deformation parameter β_2 from QMCπ-III and (b) the residuals upon comparison with available data [52]. Note that in plot (b), values from QMCπ-III are taken in their absolute values since experimental data are only in absolute values of β_2 .

As discussed in Section 3.2.2, nuclei with $\beta_2 \approx 0$ have spherical shapes while those with $\beta_2 < 0$ and $\beta_2 > 0$ correspond to oblate and prolate shapes, respectively. It is emphasized that experimental values for β_2 are only deduced from the

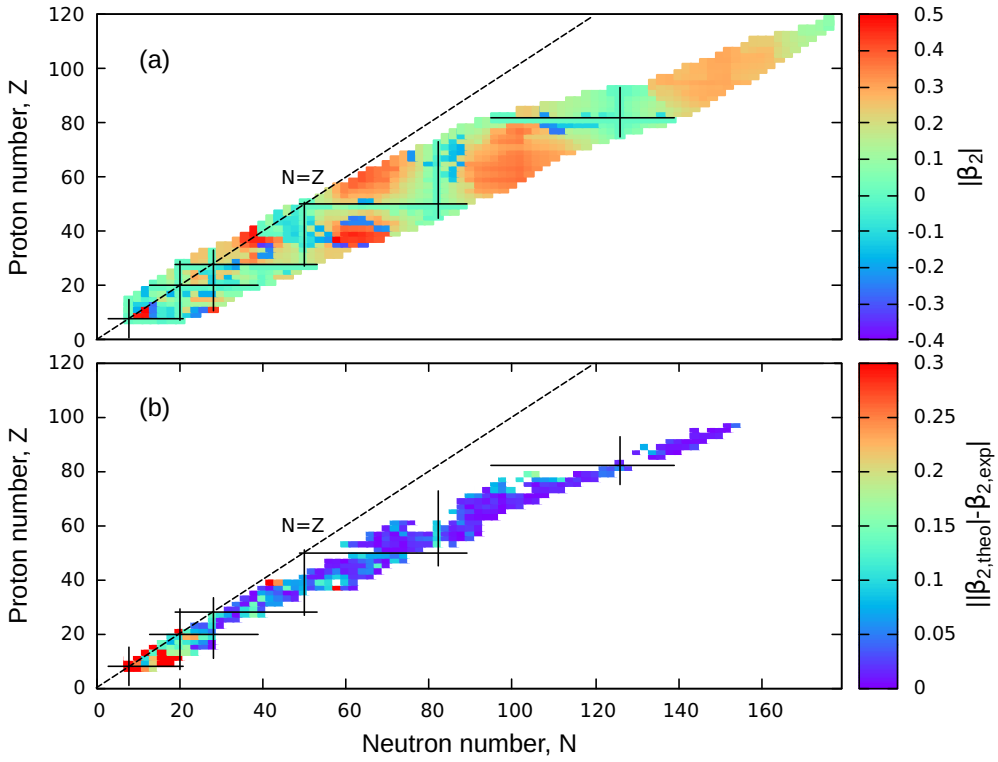

FIGURE 7.6: QMCπ-III predictions for (a) quadrupole deformation parameter, β_2, and (b) corresponding residuals upon comparison with available data [52]. Magic numbers are specified with solid lines while symmetric nuclei, $Z = N$, are shown with dashed lines.

transition probabilities, $B(E2)\uparrow$, which are good approximation only for well-deformed nuclei. For spherical nuclei, measured $B(E2)\uparrow$ may include collective excitations which may result to a non-zero value for β_2 . Dynamic deformations resulting from the vibrations in the nuclear surface may then be different in value compared to the static deformation [70].

In Figure 7.6 (a), QMCπ-III predicts that nuclei are spherical at the regions of magicity. Nuclei that are relatively far from the magic numbers, consequently at mid-shells, have relatively higher deformations. In particular, regions with high deformations are around light and heavy isotopes of the Zr chain with $N \sim 40$ and $N \sim 60$, respectively. This will be discussed in detail in Section 7.5.3. Deformation is also higher at the symmetric nucleus ^{24}Mg which will be further looked into in Section 7.5.1. Further, there are also relatively higher deformations for $Z \sim 60$ isotopes with $N \sim 60$ and $N \sim 100$. For the Gd chain with $Z = 64$, deformations are discussed in Section 7.5.5.

In Figure 7.6 (b), the absolute residuals for β_2 vary up to 0.3 and are relatively higher for light nuclei. Moreover, deviations are higher along the symmetric line

up to ^{32}S as well as at ^{40}Ca and near ^{80}Zr. Deformations for nuclei along the symmetric line will be discussed in detail in Section 7.5.1.

To compare the QMC predictions for nuclear shapes with those from other nuclear models, *rms* residuals and *rms* % deviations are listed in Table 7.4. The comparison includes a total of 324 even-even nuclei with available data for β_2 .

TABLE 7.4: Comparison of β_2 *rms* residuals and *rms* % deviations from QMCπ-III and from other nuclear models. There are a total of 324 even-even nuclei with available data for β_2 included for comparison.

Model	*rms* residual	*rms* % deviation
QMCπ-III	0.11	28
SV-min	0.16	59
UNEDF1	0.15	53
DD-MEδ	0.14	40
FRDM	0.11	30

For quadrupole deformations, QMCπ-III is seen to perform at par with FRDM, both having an *rms* residual of 0.11 and *rms* deviation of around 30%. Compared to QMCπ-III, DD-MEδ has slightly higher deviations while both SV-min and UNEDF1 have almost twice the percentage deviations.

7.5 Shape coexistence

Even at their ground-states, some nuclei are found to exhibit two or three shapes corresponding to the minimum values of deformation energies. This phenomenon, called shape coexistence, has been studied for several regions in the nuclear chart [71, 72, 73]. In this section, some of these regions will be investigated using QMCπ-III to see if the model is able to capture such behaviour.

7.5.1 Symmetric nuclei, $Z = N$

The study of shape coexistence is known to have originated from the doubly-magic and symmetric ^{16}O nucleus. It was then believed that the succeeding doubly-magic and symmetric nuclei, ^{40}Ca and ^{56}Ni, also exhibit coexisting bands in their first excited states which may mix with the ground states [71]. Although only ground states are calculated in the present research, one can easily relate the transition energy to the first 2^+ state using the β_2 parameter, as discussed in Section 3.2.2.

Figure 7.7 shows the deformation energies, E_{def} , as defined in Section 6.5, plotted against β_2 parameter calculated from QMCπ-III for all known symmetric nuclei. The doubly-magic isotopes ^{16}O, ^{40}Ca, ^{56}Ni as well as ^{100}Sn (shown in red

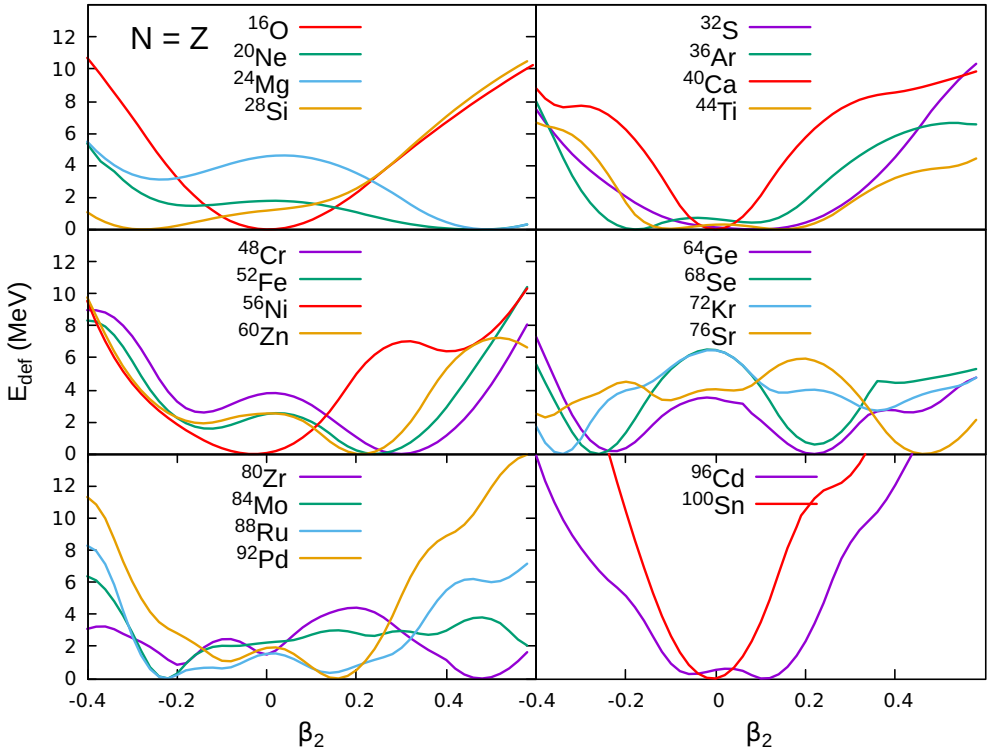

FIGURE 7.7: QMCπ-III predictions for deformation energies plotted against β_2 parameter for all known symmetric nuclei. Plot legends are placed in each of the panel.

curves) are all spherical with $\beta_2 \sim 0$. Recall that these nuclei are included in the fitting procedure and were strictly imposed to have spherical shapes. Apart from these isotopes, most of the other symmetric nuclei are predicted to exhibit shape coexistence. Starting from ^{20}Ne, a primary prolate minimum appears, while there is also an onset of a secondary oblate minimum. For ^{28}Si, only the oblate minimum at $\beta_2 \sim$ -0.3 appears. For ^{32}S, ^{36}Ar and ^{44}Ti, the minimum is rather flat, spanning oblate to spherical to prolate shapes. From ^{48}Cr to ^{68}Se, with the exception of ^{56}Ni, nuclei appear to have both oblate and prolate shapes with $|\beta_2| \sim 0.2$. The oblate minimum then slowly shifts to the left at around $\beta_2 \sim -0.35$ for ^{72}Kr where the prolate minimum vanishes. For the next symmetric nucleus, ^{76}Sr, the deformed minimum shifts to the prolate side with $\beta_2 \sim 0.45$ while the oblate shape disappears.

At the bottom plot, the symmetric ^{80}Zr isotope which has both proton and neutron numbers that are closed subshells ($Z, N = 40$), appears to have three

shapes in its ground-state as predicted by QMCπ-III. ^{80}Zr has an oblate shape with $\beta_2 \sim$ -0.2, a spherical shape with $\beta_2 \sim 0$ and a highly prolate minimum at $\beta_2 \sim 0.5$. The Zr chain will be further investigated in Section 7.5.3. From ^{88}Ru to ^{96}Cd, the nuclei are again predicted to have both oblate and prolate coexisting shapes with decreasing deformation as mass increases.

Table 7.5 lists the β_2 values corresponding to the location of deformed minima for symmetric nuclei obtained from QMCπ-III. Available data from experiment, which are only in absolute values of β_2 , as well as predictions from FRDM, are added for comparison.

TABLE 7.5: β_2 values corresponding to the locations of the first and second deformed minima for symmetric nuclei obtained from QMCπ-III. Also added for comparison are experimental data which are only available in absolute values [52], as well as FRDM results [23].

Z or N	Expt.	QMCπ-III		FRDM	Z or N	Expt.	QMCπ-III		FRDM
		1st	2nd				1st	2nd	
8	0.36	0.00	-	-0.01	30	-	0.22	-0.14	0.16
10	0.73	0.46	-0.16	0.36	32	-	0.22	-0.22	0.21
12	0.61	0.50	-0.24	0.39	34	-	-0.26	0.22	0.23
14	0.41	-0.28	-	-0.36	36	-	-0.34	-	-0.37
16	0.31	0.10	-	0.22	38	-	0.46	-	0.40
18	0.26	-0.18	0.08	-0.26	40	-	0.48	-0.20	0.43
20	0.12	0.00	-	0.00	42	-	-0.22	-	-0.23
22	0.27	0.14	-	0.00	44	-	-0.22	0.14	-0.24
24	0.34	0.30	-0.14	0.23	46	-	0.16	-0.16	0.00
26	-	0.24	-0.12	0.12	48	-	0.10	-0.06	-0.02
28	0.17	-0.02	-	0.00	50	-	0.00	-	0.00

From experimental data, the doubly-magic isotopes ^{16}O, ^{40}Ca and ^{56}Ni exhibit some value for β_2 which may come from collective vibrations upon the measurement of transition probabilities, $B(E2)\uparrow$, as discussed in Section 7.4. As said previously, these nuclei have been imposed to be spherical in the QMC fits. It must be emphasized that deformations for these nuclei may come from correlations with excited states which are not yet accessible in the present QMC calculations.

As seen in Figure 7.6, deviations are relatively higher for symmetric nuclei up to ^{32}S. From data, these nuclei appear to be highly deformed which are underestimated in QMCπ-III and even in FRDM. For symmetric nuclei with $30 \leq Z, N \leq 50$ where no data is available, QMCπ-III results are compared to those of FRDM. β_2 values from the two models are mostly comparable for the said nuclei, except for ^{68}Se where QMCπ-III predicts a primary oblate shape while FRDM

gives prolate. Note, however, that from the deformation plot in Figure 7.7, ^{68}Se exhibits shape coexistence and its secondary minimum at $\beta_2 \sim 0.22$ has almost equal deformation energy with the oblate minimum. The second minimum then compares well with FRDM results. The shape coexistence in the Se chain is further discussed in Section 7.5.5.

7.5.2 Island of inversion

Apart from symmetric nuclei, deviations for β_2 are also seen to be relatively higher near $N = 20$ isotones around Mg ($Z = 12$). This particularly interesting region is known as the island of inversion where there seems to be disappearing of shell gaps. On this island, the first excited states can mix with the ground states and in some cases can even have energies lower than that of the ground states. As a consequence, the single-particle energies are rearranged and the expected shell gaps disappear. Moreover, the supposed ground state properties such as deformation will be affected. The island of inversion, or also known as island of shell breaking, is centered at ^{32}Mg for $N = 20$ isotones. The island is also predicted to appear for $N = 28$ isotones around ^{42}Si. In this subsection, deformations and shape coexistence are studied for the said isotonic chains using QMCπ-III.

Figure 7.8 shows the deformation energies plotted against β_2 for $N = 20$ and $N = 28$ isotones calculated from QMCπ-III. Along the $N = 20$ isotonic chain, the nuclei are predicted to be spherical. For ^{32}Mg, however, a second minimum appears in the prolate side with $\beta_2 \sim 0.4$. Note that nuclei from ^{34}Si to ^{42}Ti where included in the fitting procedure with sphericity imposed.

For the $N = 28$ isotonic chain, two deformed minima appear for the lighter nuclei from ^{40}Mg to ^{46}Ar giving oblate and prolate coexisting shapes. From ^{48}Ca to ^{56}Ni, which were included in the fit procedure, the isotones are close to spherical although the minimum is slightly shifted to the oblate side from ^{50}Ti to ^{54}Fe.

7.5.3 $Z, N = 40$ subshell

In the previous sections, major shell closures were determined by looking at the separation energies across the nuclear chart. Aside from the major shells, there are predicted subshells created by a considerable gap when particles are arranged using the shell model. One of these subshells appears at $Z, N = 40$ where either the $2p_{1/2}$ or $1f_{5/2}$ state is filled and a gap appears towards the $1g_{9/2}$ state. In this

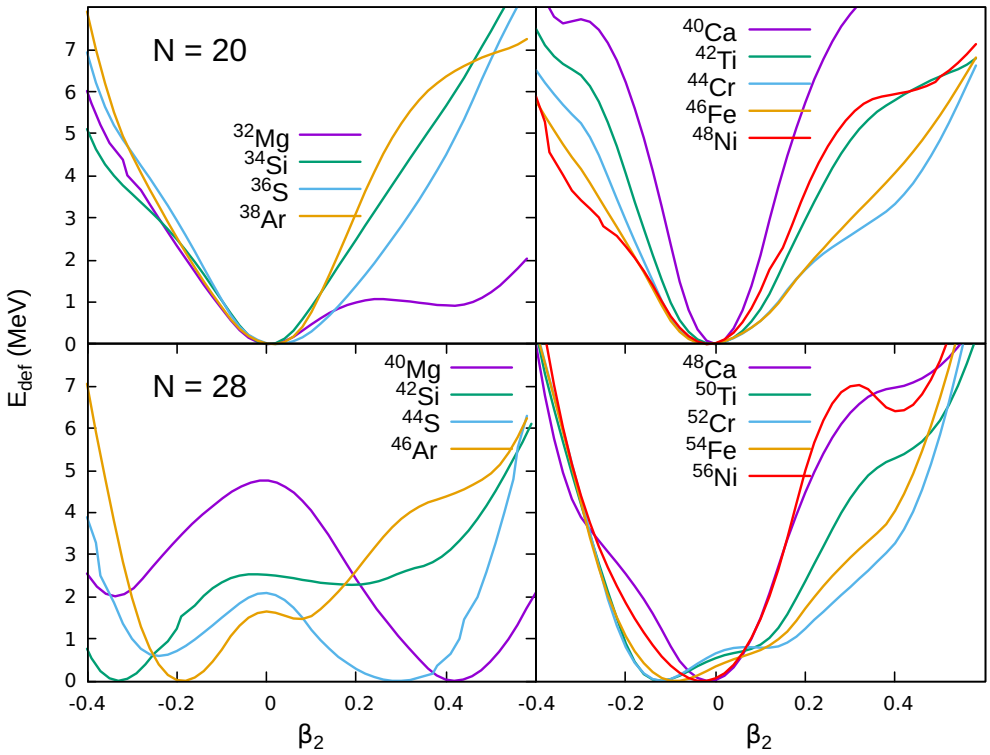

FIGURE 7.8: QMCπ-III predictions for deformation energies plotted against β_2 parameter for $N = 20$ and $N = 28$ isotones. Plot legends are placed in each of the panel.

section, deformations and shape coexistence are investigated in this particular subshell using QMCπ-III.

Figure 7.9 shows the deformation plots versus β_2 values along the $N = 40$ isotonic chain computed from QMCπ-III. Starting from ^{62}Ti to ^{68}Ni, nuclei are

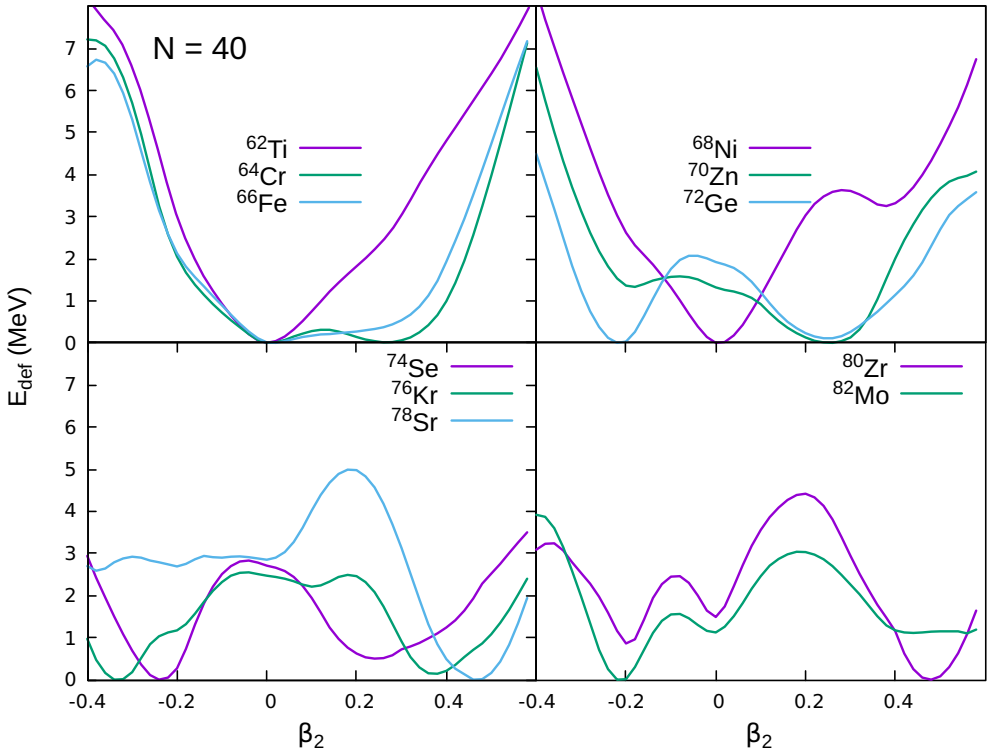

FIGURE 7.9: QMCπ-III predictions for deformation energies plotted against β_2 parameter for $N = 40$ isotonic chain. Plot legends are placed in each of the panel.

primarily spherical but with ^{64}Cr having another minimum at around $\beta_2 \sim 0.3$. From ^{70}Zn to ^{76}Kr, there appear both oblate and prolate minima which increase in deformation as the mass increases. For ^{78}Sr, the oblate minimum disappears giving only a highly prolate shape for the nuclei with $\beta_2 \sim 0.5$. As seen in Figure 7.7, the symmetric ^{80}Zr nuclei is predicted to have three shapes including a spherical one. This behaviour is also seen in the next $N = 40$ isotone, ^{82}Mo, but with the prolate shape less pronounced and the first minimum shifting to the oblate side.

For the Zr chain shown in Figure 7.10, starting on the proton-rich side, QMCπ-III predicts a highly deformed prolate shape for the $N = 38$ isotope. Again, the symmetric ^{80}Zr isotope appears to have tri-shape coexistence but with the first minimum still on the prolate side. From $N = 42$ to $N = 48$, the isotopes have oblate shapes with $\beta_2 \sim$ -0.2. For the ^{90}Zr isotope with closed neutron shell $N = 50$, the deformation energy has a flat minimum but with an almost spherical shape. The oblate minimum then continues from $N = 52$ to $N = 56$ with $\beta_2 \sim$ -0.2 but at the same time, these isotopes develop a second and third minima on

the prolate side. By $N = 58$ and up to $N = 72$, the isotopes are now primarily prolate with $\beta_2 \sim 0.4$. The now secondary oblate shape still exists which gets deeper as N increases.

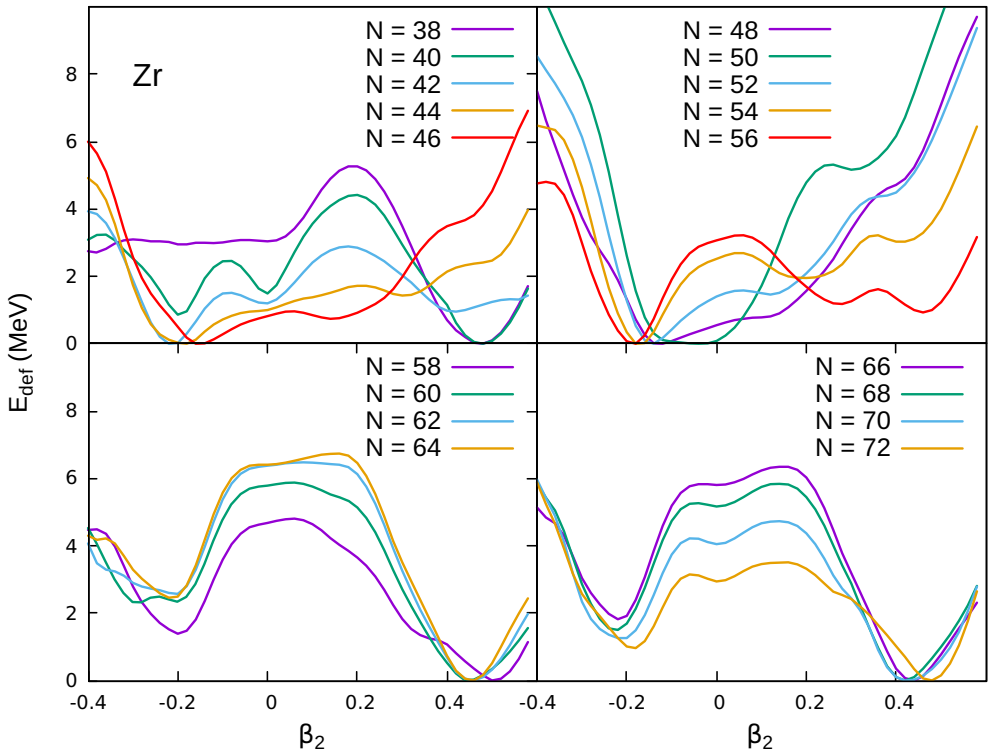

FIGURE 7.10: QMCπ-III predictions for deformation energies plotted against β_2 parameter for the Zr ($Z = 40$) isotopic chain. Plot legends are placed in each of the panel.

Table 7.6 presents the β_2 values for the $Z, N = 40$ chains from QMCπ-III along with available data from experiment which are only available in absolute values, as well as FRDM results.

For Zr isotopes with available data for β_2 , it was seen in Figure 7.6 that deviations are relatively higher on the proton-rich side. As seen from the deformation curves, most Zr isotopes are predicted to exhibit shape coexistence so that for the proton-rich side, there can be two or three possible shapes. From Table 7.6, available data give β_2 = 0.37 and β_2 = 0.25 for $N = 42$ and $N = 44$ isotopes, respectively, to which the primary shapes in QMCπ-III give relatively lower values. The β_2 corresponding to the second minimum, however, is very much comparable to the values from data where QMCπ-III gives $\beta_2 \sim 0.42$ and $\beta_2 \sim 0.30$ for $N = 42$ and $N = 44$, respectively.

The doubly-magic ^{90}Zr isotope is expected to be spherical which is replicated well by QMCπ-III. Data also gives almost spherical shapes up to $N = 56$ but

TABLE 7.6: β_2 values corresponding to the location of the first and second deformed minima for $Z, N = 40$ chains obtained from QMCπ-III. Also added for comparison are experimental data which are only available in absolute values [52], as well as FRDM results [23].

Zr isotopes					$N = 40$ isotones				
N	Expt.	QMCπ-III		FRDM	Z	Expt.	QMCπ-III		FRDM
		1st	2nd				1st	2nd	
38	-	0.48	-	0.42	22	-	0	-	0
40	-	0.48	-0.20	0.43	24	-	0	0.26	0
42	0.37	-0.22	0.42	0.44	26	-	0.02	-	0
44	0.25	-0.18	0.30	-0.24	28	0.1	0	-	0
46	0.15	-0.16	0.14	0.01	30	0.23	0.26	-0.18	0
48	0.19	-0.12	-	-0.01	32	0.24	-0.22	0.24	-0.22
50	0.09	-0.04	-	0	34	0.3	-0.24	0.24	-0.24
52	0.1	-0.14	0.12	0	36	0.41	-0.34	0.38	0.4
54	0.09	-0.18	0.20	-0.16	38	0.44	0.46	-	0.4
56	0.08	-0.18	0.46	0.24	40	-	0.48	-0.20	0.43
58	-	0.5	-0.20	0.34	42	-	-0.22	0.00	0.47
60	0.36	0.44	-0.28	0.36					
62	0.43	0.46	-0.20	0.38					
64	-	0.46	-0.22	0.38					
66	-	0.44	-0.22	0.37					
68	-	0.42	-0.22	0.36					
70	-	0.42	-0.22	0.36					
72	-	0.48	-0.18	0.36					

QMCπ-III predicts slightly oblate shapes for these isotopes. For heavier Zr with available data, shapes are fairly reproduced in QMCπ-III. Further, β_2 values for heavier nuclei without available data, are comparable to FRDM results.

Looking at the data for $N = 40$ isotones, most values are well reproduced by QMCπ-III. Note that from $Z = 32$ to $Z = 36$, where there are coexisting shapes, the second minima in deformation energy correspond better to the experimental β_2 values.

7.5.4 Subshell closures at $N = 32$ and $N = 34$

Some nuclear models suggest the presence of subshell closures in light isotones along the chains of $N = 32$ and $N = 34$ [74, 75, 76, 77]. These closures are then predicted to vanish as Z increases. In experiments using Coulomb excitation, shell closures for elements ^{54}Ti and ^{56}Cr with $N = 32$ were confirmed [63, 64]. The same experiments, however, also found that there are no $N = 34$ shell closures for ^{56}Ti and ^{58}Cr. Furthermore, both deep-inelastic heavy-ion experiments [78] and β decay studies [79] confirm that there is no closure at $N = 34$ for ^{56}Ti. The latter study, however, states that there may still be a closure for ^{54}Ca which was later confirmed via in-beam γ-ray spectroscopy [62]. In this subsection, the presence (or absence) of $N = 32$ and $N = 34$ subshell closures are investigated in the region $14 \leq Z \leq 32$, that is, from elements Si to Ge using QMCπ-III.

To first check the deformations along the $N = 32$ and $N = 34$ isotonic chains, Figure 7.11 shows the deformation curves plotted against β_2 computed from QMCπ-III. Along these chains, coexisting prolate and oblate shapes are seen for

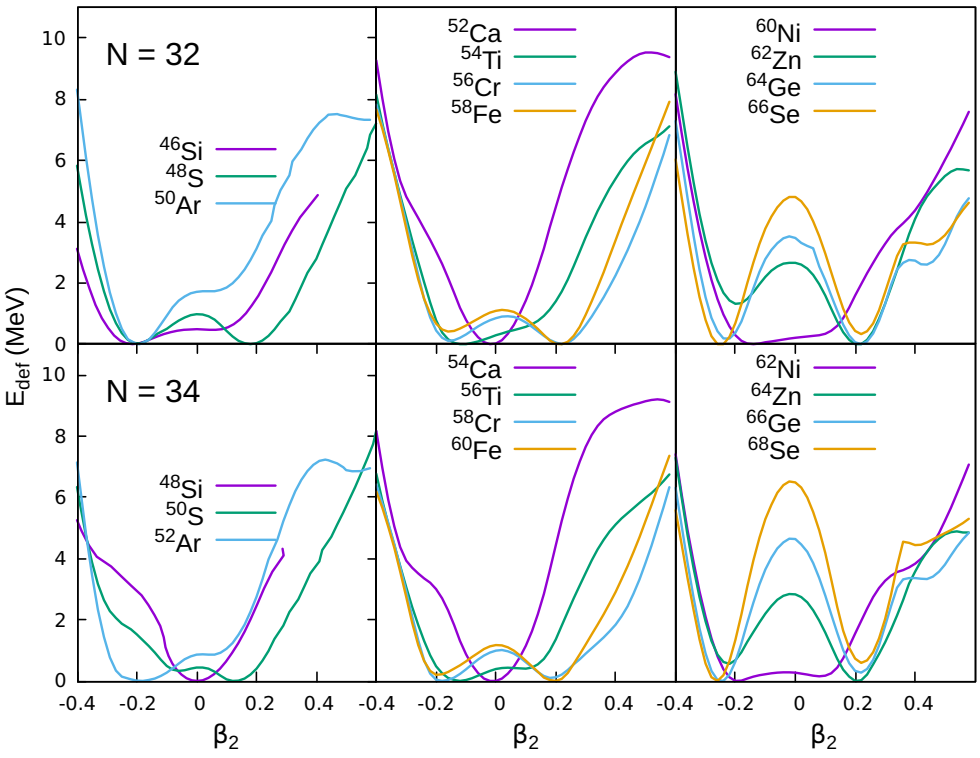

FIGURE 7.11: QMCπ-III predictions for deformation energies plotted against β_2 parameter for $N = 32$ and $N = 34$ isotonic chains. Plot legends are placed in each panel.

most of the nuclei. For $N = 32$ chain, only ^{52}Ca is predicted to have a spherical

shape while for $N = 34$ chain, ^{48}Si and ^{54}Ca both have spherical shapes. This sphericity suggests the presence of the subshell closures for the said isotopes giving them a 'magic' behaviour. The rest of the isotones appear to have both prolate and oblate minima with deformations up to around $|\beta_2| \sim 0.2$. Even the semi-magic nuclei ^{60}Ni and ^{62}Ni with $Z = 28$, are predicted to have oblate to slightly prolate shapes having almost flat minima from $\beta_2 \sim$ -0.2 to $\beta_2 \sim 0.1$.

Available data from experiment also suggest the deformed shapes for some of the $N = 32$ and $N = 34$ isotones. Table 7.7 lists the β_2 values from experiment which are only in absolute values, from QMCπ-III results, as well as from FRDM. Note that for QMCπ-III, coexisting shapes corresponding to the first and second minima in deformations are listed. It is again emphasised that β_2 values from experiment are only given in absolute values.

TABLE 7.7: β_2 values corresponding to the location of the first and second deformed minima for $N = 32$ and $N = 34$ isotones obtained from QMCπ-III. Also added for comparison are experimental data which are only available in absolute values [52], as well as FRDM results [23].

		$N = 32$				$N = 34$			
Element	Z	Expt.	QMCπ-III		FRDM	Expt.	QMCπ-III		FRDM
			1st	2nd			1st	2nd	
Si	14	-	-0.22	0.06	-0.28	-	0.00		-0.37
S	16	-	0.18	-0.19	-0.28	-	0.12	-0.06	-0.29
Ar	18	-	-0.21	0.04	-0.24	-	-0.18	0.04	-0.28
Ca	20	-	-0.02		0	-	-0.02		-0.01
Ti	22	0.18	-0.12	0.16	-0.01	-	-0.12	0.1	0.13
Cr	24	-	0.22	-0.16	0.18	0.24	-0.18	0.18	0.19
Fe	26	0.26	0.22	-0.16	0.17	0.22	0.20	-0.20	0.19
Ni	28	0.21	-0.14	0.14	0	0.2	-0.20	0.08	0.11
Zn	30	0.22	0.22	-0.20	0.2	0.24	0.20	-0.22	0.19
Ge	32	-	0.22	-0.22	0.21	-	-0.24	0.22	0.21

For isotones with available data, most β_2 values are fairly well reproduced by QMCπ-III. Note that from experiment, indeed, the semi-magic isotones ^{60}Ni and ^{62}Ni are not spherical but both exhibit deformations. For isotones without available experimental values, QMCπ-III can be compared with FRDM results. Most β_2 values are comparable from both models except for the light isotones where differences are relatively larger. For ^{48}Si, QMCπ-III predicts a spherical shape while FRDM predicts a highly oblate shape for the nuclei. The existence of this neutron-rich Si isotope is of particular interest in the study of $N = 34$ closure. QMCπ-III predicts that ^{48}Si is the heaviest isotope indicating the dripline along

the Si chain. FRDM, on the other hand, predicts a slightly negative S_{2n} value for ^{48}Si suggesting that it falls just outside the model's predicted dripline.

To investigate the possible closures at $N = 32$ and $N = 34$ in QMCπ-III, the neutron single-particle spectra along these chains plotted against β_2 are shown in Figures 7.12 and 7.13, respectively. The first and second minima corresponding to the values listed in Table 7.7 are shown as blue and red vertical dashed lines, respectively. In addition, spherical shape is indicated by a black dotted vertical line while the Fermi level is shown as a thick black dashed curve. The single-particle levels are labeled on the left side of each panel. Recall in Section 3.2.1 that single-particle states are written in the form of nlj, where n is the principal quantum number, l is the orbital angular momentum quantum number and j is the total angular momentum. The additional fraction inside the square brackets indicate the projection, m, of j to the symmetry axis.

At $N = 32$, the neutron state $2p_{3/2}$ is filled and for a subshell closure to exist, there must be a considerable gap towards the $2p_{1/2}$ state. Starting from ^{46}Si in Figure 7.12 and looking at the gap between the $2p$ states above and below the Fermi level at the location of the minima in deformation, it can be seen that the gap decreases as Z increases up to ^{54}Ti. At ^{56}Cr, the states $2p_{1/2}$ and $1f_{5/2}$ somewhat overlap and at either the first or second minima of deformation, the supposed shell closure disappears. Starting from ^{58}Fe and towards the end of the isotonic chain, $2p_{1/2}$ and $1f_{5/2}$ states are interchanged and the gap for $N = 32$ closure no longer exists.

For $N = 34$ isotones in Figure 7.13, the neutron state $2p_{1/2}$ is filled and for a shell closure to exist, there must be a considerable gap towards the $1f_{5/2}$ state. For ^{48}Si, it can be seen that there is a considerable shell gap, even relatively larger than the gap for $N = 32$ in ^{46}Si. Moreover, this gap appears to be larger than the $N = 28$ major shell gap in ^{48}Si which may suggest an $N = 34$ subshell closure for the neutron-rich Si isotope.

Starting from ^{50}S to ^{56}Ti, the shell gap tends to decrease as Z increases. Just as in $N = 32$, the states $2p_{1/2}$ and $1f_{5/2}$ again somewhat overlaps for ^{58}Cr. Looking at the single-particle levels at the location of the first minimum, the $1f_{5/2}$ comes below the Fermi level which entails that the $N = 34$ shell closure cannot exist. Further for ^{60}Fe and up to ^{66}Ge, states $2p_{1/2}$ and $1f_{5/2}$ are interchanged, suggesting that there will be no $N = 34$ shell closure for these isotopes.

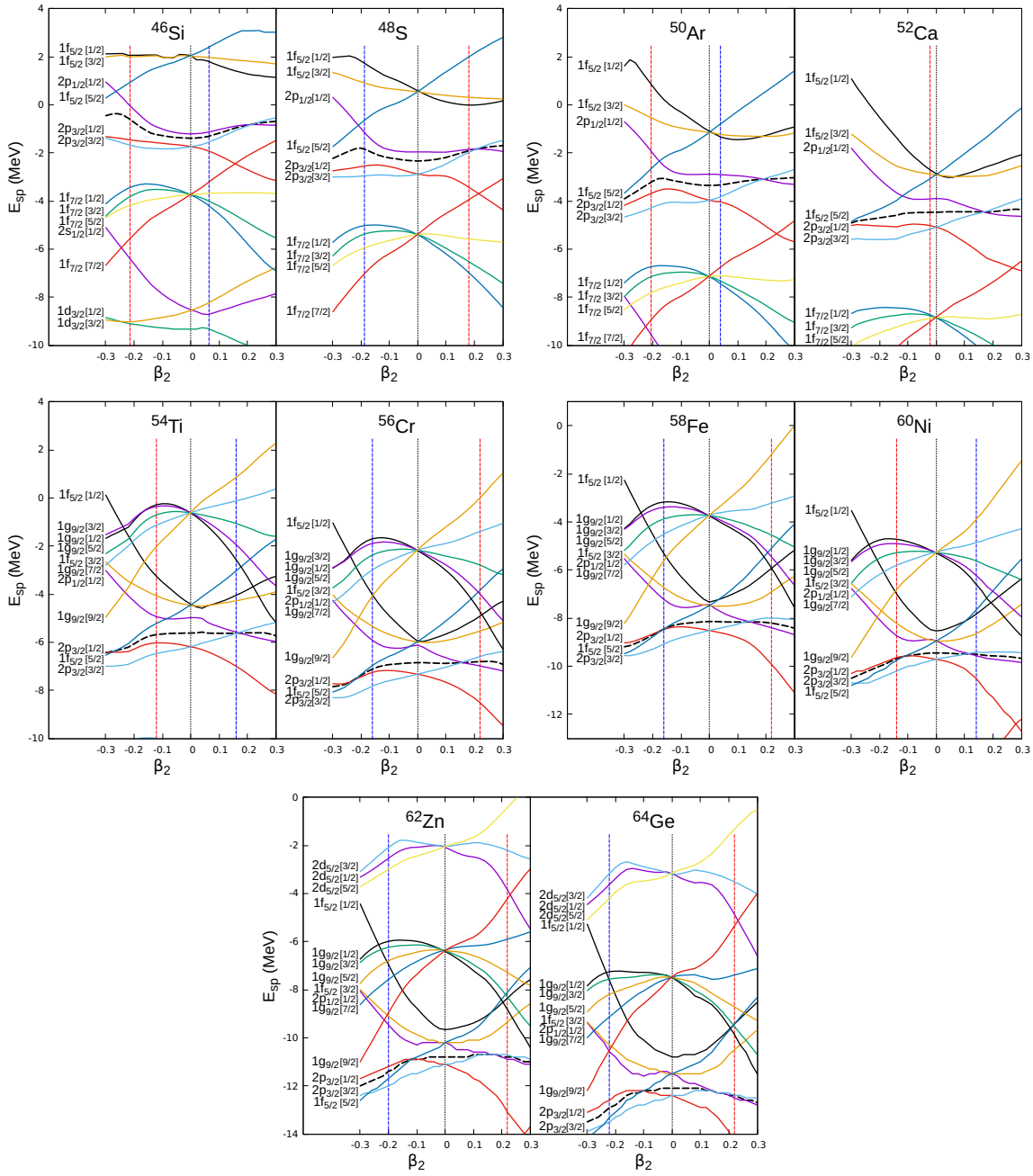

FIGURE 7.12: QMCπ-III predictions for the neutron single-particle spectra of each isotone along the $N = 32$ chain plotted against β_2 . The first and second minima corresponding to the values obtained in Figure 7.11 are shown as blue and red dashed lines, respectively. Sphericity is indicated by a black dotted vertical line while the Fermi level is shown as a thick black dashed curve. The single-particle levels are labeled on the left side of each panel.

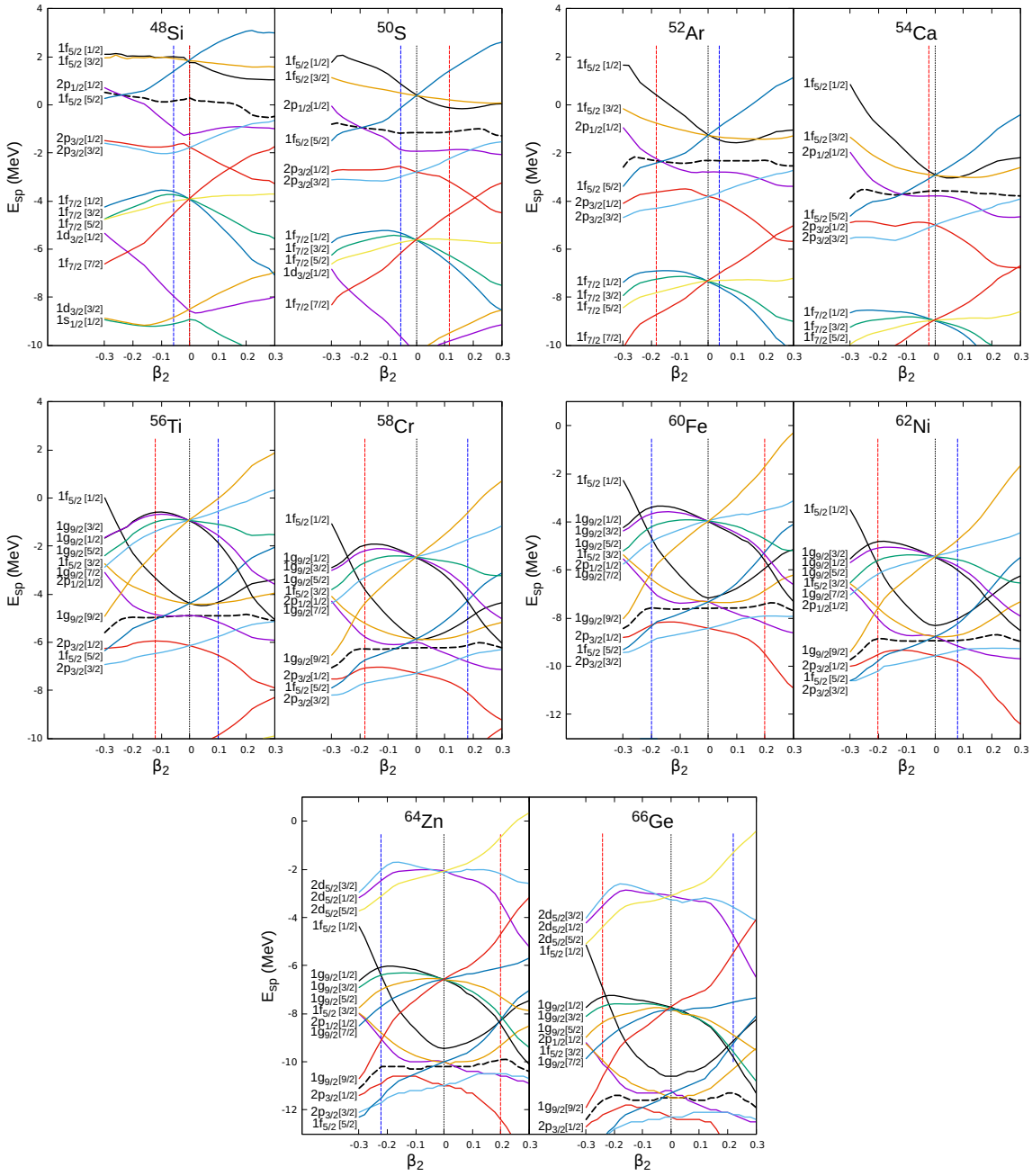

FIGURE 7.13: Same as in Figure 7.12 but for the $N = 34$ isotonic chain.

7.5.5 Se and Gd isotopes

In Figure 7.11, it was seen that heavy isotones of $N = 32$ and $N = 34$ exhibit coexisting shapes. In fact, the Se ($Z = 34$) isotopic chain is known to possess such behaviour and has been investigated in a number of studies [71, 80, 81]. Apart from the Se chain, some isotopes of the Gd ($Z = 64$) chain are also known to display shape coexistence. As seen in Figure 7.6, the region around $Z = 60$ with

$N = 40$ and $N = 60$ possess slightly higher deviations compared to other nuclei in their isotopic chains. In this subsection, deformations for the Se and Gd chains are studied.

Figure 7.14 shows the deformation curves plotted against β_2 values along the Se isotopic chain computed from QMCπ-III. It can be seen that all the the isotopes in the Se chain are predicted to have coexisting oblate and prolate shapes at around $|\beta_2| \sim 0.2$. For the semi-magic ^{84}Se with $N = 50$, the isotope is close

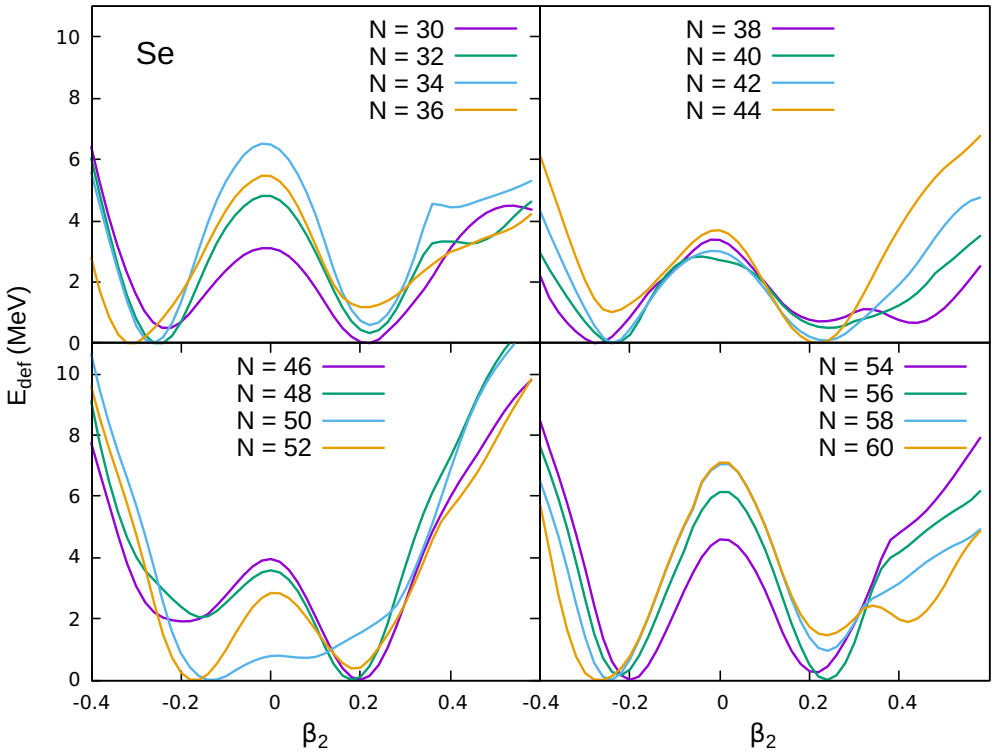

FIGURE 7.14: QMCπ-III predictions for deformation energies plotted against β_2 parameter for Se ($Z = 34$) isotopic chain. Plot legends are placed in each of the panel.

to having a flat minimum passing over a spherical shape . As N increases, however, the prolate minimum redevelops and persists along with the oblate shape throughout the Se chain. In addition, the neutron-rich ^{94}Se ($N = 60$), which is the heaviest known Se isotope, develops a third prolate minimum at around $\beta_2 \sim 0.4$.

Figure 7.15 shows the deformation curves plotted against β_2 values along the Gd isotopic chain obtained from QMCπ-III. From $N = 70$ to $N = 76$, the isotopes have prolate shapes with slowly decreasing β_2 value from around 0.4 down to 0.2. A second minimum at $\beta_2 \sim$ -0.3 also develops which becomes deeper as N increases.

Moving up the Gd chain, the $N = 78$ isotope appears to have both prolate and oblate shapes while for $N = 80$, the minimum shifts to the oblate side with $\beta_2 \sim$ -0.2. Then, the semi-magic ^{146}Gd with $N = 82$ is predicted to be spherical. The next two isotopes $N = 84$ and $N = 86$ continue to have oblate shapes but a prolate minimum also starts to develop.

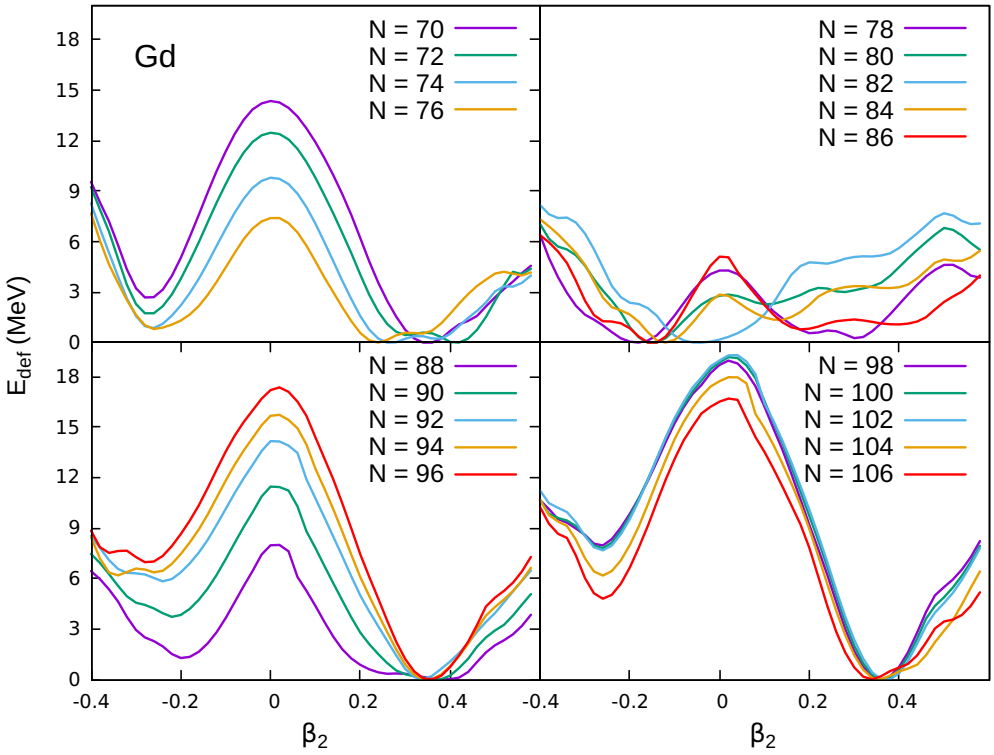

FIGURE 7.15: QMCπ-III predictions for deformation energies plotted against β_2 parameter for Gd ($Z = 64$) isotopic chain. Plot legends are placed in each of the panel.

For the rest of the Gd chain, the prolate minimum overcomes the oblate one giving $\beta_2 \sim 0.4$ for the isotopes. The secondary oblate minimum, however, still exists for these nuclei at around $\beta_2 \sim$ -0.2 which tends to vanish up to $N = 96$ then again starts to redevelop as N further increases.

Table 7.8 presents the β_2 values for Se and Gd chains from QMCπ-III along with available data from experiment and results from FRDM. Comparison with available data, shows that QMCπ-III reproduces the β_2 values fairly well. In addition, most of the β_2 values are comparable with FRDM results including those for isotopes with no available data.

TABLE 7.8: β_2 values corresponding to the location of the first and second deformed minima for Se ($Z = 34$) and Gd ($Z = 64$) isotopes obtained from QMCπ-III. Also added for comparison are experimental data which are only available in absolute values [52], as well as FRDM results [23].

Se isotopes					Gd isotopes				
N	Expt.	QMCπ-III		FRDM	N	Expt.	QMCπ-III		FRDM
		1st	2nd				1st	2nd	
30	-	0.22	-0.22	0.2	70	-	0.36	-0.28	0.32
32	-	-0.26	0.22	0.22	72	-	0.42	0.30	0.3
34	-	-0.26	0.22	0.23	74	-	0.26	0.40	0.25
36	0.31	-0.3	0.22	-0.31	76	-	0.24	0.36	0.22
38	0.22	-0.28	0.44	-0.3	78	-	-0.18	0.30	-0.18
40	0.3	-0.24	0.24	-0.24	80	-	-0.14	-	-0.15
42	0.31	-0.24	0.24	-0.25	82	-	-0.04	-	0
44	0.27	0.22	-0.24	0.17	84	-	-0.12	0.14	0
46	0.23	0.2	-0.20	0.17	86	-	-0.16	0.18	0.17
48	0.19	0.18	-0.16	0.15	88	0.21	0.38	-0.20	0.21
50	-	-0.14	-0.06	0.08	90	0.31	0.36	-0.22	0.24
52	-	-0.16	0.18	0.13	92	0.34	0.34	-0.24	0.26
54	-	-0.2	0.22	0.17	94	0.35	0.34	-0.26	0.28
56	-	0.24	-0.22	0.21	96	0.35	0.36	-0.28	0.28
58	-	-0.24	0.24	0.22	98	-	0.36	-0.26	0.29
60	-	-0.26	0.24	0.34	100	-	0.36	-0.26	0.3
	-				102	-	0.38	-0.26	0.31
	-				104	-	0.36	-0.26	0.3
	-				106	-	0.34	-0.26	0.29

7.6 Neutron-deficient Pb region

Lead isotopes, having a magic proton number, are naturally believed to have spherical shapes. FRDM and SV-min, for instance, both give $\beta_2 \sim 0$ signifying sphericity for the entire Pb chain. Data from experiment have shown, however, that the neutron-deficient Pb region as well as isotopes of Pt and Hg, exhibit shape coexistence giving these isotopes some deformation [82]. In another experiment [83], a triple shape behaviour for the ^{186}Pb isotope was confirmed. In Ref. [84], the neutron-deficient Pb isotopes are found to be primarily spherical albeit having some deformed states. In this section, deformations and shape coexistence are studied in the said region using QMCπ-III. Most importantly, the consequences of such deformations to charge radii and optical shifts are investigated.

Figure 7.16 shows the deformation energies versus β_2 for the Pt, Hg and Pb isotopic chains with $100 \leq N \leq 120$ computed from QMCπ-III. For both Pt and

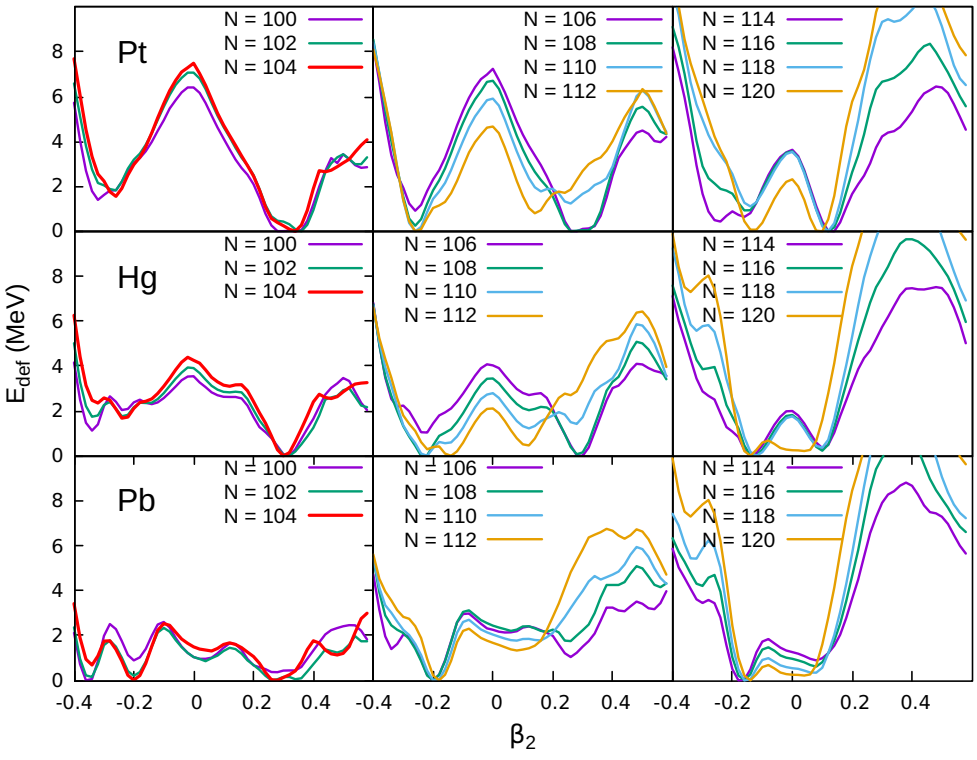

FIGURE 7.16: QMCπ-III predictions for deformation energies plotted against β_2 parameter for neutron-deficient Pt, Hg and Pb isotopic chains. Plot legends are placed in each of the panel.

Hg chains, isotopes with $100 \leq N \leq 104$ have primary prolate shapes with $\beta_2 \sim$ 0.3 but a secondary oblate minimum also develops at $\beta_2 \sim$ -0.3. Starting from

$N = 106$ to $N = 110$, the isotopes are predicted to have almost coexisting shapes on the prolate and oblate sides with $|\beta_2| \sim 0.3$. From $N = 112$ to $N = 120$, the deformations decrease towards sphericity as N increases.

For the Pb chain, isotopes with $100 \leq N \leq 104$ are predicted to have three coexisting shapes: spherical, oblate and prolate. Further, these isotopes possess two oblate and two prolate minima corresponding to low and high deformations. For $N = 106$ and $N = 108$, the prolate minima becomes relatively shallow giving these isotopes primary oblate shapes with $\beta_2 \sim$ -0.2. Starting from $N = 110$, the prolate minima redevelops but at a lower deformation with $\beta_2 \sim 0.1$ while the oblate minimum still persists. Just as in Pt and Hg, as N further increases, the deformations tend to decrease towards spherical shapes up to $N = 120$.

Figure 7.17 shows the deformation parameter from QMCπ-III plotted against N along the Pt, Hg and Pb isotopic chains. The first three minima determined from the deformation curves in Figure 7.16 are shown whenever these minima exist. Also shown are available β_2 values from experiment [52].

Comparing QMCπ-III results to available data, it can be seen that in some cases, it is not the first minimum which coincides with experiment but either the second or third identified minima from the deformation curves. In the Pt chain, the primary prolate shape is consistent with data for most of the isotopes except for $N = 110$ and $N = 112$ where the second minima are closer to experimental value. For the Hg chain, scarce data suggests almost spherical shapes for some of the isotopes. From QMCπ-III, the third minima coincides better with experiment for $100 \leq N \leq 108$ while the second minima gives the spherical shapes for the rest of chain shown in the plot. For the Pb chain, there are no available data for deformation but the isotopes are expected to be mostly spherical since they are semi-magic. From QMCπ-III deformation curves, however, it was already seen that neutron-deficient Pb can have two to three coexisting shapes. Looking at the β_2 values, the spherical shapes correspond to the third minima for $100 \leq N \leq 108$ while the second minima gives $\beta_2 \sim 0$ for $110 \leq N \leq 120$ just as in the Hg chain.

Since most of the nuclei exhibit coexisting shapes, the values for *rms* charge radius will also be affected depending on the deformation. Figures 7.18 to 7.20 show the *rms* charge radius and isotopic shifts from chosen reference nuclei along Pt, Hg and Pb chains, corresponding to the different deformations in Figure 7.17. Available data are included for comparison.

For the Pt chain in Figure 7.18, the predicted R_{ch} from QMCπ-III are slightly overestimated by up to around 0.05 fm. Nevertheless, the 'bump' that forms at

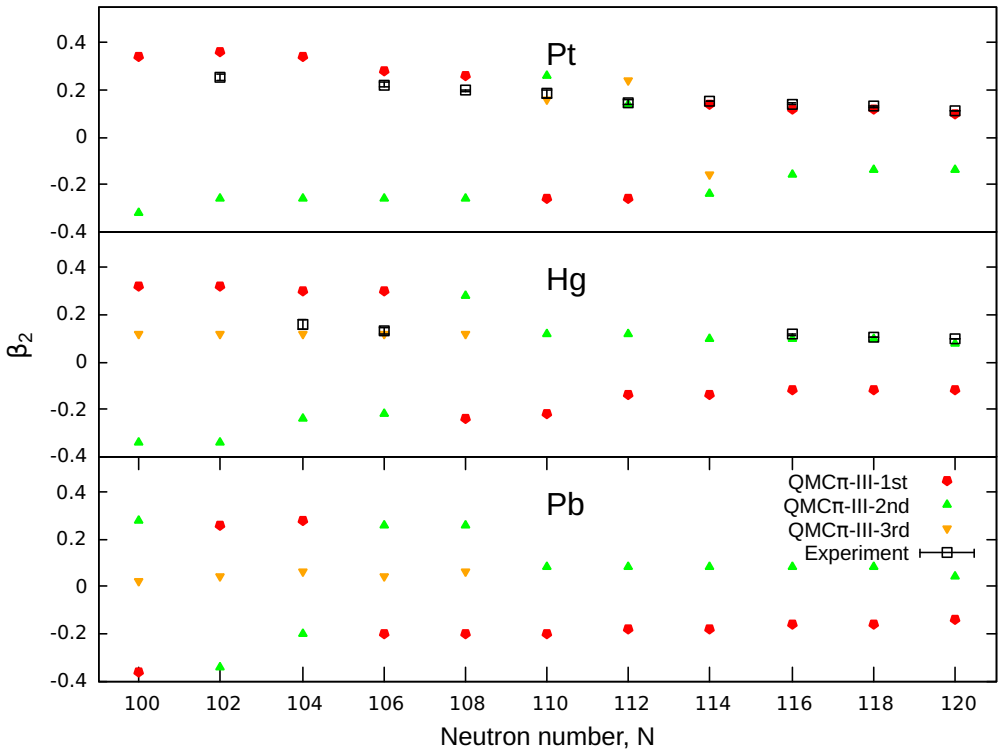

FIGURE 7.17: Deformation parameter β_2 from QMCπ-III plotted against N along the Pt, Hg and Pb isotopic chains. The first three minima determined from the deformation curves in Figure 7.16 are shown whenever these minima exist. Experimental data are taken from Ref. [52] and errors are smaller than the symbols used in the plot. Plot legend is located at the bottom panel.

$100 \leq N \leq 110$ from experiment is somewhat replicated. Further, there appears a steady increase in R_{ch} for $110 \leq N \leq 120$ which is also reproduced from QMCπ-III. Note however, that along the chain, the second or third minimum for deformation can at times give closer values for charge radius to those from data compared to the first minimum.

For the isotopic shift from the reference isotope ^{194}Pt with $N = 116$, it can again be seen that either the first or second minima give closer values to data in the lighter region of the chain. For $N = 110$ and $N = 112$, the first minimum is a bit far off from data and either the second or third minima gives better values for $\delta\langle r^2 \rangle$. For the rest of the chain, the first minima replicate the experimental values fairly well.

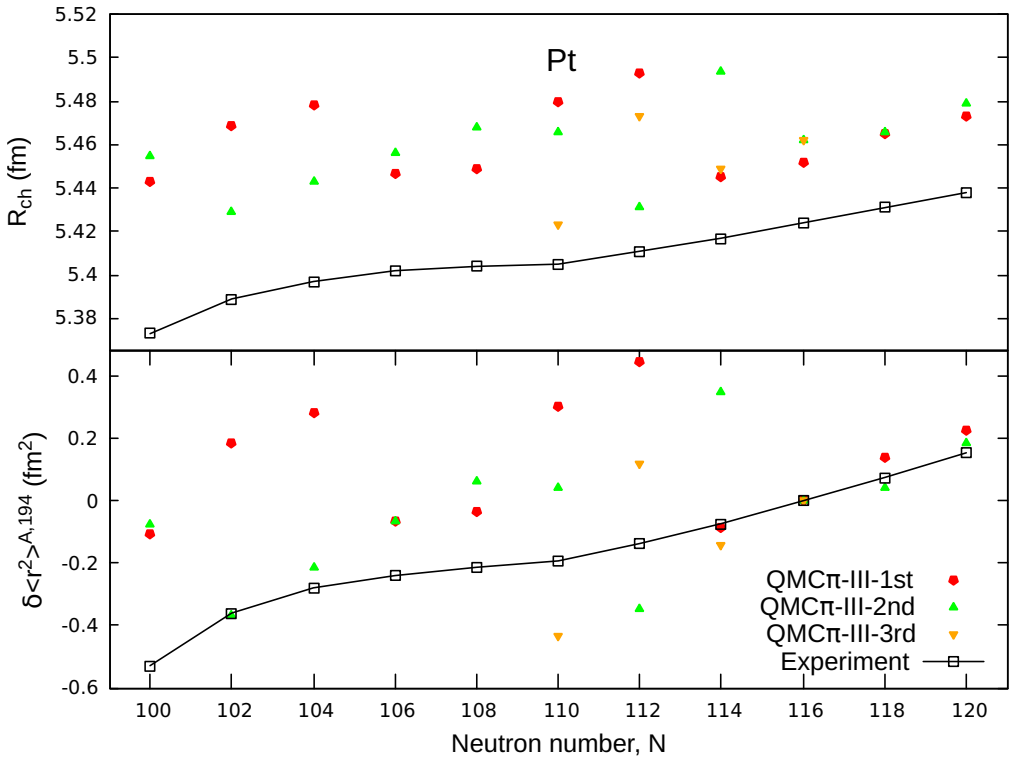

FIGURE 7.18: *rms* charge radius and isotopic shifts from $A = 194$ for Pt isotopic chain, corresponding to the β_2 values shown in Figure 7.17. Experimental data are taken from Ref. [50] and errors are smaller than the symbols used in the plot. Plot legend is located at the bottom panel.

Figure 7.19 shows the charge radii and optical shifts for the Hg chain. The 'bump' at the lighter side of the chain now barely exists, giving an almost steady increase for both R_{ch} and $\delta\langle r^2\rangle$ from experimental data. However, the first minima for deformation from QMCπ-III still predict this 'bump' at $102 \leq N \leq 110$. As seen in Figure 7.17 for the Hg chain, the third minima give the almost spherical shapes suggested by data. Thus, for charge radius, the third minima give closer values to those from experiment for lighter isotopes. For the heavier side of the chain, predictions for R_{ch} have slightly steeper slope compared to the trend from data so that residuals relatively increased. At the bottom panel for isotopic shifts from the reference isotope ^{198}Hg with $N = 118$, QMCπ-III results corresponding to the third minima, again give a steeper slope resulting in slightly higher residuals for light isotopes of Hg. The first and second minima tend to overemphasize the 'bump' on the lighter side thereby giving larger residuals compared to those from the third minima.

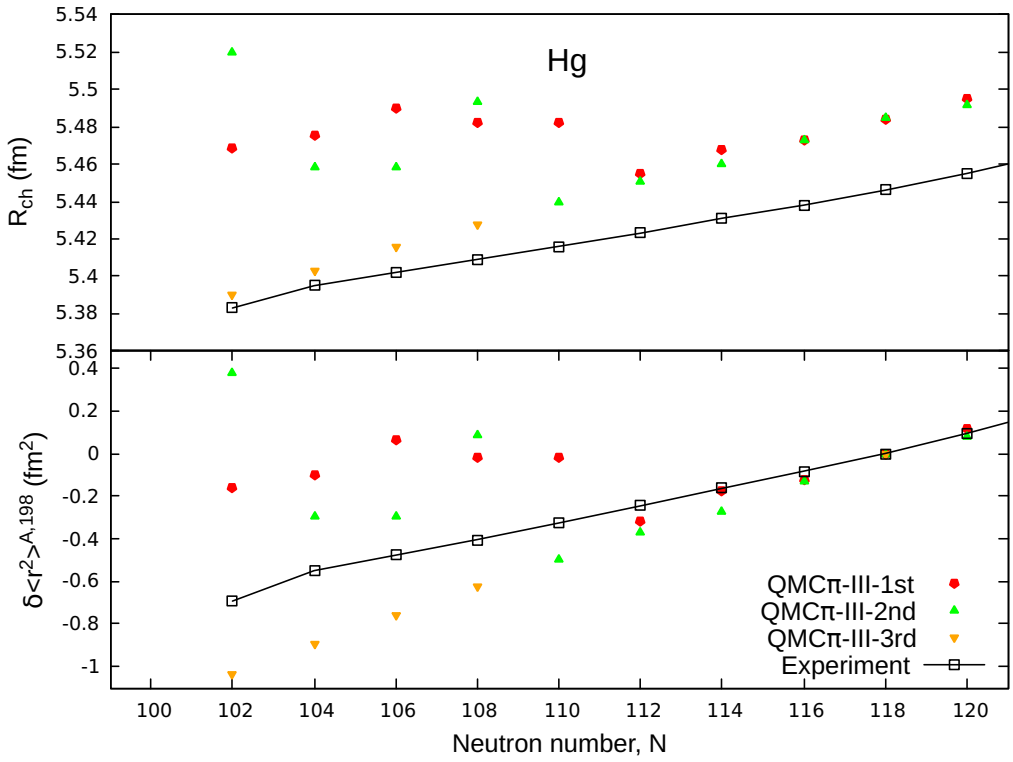

FIGURE 7.19: Same as in Figure 7.18 but for the Hg chain with reference isotope $A = 198$ for the isotopic shift.

For the Pb chain in Figure 7.20, R_{ch} again favors the spherical shapes determined by the third minima of deformation curves for the light isotopes. Then, the second minimum takes over in giving spherical shapes for the heavier isotopes in the plot, thereby resulting in lower residuals compared to the values obtained from taking the deformed shapes. The slope for R_{ch} is again slightly steeper from QMCπ-III compared to experiment, but nevertheless, the model gives small residuals of only up to around 0.03 fm. The resulting isotopic shifts in QMCπ-III from the reference isotope ^{208}Pb, differs slightly from experiment, where data shows a small 'bump' to almost linear trend on the light side of the chain.

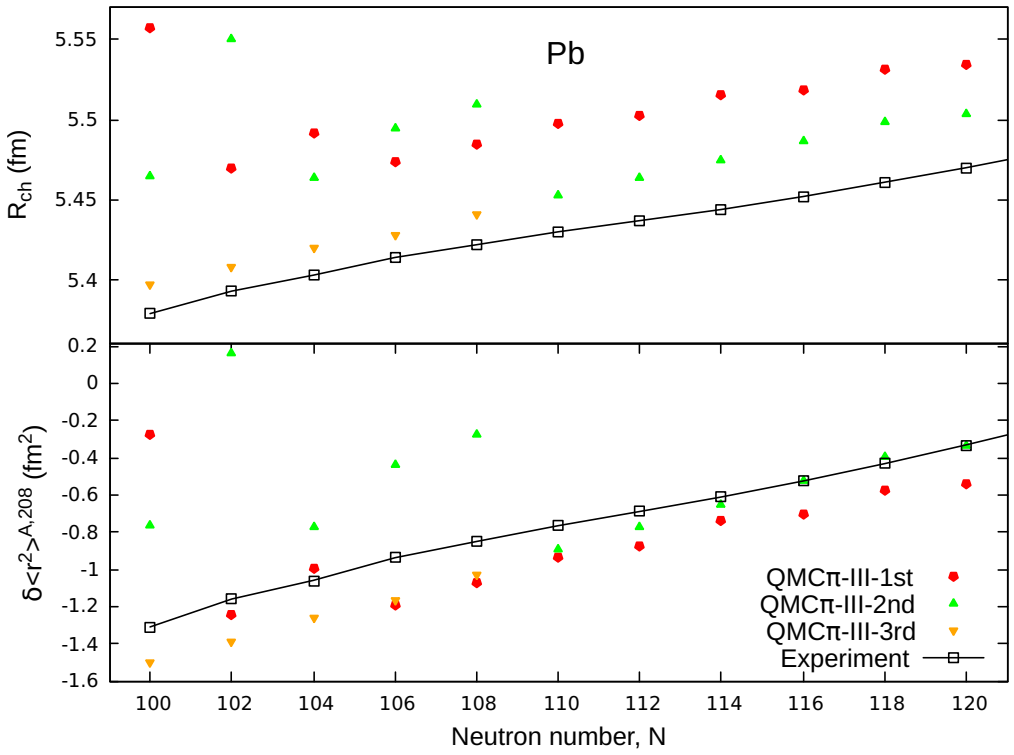

FIGURE 7.20: Same as in Figure 7.18 but for the Pb chain with reference isotope $A = 208$ for the isotopic shift.

As investigated in this chapter, the QMC model showed plausible results for several observables of even-even nuclei across the nuclear chart. Predictions for energies and radii were improved as the model developed and are even better than those of other models, despite having significantly fewer number of model parameters. Nuclear deformations, though not part of the fit, were also fairly well reproduced from the QMC model. Predictions for shape coexistence in several regions of the chart were seen from the model which are also consistent with few available data.

Chapter 8

Summary and conclusion

The quark-meson coupling (QMC) model provides a description of nuclear structure starting from quarks composing a nucleon so that the nuclear interaction is described through their exchange of mesons. In the QMC framework, the intermediate-range attraction is described through the σ meson while the short-range repulsion comes from the ω and the ρ mesons. Apart from the central part derived from QMC, full spin-orbit interaction and spin-tensor effects naturally arise in the model so that their contributions do not add new parameters to the model. In addition, long-range single-pion exchange is incorporated by employing a low density approximation. To fully describe the structure and properties of finite nuclei, the mean-field contribution coming from the QMC model is augmented by pairing interaction, Coulomb effects and center-of-mass correction. In the latest version of the model, QMCπ-III, the pairing contribution was further derived from the model itself, so that the additional pairing parameters were expressed in terms of the existing QMC parameters. QMCπ-III then contains a total of only five parameters to describe properties of both nuclear matter and finite nuclei.

Even with the significantly reduced number of parameters compared to other nuclear models, QMC has proven to be very successful in describing several nuclear properties. The improvements done in the latest model produced nuclear matter properties which are well within the acceptable ranges. Both the slope of symmetry energy and nuclear incompressibility values are improved compared to the earlier versions, thus giving values that are compatible with experimental data. Meanwhile, other saturation properties of infinite nuclear matter such as the saturation density, binding energy per nucleon and symmetry energy, are well-reproduced as before.

The success of the QMC model is even more seen in its description for the structure and properties of finite nuclei which is the focus of this research. To

obtain the best fit parameters of the model, a derivative-free optimisation algorithm, known as POUNDeRS, was employed. A set of doubly- and semi-magic nuclei with available binding energies and charge radii, were chosen to be included in the fitting procedure. These nuclear observables enter as data points in the optimisation, and the chi-squared value was minimised to find the best fit parameters. With the final set of QMC parameters, several properties of finite nuclei were then calculated and compared with available data, as well as with results from other nuclear models.

In the study of finite nuclei for this research, the QMC model was first used to calculate nuclear observables along magic chains of nuclei which were included in the fitting procedure. Binding energies and *rms* charge radii were calculated and shown to have improved values as the model developed. Aside from the fit observables, several other properties were computed along the magic chains and compared to available data. Charge density distributions for some chosen doubly-magic nuclei were shown to be compatible with data from electron scattering experiments. While the diffraction radius and surface thickness observables were not included in the optimisation of the later versions of the QMC model, it was shown that their inclusion did not alter the overall fit that much. The predictions for these two radius parameters remained almost the same even when they were included as data points in the fit.

Other observables related to the size of finite nuclei, namely the optical shift and skin thickness, were also calculated and shown to be comparable to data. Energy observables which reveal the shell structure of finite nuclei were also investigated. By computing two-neutron separation energies and shell gaps, it was shown that the QMC model was able to replicate the shell closures really well. Furthermore, single-particle energies and spin-orbit splittings of doubly-magic nuclei were fairly well reproduced within the model, even if these observables were not part of the fit. Finally for magic chains of isotopes and isotones, predictions for the proton and neutron driplines were computed from QMC to determine their bounds in the nuclear chart.

Going up the chart, the QMC model was tested in its predictions for the superheavy region. It was seen, even in its early versions, that the model was already able to give outstanding results for superheavy elements (SHE), even better compared to other existing nuclear models. With the latest developments in QMC, it was shown that nuclear properties were better resolved compared to the results from previous versions. Binding energies were much improved in QMCπ-III, giving an *rms* deviation of only 0.03% where results from previous versions were

three to four times more. This binding energy deviation was also much better compared to those of other models which yielded up to more than ten times the % deviation found using QMC. Another significant improvement from calculations using the latest model, were the predictions for subshell closures which were not seen in the previous versions. The subshell closures at neutron number $N = 152$ and $N = 162$ were very well replicated by computing the two-neutron separation energies and shell gaps in the superheavy region. These subshell closures were also revealed by computing the Q_α energies, where plots show dips in Q_α values at these closures. From Q_α energies of SHE, the half-lives against α decay were also computed using the Viola-Seaborg relationship and were shown to be of a quality comparable to the results found in other existing models. In addition, proton and neutron driplines in the superheavy region were also identified from two-particle separation energies using QMCπ-III. Nuclear shapes of SHE were investigated in detail from the deformation energy plots against the quadrupole deformation parameter, β_2. These plots reveal shape coexistence in some SHE where, in their ground-states, they can have simultaneous oblate, prolate and spherical shapes. Since there are no data for quadrupole deformations in the superheavy region, QMC predictions were instead compared with those of existing nuclear models. QMC results for β_2 were shown to be very comparable with those of its counterparts along the isotopic chains of SHE.

With the success of the QMC model in predictions along magic chains and in the superheavy region, calculations were extended to all even-even nuclei across the present nuclear chart. Note that most of these nuclei were not included in the fit, as only chosen magic nuclei were included in the parameter optimisation. Surprisingly, QMC results showed spectacular results for all even-even nuclei. Binding energies and charge radii were reproduced well and results were much improved in the QMCπ-III version, yielding *rms* deviations from experiment of only 0.29% and 0.50%, respectively. These results are even better compared to the predictions of most of the other models. The major shell closures are replicated throughout the chart as seen from computing the two-particle separation energies and shell gaps. Q_α energies and half-lives against α decay are also fairly well reproduced with residuals that are comparable with results found in other models. Interestingly, nuclear deformation which was not part of the fitting procedure was also predicted well from QMC. Results for quadrupole deformation are at par with those of the FRDM model, which has always been referenced in literature for energies and deformations. QMCπ-III and FRDM both gave an *rms* deviation of around 30% when compared to available data for β_2 values.

Related to deformations, shape coexistence was also investigated in several regions in the nuclear chart. It was shown that symmetric nuclei, some $N = 28$ isotones, the $Z, N = 40$ chains, and the Se and Gd isotopic chains, exhibit coexisting shapes in their ground states. The β_2 values obtained from QMC agree well with experimental data as well as with FRDM results. In addition, the possible shell closures for $N = 32$ and $N = 34$ isotones were also investigated where ground-state shape coexistence also exists. QMC results coincide well with present data where these two closures are seen for ^{52,54}Ca as well as up to ^{56}Cr for the $N = 32$ closure, but are no longer present starting from ^{56} Ti for the $N = 34$ closure. Further from QMCπ-III, these two closures disappear for isotones heavier than Cr.

The neutron-deficient Pb region was also studied in terms of deformations and sizes as experiments has shown that some of the light isotopes in this region exhibit shape coexistence. This was indeed seen from QMCπ-III predictions, yielding triple shapes particularly around ^{186}Pb. Due to the differing ground-state shapes, nuclear sizes in this region are also affected. It was seen that for some isotopes in this region, instead of the first minima of the deformation plots computed from QMC, the second or third minima can coincide better with experimental data.

Overall, the QMC model has been shown to be very successful in describing both nuclear matter and finite nuclear systems. It is stressed that with just five parameters in the present model, the physics of nuclear structure is well described and a number of nuclear properties are reproduced. In the future, more calculations will be performed in order to study nuclear properties in other regions of the nuclear chart. The structure of odd-mass nuclei, which was not included in this writeup, will be investigated using the QMC model. The versatility of the model may also be explored to study several other nuclear observables as well as their correlations throughout the nuclear landscape.

Appendix A

Paper publication

The developments done in the QMC model as well as in its optimisation, led to two research papers reporting significant improvements in both the model and its predictions. Summaries of these papers are outlined here accompanied by the statements of authorship.

A.1 QMCπ-II paper

K. L. Martinez, A. W. Thomas, J. R. Stone, and P. A. M. Guichon. "Parameter optimization for the latest quark-meson coupling energy-density functional". In: *Phys. Rev.* C 100 (2019), p. 024333. DOI : 10.1103/PhysRevC.100.024333. https://link.aps.org/doi/10.1103/PhysRevC.100.024333.

In this paper, the QMCπ-II version of the model, containing higher-order density dependences and both time and space components of the spin-orbit contribution, was presented. The fitting procedure through a derivative-free optimisation algorithm was also discussed along with the parameter constraints determined by nuclear matter properties and the data sets that were included in the fit to finite nuclei. After the optimisation, the final QMCπ-II parameters were used to calculate several observables of finite nuclei.

QMCπ-II results were found to be consistent to those of QMCπ-I [53] for nuclear observables included in the fit, namely, the binding energies, charge radii and pairing gaps. Compared to QMC-I [8], predictions were also improved except for binding energies where there was a slight increase in deviations. It was emphasized, however, that the slope of symmetry energy and nuclear incompressibility were significantly improved in QMCπ-II compared to the values obtained from the previous versions.

Calculations for binding energies and charge radii were also extended to all even-even nuclei across the nuclear chart. QMCπ-II yielded results which were comparable to those with other nuclear models, despite having significantly fewer number of model parameters.

Other nuclear observables, not included in the fit, were also computed. Predictions for two-nucleon separation energies reproduced the shell closures fairly well and were comparable with results from other models. Isotopic shifts in charge radii and neutron skin thickness were also calculated, where again, QMCπ-II yielded results consistent with data. In addition, the single-particle states of some chosen doubly-magic nuclei were shown to agree reasonably well with experiment. Nuclear deformations were not included in the fitting procedure, yet, QMCπ-II obtained good predictions particularly for the Gd isotopic chain. Furthermore, giant monopole resonances (GMR) of some isotopes were computed and checked against data. QMCπ-II showed satisfactory agreement with GMR data, thus confirming the low incompressibility value obtained in this version of the model. Lastly, QMCπ-II results for binding energy deviations for the superheavy region were seen to be consistent and, in some nuclei even better, compared to those of other models.

Statement of Authorship

Title of Paper	Parameter optimization for the latest quark-meson coupling energy-density functional
Publication Status	[X] Published [ ] Accepted for Publication [ ] Submitted for Publication [ ] Unpublished and Unsubmitted w ork w ritten in manuscript style
Publication Details	K. L. Martinez, A. W. Thomas, J. R. Stone, and P. A. M. Guichon Phys. Rev. C 100, 024333 – Published 27 August 2019

Principal Author

Name of Principal Author (Candidate)	Kay Marie L. Martinez
Contribution to the Paper	1) Initially drafted the paper from introduction to conclusions. 2) Performed the optimisation procedure of the QMCπ-II model to determine the final set of parameters, as laid out in the methods part of the paper. 3) Applied the model to compute several nuclear observables which are presented in the results section, except for GMR calculation, as well as provided analyses and discussions of results. 4) Wrote the concluding remarks.
Overall percentage (%)	
Certification:	This paper reports on original research I conducted during the period of my Higher Degree by Research candidature and is not subject to any obligations or contractual agreements with a third party that would constrain its inclusion in this thesis. I am the primary author of this paper.
Signature	Date: July 2, 2020

Co-Author Contributions

By signing the Statement of Authorship, each author certifies that:

i. the candidate's stated contribution to the publication is accurate (as detailed above);

ii. permission is granted for the candidate in include the publication in the thesis; and

iii. the sum of all co-author contributions is equal to 100% less the candidate's stated contribution.

Name of Co-Author	Anthony W. Thomas
Contribution to the Paper	Provided overall supervision from research and calculations to writing Contributed to writing and editing of the paper
Signature	Date: 3/7/2020

Name of Co-Author	Jirina R. Stone		
Contribution to the Paper	My contribution to the work was solely on the level of discussion and guidance appropriate for a PhD student. Kay Martinez conducted all the calculations, contributed significantly to development of the original models, selected topics of their interpretation and provided discussion of the results. I provided a software for the GMR calculations		
Signature		Date	July 4, 2020

Name of Co-Author	Pierre Guichon		
Contribution to the Paper	I have provided theoretical guidance in the development of the calculation performed by Kay Martinez		
Signature		Date	July 4, 2020

A.2 QMCπ-III paper

K. L. Martinez, A. W. Thomas, P. A. M. Guichon, and J. R. Stone. "Tensor and pairing interactions within the quark-meson coupling energy-density functional". In: *Phys. Rev.* C 102 (3 2020), p. 034304. DOI : 10.1103/PhysRevC. 102.034304. https://link.aps.org/doi/10.1103/PhysRevC.102.034304.

In this paper, the QMCπ-III version of the model containing the additional spin-tensor contributions and a QMC-derived pairing interaction, was presented. Just as in QMCπ-II, this version also includes higher-order density dependence in the σ Hamiltonian part, but was taken in its full expansion instead of using Padé approximation. This latest version also maintains both time and space components of the spin-orbit interaction.

For the model optimisation, the same algorithm was used as in QMCπ-II and the fit was done with the same set of nuclei. However, for the observables, QMCπ-III was only fitted to binding energies and charge radii, and was no longer fitted to pairing gaps. The extra pairing strength parameters were fully expressed in terms of the existing QMC parameters in this current version, which were chosen to be fitted to energies and charge radii only.

The inclusion of the spin-tensor terms in the model did not alter the final QMCπ-III parameters that much when compared to the QMCπ-II parameter set. However, its addition improved the predictions for binding energies for all even-even nuclei across the nuclear chart. These improvements were studied along semi-magic chains of Ca, Sn, Ni and Pb, where indeed, the spin-tensor contribution generally resulted to lower binding energy deviations. Meanwhile, QMCπ-III results for charge radii were seen to be almost the same as in the previous QMC versions.

The effect of spin-tensor was further investigated in single-particle (*sp*) energies and nuclear deformations. It was seen that its inclusion had a little effect on the levels of *sp* spectra of some chosen doubly-magic nuclei. It was emphasised that there were no new parameters for spin-tensor component and that the fit did not include *sp* data. For deformations, however, the spin-tensor effects were seen to alter the minimum of deformation energies for the Zr chain, by creating flatter or deeper minimum. Quadrupole deformation parameter, β_2, remained almost the same, with or without tensor along the Zr chain, and were seen to be fairly compatible with few available data.

The QMCπ-III version was subjected to both volume and surface pairing, through a constant δ force and a density-dependent δ interaction, respectively. For volume pairing, additional pairing strength parameters were fitted, while for surface pairing, the parameters were expressed in terms of the QMC parameters derived from the model itself. It was seen that the two pairing functionals yielded similar results for binding energies and charge radii. The highlight, however, was in the predictions for shell closures where the QMC-derived pairing interaction was seen to reproduce the peaks in shell gaps expected from experimental data. Particularly in the superheavy region, the previous QMC versions fail to predict the presence of some subshell closures. These closures were correctly predicted in QMCπ-III with the density-dependent pairing force.

Statement of Authorship

Title of Paper	Tensor and pairing interactions within the quark-meson coupling energy-density functional
Publication Status	[X] Published [ ] Accepted for Publication [ ] Submitted for Publication [ ] Unpublished and Unsubmitted w ork w ritten in manuscript style
Publication Details	K. L. Martinez, A. W. Thomas, P. A. M. Guichon, and J. R. Stone Phys. Rev. C 102, 034304 – Published 3 September 2020

Principal Author

Name of Principal Author (Candidate)	Kay Marie L. Martinez
Contribution to the Paper	1) Initially drafted the paper from introduction to conclusions. 2) Performed the optimisation procedure of the QMCπ-III model to determine the final set of parameters, as laid out in the methods part of the paper. 3) Applied the model to compute several nuclear observables which are presented in the results section, as well as provided analyses and discussions of results. 4) Wrote the concluding remarks.
Overall percentage (%)	
Certification:	This paper reports on original research I conducted during the period of my Higher Degree by Research candidature and is not subject to any obligations or contractual agreements with a third party that would constrain its inclusion in this thesis. I am the primary author of this paper.
Signature	Date: July 2, 2020

Co-Author Contributions

By signing the Statement of Authorship, each author certifies that:

i. the candidate's stated contribution to the publication is accurate (as detailed above);

ii. permission is granted for the candidate in include the publication in the thesis; and

iii. the sum of all co-author contributions is equal to 100% less the candidate's stated contribution.

Name of Co-Author	Anthony W. Thomas
Contribution to the Paper	Provided overall supervision from research and calculations to writing Contributed to writing and editing of the paper
Signature	Date: 3/7/2020

Name of Co-Author	Pierre Guichon		
Contribution to the Paper	I have provided theoretical guidance in the development of the calculation performed by Kay Martinez		
Signature		Date	July 4, 2020

Name of Co-Author	Jirina R. Stone		
Contribution to the Paper	My contribution to the work was solely on the level of discussion and guidance appropriate for a PhD student. Kay Martinez conducted all the calculations, contributed significantly to development of the original models, selected topics of their interpretation and provided discussion of the results.		
Signature		Date	July 4, 2020

Appendix B

Maths and derivations

B.1 Fermi traces

In the QMC model, calculation of the energy density functional involves the product of one body operators

$$H(\vec{r}) = \int d\vec{r} : AB \dots Z : \tag{B.1}$$

where the operators are in the form $A = \sum_{i,j} A_{ij} a_i^\dagger a_j$. The expectation value of the product of these operators, $\langle F| : AB \dots Z : |F\rangle$, with $|F\rangle = a_{i_1}^\dagger a_{i_2}^\dagger \dots |0\rangle$ and :: denoting normal ordering with respect to $|0\rangle$, can be expressed in terms of Fermi traces, $\tilde{\mathrm{Tr}}$, defined as

$$\tilde{\mathrm{Tr}}\left[AB \dots Z\right] = \sum_{i,j,k \dots m \in F} A_{ij} B_{jk} \dots Z_{mi} \,. \tag{B.2}$$

For instance, for a two-body operator,

$$\langle F| : AB : |F\rangle = \tilde{\mathrm{Tr}}\left[A\right] \tilde{\mathrm{Tr}}\left[B\right] - \tilde{\mathrm{Tr}}\left[AB\right] \,. \tag{B.3}$$

In this section, the necessary Fermi traces and expectation values for the calculation of the energy contributions to the total QMC Hamiltonian, are listed. The derivations of the expressions for Fermi traces can be found in Appendix C of Ref. [85].

$$\langle D \rangle = \rho$$

$$\langle \xi \rangle = \tau - \frac{1}{2} \nabla^2 \rho$$

$$\tilde{\mathrm{Tr}}\left[D^2\right] = \frac{1}{2}\sum_m \rho_m^2$$

$$\tilde{\mathrm{Tr}}\left[D\xi\right] = -\frac{1}{4}\sum_m \left(\rho_m \nabla^2 \rho_m - 2\rho_m \tau_m\right)$$

$$\tilde{\mathrm{Tr}}\left[D\vec{\nabla}D\right] = \frac{1}{2}\sum_m \rho_m \vec{\nabla}\rho_m$$

$$\tilde{\mathrm{Tr}}\left[D\nabla^2 D\right] = \frac{1}{2}\sum_m \left[\rho_m \nabla^2 \rho_m - 2\rho_m \tau_m + \frac{1}{2}\left(\vec{\nabla}\rho_m\right)^2 + J_m^2\right]$$

$$\langle D^2 \rangle = \rho^2 - \frac{1}{2}\sum_m \rho_m^2$$

$$\langle D\nabla^2 D\rangle = \rho\nabla^2\rho - \sum_m \left[\frac{1}{4}\rho_m \nabla^2 \rho_m - \rho_m \tau_m + \frac{1}{2}J_m^2\right]$$

$$\langle D^\alpha \cdot D^\alpha \rangle = \sum_{mm'}\left(mm' - \frac{1}{2}\vec{I}_{mm'}\cdot\vec{I}_{m'm}\right)\rho_m\rho_{m'} = \frac{1}{8}\sum_m \rho_m^2 - \frac{1}{2}\sum_{m\neq m'}\rho_m\rho_{m'}$$

$$\langle D^\alpha \nabla^2 D^\alpha\rangle = \sum_{mm'}\left[mm'\rho_m\nabla^2\rho_{m'} - \vec{I}_{mm'}\cdot\vec{I}_{m'm}\left(\frac{1}{4}\rho_m\nabla^2\rho_{m'} - \rho_m\tau_{m'} + \frac{1}{2}\vec{J}_m\cdot\vec{J}_{m'}\right)\right]$$

$$\tilde{\mathrm{Tr}}\left[\vec{\mathcal{J}}\right] = \vec{J}$$

$$\tilde{\mathrm{Tr}}\left[\vec{\nabla}D\right] = \vec{\nabla}\rho$$

$$\tilde{\mathrm{Tr}}\left[\vec{\mathcal{J}}\cdot\vec{\nabla}D\right] = \frac{1}{2}\sum_m \rho_m\vec{\nabla}\cdot\vec{J}_m + \frac{1}{4}\sum_m \vec{J}_m^2$$

$$\tilde{\mathrm{Tr}}\left[\vec{\mathcal{J}}_a\right] = \sum_m m\vec{J}$$

$$\tilde{\mathrm{Tr}}\left[\vec{\nabla}D_a\right] = \sum m\vec{\nabla}\rho_m$$

$$\sum_a \tilde{\mathrm{Tr}}\left[\vec{\mathcal{J}}_a\cdot\vec{\nabla}D_a\right] = \sum_{m,m'} S_{mm'}\left[\frac{1}{2}\rho_m\vec{\nabla}\cdot\vec{J}_{m'} + \frac{1}{4}\vec{J}_m\cdot\vec{J}_{m'}\right]$$

where $S_{mm'} = \delta_{mm'} m^2 + \frac{1}{2}\left(\delta_{m,m'+1} + \delta_{m',m+1}\right)$.

B.2 The fluctuation part of H_σ

Using the expression for $\langle H_\sigma^f \rangle$ in Eq. (2.15) and replacing the quantity $\frac{\partial K}{\partial \sigma}(\bar{\sigma})$ using Eq. (2.18), gives

$$\begin{aligned}\langle H_\sigma^f \rangle &= \frac{1}{2m_\sigma^2}\left[-\langle\left(D - \frac{\xi}{2M^{\star 2}}\right)^2\rangle \left(\frac{\partial M^\star}{\partial \bar{\sigma}}\right)^2 + \langle\left(D - \frac{\xi}{2M^{\star 2}}\right)\rangle^2 \left(\frac{\partial M^\star}{\partial \bar{\sigma}}\right)^2\right] \\ &\quad + \frac{1}{2m_\sigma^4}\left(\frac{\partial M^\star}{\partial \bar{\sigma}}\right)\langle\left(D - \frac{\xi}{2M^{\star 2}}\right)\nabla^2\left(\frac{\partial M^\star}{\partial \bar{\sigma}}\right)\left(-D + \frac{\xi}{2M^{\star 2}} + \langle D - \frac{\xi}{2M^{\star 2}}\rangle\right)\rangle\,.\end{aligned}$$

To simplify the expression for the fluctuation part, let

$$p = \frac{1}{m_\sigma^2}\frac{\partial M^\star}{\partial \bar{\sigma}} = -\frac{\sqrt{G_\sigma}}{m_\sigma}\left[1 - d v_0(\rho)\right], \qquad p' = \frac{\sqrt{G_\sigma}}{m_\sigma} d v_0'(\rho)\,.$$

Then,

$$\begin{aligned}\langle H_\sigma^f \rangle &= \frac{m_\sigma^2}{2}p^2\left[\left(-\langle D^2\rangle + \langle D\rangle^2 + \frac{\langle D\xi\rangle}{M^{\star 2}} - \frac{\langle D\rangle\langle\xi\rangle}{M^{\star 2}}\right)\right] \\ &\quad + \frac{p}{2}\left[\left(\nabla^2 p\right)\left(-\langle D^2\rangle + \langle D\rangle^2\right)\right] \\ &\quad + \frac{p}{2}\left[2\vec{\nabla}p\cdot\left(-\langle D\vec{\nabla}D\rangle + \langle D\rangle\vec{\nabla}\langle D\rangle\right)\right] \\ &\quad + \frac{p}{2}\left[p\left(-\langle D\nabla^2 D\rangle + \langle D\rangle\nabla^2\langle D\rangle\right)\right] \\ &= \frac{m_\sigma^2}{2}p^2\left(\tilde{\mathrm{Tr}}\left[D^2\right] - \frac{\tilde{\mathrm{Tr}}\left[D\xi\right]}{M^{\star 2}}\right) + \frac{p}{2}\left[\left(\nabla^2 p\right)\tilde{\mathrm{Tr}}\left[D^2\right]\right] \\ &\quad + p\vec{\nabla}p\cdot\tilde{\mathrm{Tr}}\left[D\vec{\nabla}D\right] + \frac{p^2}{2}\tilde{\mathrm{Tr}}\left[D\nabla^2 D\right]\,.\end{aligned}$$

Using the identities for Fermi traces in Appendix B.1,

$$\begin{aligned}\langle H_\sigma^f \rangle &= \frac{m_\sigma^2}{2}p^2\left(\frac{1}{2}\sum_m \rho_m^2 + \frac{1}{4M^{\star 2}}\sum_m\left(\rho_m\nabla^2\rho_m - 2\rho_m\tau_m\right)\right) \\ &\quad + \frac{p}{2}\left[\left(\nabla^2 p\right)\frac{1}{2}\sum_m\rho_m^2\right] + p\vec{\nabla}p\cdot\frac{1}{2}\sum_m\rho_m\vec{\nabla}\rho_m \\ &\quad + \frac{p^2}{2}\left[\frac{1}{2}\sum_m\left[\rho_m\nabla^2\rho_m - 2\rho_m\tau_m + \frac{1}{2}\left(\vec{\nabla}\rho_m\right)^2 + J_m^2\right]\right]\,.\end{aligned}$$

This can be simplified by using $p\nabla^2 p = -(\vec{\nabla} p)^2 = -p'^2(\vec{\nabla}\rho)^2$, and dropping total derivatives, to get

$$\begin{aligned}\langle H^f_\sigma \rangle &= \frac{m^2_\sigma}{4} p^2 \sum_m \rho^2_m + \frac{m^2_\sigma}{8M^{\star 2}} p^2 \sum_m \left(\rho_m \nabla^2 \rho_m - 2\rho_m \tau_m\right) - \frac{p'^2}{4}(\vec{\nabla}\rho)^2 \sum_m \rho^2_m \\ &\quad + \frac{p^2}{4} \sum_m \left[\rho_m \nabla^2 \rho_m - 2\rho_m \tau_m + \frac{1}{2}\left(\vec{\nabla}\rho_m\right)^2 + J^2_m\right] .\end{aligned}$$

Simplifying further, let

$$q = \left(\frac{m^2_\sigma}{2M^{\star 2}} + 1\right) p^2 ,$$

so that $\langle H^f_\sigma \rangle$ can be written as

$$\begin{aligned}\langle H^f_\sigma \rangle &= \left[\frac{m^2_\sigma}{4} p^2 - \frac{p'^2}{4}(\vec{\nabla}\rho)^2\right] \sum_m \rho^2_m + \frac{q}{4} \sum_m \left(\rho_m \nabla^2 \rho_m - 2\rho_m \tau_m\right) \\ &\quad + \frac{p^2}{8} \sum_m \left[\left(\vec{\nabla}\rho_m\right)^2 + 2J^2_m\right] .\end{aligned}$$

B.3 Derivation of the time and space components for spin-orbit interaction

In the last two versions of the QMC model, QMCπ-II and QMCπ-III, the calculation for the spin-orbit (SO) part is done starting from the Bonn potential. This calculation is justified by the fact that only the two-body SO interactions are kept in the derivation. To compute for the Hartree-Fock energy density, the two-body One Boson Exchange (OBE) potential is employed. The second quantised OBE is expressed as

$$\begin{aligned}V_{OBE} &= \frac{1}{2} \sum_{\sigma_1,\ldots} \int \vec{p}_1 \ldots \langle \vec{p}_1 \sigma_1 \tau_1, \vec{p}_2 \sigma_2 \tau_2 | V | \vec{p}'_1 \sigma'_1 \tau'_1, \vec{p}'_2 \sigma'_2 \tau'_2 \rangle \\ &\quad a^\dagger(\vec{p}_1 \sigma_1 \tau_1) a^\dagger(\vec{p}_2 \sigma_2 \tau_2) a(\vec{p}'_2 \sigma'_2 \tau'_2) a(\vec{p}'_1 \sigma'_1 \tau'_1) ,\end{aligned}$$

where p is the momentum, and $\sigma, \tau = \pm 1/2$ are the spin and isospin projections. With $V_{OBE} = V_\sigma + V_\omega + V_\rho$, the meson contributions for spin-orbit can then be

separately written as

$$\begin{aligned}
\langle \vec{p}_1 \ldots | V_\sigma | \vec{p}_1' \ldots \rangle &= -\frac{G_\sigma}{(2\pi)^3}\delta\left(\vec{p}_1 + \vec{p}_2 - \vec{p}_1' - \vec{p}_2'\right) \qquad \text{(B.4)}\\
&\times \bar{u}(p_1\sigma_1)u(p_1'\sigma_1')\bar{u}(p_2\sigma_2)u(p_2'\sigma_2')\delta(\tau_1,\tau_1')\delta(\tau_2,\tau_2')\,,\\
\langle \vec{p}_1 \ldots | V_\omega | \vec{p}_1' \ldots \rangle &= \frac{G_\omega}{(2\pi)^3}\delta\left(\vec{p}_1 + \vec{p}_2 - \vec{p}_1' - \vec{p}_2'\right) \qquad \text{(B.5)}\\
&\times \bar{u}(p_1\sigma_1)\left[\mu_{IS}\gamma^\mu - F_2^s\frac{p_1^\mu + p_1^{'\mu}}{2M}\right]u(p_1'\sigma_1')\\
&\times \bar{u}(p_2\sigma_2)\left[\mu_{IS}\gamma_\mu - F_2^s\frac{p_{2\mu} + p_{2\mu}'}{2M}\right]u(p_2'\sigma_2')\delta(\tau_1,\tau_1')\delta(\tau_2,\tau_2')\,,\\
\langle \vec{p}_1 \ldots | V_\rho | \vec{p}_1' \ldots \rangle &= \frac{G_\rho}{(2\pi)^3}\delta\left(\vec{p}_1 + \vec{p}_2 - \vec{p}_1' - \vec{p}_2'\right) \qquad \text{(B.6)}\\
&\times \bar{u}(p_1\sigma_1)\left[\mu_{IV}\gamma^\mu - F_2^v\frac{p_1^\mu + p_1^{'\mu}}{2M}\right]u(p_1'\sigma_1')\\
&\times \bar{u}(p_2\sigma_2)\left[\mu_{IV}\gamma_\mu - F_2^v\frac{p_{2\mu} + p_{2\mu}'}{2M}\right]u(p_2'\sigma_2')\frac{\vec{\tau}_{\tau_1\tau_1'}\cdot\vec{\tau}_{\tau_2\tau_2'}}{4}\,,
\end{aligned}$$

where τ^a $(a = 1,2,3)$ are the isospin Pauli matrices and $\mu_{IS,IV} = 1 + F_2^{s,v}$ are the isoscalar and isovector magnetic moments, respectively, with values computed from the physical magnetic moments of protons and neutrons:

$$\begin{aligned}
\mu_{IS} &= \mu_p + \mu_n \sim 0.9\,,\\
\mu_{IV} &= \mu_p - \mu_n \sim 4.7\,.
\end{aligned}$$

B.3.1 Time part

In the earlier versions, QMC-I and QMCπ-I, the time part of SO interaction was derived within the QMC framework, as discussed in Section 2.4. It is emphasised that the following derivations for the time part starting from the Bonn potential, agrees with the earlier derivations. Thus, only the space part is in fact new in the total SO contribution.

In this subsection, the time part of the SO contribution, labelled with 'SO1',

will be computed. In the calculation, the following approximations are implemented, taking only the leading term in velocity:

$$\bar{u}(p\sigma)u(p'\sigma') \sim 1 - i\frac{\vec{\sigma}_{\sigma\sigma'}\cdot\vec{p}\times\vec{p}'}{4M^2}, \tag{B.7}$$

$$\bar{u}(p\sigma)\gamma^0 u(p'\sigma') \sim 1 + i\frac{\vec{\sigma}_{\sigma\sigma'}\cdot\vec{p}\times\vec{p}'}{4M^2}. \tag{B.8}$$

For the σ exchange, from Eqs. (B.4) and (B.7),

$$\begin{aligned}\langle\vec{p}_1\ldots|V_\sigma^{SO1}|\vec{p}_1'\ldots\rangle &= i\frac{G_\sigma}{(2\pi)^3}\delta\left(\vec{p}_1+\vec{p}_2-\vec{p}_1'-\vec{p}_2'\right)\mathbb{I}_{\tau_1\tau_1'}\mathbb{I}_{\tau_2\tau_2'}\\ &\times\left[\frac{\vec{\sigma}_{\sigma_1\sigma_1'}\cdot\vec{p}_1\times\vec{p}_1'}{4M^2}+1\leftrightarrow 2\right],\end{aligned}$$

and for the ω and ρ vector mesons, from Eqs. (B.5)-(B.6) and (B.8),

$$\begin{aligned}\langle\vec{p}_1\ldots|V_\omega^{SO1}|\vec{p}_1'\ldots\rangle &= i\frac{G_\omega\left(2\mu_{IS}-1\right)}{(2\pi)^3}\delta\left(\vec{p}_1+\vec{p}_2-\vec{p}_1'-\vec{p}_2'\right)\mathbb{I}_{\tau_1\tau_1'}\mathbb{I}_{\tau_2\tau_2'}\\ &\times\left[\frac{\vec{\sigma}_{\sigma_1\sigma_1'}\cdot\vec{p}_1\times\vec{p}_1'}{4M^2}+1\leftrightarrow 2\right],\\ \langle\vec{p}_1\ldots|V_\rho^{SO1}|\vec{p}_1'\ldots\rangle &= i\frac{G_\rho\left(2\mu_{IV}-1\right)}{(2\pi)^3}\delta\left(\vec{p}_1+\vec{p}_2-\vec{p}_1'-\vec{p}_2'\right)\frac{\vec{\tau}_{\tau_1\tau_1'}\cdot\vec{\tau}_{\tau_2\tau_2'}}{4}\\ &\times\left[\frac{\vec{\sigma}_{\sigma_1\sigma_1'}\cdot\vec{p}_1\times\vec{p}_1'}{4M^2}+1\leftrightarrow 2\right],\end{aligned}$$

where $\mathbb{I}$ is the unit matrix. With the single-particle wavefunction,

$$\phi_\alpha(\vec{p},\sigma,\tau) = (2\pi)^{-3/2}\int d\vec{r}\,\phi_\alpha(\vec{r},\sigma,\tau)e^{i\vec{p}\cdot\vec{r}}, \tag{B.9}$$

from where the HF Slater determinant is built, and further using time reversal symmetry of the HF state, the σ contribution to the potential is then expressed as,

$$\begin{aligned}V_\sigma^{SO1} &= i\frac{G_\sigma}{4M^2}\sum_{\alpha_1\alpha_2\in F}\sum_{\sigma_1\ldots}\int d\mathbf{r}\epsilon_{ijk}\\ &\sigma^i_{\sigma_1\sigma_1'}\nabla_j\left[\phi^*_{\alpha_1}(\mathbf{r}\sigma_1\tau_1)\right]\nabla_k\left[\phi_{\alpha_1'}(\mathbf{r}\sigma_1'\tau_1)\right]\phi^*_{\alpha_2}(\mathbf{r}\sigma_2\tau_2)\phi_{\alpha_2'}(\mathbf{r}\sigma_2\tau_2)a^\dagger_{\alpha_1}a^\dagger_{\alpha_2}a_{\alpha_2'}a_{\alpha_1'}.\end{aligned}$$

Performing an integration by parts on ∇_j, gives

$$\begin{aligned} V_\sigma^{SO1} &= -i\frac{G_\sigma}{4M^2}\sum_{\alpha_1\alpha_2\in F}\sum_{\sigma_1\ldots}\int d\mathbf{r}\epsilon_{ijk} \\ &\quad \sigma^i_{\sigma_1\sigma_1'}\phi^*_{\alpha_1}(\mathbf{r}\sigma_1\tau_1)\nabla_k\left[\phi_{\alpha_1'}(\mathbf{r}\sigma_1'\tau_1)\right]\nabla_j\left[\phi^*_{\alpha_2}(\mathbf{r}\sigma_2\tau_2)\phi_{\alpha_2'}(\mathbf{r}\sigma_2\tau_2)\right]a^\dagger_{\alpha_1}a^\dagger_{\alpha_2}a_{\alpha_2'}a_{\alpha_1'}\,. \end{aligned}$$

Now, recall the operators

$$\begin{aligned} D(\mathbf{r}) &= \sum_{\sigma\tau}\sum_{\alpha\alpha'}\phi^*_\alpha(\mathbf{r}\sigma\tau)\phi_{\alpha'}(\mathbf{r}\sigma\tau)a^\dagger_\alpha a_{\alpha'}\,, \\ \vec{\mathcal{J}}(\mathbf{r}) &= i\sum_{\sigma\sigma'\tau}\sum_{\alpha\alpha'}\phi^*_\alpha(\mathbf{r}\sigma\tau)\vec{\sigma}_{\sigma\sigma'}\times\vec{\nabla}\phi_{\alpha'}(\mathbf{r}\sigma'\tau)a^\dagger_\alpha a_{\alpha'}\,. \end{aligned}$$

For the expectation value,

$$\begin{aligned} \langle a^\dagger_{\alpha_1}a^\dagger_{\alpha_2}a_{\alpha_2'}a_{\alpha_1'}\rangle = & \qquad\qquad (B.10) \\ & \left[\delta(\alpha_1,\alpha_1')\delta(\alpha_2,\alpha_2') - \delta(\alpha_1,\alpha_2')\delta(\alpha_2,\alpha_1')\right]\Theta(\alpha_1\in F)\Theta(\alpha_2\in F)\,, \end{aligned}$$

where the direct (Hartree term) gives zero. Then,

$$\langle V_\sigma^{SO1}\rangle = \frac{G_\sigma}{4M^2}\int d\mathbf{r}\langle :\vec{\mathcal{J}}\cdot\vec{\nabla}D:\rangle\,.$$

The expectation value is solved using the Fermi traces in Appendix (B.1) which gives

$$\begin{aligned} \langle :\vec{\mathcal{J}}\cdot\vec{\nabla}D:\rangle &= \tilde{\mathrm{Tr}}\left[\vec{\mathcal{J}}\right]\cdot\tilde{\mathrm{Tr}}\left[\vec{\nabla}D\right] - \tilde{\mathrm{Tr}}\left[\vec{\mathcal{J}}\cdot\vec{\nabla}D\right]\,, \\ \langle :\vec{\mathcal{J}}\cdot\vec{\nabla}D:\rangle &= \vec{J}\cdot\vec{\nabla}\rho - \frac{1}{2}\sum_m\rho_m\vec{\nabla}\cdot\vec{J}_m - \frac{1}{4}\sum_m J_m^2\,. \end{aligned}$$

This is just the same computation for the ω meson except for the factor. Hence, for the isoscalar part, the σ and ω contribution to the time part of the spin-orbit is

$$\begin{aligned} \langle V_{\sigma\omega}^{SO1}\rangle &= \frac{G_\sigma + G_\omega(2\mu_{IS}-1)}{4M^2}\int d\mathbf{r}\langle :\vec{\mathcal{J}}\cdot\vec{\nabla}D:\rangle \\ &= -C_{IS}\left[\rho\vec{\nabla}\cdot\vec{J} + \frac{1}{2}\sum_m\rho_m\vec{\nabla}\cdot\vec{J}_m + \frac{1}{4}\sum_m J_m^2\right]\,, \end{aligned}$$

where

$$C_{IS} = \frac{1}{4M^2}\left[G_\sigma + G_\omega\left(2\mu_{IS} - 1\right)\right].$$

In the same way for the isovector case,

$$\langle V_\rho^{SO1}\rangle = \frac{G_\rho(2\mu_{IV}-1)}{4M^2}\langle\sum_a\int d\mathbf{r} : \vec{\mathcal{J}}_a\cdot\vec{\nabla}D_a :\rangle .$$

Using Fermi traces for the expectation value yields

$$\begin{aligned}\langle\sum_a : \vec{\mathcal{J}}_a\cdot\vec{\nabla}D_a :\rangle &= \sum_a \tilde{\mathrm{Tr}}\left[\vec{\mathcal{J}}_a\right]\cdot\tilde{\mathrm{Tr}}\left[\vec{\nabla}D_a\right] - \sum_a\tilde{\mathrm{Tr}}\left[\vec{\mathcal{J}}_a\cdot\vec{\nabla}D_a\right]\\ &= \left(\sum_m m\vec{J}_m\right)\cdot\left(\sum_m m\vec{\nabla}\rho_m\right)\\ &\quad - \sum_{m,m'} S_{mm'}\left(\frac{1}{2}\rho_m\vec{\nabla}\cdot\vec{J}_{m'} + \frac{1}{4}\vec{J}_m\cdot\vec{J}_{m'}\right),\end{aligned}$$

where $S_{mm'} = \delta_{mm'}m^2 + \frac{1}{2}\left(\delta_{m,m'+1} + \delta_{m',m+1}\right)$ with $m = 1/2$ for proton and $m = -1/2$ for neutron. Upon simplification, the ρ contribution for the time part of the spin-orbit is then

$$\langle V_\rho^{SO1}\rangle = -C_{IV}\left[\frac{3}{8}\sum_m\rho_m\vec{\nabla}\cdot\vec{J}_m + \frac{1}{8}J^2 - \frac{1}{16}\sum_m J_m^2\right], \tag{B.11}$$

where

$$C_{IV} = \frac{1}{4M^2}\left(2\mu_{IV}-1\right)G_\rho .$$

B.3.2 Space part of the vector mesons

Just as in the time part, only the leading term in the spin-orbit contribution are kept for the space component of the vector mesons using the approximation:

$$\bar{u}(p\sigma)\vec{\gamma}u(p'\sigma') \sim \frac{\vec{p}+\vec{p}'}{2M} + i\frac{\vec{\sigma}_{\sigma\sigma'}\times(\vec{p}-\vec{p}')}{2M}. \tag{B.12}$$

Using Eqs. (B.5) and (B.12), the space components, labelled with 'SO2', are given by,

$$\begin{aligned}\langle \vec{p}_1 \ldots | V_\omega^{SO2} | \vec{p}'_1 \ldots \rangle &= -\frac{G_\omega}{(2\pi)^3}\delta\left(\vec{p}_1+\vec{p}_2-\vec{p}'_1-\vec{p}'_2\right) \\ &\times \left[\frac{\vec{p}_1+\vec{p}'_1}{2M}+i\mu_{IS}\frac{\vec{\sigma}_{\sigma_1\sigma'_1}\times(\vec{p}_1-\vec{p}'_1)}{2M}\right] \\ &\times \left[\frac{\vec{p}_2+\vec{p}'_2}{2M}+i\mu_{IS}\frac{\vec{\sigma}_{\sigma_2\sigma'_2}\times(\vec{p}_2-\vec{p}'_2)}{2M}\right],\end{aligned}$$

and a similar expression coming from the ρ meson using Eqs. (B.6) and (B.12). Upon simplification and noting that $\vec{p}_2-\vec{p}'_2=\vec{p}'_1-\vec{p}_1$, the following expressions are obtained,

$$\begin{aligned}\langle \vec{p}_1 \ldots | V_\omega^{SO2} | \vec{p}'_1 \ldots \rangle &= i\frac{G_\omega\mu_{IS}}{(2\pi)^3}\delta\left(\vec{p}_1+\vec{p}_2-\vec{p}'_1-\vec{p}'_2\right)\mathbb{I}_{\tau_1\tau'_1}\mathbb{I}_{\tau_2\tau'_2} \\ &\times \left[\frac{\vec{\sigma}_{\sigma_2\sigma'_2}\cdot\vec{p}_1\times\vec{p}'_1}{2M^2}+1\leftrightarrow 2\right], \\ \langle \vec{p}_1 \ldots | V_\rho^{SO2} | \vec{p}'_1 \ldots \rangle &= i\frac{G_\rho\mu_{IV}}{(2\pi)^3}\delta\left(\vec{p}_1+\vec{p}_2-\vec{p}'_1-\vec{p}'_2\right)\frac{\vec{\tau}_{\tau_1\tau'_1}\cdot\vec{\tau}_{\tau_2\tau'_2}}{4} \\ &\times \left[\frac{\vec{\sigma}_{\sigma_2\sigma'_2}\cdot\vec{p}_1\times\vec{p}'_1}{4M^2}+1\leftrightarrow 2\right].\end{aligned}$$

Isoscalar case

Using Eq. (B.9) for the single-particle wavefunction, the space component of spin-orbit potential coming from the ω meson can be expressed as

$$\begin{aligned}V_\omega^{SO2} &= i\frac{G_\omega\mu_{IS}}{2M^2}\sum_{\alpha_1\alpha_2\in F}\sum_{\sigma_1\ldots}\int d\mathbf{r}\mathbb{I}_{\tau_1\tau'_1}\mathbb{I}_{\tau_2\tau'_2}\epsilon_{ijk}\sigma^i_{\sigma_2\sigma'_2} \\ &\nabla_j\left[\phi^*_{\alpha_1}(\mathbf{r}\sigma_1\tau_1)\right]\nabla_k\left[\phi_{\alpha'_1}(\mathbf{r}\sigma'_1\tau'_1)\right]\phi^*_{\alpha_2}(\mathbf{r}\sigma_2\tau_2)\phi_{\alpha'_2}(\mathbf{r}\sigma'_2\tau'_2)a^\dagger_{\alpha_1}a^\dagger_{\alpha_2}a_{\alpha'_2}a_{\alpha'_1}.\end{aligned}$$

Its expectation value is calculated using Eq. (B.10), to get

$$\begin{aligned}\langle V_\omega^{SO2}\rangle &= -i\frac{G_\omega \mu_{IS}}{2M^2}\sum_{\alpha_1\alpha_2\in F}\sum_{\sigma_1\ldots}\int d\mathbf{r}\epsilon_{ijk}\sigma^i_{\sigma_2\sigma_2'}\\ &\quad \nabla_j\left[\phi^*_{\alpha_1}(\mathbf{r}\sigma_1\tau_1)\right]\nabla_k\left[\phi_{\alpha_2}(\mathbf{r}\sigma_1\tau_1)\right]\phi^*_{\alpha_2}(\mathbf{r}\sigma_2\tau_2)\phi_{\alpha_1}(\mathbf{r}\sigma_2'\tau_2)\\ &= -i\frac{G_\omega \mu_{IS}}{2M^2}\sum_{\alpha_1\alpha_2\in F}\sum_{\sigma_1\ldots}\int d\mathbf{r}\epsilon_{ijk}\phi_{\alpha_1}(\mathbf{r}\sigma_2'\tau_2)\\ &\quad \nabla_j\left[\phi^*_{\alpha_1}(\mathbf{r}\sigma_1\tau_1)\right]\nabla_k\left[\phi_{\alpha_2}(\mathbf{r}\sigma_1\tau_1)\right]\phi^*_{\alpha_2}(\mathbf{r}\sigma_2\tau_2)\sigma^i_{\sigma_2\sigma_2'}\,.\end{aligned}$$

If HF state has axial symmetry, one can write:

$$\sum_{\alpha\in F}\phi_\alpha(\mathbf{r}\sigma f)\vec{\nabla}\left[\phi^*_\alpha(\vec{r}\sigma' f')\right] = \frac{\delta_{ff'}}{4}\left[\delta_{\sigma\sigma'}\vec{\nabla}\rho_f + i\vec{J}_f\times\vec{\sigma}_{\sigma\sigma'}\right], \tag{B.13}$$

$$\sum_{\alpha\in F}\vec{\nabla}\left[\phi_\alpha(\vec{r}\sigma f)\right]\phi^*_\alpha(\mathbf{r}\sigma' f') = \frac{\delta_{ff'}}{4}\left[\delta_{\sigma\sigma'}\vec{\nabla}\rho_f + i\vec{\sigma}_{\sigma\sigma'}\times\vec{J}_f\right], \tag{B.14}$$

which then allows to write

$$\begin{aligned}\langle V_\omega^{SO2}\rangle &= -i\frac{G_\omega \mu_{IS}}{32M^2}\sum_{\sigma_1\ldots}\int d\mathbf{r}\epsilon_{ijk}\\ &\quad \left(\delta_{\sigma_2'\sigma_1}\vec{\nabla}\rho_{\tau_1} - i\vec{\sigma}_{\sigma_2'\sigma_1}\times\vec{J}_{\tau_1}\right)_j\left(\delta_{\sigma_1\sigma_2}\vec{\nabla}\rho_{\tau_1} + i\vec{\sigma}_{\sigma_1\sigma_2}\times\vec{J}_{\tau_1}\right)_k\sigma^i_{\sigma_2\sigma_2'}\\ &= -i\frac{G_\omega \mu_{IS}}{32M^2}\sum_{\sigma_1\ldots}\int d\mathbf{r}\\ &\quad \left(\delta_{\sigma_2'\sigma_1}\vec{\nabla}\rho_\tau - i\vec{\sigma}_{\sigma_2'\sigma_1}\times\vec{J}_\tau\right)\cdot\left[\left(\delta_{\sigma_1\sigma_2}\vec{\nabla}\rho_\tau + i\vec{\sigma}_{\sigma_1\sigma_2}\times\vec{J}_\tau\right)\times\vec{\sigma}_{\sigma_2\sigma_2'}\right]\\ &= -i\frac{G_\omega \mu_{IS}}{32M^2}\sum_{\sigma_1\ldots}\int d\mathbf{r}\\ &\quad \delta_{\sigma_2'\sigma_1}\vec{\nabla}\rho_\tau\cdot\left(\delta_{\sigma_1\sigma_2}\vec{\nabla}\rho_\tau\times\vec{\sigma}_{\sigma_2\sigma_2'}\right) - i\vec{\sigma}_{\sigma_2'\sigma_1}\times\vec{J}_\tau\cdot\left(\delta_{\sigma_1\sigma_2}\vec{\nabla}\rho_\tau\times\vec{\sigma}_{\sigma_2\sigma_2'}\right)\\ &\quad -\delta_{\sigma_2'\sigma_1}\vec{\nabla}\rho_\tau\cdot\left[\vec{\sigma}_{\sigma_2\sigma_2'}\times i\left(\vec{\sigma}_{\sigma_1\sigma_2}\times\vec{J}_\tau\right)\right]\\ &\quad -\left(\vec{J}_\tau\times\vec{\sigma}_{\sigma_1\sigma_2}\right)\cdot\left[\vec{\sigma}_{\sigma_2\sigma_2'}\times\left(\vec{\sigma}_{\sigma_2'\sigma_1}\times\vec{J}_\tau\right)\right],\end{aligned}$$

where in the last term, the identity $\vec{A}\cdot\left(\vec{B}\times\vec{C}\right) = \vec{B}\cdot\left(\vec{C}\times\vec{A}\right)$ is used.

This is further simplified by using the spin formulae:

$$\sum_{\sigma\sigma'}\left(\vec{\sigma}_{\sigma\sigma'}\times\vec{A}\right)\cdot\left(\vec{\sigma}_{\sigma'\sigma}\times\vec{B}\right) = 4\vec{A}\cdot\vec{B}\,, \tag{B.15}$$

$$\sum_{\sigma\sigma'}\vec{\sigma}_{\sigma\sigma'}\times\left(\vec{\sigma}_{\sigma'\sigma}\times\vec{B}\right) = -4\vec{B}\,, \tag{B.16}$$

$$\sum_{\sigma\sigma'\sigma''}\left(\vec{A}\times\vec{\sigma}_{\sigma\sigma'}\right)\cdot\vec{\sigma}_{\sigma'\sigma''}\times\left(\vec{\sigma}_{\sigma''\sigma}\times\vec{B}\right) = -4i\vec{A}\cdot\vec{B}\,. \tag{B.17}$$

so that

$$\langle V_\omega^{SO2}\rangle = -i\frac{G_\omega\mu_{IS}}{32M^2}\int d\mathbf{r}\sum_\tau\left[4i\vec{J}_\tau\cdot\vec{\nabla}\rho_\tau+4\vec{\nabla}\rho_\tau\cdot i\vec{J}_\tau+4i\vec{J}_\tau\cdot\vec{J}_\tau\right].$$

The final expression for the ω meson contribution to the space part of the spin-orbit term is then,

$$\langle V_\omega^{SO2}\rangle = \frac{G_\omega\mu_{IS}}{4M^2}\int d\mathbf{r}\sum_\tau\left[\vec{J}_\tau\cdot\vec{\nabla}\rho_\tau+\frac{1}{2}\vec{J}_\tau\cdot\vec{J}_\tau\right].$$

Isovector case

For the ρ meson, the following operators are defined

$$\vec{\mathcal{P}}_a = \frac{1}{i}\sum_{\sigma\tau\tau'}\sum_{\alpha\alpha'}\phi_\alpha^*(\mathbf{r}\sigma\tau)\frac{\tau^a_{\tau\tau'}}{2}\vec{\nabla}\phi_{\alpha'}(\mathbf{r}\sigma\tau')a_\alpha^\dagger a_{\alpha'}\,,$$

$$\vec{\Sigma}_a = \sum_{\sigma\sigma'\tau\tau'}\sum_{\alpha\alpha'}\phi_\alpha^*(\mathbf{r}\sigma\tau)\frac{\tau^a_{\tau\tau'}}{2}\vec{\sigma}_{\sigma\sigma'}\phi_{\alpha'}(\mathbf{r}\sigma'\tau')a_\alpha^\dagger a_{\alpha'}\,,$$

which after integration by parts gives

$$V_\rho^{SO2} = -\frac{G_\rho\mu_{IV}}{2M^2}\sum_a\int d\mathbf{r}:\mathcal{P}_a\cdot\vec{\nabla}\times\vec{\Sigma}_a:\,.$$

Again, the expectation value is computed using Eq. (B.10) so that

$$\begin{aligned}\langle : \mathcal{P}_a \cdot \vec{\nabla} \times \vec{\Sigma}_a : \rangle &= -\frac{1}{i} \sum_{\alpha_1\alpha_2 \in F} \sum_{\sigma_1 \ldots} \left[\phi^*_{\alpha_1}(\mathbf{r}\sigma_1\tau_1) \frac{\tau^a_{\tau_1\tau_1'}}{2} \vec{\nabla} \phi_{\alpha_2}(\mathbf{r}\sigma_1\tau_1') \right] \cdot \\ &\quad \vec{\nabla} \times \left[\phi^*_{\alpha_2}(\mathbf{r}\sigma_2\tau_2) \frac{\tau^a_{\tau_2\tau_2'}}{2} \vec{\sigma}_{\sigma_2\sigma_2'} \phi_{\alpha_1}(\mathbf{r}\sigma_2'\tau_2') \right] \\ &= -\frac{1}{i} \epsilon_{ijk} \sum_{\alpha_1\alpha_2 \in F} \sum_{\sigma_1 \ldots} \phi^*_{\alpha_1}(\mathbf{r}\sigma_1\tau_1) \frac{\tau^a_{\tau_1\tau_1'}}{2} \\ &\quad \nabla_i \phi_{\alpha_2}(\mathbf{r}\sigma_1\tau_1') \nabla_j \phi^*_{\alpha_2}(\mathbf{r}\sigma_2\tau_2) \frac{\tau^a_{\tau_2\tau_2'}}{2} \sigma^k_{\sigma_2\sigma_2'} \phi_{\alpha_1}(\mathbf{r}\sigma_2'\tau_2') \,.\end{aligned}$$

Performing an integration by parts on ∇_j, gives

$$\begin{aligned}\langle : \mathcal{P}_a \cdot \vec{\nabla} \times \vec{\Sigma}_a : \rangle &= \frac{1}{4i} \epsilon_{ijk} \sum_{\alpha_1\alpha_2 \in F} \sum_{\sigma_1 \ldots} \phi_{\alpha_1}(\mathbf{r}\sigma_2'\tau_2') \\ &\quad \nabla_j \phi^*_{\alpha_1}(\mathbf{r}\sigma_1\tau_1) \tau^a_{\tau_1\tau_1'} \nabla_i \phi_{\alpha_2}(\mathbf{r}\sigma_1\tau_1') \phi^*_{\alpha_2}(\mathbf{r}\sigma_2\tau_2) \tau^a_{\tau_2\tau_2'} \sigma^k_{\sigma_2\sigma_2'} \\ &= \frac{1}{4i} \epsilon_{ijk} \sum_{\sigma_1 \ldots} X^j_{\tau_1} \delta_{\tau_2'\tau_1} \tau^a_{\tau_1\tau_1'} X^i_{\tau_2} \delta_{\tau_1'\tau_2} \tau^a_{\tau_2\tau_2'} \sigma^k_{\sigma_2\sigma_2'} \end{aligned} \tag{B.18}$$

where Eq. (B.13) is used so that the coefficients $X^{j,i}_{\tau_{1,2}}$ are defined as

$$X^j_{\tau_1} = \frac{1}{4} \left(\delta_{\sigma_2'\sigma_1} \vec{\nabla} \rho_{\tau_1} - i \vec{\sigma}_{\sigma_2'\sigma_1} \times \vec{J}_{\tau_1} \right)_j , \tag{B.19}$$

$$X^i_{\tau_2} = \frac{1}{4} \left(\delta_{\sigma_1\sigma_2} \vec{\nabla} \rho_{\tau_2} + i \vec{\sigma}_{\sigma_1\sigma_2} \times \vec{J}_{\tau_2} \right)_i . \tag{B.20}$$

Using the isospin sum:

$$\sum_a X_{\tau_1} \delta_{\tau_2'\tau_1} \tau^a_{\tau_1\tau_1'} X_{\tau_2} \delta_{\tau_1'\tau_2} \tau^a_{\tau_2\tau_2'} = \sum_a X_{\tau_1} \tau^a_{\tau_1\tau_2} \tau^a_{\tau_2\tau_1} X_{\tau_2} = 4 S_{\tau_1\tau_2} X_{\tau_1} X_{\tau_2} \,,$$

where $S_{\tau_1\tau_2} = \delta_{\tau_1\tau_2}\tau^2 + \frac{1}{2}(\delta_{\tau_1})$, allows Eq. (B.18) to be written as

$$\begin{aligned}\langle : \mathcal{P}_a \cdot \vec{\nabla} \times \vec{\Sigma}_a : \rangle &= \frac{1}{i} \epsilon_{ijk} \sum_{\sigma_1 \ldots} S_{\tau_1\tau_2} X^j_{\tau_1} X^i_{\tau_2} \sigma^k_{\sigma_2\sigma_2'} \\ &= \frac{1}{i} \sum_{\sigma_1 \ldots} S_{\tau_1\tau_2} \vec{X}_{\tau_1} \cdot \left[\vec{\sigma}_{\sigma_2\sigma_2'} \times \vec{X}_{\tau_2} \right]\end{aligned}$$

Rewriting the expressions for $X^{j,i}_{\tau_{1,2}}$ in Eqs. (B.19) and (B.20) gives

$$\begin{aligned}
\langle : \mathcal{P}_a \cdot \vec{\nabla} \times \vec{\Sigma}_a : \rangle &= \frac{1}{16i} \sum_{\sigma_1 \ldots} S_{\tau_1\tau_2} \left(\delta_{\sigma_2'\sigma_1} \vec{\nabla}\rho_{\tau_1} - i\vec{\sigma}_{\sigma_2'\sigma_1} \times \vec{J}_{\tau_1} \right) \cdot \\
&\quad \left[\vec{\sigma}_{\sigma_2\sigma_2'} \times \left(\delta_{\sigma_1\sigma_2} \vec{\nabla}\rho_{\tau_2} + i\vec{\sigma}_{\sigma_1\sigma_2} \times \vec{J}_{\tau_2} \right) \right] \\
&= \frac{1}{16i} \sum_{\sigma_1 \ldots} S_{\tau_1\tau_2} \left[\delta_{\sigma_2'\sigma_1} \vec{\nabla}\rho_{\tau_1} \cdot \left(\vec{\sigma}_{\sigma_2\sigma_2'} \times \delta_{\sigma_1\sigma_2} \vec{\nabla}\rho_{\tau_2} \right) \right] \\
&\quad - S_{\tau_1\tau_2} \left[\left(i\vec{\sigma}_{\sigma_2'\sigma_1} \times \vec{J}_{\tau_1} \right) \cdot \left(\vec{\sigma}_{\sigma_2\sigma_2'} \times \delta_{\sigma_1\sigma_2} \vec{\nabla}\rho_{\tau_2} \right) \right] \\
&\quad + S_{\tau_1\tau_2} \left[\delta_{\sigma_2'\sigma_1} \vec{\nabla}\rho_{\tau_1} \cdot \vec{\sigma}_{\sigma_2\sigma_2'} \times \left(i\vec{\sigma}_{\sigma_1\sigma_2} \times \vec{J}_{\tau_2} \right) \right] \\
&\quad + S_{\tau_1\tau_2} \left[\left(\vec{J}_{\tau_2} \times \vec{\sigma}_{\sigma_1\sigma_2} \right) \cdot \vec{\sigma}_{\sigma_2\sigma_2'} \times \left(\vec{\sigma}_{\sigma_2'\sigma_1} \times \vec{J}_{\tau_1} \right) \right] .
\end{aligned}$$

This is further simplified by using the spin formulae in Eq. (B.15) to get

$$\begin{aligned}
\langle : \mathcal{P}_a \cdot \vec{\nabla} \times \vec{\Sigma}_a : \rangle &= \frac{1}{16i} \sum_{\tau_1\tau_2} S_{\tau_1\tau_2} \left[-4i\vec{\nabla}\rho_{\tau_2} \cdot \vec{J}_{\tau_1} - 4i\vec{\nabla}\rho_{\tau_1} \cdot \vec{J}_{\tau_2} - 4i\vec{J}_{\tau_2} \cdot \vec{J}_{\tau_1} \right] \\
&= -\frac{1}{2} \sum_{\tau\tau'} S_{\tau\tau'} \left[\vec{J}_{\tau'} \cdot \vec{\nabla}\rho_{\tau} + \frac{1}{2} \vec{J}_{\tau} \cdot \vec{J}_{\tau'} \right] .
\end{aligned}$$

Hence, for the ρ meson, the space component in the spin-orbit term is

$$\langle V_\rho^{SO2} \rangle = \frac{G_\rho \mu_{IV}}{4M^2} \sum_{\tau\tau'} S_{\tau\tau'} \int d\mathbf{r} \left[\vec{J}_{\tau'} \cdot \vec{\nabla}\rho_{\tau} + \frac{1}{2} \vec{J}_{\tau} \cdot \vec{J}_{\tau'} \right] \tag{B.21}$$

B.3.3 Summary for spin-orbit contribution

To summarise, the full two-body spin-orbit Hamiltonian from QMC with both time and space parts, is expressed as,

$$\begin{aligned}
\langle H_{SO} \rangle &= -\left(C_{IS} + \frac{G_\rho \mu_{IV}}{8M^2} \right) \rho \vec{\nabla} \cdot \vec{J} \\
&\quad - \left(\frac{1}{2} C_{IS} + \frac{3}{8} C_{IV} + \frac{G_\omega \mu_{IS}}{4M^2} - \frac{G_\rho \mu_{IV}}{16M^2} \right) \sum_m \rho_m \vec{\nabla} \cdot \vec{J}_m \\
&\quad - \left(\frac{1}{8} C_{IV} - \frac{G_\rho \mu_{IV}}{16M^2} \right) J^2 \\
&\quad - \left(\frac{1}{4} C_{IS} - \frac{1}{16} C_{IV} - \frac{G_\omega \mu_{IS}}{8M^2} + \frac{G_\rho \mu_{IV}}{32M^2} \right) \sum_m J_m^2 ,
\end{aligned} \tag{B.22}$$

where, again, the coefficients $C_{IS,IV}$ are defined as

$$
\begin{aligned}
C_{IS} &= \frac{1}{4M^2}\left[G_\sigma + (2\mu_{IS} - 1)\, G_\omega\right] , \\
C_{IV} &= \frac{1}{4M^2}\,(2\mu_{IV} - 1)\, G_\rho \, .
\end{aligned}
$$

The spin-tensor J^2 terms, which are the last two terms of Eq. (B.22), can be further simplified so that

$$
\langle H_{SO}^{J^2} \rangle = \frac{G_\rho}{32M^2} J^2 - \frac{1}{16M^2}\left[(G_\sigma - G_\omega) + \frac{1}{4} G_\rho\right] \sum_m J_m^2 \, .
$$

B.4 Derivation of single-pion exchange contribution

In this section, derivation for the single-pion contribution, taken from Ref. [25], is laid out. Consider a nucleon in a nuclear pion field ϕ^α. The pionic interaction at the baryon level for all flavors, is given by

$$
\frac{3g_A}{5f_\pi} \int d\vec{r}\, \vec{j}_\pi^{\,\alpha}(\vec{r}) \cdot \vec{\nabla}\phi^\alpha(\vec{r}) \, ,
$$

where $g_A = 1.26$ and $f_\pi = 0.93$ MeV. For proton and neutron flavors, the density of pionic source is defined as

$$
\vec{j}_\pi^{\,\alpha}(\vec{r}) = \vec{\nabla} \cdot \sum_{i,j} \sum_{\sigma,\sigma',m,m'} \Phi^{*i}(\vec{r},\sigma,m)\tau^\alpha_{m,m'}\vec{\sigma}_{\sigma,\sigma'}\Phi^j(\vec{r},\sigma',m')a_i^\dagger a_j \, .
$$

The pionic contribution to the total energy, upon elimination of static pion field, is then,

$$
H_\pi = -\frac{1}{2}\left(\frac{g_A}{2f_\pi}\right)^2 \int d\vec{r}d\vec{r}'\, \vec{j}_\pi^{\,\alpha}(\vec{r}) G(\vec{r}-\vec{r}')\vec{j}_\pi^{\,\alpha}(\vec{r}') \, ,
$$

with $G(\vec{r}-\vec{r}') = (2\pi)^{-3}\int d\vec{q} e^{i\vec{q}\cdot(\vec{r}-\vec{r}')}/(q^2+m_\pi^2)$. Taking the expectation value yields

$$
\langle H_\pi \rangle = -\frac{1}{2}\left(\frac{g_A}{2f_\pi}\right)^2 \int d\vec{r}d\vec{r}'\, G(\vec{r}-\vec{r}')\left[\tilde{\mathrm{Tr}}\left[\vec{j}_\pi^{\,\alpha}(\vec{r})\right]\tilde{\mathrm{Tr}}\left[\vec{j}_\pi^{\,\alpha}(\vec{r}')\right] - \tilde{\mathrm{Tr}}\left[\vec{j}_\pi^{\,\alpha}(\vec{r})\vec{j}_\pi^{\,\alpha}(\vec{r}')\right]\right] \, .
$$

where the direct term vanishes due to time reversal symmetry. Thus,

$$\begin{aligned}
\langle H_\pi \rangle &= \frac{1}{2}\left(\frac{g_A}{2f_\pi}\right)^2 \int d\vec{r}d\vec{r}' G(\vec{r}-\vec{r}') \sum_{i,j\in F} \vec{\nabla}\left[\Phi^{*i}\vec{\sigma}\tau^\alpha\Phi^j\right]_r \vec{\nabla}\left[\Phi^{*j}\vec{\sigma}\tau^\alpha\Phi^i\right]_{r'} \\
&= \frac{1}{2}\left(\frac{g_A}{2f_\pi}\right)^2 \int d\vec{r}d\vec{r}' \vec{\nabla}_r\vec{\nabla}_{r'}[G(\vec{r}-\vec{r}')] \sum_{i,j\in F} \left[\Phi^{*i}\vec{\sigma}\tau^\alpha\Phi^j\right]_r \left[\Phi^{*j}\vec{\sigma}\tau^\alpha\Phi^i\right]_{r'} \\
&= \frac{1}{2}\left(\frac{g_A}{2f_\pi}\right)^2 \int \frac{1}{(2\pi)^3} d\vec{q}d\vec{r}d\vec{r}' \frac{e^{i\vec{q}\cdot(\vec{r}-\vec{r}')}}{q^2+m_\pi^2} \tilde{\mathrm{Tr}}\left[\vec{\sigma}\cdot\vec{q}\tau^\alpha\rho(\vec{r},\vec{r}')\vec{\sigma}\cdot\vec{q}\tau^\alpha\rho(\vec{r}',\vec{r})\right] .
\end{aligned}$$

In the last equation, the non-local density is defined as $\rho(\vec{r},\vec{r}') = \sum_{i,j\in F}\phi^i(r)\phi^{*i}(r')$ for each flavor. Solving for the traces gives

$$\langle H_\pi \rangle = \frac{1}{2}\left(\frac{g_A}{2f_\pi}\right)^2 \int \frac{1}{(2\pi)^3} d\vec{q}d\vec{r}d\vec{r}' e^{i\vec{q}\cdot(\vec{r}-\vec{r}')}\left(1-\frac{m_\pi^2}{q^2+m_\pi^2}\right)\rho_m(\vec{r},\vec{r}')\rho_n(\vec{r}',\vec{r}) .$$

Within the local density approximation, the density $\rho(\vec{r},\vec{r}')$ is computed at $\vec{R} = (\vec{r}+\vec{r}')/2$ using the Fermi gas approximation so that

$$\rho(\vec{r},\vec{r}') = \frac{3\pi^2}{k_F^2(\vec{R})}\int_0^{k_F(\vec{R})} d\vec{k}\frac{1}{(2\pi)^3}\rho(\vec{R})e^{i\vec{k}\cdot(\vec{r}-\vec{r}')} ,$$

where k_F is the Fermi momentum at the local density $\vec{R}$. Finally, the energy from the single-pion exchange can be expressed as

$$\begin{aligned}
\langle H_\pi \rangle_{mn} &= -\frac{9m_\pi^2 g_A^2}{32f_\pi^2}\int d\vec{R}\frac{\rho_m(\vec{R})\rho_n(\vec{R})}{k_{Fm}^3(\vec{R})k_{Fn}^3(\vec{R})} \\
&\quad \int_0^{k_{Fm}(\vec{R})} dk \int_0^{k_{Fn}(\vec{R})} dk' \int_{-1}^{1} du \frac{k^2k'^2}{k^2+k'^2-2kk'u+m_\pi^2} .
\end{aligned}$$

Bibliography

[1] B. D. Serot and J. D. Walecka. "The Relativistic Nuclear Many Body Problem". In: *Adv. Nucl. Phys.* 16 (1986), pp. 1–327.

[2] B. D. Serot and J. D. Walecka. "Recent progress in quantum hadrodynamics". In: *Int. J. Mod. Phys.* E 6 (1997), pp. 515–631.

[3] L.M. Robledo, T.R. Rodríguez, and R.R. Rodríguez-Guzmán. "Mean field and beyond description of nuclear structure with the Gogny force: A review". In: *J. Phys.* G 46.1 (2019), p. 013001. DOI: 10.1088/1361-6471/aadebd.

[4] P G Reinhard. "The relativistic mean-field description of nuclei and nuclear dynamics". In: *Rep. Prog. Phys.* 52.4 (1989), pp. 439–514. DOI: 10.1088/0034-4885/52/4/002.

[5] M. Dutra, O. Lourenço, S.S. Avancini, B.V. Carlson, A. Delfino, D.P. Menezes, C. Providência, S. Typel, and J.R. Stone. "Relativistic Mean-Field Hadronic Models under Nuclear Matter Constraints". In: *Phys. Rev.* C 90.5 (2014), p. 055203. DOI: 10.1103/PhysRevC.90.055203.

[6] A. W. Thomas. "QCD and a New Paradigm for Nuclear Structure". In: *EPJ Web Conf.* 123 (2016), p. 01003. DOI: 10.1051/epjconf/201612301003.

[7] P. A. M. Guichon. "A possible quark mechanism for the saturation of nuclear matter". In: *Phys. Lett.* B 200 (1988), pp. 235 –240. ISSN: 0370-2693. DOI: https://doi.org/10.1016/0370-2693(88)90762-9.

[8] J. R. Stone, P. A. M. Guichon, P. G. Reinhard, and A. W. Thomas. "Finite Nuclei in the Quark-Meson Coupling Model". In: *Phys. Rev. Lett.* 116 (9 2016), p. 092501. DOI: 10.1103/PhysRevLett.116.092501.

[9] P. A. M. Guichon and A. W. Thomas. "Quark structure and nuclear effective forces". In: *Phys. Rev. Lett.* 93 (2004), p. 132502. DOI: 10.1103/PhysRevLett.93.132502.

[10] P. A. M. Guichon, H. H. Matevosyan, N. Sandulescu, and A. W. Thomas. "Physical origin of density dependent force of the skyrme type within the quark meson coupling model". In: *Nucl. Phys.* A 772 (2006), pp. 1–19. DOI: 10.1016/j.nuclphysa.2006.04.002.

[11] X. Jin and B. K. Jennings. "Recovering relativistic nuclear phenomenology from the quark-meson coupling model". In: *Phys. Lett.* B 374 (1996), pp. 13–19. ISSN: 0370-2693.

[12] M. E. Bracco, G. Krein, and M. Nielsen. "Quark-meson coupling model with constituent quarks: Exchange and pionic effects". In: *Phys. Lett.* B 432 (1998), pp. 258 –265. ISSN: 0370-2693. DOI: https://doi.org/10.1016/S0370-2693(98)00654-6.

[13] G. Krein, A. W. Thomas, and K. Tsushima. "Fock terms in the quark-meson coupling model". In: *Nucl. Phys.* A 650 (1999), pp. 313–325. ISSN: 0375-9474.

[14] S. Nagai, T. Miyatsu, K. Saito, and K. Tsushima. "Quark–meson coupling model with the cloudy bag". In: *Phys. Lett.* B 666 (2008), pp. 239–244. ISSN: 0370-2693.

[15] J. R. Stone, P. A. M. Guichon, H. H. Matevosyan, and A. W. Thomas. "Cold uniform matter and neutron stars in the quark-mesons-coupling model". In: *Nucl. Phys.* A 792 (2007), pp. 341–369. DOI: 10.1016/j.nuclphysa.2007.05.011.

[16] A. W. Thomas, D. L. Whittenbury, J. D. Carroll, K. Tsushima, and J. R. Stone. "Equation of State of Dense Matter and Consequences for Neutron Stars". In: *EPJ Web Conf.* 63 (2013), p. 03004. DOI: 10.1051/epjconf/20136303004.

[17] D. L. Whittenbury, J. D. Carroll, A. W. Thomas, K. Tsushima, and J. R. Stone. "Quark-meson coupling model, nuclear matter constraints, and neutron star properties". In: *Phys. Rev.* C 89 (6 2014), p. 065801. DOI: 10.1103/PhysRevC.89.065801.

[18] N. Barik, R. N. Mishra, D. K. Mohanty, P. K. Panda, and T. Frederico. "Nuclear equation of state in a relativistic independent quark model with chiral symmetry and dependence on quark masses". In: *Phys. Rev.* C 88 (2013). ISSN: 0556-2813.

[19] R. N. Mishra, H. S. Sahoo, P. K. Panda, N. Barik, and T. Frederico. "Nuclear symmetry energy in a modified quark-meson coupling model". In: *Phys. Rev.* C 92 (4 2015), p. 045203. DOI: 10.1103/PhysRevC.92.045203.

[20] P. A. M. Guichon, K. Saito, E. N. Rodionov, and A. W. Thomas. "The Role of nucleon structure in finite nuclei". In: *Nucl. Phys.* A 601 (1996), pp. 349–379. DOI: 10.1016/0375-9474(96)00033-4.

[21] P. G. Blunden and G. A. Miller. "Quark-meson coupling model for finite nuclei". In: *Phys. Rev.* C 54 (1 1996), pp. 359–370. DOI: 10.1103/PhysRevC.54.359.

[22] K. Saito, K. Tsushima, and A. W. Thomas. "Nucleon and hadron structure changes in the nuclear medium and impact on observables". In: *Prog. Part. Nucl. Phys.* 58 (2007), pp. 1–167. DOI: 10.1016/j.ppnp.2005.07.003.

[23] P. Möller, A. J. Sierk, T. Ichikawa, and H. Sagawa. "Nuclear ground-state masses and deformations: FRDM(2012)". In: *Atom. Data Nucl. Data Tabl.* 109-110 (2016), pp. 1–204. DOI: 10.1016/j.adt.2015.10.002.

[24] P. Klüpfel, P. G. Reinhard, T. J. Bürvenich, and J. A. Maruhn. "Variations on a theme by Skyrme: A systematic study of adjustments of model parameters". In: *Phys. Rev.* C 79 (3 2009), p. 034310. DOI: 10.1103/PhysRevC.79.034310.

[25] P. A. M. Guichon, J. R. Stone, and A. W. Thomas. "Quark-Meson-Coupling (QMC) model for finite nuclei, nuclear matter and beyond". In: *Prog. Part. Nucl. Phys.* 100 (2018), pp. 262–297. DOI: 10.1016/j.ppnp.2018.01.008.

[26] M. Kortelainen, T. Lesinski, J. Moré, W. Nazarewicz, J. Sarich, N. Schunck, M. V. Stoitsov, and S. Wild. "Nuclear energy density optimization". In: *Phys. Rev.* C 82 (2 2010), p. 024313. DOI: 10.1103/PhysRevC.82.024313.

[27] J. C. Slater. "A Simplification of the Hartree-Fock Method". In: *Phys. Rev.* 81 (3 1951), pp. 385–390. DOI: 10.1103/PhysRev.81.385.

[28] M. Kortelainen, J. McDonnell, W. Nazarewicz, P.-G. Reinhard, J. Sarich, N. Schunck, M. V. Stoitsov, and S. M. Wild. In: *Phys. Rev.* C 85 (2 2012), p. 024304. DOI: 10.1103/PhysRevC.85.024304.

[29] J. R. Stone, N. J. Stone, and S. A. Moszkowski. "Incompressibility in finite nuclei and nuclear matter". In: *Phys. Rev.* C 89 (4 2014), p. 044316. DOI: 10.1103/PhysRevC.89.044316.

[30] M. Dutra, J. S. Sá Martins, A. Delfino, J. R. Stone, and P. D. Stevenson. "Skyrme interaction and nuclear matter constraints". In: *Phys. Rev.* C 85 (3 2012), p. 035201. DOI: 10.1103/PhysRevC.85.035201.

[31] J. R. Stone and P. G. Reinhard. "The Skyrme Interaction in finite nuclei and nuclear matter". In: *Prog. Part. Nucl. Phys.* 58 (2007), pp. 587–657. DOI: 10.1016/j.ppnp.2006.07.001.

[32] B. Li and X. Han. "Constraining the neutron–proton effective mass splitting using empirical constraints on the density dependence of nuclear symmetry energy around normal density". In: *Phys. Lett.* B 727 (2013), pp. 276 –281. ISSN: 0370-2693. DOI: https://doi.org/10.1016/j.physletb.2013.10.006.

[33] N. Wan, C. Xu, and Z. Ren. "Density slope of the symmetry energy $L(\rho_0)$ constrained by proton radioactivity". In: *Phys. Rev.* C 94 (4 2016), p. 044322. DOI: 10.1103/PhysRevC.94.044322.

[34] P. Ring and P. Schuck. *The Nuclear Many-Body Problem*. Berlin, Germany: Springer-Verlag, 1980.

[35] B. R. Martin. *Nuclear and particle physics*. West Sussex, England: John Wiley & Sons, Ltd., 2006.

[36] C. Amsler. *Nuclear and particle physics*. Bristol, England: IOP Publishing, 2015. ISBN: 0-7503-1103-7.

[37] H. Grawe, K. Langanke, and G. Martínez-Pinedo. "Nuclear structure and astrophysics". In: *Rep. Prog. Phys.* 70 (2007), p. 1525.

[38] M. Wang, G. Audi, F.G. Kondev, W. J. Huang, S. Naimi, and X. Xu. "The AME2016 atomic mass evaluation (II). Tables, graphs and references". In: *Chin. Phys.* C 41 (2017), p. 030003.

[39] A.I. Budaca, R. Budaca, and I. Silisteanu. "Extended systematics of alpha decay half lives for exotic superheavy nuclei". In: *Nucl. Phys.* A 951 (2016), pp. 60 –74. ISSN: 0375-9474. DOI: https://doi.org/10.1016/j.nuclphysa.2016.03.048.

[40] K. J. Pototzky, J. Erler, P. G. Reinhard, and V. O. Nesterenko. "Properties of odd nuclei and the impact of time-odd mean fields: A systematic Skyrme-Hartree-Fock analysis". In: *Eur. Phys. J.* A 46 (2010), pp. 299–313. ISSN: 1434-601X. DOI: 10.1140/epja/i2010-11045-6.

[41] M. Bender, K. Rutz, P. G. Reinhard, and J. A. Maruhn. "Pairing gaps from nuclear mean field models". In: *Eur. Phys. J.* A 8 (2000), pp. 59–75. DOI: 10.1007/s10050-000-4504-z.

[42] K. W. Schmid and F. Grummer. In: *Rep. on Prog. in Phys.* 50 (1987), p. 731.

[43] R. C. Barrett and D.F. Jackson. *Nuclear sizes and structure*. Oxford, UK: Clarendon Press, 1977.

[44] J. Friedrich and N. Voegler. "The salient features of charge density distributions of medium and heavy even-even nuclei determined from a systematic analysis of elastic electron scattering form factors". In: *Nucl. Phys.* A 373 (1982), pp. 192 –224. ISSN: 0375-9474. DOI: https://doi.org/10.1016/0375-9474(82)90147-6.

[45] K. A. Olive et al. "Rev. Part. Phys." In: *Chin. Phys.* C 38 (2014), p. 090001. DOI: 10.1088/1674-1137/38/9/090001.

[46] M. Bender, P.-H. Heenen, and P.-G. Reinhard. "Self-consistent mean-field models for nuclear structure". In: *Rev. Mod. Phys.* 75 (1 2003), pp. 121–180. DOI: 10.1103/RevModPhys.75.121.

[47] S. Mizutori, J. Dobaczewski, G. A. Lalazissis, W. Nazarewicz, and P. G. Reinhard. "Nuclear skins and halos in the mean field theory". In: *Phys. Rev.* C 61 (2000), p. 044326. DOI: 10.1103/PhysRevC.61.044326.

[48] J. Piekarewicz, A. R. Linero, P. Giuliani, and E. Chicken. "Power of two: Assessing the impact of a second measurement of the weak-charge form factor of ^{208}Pb". In: *Phys. Rev.* C 94 (3 2016), p. 034316. DOI: 10.1103/PhysRevC.94.034316.

[49] I. Angeli. "A consistent set of nuclear rms charge radii: properties of the radius surface R(N,Z)". In: *Atom. Data Nucl. Data Tabl.* 87 (2004), pp. 185 – 206. ISSN: 0092-640X. DOI: https://doi.org/10.1016/j.adt.2004.04.002.

[50] I. Angeli and K.P. Marinova. "Table of experimental nuclear ground state charge radii: An update". In: *Atom. Data Nucl. Data Tabl.* 99 (Jan. 2013). DOI: 10.1016/J.ADT.2011.12.006.

[51] X. Roca-Maza, M. Centelles, X. Viñas, and M. Warda. "Neutron Skin of ^{208}Pb, Nuclear Symmetry Energy, and the Parity Radius Experiment". In: *Phys. Rev. Lett.* 106 (25 2011), p. 252501. DOI: 10.1103/PhysRevLett.106.252501.

[52] S. Raman, C. W. G. Nestor Jr, and P. Tikkanen. "Transition probability from the ground to the first-excited 2+ state of even-even nuclides". In: *Atom. Data Nucl. Data Tabl.* 78 (2001), pp. 1–128. DOI: 10.1006/adnd.2001.0858.

[53] J. Stone, P. Guichon, and A. Thomas. "Superheavy Nuclei in the Quark-Meson-Coupling Model". In: *EPJ Web Conf.* 163 (2017), p. 00057. DOI: 10.1051/epjconf/201716300057.

[54] K. L. Martinez, A. W. Thomas, J. R. Stone, and P. A. M. Guichon. "Parameter optimization for the latest quark-meson coupling energy-density functional". In: *Phys. Rev.* C 100 (2 2019), p. 024333. DOI: 10.1103/PhysRevC.100.024333.

[55] K. L. Martinez, A. W. Thomas, P. A. M. Guichon, and J. R. Stone. "Tensor and pairing interactions within the quark-meson coupling energy-density functional". In: *Phys. Rev. C* 102 (3 2020), p. 034304. DOI: 10.1103/PhysRevC.102.034304.

[56] S. Balay, S. Abhyankar, M. F. Adams, J. Brown, P. Brune, K. Buschelman, L. Dalcin, V. Eijkhout, W. D. Gropp, D. Kaushik, M. G. Knepley, L.C. McInnes, K.R., B.F. Smith, S. Zampini, and H. Zhang. *PETSc Users Manual*. Tech. rep. ANL-95/11 - Revision 3.7. Argonne National Laboratory, 2016.

[57] S. Balay, W. D. Gropp, L. C. McInnes, and B. F. Smith. "Efficient Management of Parallelism in Object Oriented Numerical Software Libraries". In: *Modern Software Tools in Scientific Computing*. Ed. by E. Arge, A. M. Bruaset, and H. P. Langtangen. Birkhäuser Press, 1997, pp. 163–202.

[58] T. Munson, J. Sarich, S. Wild, S. Benson, and L.C. McInnes. *Toolkit for Advanced Optimization (TAO) Users Manual*. Tech. rep. ANL/MCS-TM-322 - Revision 3.5. Argonne National Laboratory, 2014.

[59] H. De Vries, C. W. De Jager, and C. De Vries. "Nuclear charge and magnetization density distribution parameters from elastic electron scattering". In: *Atom. Data Nucl. Data Tabl.* 36 (1987), pp. 495–536. DOI: 10.1016/0092-640X(87)90013-1.

[60] A. Trzcińska, J. Jastrzębski, P. Lubiński, B. Kłos, F. J. Hartmann, T. von Egidy, and S. Wycech. "Antiprotonic atoms - a tool for the investigation of the nuclear periphery". In: *AIP Conf. Proc.* 793 (2005), pp. 214–221. DOI: 10.1063/1.2121984.

[61] M. Grasso. "Magicity of the ^{52}Ca and ^{54}Ca isotopes and tensor contribution within a mean-field approach". In: *Phys. Rev.* C 89 (3 2014), p. 034316. DOI: 10.1103/PhysRevC.89.034316.

[62] D. Steppenbeck et al. "Investigating the strength of the N = 34 subshell closure in54Ca". In: *J. Phys.* 445 (2013), p. 012012. DOI: 10.1088/1742-6596/445/1/012012.

[63] D.-C. Dinca et al. "Reduced transition probabilities to the first 2^+ state in ^{52,54,56}Ti and development of shell closures at $N = 32, 34$". In: *Phys. Rev.* C 71 (4 2005), p. 041302. DOI: 10.1103/PhysRevC.71.041302.

[64] A. Bürger et al. "Relativistic Coulomb excitation of neutron-rich 54,56,58Cr: On the pathway of magicity from N=40 to N=32". In: *Phys. Lett.* B 622 (2005), pp. 29 –34. ISSN: 0370-2693. DOI: https://doi.org/10.1016/j.physletb.2005.07.004.

[65] O. B. Tarasov et al. "Discovery of ^{60}Ca and Implications For the Stability of ^{70}Ca". In: *Phys. Rev. Lett.* 121 (2 2018), p. 022501.

[66] A. V. Afanasjev and S. E. Agbemava. "Covariant energy density functionals: Nuclear matter constraints and global ground state properties". In: *Phys. Rev.* C 93 (5 2016), p. 054310. DOI: 10.1103/PhysRevC.93.054310.

[67] E. Wigner. "On the Consequences of the Symmetry of the Nuclear Hamiltonian on the Spectroscopy of Nuclei". In: *Phys. Rev.* 51 (2 1937), pp. 106–119. DOI: 10.1103/PhysRev.51.106.

[68] W. Satuła, D.J. Dean, J. Gary, S. Mizutori, and W. Nazarewicz. "On the origin of the Wigner energy". In: *Phys. Lett.* B 407.2 (1997), pp. 103 –109. ISSN: 0370-2693. DOI: https://doi.org/10.1016/S0370-2693(97)00711-9.

[69] C. Qi and R. Wyss. "$N = Z$ nuclei: A laboratory for neutron-proton collective mode". In: *Phys. Scripta* 91 (2016), p. 013009. DOI: 10.1088/0031-8949/91/1/013009.

[70] I. Boboshin, V. Varlamov, B. Ishkhanov, S. Komarov, and V. Orlin. "Quadrupole deformation of the nucleus and dynamic vibrations of its surface". In: *Bulletin of The Russian Academy of Sciences: Physics* 71 (Mar. 2007), pp. 320–324. DOI: 10.3103/S1062873807030045.

[71] K. Heyde and J.L. Wood. "Shape coexistence in atomic nuclei". In: *Rev. Mod. Phys.* 83 (4 2011), pp. 1467–1521. DOI: 10.1103/RevModPhys.83.1467.

[72] J.L. Wood and K. Heyde. "A focus on shape coexistence in nuclei". In: *J. Phys. G Nucl. Part. Phys.* 43 (2016), p. 4. ISSN: 0954-3899.

[73] A. Poves. "Shape coexistence in nuclei". In: *J. Phys. G Nucl. Part. Phys.* 43 (2016), p. 020401. DOI: 10.1088/0954-3899/43/2/020401.

[74] G. Co', M. Anguiano, and A.M. Lallena. "Shell closure at N = 34 and the 48Si nucleus". In: *Int. J. Mod. Phys.* E 28.07 (2019), p. 1950054. DOI: 10.1142/S021830131950054X.

[75] B. Kumar, S.K. Biswal, and S.K. Patra. "Evolution of N = 32,34 shell closure in relativistic mean field theory". In: *DAE Symp. Nucl. Phys.* 61 (2016). Ed. by B.V. John, D. Dutta, and A. Saxena, pp. 196–197.

[76] T. R. Rodríguez and J. L. Egido. "On the robustness of sub-shell closures: A high angular momentum analysis of the titanium isotopes". In: *Phys. Lett.* B 804 (2020), p. 135359. ISSN: 0370-2693. DOI: https://doi.org/10.1016/j.physletb.2020.135359.

[77] G. Saxena and M. Kaushik. "Behaviour of the pf shell under the RMF+BCS description". In: *Chin. J. Phys.* 55.4 (2017), pp. 1149 –1161. ISSN: 0577-9073. DOI: https://doi.org/10.1016/j.cjph.2017.03.022.

[78] B. Fornal et al. "Development of shell closures at $N = 32, 34$. II. Lowest yrast excitations in even-even Ti isotopes from deep-inelastic heavy-ion collisions". In: *Phys. Rev.* C 70 (6 2004), p. 064304. DOI: 10.1103/PhysRevC.70.064304.

[79] S. N. Liddick et al. "Lowest Excitations in ^{56}Ti and the Predicted $N = 34$ Shell Closure". In: *Phys. Rev. Lett.* 92 (7 2004), p. 072502. DOI: 10.1103/PhysRevLett.92.072502.

[80] J. Ljungvall et al. "Shape Coexistence in Light Se Isotopes: Evidence for Oblate Shapes". In: *Phys. Rev. Lett.* 100 (10 2008), p. 102502. DOI: 10.1103/PhysRevLett.100.102502.

[81] J. Henderson et al. "Localizing the Shape Transition in Neutron-Deficient Selenium". In: *Phys. Rev. Lett.* 121 (8 2018), p. 082502. DOI: 10.1103/PhysRevLett.121.082502.

[82] K. Wrzosek-Lipska and L.P. Gaffney. "Unique and complementary information on shape coexistence in the neutron-deficient Pb region derived from Coulomb excitation". In: *J. Phys. G Nucl. Part. Phys.* 43 (2016), p. 024012.

[83] A. N. Andreyev et al. "A triplet of differently shaped spin-zero states in the atomic nucleus 186Pb". In: *Nature* 405 (2000), pp. 430–433.

[84] H. De Witte et al. "Nuclear Charge Radii of Neutron-Deficient Lead Isotopes Beyond $N = 104$ Midshell Investigated by In-Source Laser Spectroscopy". In: *Phys. Rev. Lett.* 98 (11 2007), p. 112502. DOI: 10.1103/PhysRevLett.98.112502.

[85] H. H. Matevosyan. "Exploring the quark-gluon content of hadrons: from mesons to nuclear matters". LSU Doctoral Dissertations. 2007.